Paleoenvironmental reconstruction of a Neoarchean oxygen oasis

Dissertation

der Mathematisch-Naturwissenschaftlichen Fakultät
der Eberhard Karls Universität Tübingen
zur Erlangung des Grades eines
Doktors der Naturwissenschaften
(Dr. rer. nat.)

vorgelegt von
Dipl.-Min. Sümeyya Eroğlu
aus Herrenberg

Tübingen
2016

Gedruckt mit Genehmigung der Mathematisch-Naturwissenschaftlichen Fakultät der Eberhard Karls Universität Tübingen.

Tag der mündlichen Prüfung:	27. 10. 2016
Dekan:	Prof. Dr. Wolfgang Rosenstiel
1. Gutachter:	Prof. Dr. Ronny Schönberg
2. Gutachter:	Prof. Dr. Andreas Kappler

Ich erkläre hiermit, dass ich die zur Promotion eingereichte Arbeit mit dem Titel „Paleoenvironmental reconstruction of a Neoarchean oxygen oasis“ selbstständig verfasst, nur die angegebenen Quellen und Hilfsmittel benutzt und wörtlich oder inhaltlich übernommene Stellen (alternativ: Zitate) als solche gekennzeichnet habe. Ich erkläre, dass die Richtlinien zur Sicherung guter wissenschaftlicher Praxis der Universität Tübingen (Beschluss des Senats vom 25.05.2000) beachtet wurden. Ich versichere an Eides statt, dass diese Angaben wahr sind und, dass ich nichts verschwiegen habe. Mir ist bekannt, dass die falsche Angabe einer Versicherung an Eides statt mit Freiheitsstrafe bis zu drei Jahren oder mit Geldstrafe bestraft wird.

Ort, Datum Unterschrift

Tübingen, 11.09.2016

A Geochemistry Ditty

- by Christopher Pearce

As I sit here watching my columns drip,
I thought I'd put together a little writ.
It's about something that's not always so plain to see;
the hidden world of isotope geochemistry.

It starts with a rock, water or gas
that contains an element of interest with a particular mass.
You crush, dissolve, evaporate or ash
until it resembles nothing more than a residual splash.

Next, with hands as steady as they can be,
weigh out some spike so that you can perform ID.
(Of course if you are feeling particularly pious,
using a DS will enable you to correct for subsequent mass bias.)

A drop more acid then on we go,
to run the columns that flow slow slow slow!
With resin and frits that just won't sit right,
they'll keep you stuck in the lab until late at night.

But finally it's done and the samples are now ready
to be aspirated and analysed by mass spectrometry.
You tweak and you tune and you wait all day long,
but the blasted machine won't behave unless you play its favorite song.

Eventually the standards come down to a value that's alright,
at just about the time you planned to call it a night.
However the lure of the data means you set the run going,
while keeping everything crossed that the nebulizer stays flowing.

The next day… oh joy, what fun, can you see?
A brand new delta value that's been generated just by me!
Now back to the lab to clean all that plastic;
a few hundred more runs like this doesn't sound too drastic…

To end, while I think that it's absolutely fab,
sitting on my own running columns in the lab.
I do so wish there was someone who wanted a PhD,
that would come and run all these wretched samples for me!

Acknowledgment

Ronny Schönberg designed this great project and gave me the opportunity to work on it. He supported me all those years, and I am very grateful for his guidance, expertise, enthusiasm, tolerance, and that his door was always open. Thank you, Ronny!!!

I also want to thank Heiner Taubald and Martin Wille, who were great advisors during the last years. Their critical thinking and new ideas were essential for this project and they always pushed me to think out of the box.

I am deeply thankful to Betsy Swanner, who brought with her brilliant ideas a whole new dynamic in this project. She always motivated, encouraged and supported me in Tübingen and during my research visit at the Iowa State University. The project would have never reached the stage where it is today if it weren't for her.

I owe 'Prof Nic' Beukes my gratitude for his help during the field work in South Africa. He is an amazing scientist and teacher and it was an honor to work with him.

Mark van Zuilen introduced me into the Raman world and gave me the opportunity to work in his Lab. He is a great advisor and his expertise is just remarkable.

This project was funded by grants from the Deutsche Forschungsgemeinschaft, the Carl-Zeiss Stiftung, and the "Nachwuchswissenschaftlerinnen"-Grant by the University of Tübingen. Another grant from the Fulbright Commission allowed me to spend 5 months at the Iowa State University in Ames, which was a wonderful experience. I met a lot of great people, and especially I want to thank Maddie, Jared, Hsin, Tom, Emily and Nic from the office, as well as Jacqueline, Suzy, Franek, Paul, Mark, Bill, Al, Neil and DeAnn for their help during my stay.

The last 8 years I spent in the Isotope Geochemistry Group were just awesome and I met some wonderful people there. Thanks to all of you guys for the great time in the lab and at the 'Kaffeerunde'. In particular, I want to thank Elmar, Bernd, Doro, Dagmar, Ilka, Kerstin, Felix, Daniel, Luthi, Mario, and Vanessa for their help and advice during the analytical work. Special thanks goes to Florian and Gülüm, who shared the office with me the last couple of years and always lightened the mood :-).

I also want to thank the Geomicrobiology Group here in Tübingen, in particular Elif Köksoy, Wenfang Wu, Anneli Sundman, Markus Maisch, and Timm Bayer, for helpful and interesting discussions over the last years.

Thanks also goes to Simone Schafflick, Indra Gill-Kopp, and Per Jeisecke, who prepared numerous thin sections for me.

I want to thank Thomas Wendel, Bernice Nisch, and Ellen Struve from the *Zentrum für Angewandte Geowissenschaften* for their support during TOC analyses.

Sakura Pascarelli and Florian Perrin from the ESRF in Grenoble are thanked for their support during synchrotron measurements.

Sabine Goldberg is thanked for providing analytical data of Mo adsorption on carbonates.

Martin Danisik always inspired me and is a great mentor. Thanks Martin for all your encouragement and advice over the last years!

In my 11 years here in Tübingen, I met a lot of great people. In particular I want to thank the 'Saunagruppe', the 'Strickgruppe', and the 'Mensagruppe' for their friendship and moral support. Especially I want to thank Sarah and Elena.

My family was always there for me with their support, patience, advice, fun, warmth, love and food :). THANK YOU!!!

Abir, I don't know if I could have done that without you … you will always be my person.

Contributions of others

For this study about 70 % of the laboratory work and data collection, about 90 % of the data evaluation and interpretation, and about 85 % of writing were done by me. In the following the scientific contributions of others are listed:

1. Project idea

The main idea of this project is from Prof. Ronny Schönberg (University of Tübingen), who was funded together with Dr. Martin Wille and Dr. Heinrich Taubald (both from University of Tübingen) by the Deutsche Forschungsgemeinschaft (SCHO1071/4-1) and the Carl-Zeiss Stiftung. Prof. Elizabeth Swanner (Iowa State University) had the idea to investigate the Fe systematics on Ca-Mg carbonates and was funded by the Nachwuchswissenschaftlerinnen Grant from the University of Tübingen.

2. Sampling and drill core logging

During an earlier field campaign in 2010 some of the here investigated samples of the KMF-5 drill core were sampled by Prof. Ronny Schönberg, Dr. Kirsten van Zuilen, and Dr. Mark van Zuilen (both at the Institut de Physique du Globe de Paris (IPGP)). During the field campaign in 2012, Ilka Kleinhanns, Tobias Renz, Florian Kurzweil (from University of Tübingen) assisted Prof. Ronny Schönberg and me during sampling of the KMF-5 and of the Kuruman Kop. Samples of BH-1 were provided by Prof. Nicolas Beukes (University of Johannesburg). The logging of the KMF-5 was solely done by Prof. Nicolas Beukes during the field campaign in 2012.

3. Analyses and sample preparation

Dr. Kerstin Drost (now at Helmholtz-Zentrum Dresden-Rossendorf) conducted trace element analyses at the facilities of the Isotope Geochemistry Group at the University of Tübingen, with my assistance during laboratory work. She also did the data reduction and helped me with the evaluation of the data.

Sabine Goldberg (United States Department of Agriculture) performed all experiments about Mo adsorption on calcite and generously provided all the information and data.

Bernd Steinhilber conducted all carbon and oxygen analyses at the facilities of the Isotope Geochemistry Group at the University of Tübingen. Preparation of the carbonate and mudrock samples for the analyses was done by Felix Hüttemann and me.

Prof. Elizabeth Swanner conducted about 50 % of the synchrotron analyses at ESRF. Dr. Sakura Pascarelli supervised the measurements.

Dr. Mark van Zuilen conducted Raman analyses at the IPGP during the first sample series in 2014, and helped me during the second samples series in 2015.
Simone Schafflick, Indra Gill-Kopp, and Per Jeisecke prepared thin sections from carbonate and mudrock samples at the University of Tübingen.
TOC and TC analyses were conducted at the Zentrum für Angewandte Geowissenschaften (ZAG) at the University of Tübingen by Bernice Nisch and Ellen Struve. Sample preparation was mainly done by me and partly by Bernice Nisch.
Christian Luthardt, Mario Säussele and Daniel Schöckle prepared some of the fused glass beads for XRF analyses at the facilities of the Isotope Geochemistry Group at the University of Tübingen, which were conducted by Daniel Schöckle and Dr. Heinrich Taubald.
Dorothea Mühlbayer-Renner milled some of the here analyzed samples.
Scott Schlorholtz conducted XRD analyses at the Material Analyses and Research Lab (MARL) at the Iowa State University.

4. Text, figures, and tables

Prof. Nicolas Beukes wrote most of Chapter 2.1.1 (Description of KMF-5), and edited Chapter 2 (Geological Overview). Dr. Ronny Schönberg, Dr. Martin Wille, Prof. Elizabeth Swanner, Dr. Mark van Zuilen, Dr. Kerstin Drost, and Dr. Heinrich Taubald edited and reviewed parts of this the text and improved it. Parts of this thesis have been published and went through a peer-review process (*S. Eroglu, R. Schoenberg, M. Wille, N.J. Beukes, and H. Taubald (2015), Geochemical stratigraphy, sedimentology, and Mo isotope systematics of the ca. 2.58-2.50 Ga-old Transvaal Supergroup carbonate platform, South Africa, Precambrian Research 266, 27-46*).
All figures and tables were prepared by me. Dr. Nicolas Beukes provided the log of the KMF-5 in Figure 2-3. Dr. Elizabeth Swanner provided the information in Table 4-11.

5. Scientific ideas

Numerous discussions with Prof. Ronny Schönberg, Dr. Martin Wille, Prof. Elizabeth Swanner, Dr. Mark van Zuilen, Prof. Nicolas Beukes, Dr. Heinrich Taubald, as well es other members of the Isotope Geochemistry Group and of the Geomicrobiology Group (University of Tübingen), helped and inspired me to interpret the data.

Contents

Abstract

The Neoarchean-Paleoproterozoic Transvaal Supergroup in South Africa contains the Campbellrand-Malmani carbonate platform (CMCP), which was deposited in shallow seawater between ~2.58 to 2.50 billion years ago, about 200 million years before the rise of atmospheric oxygen (Great Oxidation Event - GOE). The platform is mainly composed of alternating stromatolitic carbonates and siliciclastic mudrocks and is a prominent candidate for (isotope-) geochemical mapping to investigate the appearance of very small amounts of free oxygen that accumulated in shallow seawater preceding the GOE. Thus, the CMCP might represent an Archean 'oxygen oasis' in an otherwise anoxic environment.

The goal of this study was to reconstruct the paleoenvironmental conditions and the redox state of the CMCP over its time of deposition in order to understand if and how an oxygen oasis evolved in this setting. To do so, carbonate and mudrock samples from the platform facies of the CMCP were analyzed for their major and trace element composition as well as carbon, molybdenum, and iron isotope signatures. Additionally, Raman analyses, synchrotron-based X-Ray absorption spectroscopy, and oxygen and silicon isotope analyses were conducted to gain information on the diagenetic history of the samples and their Fe speciation. Results were combined with sedimentological observations and published data from other studies about the slope facies of the CMCP.

Geochemical indicators, such as Fe-to-Mn ratios and REE+Y abundances reveal a dependence on water depth and changing influxes of different water sources from the open ocean and the continent. Furthermore, those abundances reveal the preservation of primary geochemical signatures despite large scale dolomitization and silicification. Raman spectra reveal that the CMCP experienced only lower greenschist metamorphic conditions and imply, in addition to $\delta^{18}O$ signatures, that the here investigated samples are well preserved and reflect original signatures of some geochemical indicators that allow a paleoenvironmental reconstruction of the CMCP.

Results indicate molybdenum and iron redox cycling within the carbonates and mudrocks, which was dominated by secondary processes within the soft sediment during early diagenesis and different respiration pathways of organic matter. However, heavy $\delta^{98}Mo$ signatures of up to +1.40 ‰ in carbonates and mudrocks throughout the complete CMCP succession indicate the presence of free oxygen in the atmosphere-ocean system at the time of deposition and can be considered as a minimum value for Neoarchean seawater, which is in agreement with earlier molybdenum isotope studies on carbonates and mudrocks from the slope facies. Similarly, coupled light $\delta^{56}Fe$ values and low iron concentrations of pure carbonates

that were deposited during open marine conditions, can be explained by Rayleigh distillation through partial Fe oxidation between ferruginous deeper water and oxygenated shallow water, although a fractionation by anaerobe photoferrotrophs cannot be ruled out. Concentration estimates of aqueous Fe(II) imply that concentrations on the platform were about three times lower than along the slope, and are strongly dependent on water temperature, sedimentation rate and Ca^{2+} concentration in the seawater. Overall, the Mo and Fe isotope composition of CMCP sediments support the presence of molecular oxygen in the shallow-marine system and emphasize the utility of Ca-Mg carbonates as proxies for trace metal systematics in the aqueous environment.

Earlier studies showed that the CMCP developed from a steep ramp architecture in the lower part of the succession to a rimmed margin architecture in the upper part, which changed the dynamics of relative water influxes from the open ocean and the continent. The lower CMCP was rather exposed to reducing hydrothermal fluids from the open ocean. This reducing power was further fueled by the flux of organic material in the platform facies, and is reflected in Ca-Mg carbonates that are dominated by Fe(II)-species. With the development of the rimmed margin, the influx of open ocean water was diminished, which probably impacted the respiration pathways of the local ecosystem, changing from anaerobe photo- and chemolithotrophs to dominantly aerobe phototrophs. This change in respiration together with the increased supply of nutrients from the continent under aerobe water column conditions might have fueled primary production in the platform facies of the upper CMCP. This increased the burial rate of microbially produced organic material in siliciclastic mudrocks along the slope, resulting in a depletion of the dissolved inorganic carbon pool of the restricted platform interior in light ^{12}C, which is reflected in a shift to higher $\delta^{13}C_{carb}$ signatures in the platform carbonates. All these factors imply a higher oxidation state in the upper CMCP compared to the lower CMCP, which is also reflected in the preservation of Fe(III)-species in the platform carbonates of the upper CMCP that might be explained by an aerobe oxidation of aqueous Fe(II) during adsorption on the carbonate surface.

This study provides multiple indications that the CMCP represents an ancient oxygen oasis. However, it also shows that special environmental and depositional conditions were necessary to induce this development, in particular the formation of the rimmed margin and the restriction of the platform interior from the open ocean. In this restricted environment, oxygen production by aerobe photosynthesis could have increased relative to oxygen consumption by reducing species and induced an increasing oxidation of the shallow-marine environment over time.

Zusammenfassung

Die Neoarchaisch-Paläoproterozoische Transvaal Supergroup (Südafrika) beinhaltet die Campbellrand-Malmani Karobonatplattform (CMKP), die im küstennahen Flachwasser zwischen ~2.58 bis 2.50 Milliarden Jahren abgelagert wurde, 200 Millionen Jahre vor dem Anstieg von freiem Sauerstoff in der Atmosphäre („Great Oxidation Event“ – GOE). Die CMKP besteht größtenteils aus stromatolitischen Karbonaten und Schwarzschiefern und wurde bereits in früheren Studien hinsichtlich ihrer isotopengeochemischen Signaturen untersucht, um mögliche Rückschlüsse auf das Vorkommen von Sauerstoff im flachmarinen Milieu, noch vor dem GOE, zu ziehen. Daher könnte die CMKP eine sogenannte ‘Sauerstoffoase’ in einer ansonsten sauerstoff-freien Umwelt darstellen.

Das Ziel dieser Studie war es, die Paläo-Umweltbedingungen sowie die Redox-Bedingungen über den Ablagerungszeitraum der CMKP zu rekonstruieren und zu verstehen, ob und wie sich eine Sauerstoffoase in diesem Ablagerungmilieu bilden konnte. Dabei wurden Karbonate und Schwarzschiefer von der Schelfplattform hinsichtlich ihrer Haupt- und Spurenelementzusammensetzung untersucht, sowie die Isotopenzusammensetzung von Kohlenstoff, Molybdän und Eisen in diesen Gesteinen ermittelt. Zusätzlich dazu wurden noch Raman und Synchroton Analysen, sowie Sauerstoff und Silizium Isotopenanalysen durchgeführt, um die diagenetische Überprägung und Eisenspeziierung der CMKP zu beurteilen. Die Ergebnisse wurden mit sedimentologischen Erkenntnissen und Daten von früheren Studien über den Kontinentalhang der CMKP in Zusammenhang gebracht.

Geochemische Signaturen, wie das Fe zu Mn Verhältnis sowie Seltene Erd Muster zeigen eine Abhängigkeit von der Wassertiefe sowie von einer sich ändernden Zufuhr von Ozeanwasser und meteorischem Wässern. In Kombination mit Raman Spektren und $\delta^{18}O$ Signaturen kann gezeigt werden, dass die CMKP sehr gut erhalten ist und immer noch primäre geochemische Signaturen aufweist, trotz Dolomitisierung und Silizifizierung.

Die Ergebnisse deuten darauf hin, dass Molybdän und Eisen frühdiagenetisch im Sediment durch Redoxprozesse, insbesondere im Zusammenhang mit der Degradation von Organik, beeinflusst wurden. Allerdings deuten schwere $\delta^{98}Mo$ Signaturen von bis zu +1.40 ‰ in Karbonaten und Schwarzschiefern auf freien Sauerstoff im Atmosphären-Ozean System hin und kann als Minimumwert für den Neoarchaischen Ozean angesehen werden, worauf schon zuvor Studien über Molybdän Isotopensignaturen am Kontinentalhang hingewiesen haben. Auch Eisen Isotopensignaturen und Konzentrationen in Karbonaten lassen Rückschlüsse auf eine

partielle Oxidation von Eisen zwischen anoxischem, eisenreichem Tiefenwasser und oxischem Flachwasser ziehen, obwohl eine anaerobe Oxidation durch photoferrotrophe Organismen nicht ausgeschlossen werden kann. Berechnungen über die Konzentration von gelöstem Fe(II) im Meerwasser lassen auf eine niedrigeren Eisengehalt im Schelfberich als am Kontinentalhang schließen. Die Konzentration ist dabei stark abhängig von der Wassertemperatur, der Sedimentationsrate und der Ca^{2+} Konzentration. Zusammenfassend lässt sich sagen, dass die Molybdän und Eisen Isotopenzusammensetzung der CMKP auf freien Sauerstoff im Flachwassermilieu hindeutet. Des Weiteren wird das Potential von Ca-Mg Karbonaten als Proxy für die Systematik von redox-sensitive Spurenmetallen im aquatischen Milieu gezeigt.

Frühere Studien haben gezeigt, dass die CMKP zunächst eine rampenartige Struktur hatte (untere CMKP), die dem Zufluß von reduzierenden hydrothermalen Fluiden vom offenen Ozean ausgesetzt war. Die reduzierenden Bedingungen auf dem Schelf wurden noch zusätzlich verstärkt durch die Ablagerung von organischem Material, was dazu führte, dass die Karbonate von Fe(II) Spezies dominiert sind. Im Laufe der weiteren Ablagerung bildete sich ein Riff (obere CMKP), dass die Lagune vom Kontinentalhang getrennt hat, was den Zufluß von offenem Ozeanwasser signifikant eingeschränkte. Dies hatte wahrscheinlich auch Auswirkungen auf das Ökösystem, welches sich von einem anaerob photo- und chemolithotroph dominierten hin zu einem hauptsächlich aerob phototrophen entwickelte. Diese Entwicklung hat wahrscheinlich die Primärproduktion signifikant gesteigert und zu einer erhöhten Ablagerung von organischem Material entlang des Riffs geführt, was zu einer Verarmung des gelösten anorganischen Kohlenstoffpools in der quasi geschlossenen Lagune an leichtem ^{12}C führte. Dies wird anhand von $\delta^{13}C_{carb}$ Signaturen in den dort abgelagerten Karbonaten angezeigt, die leicht positivere Werte aufweisen als die Karbonate des Kontinentalhangs.

All diese Faktoren weisen auf einen höheren Oxidationszustand im Lagunenbereich der oberen CMKP hin, welches auch durch die Erhaltungen von Fe(III)-Spezies in den dort abgelagerten Karbonaten gezeigt wird.

Diese Studie zeigt verschiedene Indizien dafür auf, dass die CMKP eine Sauerstoffoase war. Damit sich diese entwickeln konnte, waren bestimmte Umwelt- und Ablagerungsbedingungen notwendig, wobei die Riffbildung und der eingeschränkte Zufluß von Ozeanwasser von entscheidener Bedeutung war. Dadurch wurde es ermöglicht, dass die Sauerstoffproduktion durch Photosynthese relativ zum Sauerstoffverbrauch steigen konnte und sich so insgesamt ein höherer Oxidationszustand im flachmarinen Milieu einstellen konnte.

1. Introduction

1.1. Motivation and significance of the study

Archean shallow-marine settings are considered as a key element for the evolution and thriving of oxygenic photosynthesis on our planet (e.g. Cloud, 1968; Holland, 2006; Kasting, 1992) and the rise of atmospheric oxygen (Great Oxidation Event – GOE) at the Archean-Proterozoic transition (e.g. Canfield, 2005; Holland, 1962; Holland, 2006). Large-scale carbonate platforms deposited in these settings mostly consist of stromatolites, lithified microbial mats, that likely contained oxygen producing cyanobacteria and reveal geochemical signatures and biomarkers that support the local accumulation of oxygen in these *'oxygen oases'* (e.g. Eigenbrode et al., 2008; Riding et al., 2014; Waldbauer et al., 2009). However, the geochemical and biological signatures can be ambiguous and complex (e.g. Posth et al., 2013) and challenge the interpretation and the usage of those proxies (e.g. Heimann et al., 2010; Johnson et al., 2013).

In this study, the ~2.58 to 2.50 billion year (Ga) old Campbellrand-Malmani carbonate platform (CMCP; Transvaal Supergroup, South Africa) was investigated. The platform is well-preserved, contains carbonate and siliciclastic mudrock sediments deposited in supratidal to deep subtidal settings, about 200 Ma before the GOE and within the timeframe of supposedly early localized production of oxygen in the marine environment (Fig. 1-1). Previous sedimentological and geochemical studies mainly investigated the slope facies of the CMCP in the context of the *Agouron-Griqualand Paleoproterozoic Drilling Project* (e.g. Fischer et al., 2009; Schroeder et al., 2006; Voegelin et al., 2010; Waldbauer et al., 2009; Wille et al., 2007). Here, the focus is set on the platform facies with conjunction of major and trace elements and isotope signatures of redox-sensitive elements as well as geological and sedimentological observations. The main aims of this study are:

(1) The paleoenvironmental reconstruction of the CMCP in the interface of marine and terrestrial systems

(2) The reconstruction of the redox conditions in the CMCP

(3) The evaluation of ancient Ca-Mg carbonates as proxies for trace metal systematics in the shallow seawater

Constraining the environmental requirements that allowed the accumulation of oxygen in the oceans and the atmosphere are still debated and makes it necessary to better understand the systematics in potential oxygen oases on Earth, also regarding future studies about the development of life on other planets.

1.2. Scope of the study

This study is subdivided into nine chapters. Chapter 1 provides the scientific background, including a short review of the GOE, Archean carbonate platforms, and the concept of 'oxygen oases'. Furthermore, the principles of stable isotope geochemistry and (non-)traditional stable isotopes is presented, with emphasize on carbon, molybdenum, and iron.

Chapter 2 gives an overview of the geological setting of the lower Transvaal Supergroup and a detailed description of the KMF-5 drill core. Chapter 3 describes the analytical techniques used during this study and results are presented in Chapter 4.

Chapter 5 discusses the depositional conditions and preservation of the CMCP, based on data of major elements, trace elements, oxygen isotopes and Raman analyses. This is crucial in order to evaluate the quality of geochemical and isotope signatures of the sediments. To do so, possible influence by early and late diagenetic processes is discussed, in particular the impact of dolomitization, silicification, and the intrusion of the Bushveld igneous complex. Furthermore, a paeoenvironmental reconstruction of the CMCP over time is provided.

Chapter 6 focuses on the implications for the carbon cycle of the CMCP. The combination of the here presented data with previously published data from the slope facies (Fischer et al., 2009; Horstmann and Beukes, 2002) allows to investigate the temporal evolution of the inorganic carbon pool and the ecosystems from the continental slope onto the shallow-water platform.

Chapter 7 reconstructs the molybdenum systematics of the CMCP and discusses environmental and diagenetic effects controlling molybdenum concentration and isotope signature in these ancient Ca-Mg carbonates. Data were combined with earlier Mo studies from the slope succession (Voegelin et al., 2010; Wille et al., 2007).

Chapter 8 reconstructs the iron systematics of the CMCP. Thereby, the focus is set on the Ca-Mg carbonates with the goal to evaluate if those are good proxies for aqueous Fe(II) in seawater. Data were combined with Fe analyses from an earlier study on the slope region (Czaja et al., 2012) in order to compare different depositional settings along the CMCP.

Chapter 9 provides a summary of the main findings of this study, a detailed temporal reconstruction of the CMCP, and changes in the biogeochemical cycles and redox state. Furthermore, it is discussed if the CMCP represents an oxygen oasis.

1.3. The rise of oxygen in the hydrosphere-atmosphere system

The *Great Oxidation Event* (GOE) describes the first global rise of free atmospheric oxygen at the Archean-Proterozoic transition and is widely considered one of the most profound environmental changes in Earth's history (Farquhar et al., 2011; Holland, 1962, 2006; Kasting, 2013; Kump et al., 2013; Lyons et al., 2014). Constraining and exploring the requirements to achieve such a net accumulation of oxygen in the atmosphere, when oxygen production exceeded oxygen consumption, is still scientifically debated and is part of multiple studies that are based on the usage of geochemical and mineralogical proxies (Fig. 1-1). In the case of the GOE, the disappearance of the mass-independent sulfur isotope fractionations (MIF-S) in marine sediments about 2.33 Ga ago is probably the strongest indicator for an increase in atmospheric oxygen over 10^{-5} of the present atmospheric level (PAL) (Farquhar et al., 2000; Luo et al., 2016; Pavlov and Kasting, 2002). Other mineralogical clues for higher oxygen levels are the widespread appearance of Fe(III)-oxides in paleosols and redbeds and the disappearance of uraninite, siderite and pyrite as a detrital component of fluvial systems (Beukes, 1987; Beukes et al., 2002; Johnson et al., 2014; Rasmussen et al., 1999; Young et al., 2001).

In recent years several studies on Archean marine samples argue for an at least localized accumulation of oxygen in the atmosphere-hydrosphere system ('whiffs of oxygen') several hundred million years before the GOE, causing oxidative cycling of redo-sensitive elements (Anbar et al., 2007; Crowe et al., 2013; Duan et al., 2008; Kendall et al., 2010; Planavsky et al., 2014; Wille et al., 2007) (Fig. 1-1). In fact, the appearance of cyanobacteria and therefore the onset of oxygenic photosynthesis is proposed to have happened by about 2.7 Ga ago, as indicated by biomarkers (Brocks et al., 1999; Eigenbrode et al., 2008; Waldbauer et al., 2009), although the quality of some of those markers are questioned (Brocks, 2011; Rasmussen et al., 2008) and can even indicate anaerobe microbial activity (Fischer et al., 2005). Other studies suggest the evolution of cyanobacteria as early as 3.7 Ga (Frei et al., 2016; Rosing and Frei, 2004) or 3.5 Ga (Schopf, 1993; Van Kranendonk, 2006) ago, based on the presence of microfossils, carbonaceous material and stromatolite structures, although the biogenicity of these old samples is doubted (e.g. Brasier et al., 2002). Stromatolitic features and carbon isotope signatures of organic carbon in the 2.9 Ga old Pongola Supergroup (South Africa) (Noffke et al., 2008), the 2.8 Ga old Steep Rock (Canada) (Grassineau et al., 2006), the 2.7 Ga old Hamersley Basin (Australia) (Buick, 1992; Eigenbrode and Freeman, 2006), and the 2.6 Ga old CMCP (South Africa) (Altermann and Schopf, 1995) give stronger indications for the presence of cyanobacteria, although

anaerobe processes can also form those microbial structures (Bosak et al., 2007) and isotope signatures (e.g. Hayes, 2001; Robinson et al., 2003). Nevertheless, evidence for the onset of oxygenic photosynthesis accumulate from ~ 2.7 Ga on (Fig. 1-1). In an otherwise anoxic world it was necessary to increase the oxygen production and to decrease the oxygen consumption by reducing species to ultimately gain a net production of oxygen. It has been suggested that the formation of large, stable cratons and shallow oceans during Meso- to Neoarchean times allowed on the one hand the development of carbonate platforms in the shallow-marine environment, where cyanobacterial communities could thrive and on the other hand enabled enhanced burial of organic carbon, which prevented consumption of oxygen via respiration and decomposition of these organics (Falkowski and Isozaki, 2008; Kump and Barley, 2007). Continental growth could have also caused a shift from submarine to subaerial volcanism, which led to a change from a reduced to an oxidized state of volcanic gases (Gaillard et al., 2011; Kump and Barley, 2007). Additionally, hydrogen escape to space prior to reaction with oxygen by ultraviolet photolysis of abundant methane has been proposed as another mechanism for irreversible atmospheric oxidation (Catling et al., 2001). Either way, the investigation of carbonate platforms as settings of large-scale oxygen production is crucial to understand the arrangements leading to the first global rise of atmospheric oxygen.

1.4. Archean carbonate platforms and oxygen oases

Carbonate platforms are thick sequences of carbonate rocks typically deposited in a shallow-marine environment, e.g. along passive continental margins and in intracratonic basins. They can reach extensive scales and can give valuable information about seawater chemistry and dynamics, the interplay between the marine and terrestrial environment, the ecology, and even about the regional tectonic settings.

The Meso- to Neoarchean time range was marked by the development of stable continental shelves and epicontinental seas and the weathering and erosion of emerged landmasses (Kump and Barley, 2007). These settings provided the required accommodation space and shallow marine conditions for large scale carbonate platform growth, probably for the first time in Earth's history (Grotzinger, 1989; Hoffman, 1988; Hoffman and Grotzinger, 1988; Sumner and Grotzinger, 1996). These platforms could have been the site of early oxygen production on our planet, as Archean carbonates largely consist of stromatolites. These are the laminated, organosedimentary, non-skeletal products of microbial communities, which may have included oxygen-producing cyanobacteria (Burne and Moore, 1987).

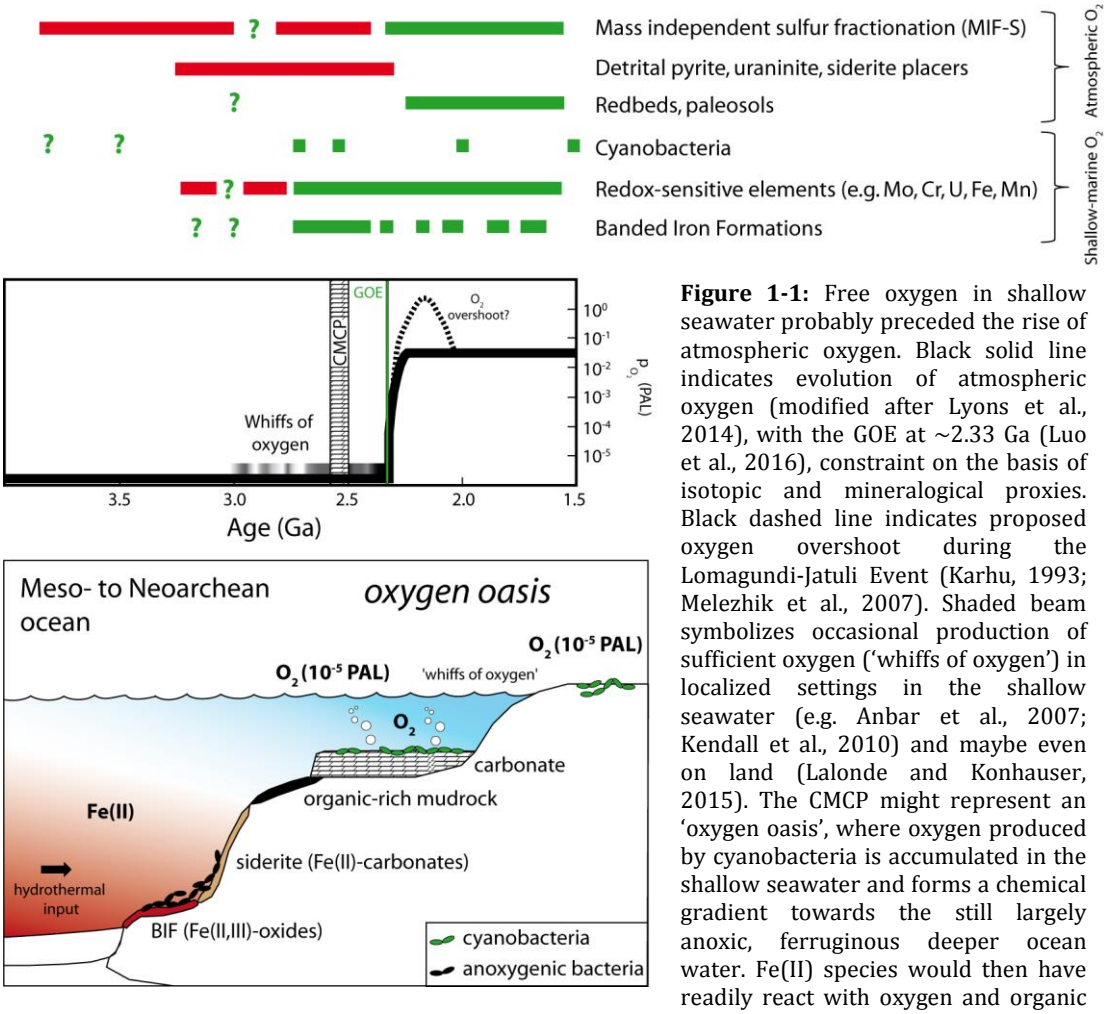

Figure 1-1: Free oxygen in shallow seawater probably preceded the rise of atmospheric oxygen. Black solid line indicates evolution of atmospheric oxygen (modified after Lyons et al., 2014), with the GOE at ~2.33 Ga (Luo et al., 2016), constraint on the basis of isotopic and mineralogical proxies. Black dashed line indicates proposed oxygen overshoot during the Lomagundi-Jatuli Event (Karhu, 1993; Melezhik et al., 2007). Shaded beam symbolizes occasional production of sufficient oxygen ('whiffs of oxygen') in localized settings in the shallow seawater (e.g. Anbar et al., 2007; Kendall et al., 2010) and maybe even on land (Lalonde and Konhauser, 2015). The CMCP might represent an 'oxygen oasis', where oxygen produced by cyanobacteria is accumulated in the shallow seawater and forms a chemical gradient towards the still largely anoxic, ferruginous deeper ocean water. Fe(II) species would then have readily react with oxygen and organic carbon (modified after Beukes and Gutzmer, 2008) and were components of anoxygenic microbial activity (Johnson et al., 2008b; Kappler et al., 2005).

Indeed, some of these shelves' marine sediments exhibit geochemical and sedimentological features for transient oxygen in surface ocean water masses (Fig. 1-1). The CMCP, for example, documents signs of oxygenation, like (i) high abundances of authigenic rhenium and molybdenum in mudrocks indicating redox-cycling of these elements fostered by oxidative weathering combined with reductive adsorption in these marine sediments (Kendall et al., 2010; Wille et al., 2007), (ii) heavy Mo isotope signatures in mudrocks (Wille et al., 2007 and this study) and microbial carbonates (Voegelin et al., 2010 and this study) that indeed indicate the presence of oxidized molybdenum in the form of molybdate in the water column, (iii) heavy N signatures in slope dolostones and mudrocks that might reflect the onset of oxic nitrogen cycling (Garvin et al., 2009; Godfrey and Falkowski, 2009), and (vi) biomarkers indicating an aerobe ecosystem (Waldbauer et al., 2009). Similar observations are reported for marine sediments from the Hamersley basin (2.6 Ga, Australia), showing heavy Mo

isotope signatures (Duan et al., 2010) and authigenic enrichment of redox-sensitive elements (Anbar et al., 2007) in mudrocks and C isotope signatures of organic material, implying a shift from an anaerobe to an aerobe ecosystem (Eigenbrode and Freeman, 2006; Eigenbrode et al., 2008). The carbonate platform of Steep Rock (2.8 Ga, Canada) also provides C isotope signatures (Grassineau et al., 2006) that were interpreted as signs of oxygen photosynthesizers, which is reinforced by the appearance of a mild negative Ce anomaly in the very shallow water carbonates (Riding et al., 2014) and argues for a stratified water column with oxygenated shallow water and anoxic deeper water (Fig. 1-1).

The similarities of those geochemical 'fingerprints' incline towards the suggestion that Archean carbonate platform settings represent 'oxygen oases' (Fig. 1-1) (Olson et al., 2013; Riding et al., 2014). (Fischer, 1965) first used this expression to describe a restricted pool of net oxygen production by aerobe ecosystems in an otherwise anoxic world, which might have reached oxygen levels of up to 0.08 PAL (Kasting, 1991, 1992). The production and the accumulation of oxygen within platform 'oases' would have occurred effectively due to physical sheltering from upwelling deep ocean water masses (Sumner and Beukes, 2006), which contain chemically reducing hydrothermal species. Before the evolution of oxygenic photosynthesis, the reducing Archean environment was dominated by an anaerobic microbial biosphere, largely based on chemolithoautotrophic microorganisms centered near hydrothermal vents (Nisbet and Sleep, 2001). Early forms of anoxygenic photosynthesis depended on reduced hydrothermal fluids, using dissolved H_2, H_2S or Fe(II) as electron donors for their metabolism. This situation drastically changed with the evolution of oxygenic photosynthesis (Des Marais, 2001). This form of metabolism marked a major innovative step in the evolution of life, since it allowed microorganisms to use water itself as a source of electrons, which and therefore enabled photosynthetic organisms to diversify into the photic zone of any aquatic setting, sovereign from hydrothermal flux. The release of free molecular oxygen subsequently triggered the shift towards an aerobic biosphere, dominated by oxygenic photosynthesis and heterotrophic respiration (Eigenbrode and Freeman, 2006; Kasting and Siefert, 2002). A computer simulation ran by Olson et al. (2013) confirmed that a decreasing availability of other hydrothermal electron donors (e.g. Fe(II) and H_2S) greatly influence the dominance of anoxygenic and oxygenic phototrophs and therefore the spatial extend of oxygen oases and oxygen concentrations maybe up to 10 µM (Reinhard et al., 2013). However, even though oxygen was produced on those sites, it was probably not sufficient enough to globally oxidize the atmosphere. Any oxygen released from the ocean water could have been

immediately consumed by the reducing atmosphere (Olson et al., 2013). Thus, an alternative explanation for oxidative weathering of sulfides for trace element mobilization, i.e. Mo, is the existence of terrestrial microbial mats, which allowed local oxidation on land and not within the shallow marine environment (Lalonde and Konhauser, 2015; Reinhard et al., 2013), as microbial mats likely kept the oxygen within their structure (Sumner et al., 2015). In a modern 'oxygen oasis' analogue in the Antarctic is has been shown that microbial mats can contain high amounts of oxygen without even temporarily oxidizing the overlying anoxic water column (Sumner et al., 2015), which has also been postulated for the Precambrian world by Herman and Kump (2005). Riding et al. (2014) proposed a minimum oxygen concentration in shallow seawater of 10.25 µM based on siderite-calcite equilibrium calculations, which corresponds an oxygen level of 0.06 PAL and is therefore in the proposed range of 0.08 PAL (Kasting, 1991, 1992).

1.5. Traditional and non-traditional stable isotope systematics

Each chemical element is defined by its atomic number, which is the number of protons in its nucleus. The atomic mass of an element is the sum of protons and neutrons in its nucleus. The number of neutrons can vary, which results in the phenomenon that the atoms of one element can have different atomic mass and are termed as *isotopes*. Isotopes can be radioactive, i.e. they are unstable and decay with a specific decay constant that is usually expressed in form of the half-life (e.g. ^{238}U decays to ^{206}Pb and has a half-life of $4.47 \cdot 10^9$ years). *Stable isotopes* do not undergo radioactive decay (e.g. ^{206}Pb) or have such an exceptional long half-life that they are quasi-stable (e.g. ^{209}Bi with a half-life of $1.9 \cdot 10^{19}$ years).

Stable isotope analyses are a widely used tool in the natural sciences to unravel physicochemical and biological processes that are mass-(in)dependent. Those analyses have been conducted on mass spectrometers since the 1950, in particular on the light stable isotopes oxygen (O), carbon (C), sulfur (S), hydrogen (H), and nitrogen (N), and are thus termed *traditional stable isotopes*. In the last two decades, the improvement of instrumentation, in particular of multicollector inductively coupled plasma mass spectrometers (MC-ICPMS), and development of novel chemical and analytical techniques, like the double-spike method, paved the way for the analyses of a long list of other elements, e.g. Mg, Ca, Fe, Zn, Cu, Li, Mo, Cr, and Si, the *non-traditional stable isotopes* (e.g. Johnson et al., 2004).

In this study, the focus is set on the isotope systems of carbon, molybdenum and iron and will thus be described below in detail. Additionally, silicon and oxygen isotopes were analyzed to complement the data.

1.5.1. Principles of mass-dependent stable isotope fractionation

During the chemical reaction of two molecules, A and B, a fractionation of the isotopes of an element X can be induced. The isotope abundance of X is given as the ratio of the heavy and the light isotope:

$$R = \frac{\text{heavy}-X}{\text{light}-X}$$

Normally, the isotope difference of a sample is given relative to a reference standard and is defined as the delta value and expressed in permille:

$$\delta X_{\text{sample}}(‰) = \frac{(R_{\text{sample}} - R_{\text{standard}})}{R_{\text{standard}}} \times 1000\,.$$

The isotope fractionation between two molecules A and B is following a fractionation factor α, whereby

$$\alpha_{A-B} = \frac{R_A}{R_B}$$

Converted in permille, α can be expressed in a ε value:

$$\varepsilon_{A\text{-}B}\,(‰) = (\alpha\text{-}1) \times 1000$$

Furthermore, α is often converted as to Δ_{A-B}, according to the approximation:

$$\Delta_{A-B} = \delta_A - \delta_B \approx 1000 \ln \alpha$$

Mass-dependent stable isotope fractionation is basically the result of quantum mechanical effects, where bond energies of molecules depend on the mass of the isotopes of an element, making molecules with the heavier isotope more stable, as the bond energy is higher and the vibrational frequency is lower (Urey, 1947). The vibrational frequency of a molecule is thereby linked with the Zero-Point Energy (ZPE). The ZPE basically depends on the isotopic mass and defines the bond energy (Fig. 1-2). It is defined as:

$$E_{ZPE} = \frac{1}{2} \times h \times v$$

with $v = \frac{1}{2} \times \pi \times \sqrt{\frac{f}{\mu}}$

and $\mu = \frac{m_A \times m_B}{m_A + m_B}$

h: Planck constant (6.6×10^{23} Js)

v: Vibration frequency (s^{-1})

f: force constant

μ: reduced mass

m_A, m_B: mass of atom A and B

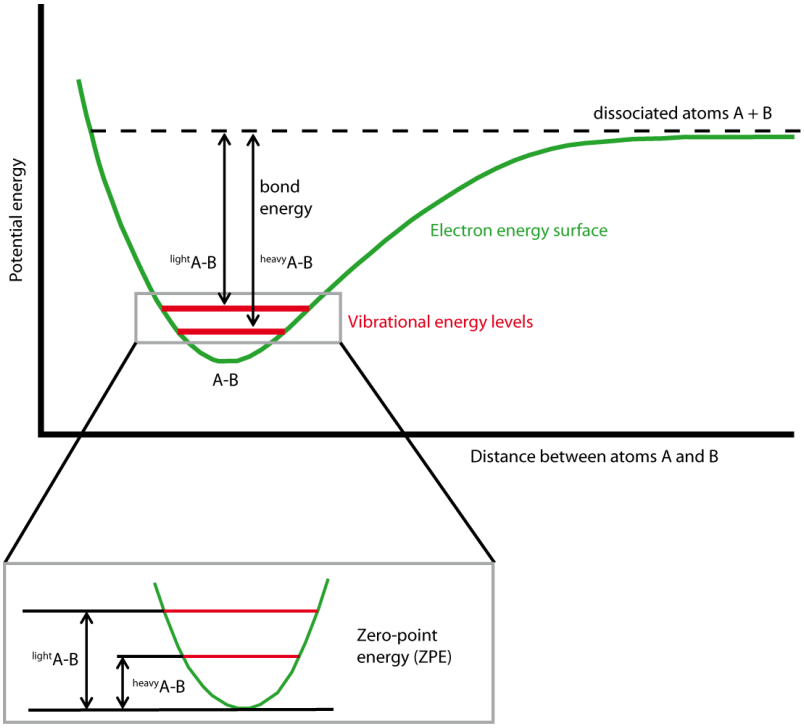

Figure 1-2: Potential energy of a molecule A-B and the ZPE levels, which change their location, depending on the mass of the isotope in the bond of the molecule. Modified after Anbar and Rouxel (2007).

Mass-dependent stable isotope fractionation can occur under *equilibrium* conditions, where the isotopes of an element are exchanged in a closed system between two molecules until the system reaches equilibrium (A ↔ B). Fractionation decreases with increasing temperature ($\sim 1/T_2$), increasing atomic mass, and decreasing relative mass difference between the isotopes of an element. Equilibrium fractionation is typical for inorganic reactions and is dependent on the bond energy, which basically means that heavy isotopes are preferred in the molecule with the highest bond energy that correlates with increasing oxidation state, low coordination number, type of bonding partners, high covalent bonds, and low-spin electron configuration.

Kinetically driven fractionation is a unidirectional reaction (A → B). In this case isotopes of the product and the educt of a reaction are not exchanging isotopes, and can therefore not reach equilibrium. Kinetic fractionation typically happens during biological processes, and during evaporation and diffusion. It is dependent on the reaction rate and the pathways of the reaction, according to:

$$E = \frac{1}{2} m \times v^2 = \frac{3}{2} \times k \times T, \text{ where } v = \sqrt{\frac{3 \times k \times T}{m}}$$

with

E: kinetic energy of the molecule m: mass of the molecule

v: velocity of the molecule k: Boltzmann's constant

T: absolute temperature

This means that a molecule with a heavier isotope and thus higher mass has a smaller velocity than a molecule with a lighter isotope and thus lower mass. During reactions this results in the phenomenon that the lighter isotopes are preferentially enriched in the product.

Detailed reviews about stable isotope fractionation are provided by Chacko et al. (2001) and Schauble (2004).

1.5.2. Carbon systematics

Carbon is a key element of life and plays a major role in biological, (bio)geochemical, and climate cycles. It has two stable isotopes (with natural abundances): ^{12}C (98.93 %), and ^{13}C (1.07 %) (de Laeter et al., 2003). Carbon isotope signatures are typically reported as $\delta^{13}C$, relative to the Vienna PeeDee belemnite standard (VPDB) (Craig, 1957). The C cycle is rather complex and consists of several sub-cycles, each of them recycle carbon on very different time scales. Those are, ordered after increasing time of C recycling and increasing size of C reservoir, the atmosphere-hydrosphere-biosphere sub-cycle (minutes to 10^3 years), the sedimentary sub-cycle (10^3 to 10^8 years), the higher metamorphic and igneous sub-cycle (10^6 to 10^9 years), and the mantle sub-cycle (10^9 years) (Fig. 1-3; for a detailed review see Des Marais (2001)). Sources of CO_2 are from outgassing from mid-ocean ridges and volcanoes, from carbonate sedimentation and metamorphism, and from decomposition of organic carbon. In the oceanic system at circumneutral conditions the largest carbon reservoir is dissolved inorganic carbon (DIC), which consists to >99 % of HCO_3^- and CO_3^{2-} and traces of CO_2 and H_2CO_3 (Fig. 1-3), depending on the pH, salinity, pressure and temperature (Zeebe and Wolf-Gladrow, 2001). Oceanic DIC isotopically exchanges under equilibrium with atmospheric CO_2 with a fractionation factor $\Delta^{13}C_{DIC\text{-}CO2}$ of about +9 ‰ (Emrich and Vogel, 1970; Mook et al., 1974; Vogel et al., 1970). DIC typically reacts under equilibrium with Ca^{2+} ions to calcium-carbonate via

$Ca^{2+} + 2HCO_3^- \leftrightarrow CaCO_3 + CO_2 + H_2O$ and $Ca^{2+} + CO_3^{2-} \leftrightarrow CaCO_3$

with isotope fractionation factors $\Delta^{13}C_{CaCO3\text{-}DIC}$ of about +0.9 ‰ for calcite (e.g. Emrich and Vogel, 1970; Rubinson and Clayton, 1969). The other important although significantly smaller oceanic carbon reservoir is organic carbon, where organisms take up CO_2 to produce organic molecules. In the modern world the most important metabolic pathway is via photosynthesis/heterotrophic respiration:

$CO_2 + H_2O \leftrightarrow CH_2O + O_2$.

In contrast to the inorganic carbon system, which is driven by isotopic equilibrium exchange reactions, organic carbon production fractionates kinetically,

with a concentration of light ^{12}C into organic matter and thus showing depleted $\delta^{13}C$ signatures, which strongly varies depending on the microbial species (Hayes et al., 1989). 'Fresh' organic matter has rapid pathways and is an important reactant and electron donor in other major biogeochemical cycles of iron, manganese, nitrogen and sulfur (e.g. Berner, 1989; Froelich et al., 1979). This causes that ~99.9 % of organic matter is recycled again and thus basically dominates the short-term carbon cycle (minutes to 10^3 years) on Earth's surface by its production and decomposition (Broecker and Peng, 1982; Des Marais, 1995). The input of C today is from the oceans, the atmosphere, and land. However, the input of C from land was probably very limited during the Neoarchean, because no land plants existed yet, which are the main source of terrestrial C. Moreover, the input of terrestrial organic C and its oxidation in the shallow-marine environment would have rather caused a decrease in $\delta^{13}C_{carb}$ (Holmden et al., 1998; Immenhauser et al., 2003; Oehlert and Swart, 2014). Thus, the important input sources of C in the Neoarchean shallow-marine environment were probably from the atmosphere and the oceans, with the oceanic C pool being significant larger (~37,000 Gt) than the atmospheric C pool (~700 Gt) (Fig. 1-3).

The most important sedimentary reservoirs are sedimentary carbonate carbon (60,000,000 Gt) and organic carbon (14,000,000 Gt), which due to its much larger C reservoir ultimately influence the carbon system of ocean and atmosphere on a time scale of 10^3 to 10^8 years (Derry et al., 1992; Garrels and Perry, 1974). This long-term global carbon cycle is controlled by the isotope mass balance relation

$$\delta^{13}C_{input} = f_{carb} \times \delta^{13}C_{carb} + f_{org} \times \delta^{13}C_{org} \Rightarrow f_{org} = \frac{\delta^{13}C_{carb} - \delta^{13}C_{input}}{\delta^{13}C_{carb} - \delta^{13}C_{org}}$$

which is normally used for the global carbon cycle, where f_{org} is the fraction of the (global) influx of carbon (C_{input}) buried as organic carbon (C_{org}), which ultimately defines f_{carb} as the fraction of buried inorganic carbon (C_{carb}), as $f_{carb} = 1 - f_{org}$. When f_{org} increases, f_{carb} will decrease and $\delta^{13}C_{carb}$ and $\delta^{13}C_{org}$ values simultaneously increase to satisfy the mass balance equation (Wickman, 1956). Furthermore, according to the equation

$$CO_2 + H_2O \leftrightarrow CH_2O + O_2$$

with each mole of organic carbon buried, a mole of oxygen is released to the atmosphere and not consumed by oxidation of organic matter. A prominent example for this relationship is the Lomagundi-Jatuli Event (2.20 – 2.06 Ga) (Karhu, 1993; Melezhik et al., 2007), which is defined by a global excursion of $\delta^{13}C_{carb}$ up to +10 ‰. It was suggested that this excursion was caused by a coeval large-scale burial of organic matter, even though this is still under debate. Such a massive event of organic carbon burial probably also induced an overshoot of oxygen in the atmosphere (Fig. 1-1).

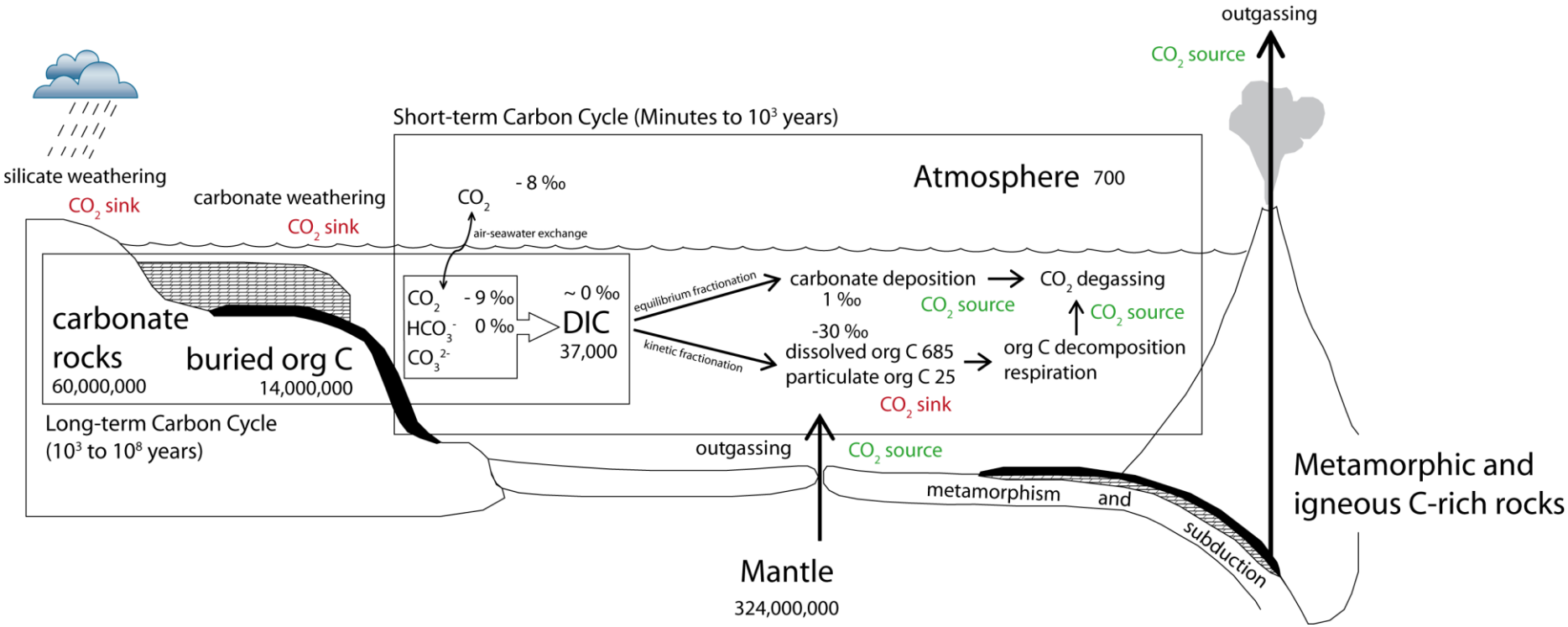

Figure 1-3: Global carbon cycle. Main sources and sinks of CO_2 as well as reservoirs (mass × 10^{15} g C, modern values) and processes within the short-term and long-term carbon cycles. This illustration does not include the input of terrestrial biota, as those had not evolved yet in the Neoarchean.

1.5.3. Molybdenum systematics

Molybdenum is a trace element in the average continental crust with a concentration of only about 1.1 µg/g (Rudnick and Gao, 2004) and has seven stable isotopes (with natural abundances): ^{92}Mo (14.65 %), ^{94}Mo (9.19 %), ^{95}Mo (15.87 %), ^{96}Mo (16.67 %), ^{97}Mo (9.58 %), ^{98}Mo (24.29 %), ^{100}Mo (9.74 %) (de Laeter et al., 2003). It shows variations of its isotopic composition and concentration in chemical sediments depending on the redox potential of the ambient ocean and pore fluids (e.g. Barling et al., 2001; Emerson and Huested, 1991; Shimmield and Price, 1986; Siebert et al., 2003). In the modern oxygen-rich environment Mo is normally oxidized during oxidative continental weathering from its tetravalent oxidation state in sulphides, the main source of Mo, to a hexavalent state, forming soluble oxy-molybdate MoO_4^{2-}, which then enters the ocean (Barling et al., 2001; Greber et al., 2015; Miller et al., 2011; Morford and Emerson, 1999). Molybdate with a crustal $\delta^{98}Mo_{input}$ value of ca. -0.2 to +0.6 ‰ (relative to $NIST_{3134}$ standard solution, set to +0.25 ‰, following Naegler et al. (2014)) is transported by rivers and groundwater, which can show signatures of about +0.7 ‰ (Archer and Vance, 2008), to the oceans, where it behaves conservatively with a long residence time of 440.000 to 800.000 years at a homogenous concentration of ~100 nM (Collier, 1985; Emerson and Huested, 1991; Greber et al., 2011; Miller et al., 2011; Morford and Emerson, 1999; Voegelin et al., 2014). Light Mo isotopes are preferentially adsorbed onto oxic sediments, predominantly pelagic Fe-Mn crusts and nodules, due to sorption of molybdate to the reactive surfaces of Mn- and Fe-oxide minerals. This process results in an isotopic difference for $\Delta^{98}Mo_{seawater\text{-}FeMn\ crust}$ of +2.7 to +3.2 ‰ (Fig. 1-4) (Barling and Anbar, 2004; Goldberg et al., 2009; McManus et al., 2006; Naegler et al., 2014; Siebert et al., 2001; Siebert et al., 2003; Tossell, 2005). Under slightly euxinic conditions, where H_2S is present in the water column or in pore water at concentrations below 11 µM, molybdate is incompletely transformed to (oxy)thio-molybdates $Mo^{(VI)}O_{4-x}S_x^{2-}$, which readily adsorb on positively charged particle surfaces, like organic matter or Fe sulfide phases of sediments (Helz et al., 1996; McManus et al., 2002; Naegler et al., 2011; Tribovillard et al., 2006). However, transformation favors the lighter Mo to be incorporated within the thiomolybdate. Therefore, the preferential incorporation of isotopically light Mo in oxic to slightly euxinic sediments results in a heavy open ocean water δ^{98}Mo of +2.3 ‰, which is homogenous due to the long mean ocean residence time of Mo. Above a threshold value of 11 µM H_2S the transition from oxy-molybdate to thio-molybdate is very effective and Mo is nearly quantitatively scavenged into reduced sediments, such as mudrocks (i.e.

black shales), whereby this authigenic Mo mirrors the isotopic composition of the coeval seawater (Arnold et al., 2004; Barling et al., 2001; Erickson and Helz, 2000; Helz et al., 1996; Siebert et al., 2003). Between these two "end-members" of sedimentary redox conditions (oxic and euxinic), authigenic Mo enrichments in sediments show a broad range in their isotopic composition and are mainly controlled by redox gradients in the sediment pore fluids, induced by early diagenesis (Brucker et al., 2009; Dahl et al., 2010; Naegler et al., 2011; Romaniello et al., 2016; Scott and Lyons, 2012).

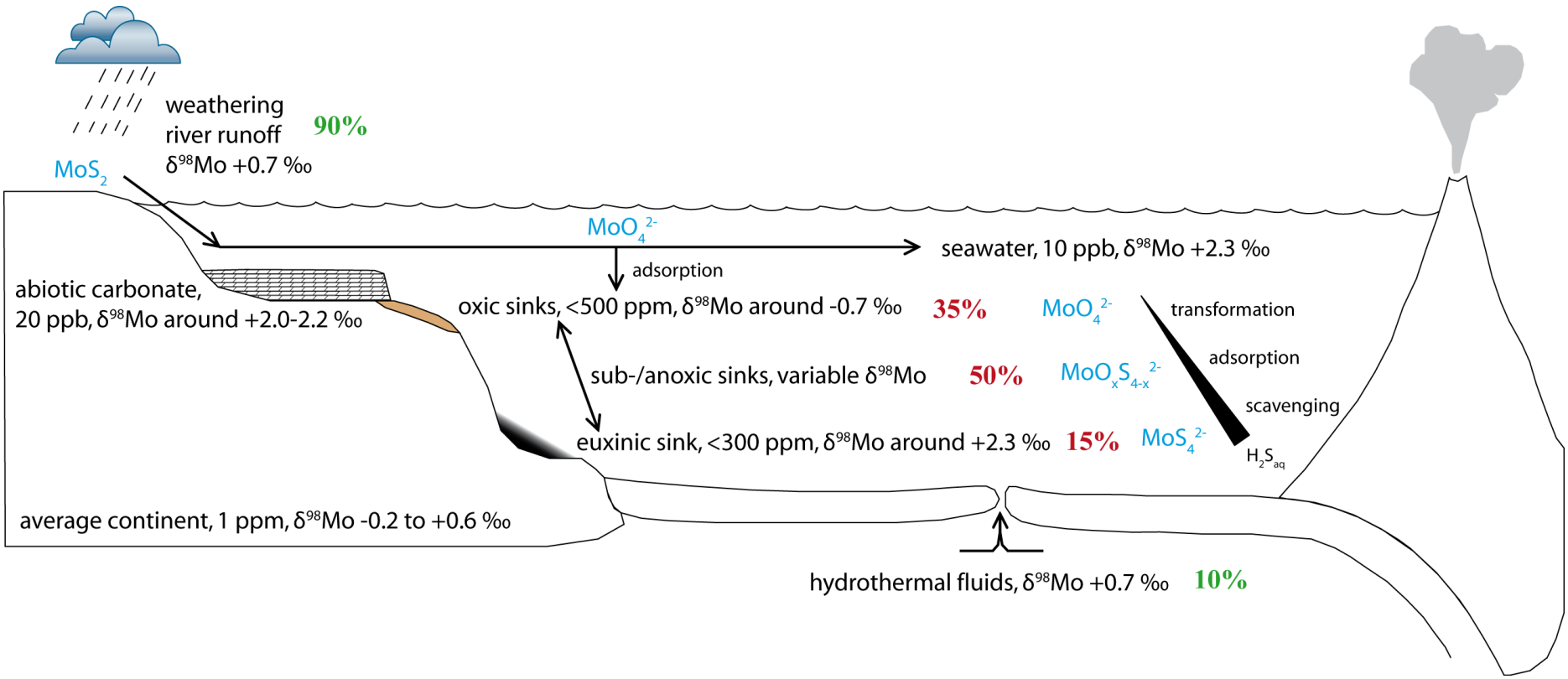

Figure 1-4: Mo systematics in modern ocean system. Mo concentrations and isotope signatures of average continental crust are from Voegelin et al. (2014). Mo enters the ocean via riverine and hydrothermal input (relative fluxes are in green (Archer and Vance, 2008; McManus et al., 2006)), where it is homogeneously distributed as MoO_4^{2-} and behaves conservatively. Relative fluxes of Mo-sinks are in red (Brucker et al., 2009 and references therein). Adsorption onto oxic sediments prefers light Mo isotopes, resulting in an isotopically heavier oceanic Mo pool. Transformation to reactive thio-molybdate and subsequent near-quantitative removal into euxinic sediments might transfer the oceanic isotope signature. Marine abiotic carbonates might also incorporate Mo without fractionation and thus reflect the seawater signature (Voegelin et al., 2009).

1.5.4. Iron systematics

Iron is a major element of the silicate Earth and has four stable isotopes (with natural abundances): ^{54}Fe (5.85 %), ^{56}Fe (91.75 %), ^{57}Fe (2.12 %), and ^{58}Fe (0.28 %) (de Laeter et al., 2003). Isotope values are usually given as $\delta^{56}Fe$ relative to the reference standard IRMM-014, from the Institute for Reference Material and Measurements (IRMM) in Geel, Belgium (Taylor et al., 1992). Magmatic differentiation can cause a slight isotope fractionation, and thus values for igneous rocks between -0.1 and +0.2 ‰ have been reported (e.g. Beard et al., 2003b; Craddock et al., 2013; Schoenberg and von Blanckenburg, 2006; Wang et al., 2014; Weyer et al., 2005).

In the modern oxygenated ocean, Fe is heterogeneously distributed with a low residence time of less than a 100 years (Bruland et al., 1994) and a low concentration of aqueous Fe between 0.05 and 2 nM (e.g. de Baar and de Jong, 2001; Landing and Bruland, 1987; Martin et al., 1990). This is due to the poor solubility of Fe(III) particles in oxic seawater. Thus, even though aqueous Fe is scarce, colloidal and particulate Fe(II) and Fe(III) species are very common, as they rapidly react with other chemical species, such as sulfur, oxygen, and organics. Sorption of aqueous Fe species on particulate Fe, minerals and organics can cause isotope fractionation and catalyze oxidation (Icopini et al., 2004; Swanner et al., 2015b; Teutsch et al., 2005). Under microoxic and anoxic conditions, Fe is an essential nutrient for many organisms (Martin and Fitzwater, 1988; Moore et al., 2002) and can either act as an electron donor (Fe(II)) or as an electron acceptor (Fe(III)) in biogeochemical cycles (e.g. Boyd and Ellwood, 2010; Boyd et al., 2000; Coale et al., 2004; Froelich et al., 1979; Pollard et al., 2009). All those aspects make the marine Fe cycle very complex (Fig. 1-5).

In the low-temperature conditions of the marine environment, Fe isotope fractionations driven by equilibrium and/or kinetic effects can be large and influenced by microbial processes in the water column, the porewater and the sediment. The pathway under circumneutral conditions from $Fe(II)_{aq}$ to precipitation of Fe(III) includes the (aerobe) oxidation of $Fe(II)_{aq}$ to $Fe(III)_{aq}$ that quickly equilibrate and result in an isotopic fractionation $\varepsilon Fe(III)_{aq}$-$Fe(II)_{aq}$ of ~3 ‰ (Welch et al., 2003). The precipitation of $Fe(III)_{ppt}$ is kinetically driven and leads to depletion of heavy Fe isotopes in the precipitate by 1-2 ‰ (Skulan et al., 2002), so the overall fractionation factor of oxidation and precipitation from $Fe(II)_{aq}$ to $Fe(III)_{ppt}$ is between 1-2 ‰ (Beard et al., 2003a; Bullen et al., 2001). Similar fractionation factors are also reported for anaerobe microbial-induced Fe(II) oxidation (Croal et al., 2004; Swanner et al., 2015b), and assimilatory/dissimilatory processes (Beard et al., 1999; Beard et al., 2003a; Crosby

et al., 2007; Icopini et al., 2004; Kappler and Straub, 2005), making it challenging to distinguish abiotic from biotic oxidation only based on the Fe isotope signature.

There are multiple Fe sources to the marine environment, such as riverine and groundwater as well as aeolian dust, pore fluids from continental margin sediments and hydrothermal fluids (Anbar and Rouxel, 2007 and references therein), whereby the input from aeolian dust and continental margins are the most significant ones (Duce and Tindale, 1991; Elrod et al., 2004). Fe is subsequently removed, oxidized, precipitated, and re-dissolved by various biogeochemical processes and mainly deposited in estuaries, oxic, anoxic-euxinic, and pelagic sediments (Fig. 1-5) (de Baar and de Jong, 2001; Elrod et al., 2004). Those redox-processes are in particular active in estuaries and continental margins and can induce low δ^{56}Fe signatures (down to -3 ‰) in porewaters (e.g. Severmann et al., 2006; Staubwasser et al., 2006) and in some cases even kinetically driven fractionation down to -5 ‰ (Rouxel et al., 2008). Secondary minerals, like Fe-carbonates and Fe-mono-and -di-sulphides, formed from such isotopically depleted waters usually also obtain light δ^{56}Fe signatures (Beard et al., 2003a; Butler et al., 2005; Préat et al., 2011; Rouxel et al., 2008; Severmann et al., 2006; Wiesli et al., 2004).

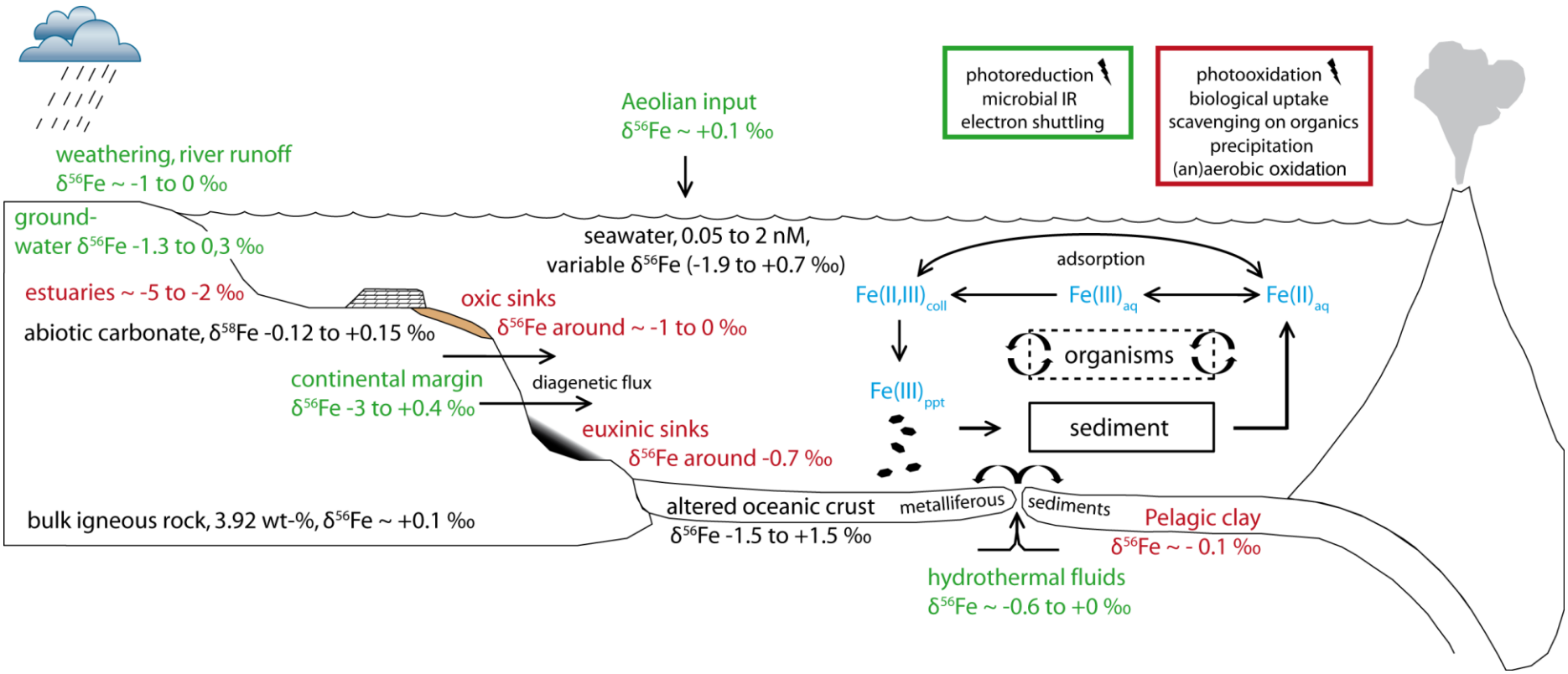

Figure 1-5: Iron sources are in green, sinks are in red. The dissolved iron pool is controlled by the mass balance of those sinks and sources. >99% of iron from hydrothermal vents is rapidly deposited along the vent system (Fitzsimmons et al., 2014). Thus, input from aeolian dust and fluids from continental margins are the most important sources. Two boxes name important aqueous Fe removal (red) and release (green) processes under circumneutral conditions in the marine environment. In blue are typical pathways of Fe species in the seawater-sediment interface (modified from Achterberg et al. (2001)). Isotope values and concentrations from Anbar and Rouxel (2007) and references therein, von Blanckenburg et al. (2008), Chever et al. (2015), Radic et al. (2011), and Rouxel et al. (2008).

2. Geological Setting

2.1. The Campbellrand-Malmani carbonate platform

The Neoarchean to Paleoproterozoic Transvaal Supergroup (TSG) consists of chemical and siliciclastic sedimentary rocks with subordinate volcanic units (Dorland, 1999) (Fig. 2-1 a). It rests unconformably on older supracrustal volcano-sedimentary granite-greenstone terrains of the Kaapvaal Craton in southern Africa. The lower part of the TSG represents one of the first large carbonate platform systems on Earth known as the Campbellrand-Malmani carbonate succession (Beukes, 1987). It was deposited between ~2.58 and 2.50 Ga due to extensive flooding of the Kaapvaal Craton, a result of its thermal subsidence possibly related to prior 2.74-2.69 Ga Ventersdorp magmatism (Sumner and Beukes, 2006). The carbonate succession originally covered an area of approximately 600.000 km^2 (Fig. 2-1 a) (Beukes, 1987), while today's dimensions of ~190.000 km^2 are erosionally preserved in the Transvaal area (TA) in the eastern part and the Griqualand West area (GWA) in the western part of the Kaapvaal Craton, as well as the Kanye area (KA) in the north-central part of the platform (Fig. 2-1 a). The carbonate successions in these three areas are divided into several formations, which can be correlated by sedimentological characteristics and sometimes by U-Pb zircon geochronology of rare ash layers within the succession (Altermann and Nelson, 1998; Coetzee, 2001; Martin et al., 1998; Sumner and Beukes, 2006).

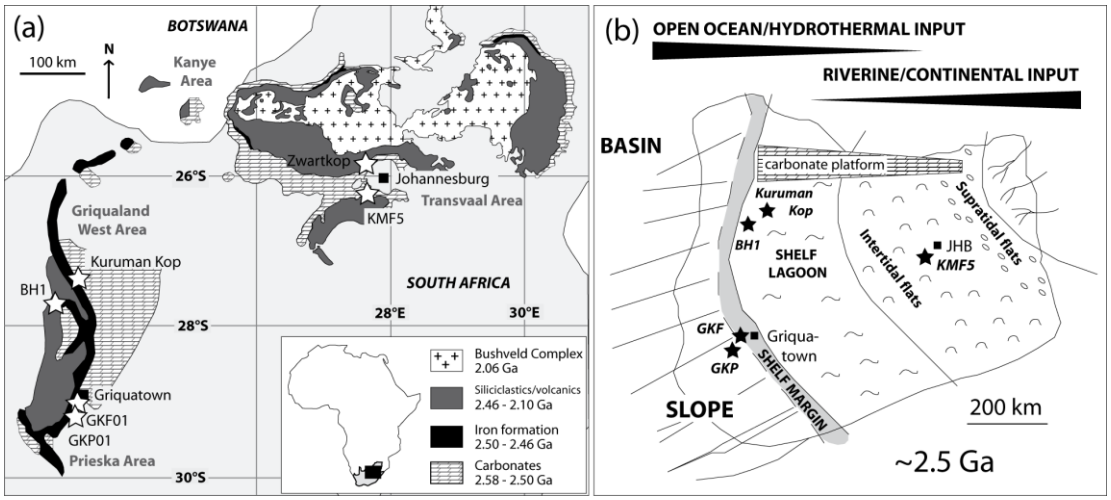

Figure 2-1: (a) Geological overview of the Transvaal Supergroup (TSG), modified after Coetzee (2001) and Sumner and Grotzinger (2004). The TSG is divided into three basins (Transvaal, Kanye and Griqualand West basins); asterisks indicate the locations of the four drill cores KMF-5, BH-1, GKF01 and GKP01. (b) Paleoreconstruction of the Kaapvaal Craton 2.5 Ga ago, modified after Beukes (1987).

The ca. 2000 m thick Malmani Subgroup of the TA in the NE consists of mainly peritidal carbonates, while the contemporaneous shallow shelf carbonates of the Campbellrand Subgroup of the GWA in the SW were deposited under shallow subtidal conditions (Fig. 2-1 b). The far southwestern slope and basinal succession of the Campbellrand Subgroup in the GWA has been sub-classified as the Prieska facies, which is only 500 m thick compared to the up to >2400 m thick shallow carbonate shelf succession (Fig. 2-2), due to lower sedimentation rates within this marginal environment (Beukes, 1987; Sumner and Beukes, 2006). Reconstructions of the transition between shelf and basinal facies in the Campbellrand Subgroup in the GWA have been aided by detailed geochemical and sedimentological studies of drill cores GKP01 and GKF01, both from the Prieska facies, as well as drill core BH-1 that intersected the Campbellrand shelf facies on the farm Sacha near Sishen (GWA) (Fig. 2-1 a) (Altermann and Siegfried, 1997; Knoll and Beukes, 2009; Schroeder et al., 2006).

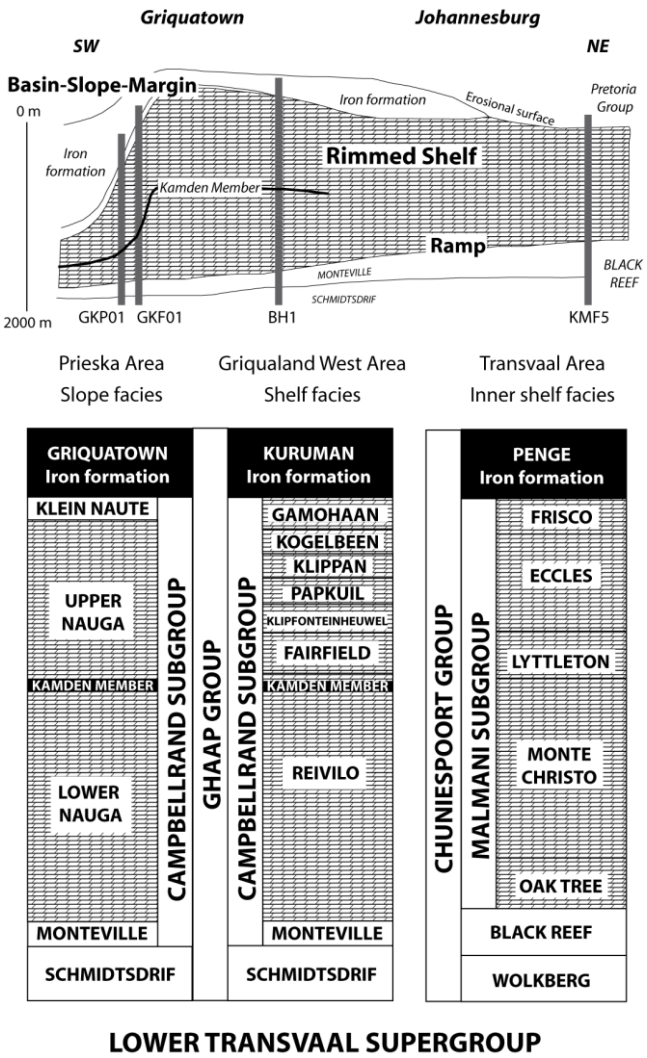

Figure 2-2: Cross section through chemical sediments of the lower TSG and schematic location of drill cores, modified after Beukes and Gutzmer (2008).

This study is focused on the shelf facies of the CMCP. Thus, in the following, a detailed sedimentological and stratigraphically description of the KMF-5 drill core is provided, as well as a short review of the BH-1 drill core and the Kuruman Kop outcrop, which contains carbonates from the shelf facies of the upper Campbellrand Subgroup (Sumner, 2002).

2.1.1. Extended description of the KMF-5 drill core (Malmani Subgroup)

The KMF-5 drill core contains a ca. 1200 m thick intersection of the Malmani succession from the Transvaal area near Johannesburg (Fig. 2-1 a), which was sampled by courtesy of *Gold Fields of South Africa Limited* (now *Sibanye Gold Limited*). The core was holed at 26°24‘28.16“S/27°37‘40.87“E, is preserved at the core store facility of Sibanya Gold Ltd at Oberholzer and intersected the Malmani Subgroup from the erosional base of the overlying Rooihoogte Formation of the Pretoria Group to the conformably underlying Black Reef Formation and its erosional contact with Ventersdorp Lava (Fig. 2-3 a). Four of the five formations of the Malmani Subgroup are preserved in the core, the upper Frisco Formation (Sumner and Beukes, 2006) and part of the Eccles Formation having been removed by erosion prior to deposition of the siliciclastics of the overlying Rooihoogte Formation (Fig. 2-3 a). The drill core is located outside of the main metamorphic aureole of the Bushveld Complex. The Transvaal succession in this area close to Carltonville experienced at most lower greenschist facies metamorphism. The Malmani dolomites are thus for the most part very little recrystallized and preserve original microbial laminations often to the finest detail. The same applies to early diagentic chert bands in the succession that preserve sedimentary textures and structures even better than what is the case in adjacent unsilicified carbonate beds. The only exception to this is where the succession is intruded by relatively thin diabase sills (Fig. 2-3 a). These are most probably similar in age to the 2.054 Ga Bushveld Complex (Buick et al., 2001). Immediately adjacent to the sills the dolomites are altered, have a yellowish to brownish color and contain abundant ankerite and siderite. KMF-5 is situated in the inner shelf area of the CMCP where the succession is dominated by intertidal to supratidal light grey, partly silicified (chertified) dolomite of the Monte Christo and Eccles Formations with subordinate shallow subtidal dark grey chert-free dolomite of the Oaktree and Lyttleton Formations (Figs. 2-1 b, 2-3 a). Carbonate deposition was occasionally interrupted by influx of fine siliciclastic muds during marine regressions forming mudrock interbeds (Fig. 2-3 a). The basal Black Reef Formation is 22 m thick in KMF-5 and overlies Ventersdorp Lava with a sharp erosional contact. The lower part of the formation comprises of poorly

sorted pebbly fluvial quartzite with interbeds of mudrock and well-sorted marine orthoquartzite. This mixed fluvial to marine siliciclastic facies change upwards into an intertidal to shallow subtidal mixed siliciclastic-carbonate facies consisting of alternating dolarenite, stromatolitic dolomite, carbonaceous mudrock and orthoquartzite. The transition to inter- and shallow subtidal facies is quite rapid, marking a major transgression of the Kaapvaal craton and the onset of Malmani carbonate platform deposition.

The subdivision of the Malmani Subgroup into different formations is based simply on the presence or absence of early diagenetic chert bands (Button, 1973; Eriksson and Truswell, 1974). This is a very practical subdivision that works very well both in outcrop and drill core intersections. The Oaktree and Lyttleton formations are chert-free and the Monte Christo and Eccles formations chert-bearing (Fig. 2-3 a). Another conspicuous difference, applicable in both outcrop and drill core, is that the chert-free Oaktree and Lyttleton formations are dominantly composed of very dark grey fine micritic dolomite, whereas the dolomites of the chert-bearing Monte Christo and Eccles formations are dominantly medium to light grey in color with abundant sparry fenestral and sugary dolarenite interbeds. In outcrop the micritic dolomites of the Oaktree and Lyttleton formations weather to a chocolate brown and those of the Monte Christo and Eccles formations to mainly grey colors. This difference is ascribed to the higher concentration of manganese in the structure of dolomites of the Oaktree and Lyttleton fomations relative to that in the other two formations (Button, 1973; Eriksson, 1977; Eriksson et al., 1975). Similar principles of stratigraphic subdivisions apply to the dolomites of the Campbellrand Subgroup in Griqualand West but with additional well-preserved primary limestone members (Beukes, 1987).

When it comes to reconstruction of depositional environments of the carbonate succession it is very difficult and in some cases even impossible, to do that based merely on drill core intersections. The reason is that many, if not most, of the stromatolite structures have diameters larger than that of the core. These can therefore often be identified with some degree of certainty by making use of distinctive subordinate microbial laminations and textures as known from outcrops. Fortunately, the Zwartkop outcrop reference profile of the Malmani Subgroup is situated in rather close proximity to core KMF-5 (Fig. 2-1 a). Detailed descriptions of that profile by Eriksson and Truswell (1973, 1974) and Truswell and Eriksson (1972, 1975) could be used to reconstruct depositional environments of the succession in core KMF-5.

In KMF-5 the bottom *Oaktree Formation* of the Malmani Subgroup is 126 m thick and essentially composed of chert-free dark grey fine micritic dolomite with several 5

20 cm thick black carbonaceous mudrock partings (Fig. 2-3 a). The micritic dolomite appears rather massive in the core except for the occasional fine wrinkled microbial laminations, features typical of giant elongated stromatolitic mounds as it is known from outcrops of the formation (Eriksson and Truswell, 1973).

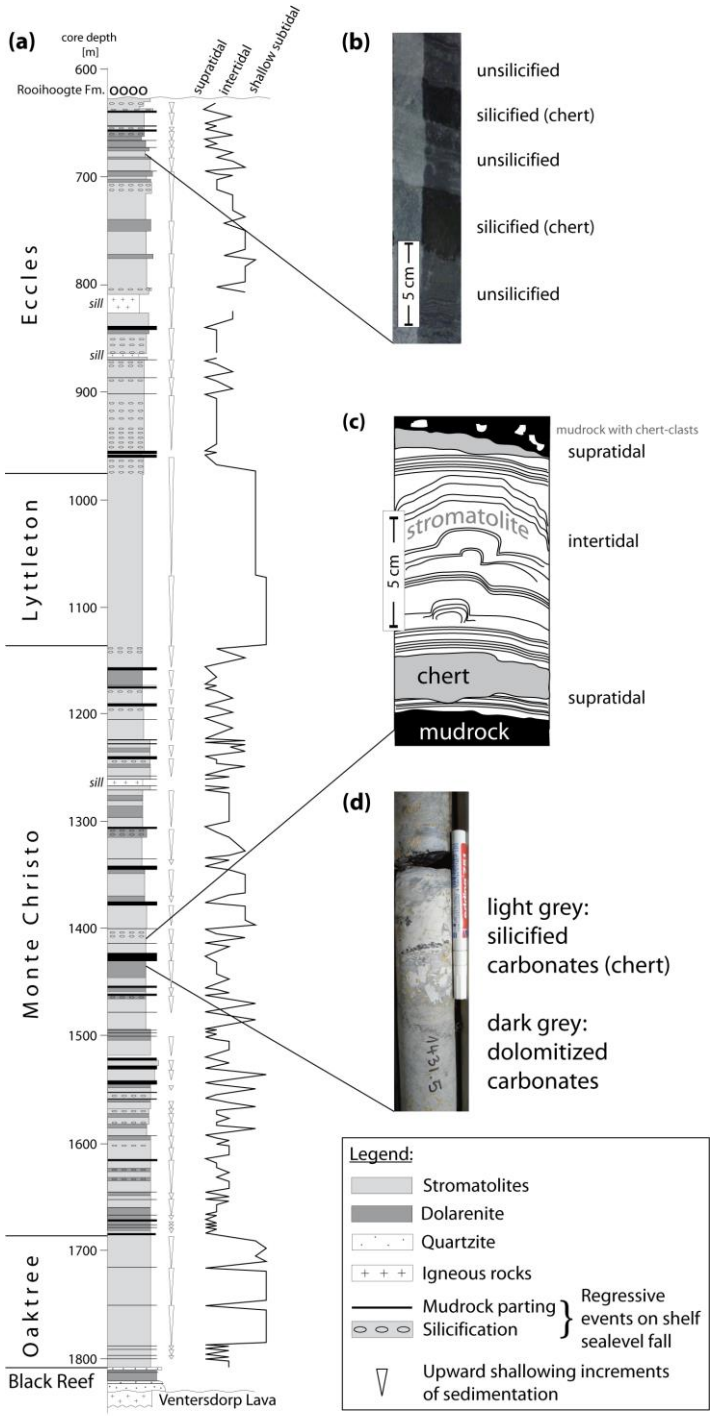

Figure 2-3: (a) Stratigraphy of the KMF-5 drill core with tidal conditions (supra-, inter- and subtidal) based on sedimentological observations as well as trans- and regressional fluctuations plotted alongside. (b) Silicified carbonate in the Monte Christo Formation, showing rip-up clasts of chert layer. (c) Exemplified Mini-Cycle in the Monte Christo Formation, ranging from mudrock to silicified carbonate and stromatolite structures back to silicified zones and eventually mudrock again. (d) Silicified and unsilicified carbonate alternating in the Eccles Formation within cm-scales.

Mudrock partings, spaced at stratigraphic intervals of 3-8 m, are especially abundant in the lower 20 m of the formation in close proximity to the underlying mixed siliciclastic-carbonate succession of the upper part of the Black Reef Formation (Fig. 2 3 a). The upper 100 m of the formation contain only two thin mudrock partings spaced about 35 m apart. The top of the formation is marked by a prominent 2 m thick mudrock with chert and mudrock rip-up clasts (Fig. 2-3 a). Such mudrock beds represent regressive sedimentary units in the succession, related to relative falls in sea level, decrease in accommodation space and influx of fine siliciclastic mud over the carbonate platform (Schroeder et al., 2009; Sumner and Beukes, 2006; Truswell and Eriksson, 1975). In contrast intervening giant stromatolitic mounds were most probably deposited in shallow subtidal environments (Eriksson, 1977; Truswell and Eriksson, 1975) at depths of not more than about 3-20 m as stromatolitic "reefs" elongated in line with dominant tidal currents in a carbonate ramp setting (Beukes, 1987; Sumner and Beukes, 2006).

The overlying *Monte Christo Formation* is 547 m thick in core KMF-5. It comprises of some 86 stacked upward-shallowing subtidal to intertidal and supratidal carbonate increments of sedimentation draped by regressive mudrock partings or beds (Fig. 2-3 a). The intertidal units are represented by complex assemblages of small columnar, pseudo-columnar and domal stromatolites with associated rippled dolarenite and occasional oolites (Eriksson, 1977; Sumner and Grotzinger, 2004; Truswell and Eriksson, 1975). Laminoid fenestrae are common in some of the subtidal stromatolite beds whereas precipitated small domal stromatolites, characterized by very even laminations (Sumner and Grotzinger, 2004) are typical for many of the intertidal units. Rippled dolarenite beds, sometimes associated with imbricated rip-up carbonate clasts often cap the shallowing-upward subtidal to intertidal increments of sedimentation and are considered to represent supratidal deposits. Early diagenetic silicification, represented by chert bands (Fig. 2-3 b), are essentially restricted to intertidal carbonate units and most typically developed in supratidal beds immediately below regressive mudrock beds (Fig. 2-3 c), that in turn may contain abundant rip-up clasts of chert (Fig. 2-3 c, d). This testifies to very early diagenetic or synsedimentary silicification of carbonate beds.

Upward-shallowing increments of sedimentation are typically only a few meters thick in the lower part of the succession and in general become thicker, up to about 20-30 m, upwards in the succession (Fig. 2-3 a). Some of the most prominent mudrock beds are present in the middle part of the Oaktree Formation (Fig. 2-3 a) indicating abundant supply of fine siliciclastic muds in these times during regressions. Organic carbon

supply and preservation were also higher as indicated by the black carbonaceous nature of the mudrocks. This stands in contrast to the light grey, organic poor nature of adjacent dolarenite and stromatolitic carbonate beds. Framboidal Fe-sulfide minerals (e.g. marcasite or pyrite) present in some mudrock layers coupled with preservation of organic carbon (Fig. 2-4) indicate highly reducing anoxic diagenetic conditions that could be compared with suboxic to perhaps even oxic conditions in the diagenetic environments of the carbonate beds. Such stark contrasts in redox state of diagenetic environments over centimeter stratigraphic scale is well known from modern tidal flat systems (Kowalski, 2010).

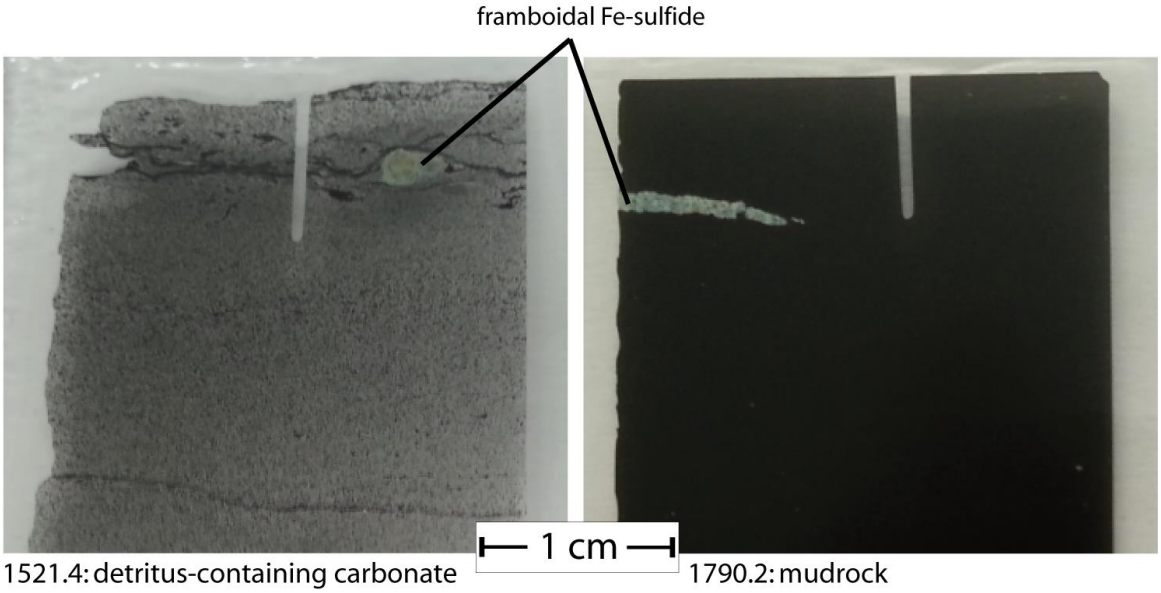

Figure 2-4: Framboidal Fe-sulfide minerals in carbonate sample 1521.4 (Monte Christo Formation) and mudrock sample 1790.2 (Oaktree Formation) indicate oxygen-poor conditions with abundant organic carbon, iron and sulfur to form Fe-sulfides.

The *Lyttleton Formation* has a thickness of 162 m in core KMF-5 (Fig. 2-3 a). It is composed of chert-free dolomite that is grey laminoid fenestral in the lower 66 m of the succession and dark grey fine micritic in the upper 96 m. The lower laminoid fenestral dolomite unit has a thin dark grey micritic dolomite basal unit that overlies intertidal partly silicified (chertified) small precipitated domal stromatolites of the Monte Christo Formation with sharp transgressive contact. The laminoid fenestral dolomites like that forming the lower part of the Lyttleton Formation are very well developed in parts of the Campbellrand Subgroup in GWA. Here they represent dolomitized equivalents of laminoid fenestral limestones interpreted to have been deposited in shallow subtidal carbonate platform lagoonal environments (Beukes, 1987; Sumner and Beukes, 2006). Similar to the Oaktree Formation, the dark grey fine micritic dolomite forming the upper part of the Lyttleton Formation, most probably represent giant microbial mounds

deposit as stromatolitic "reefs" in a shallow subtidal carbonate ramp environment. Overall this upper unit represents an upward-shallowing succession because fingerlike columns, oolite and dolarenite layers become more abundant to the top. Although the depositional environment of the Lyttleton Formation can be compared in broad terms to that of the Oaktree Formation there are significant differences. The Lyttleton is much more homogeneous than the Oaktree and is completely free of any mudrock partings (Fig. 2-3 a).

The contact between the Lyttleton Formation and overlying Eccles Formation is gradational. The lowermost unit of the Eccles Formation is composed of partly silicified laminoid fenestral shallow subtidal lagoonal dolomite overlain by a prominent 5 m thick carbonaceous mudrock with interbeds of fenestral dolomite (Fig. 2-3 a). This succession thus represents a rapid regression with lagoonal carbonates draping the giant stromatolitic reefs to be covered in turn by siliciclastic muds derived from the far landward interior of the carbonate platform.

About 330 m of the *Eccles Formation* is preserved in core KMF-5 below the erosional unconformity at the base of the Rooihoogte Formation of the overlying Pretoria Group (Figs. 2-2 and 2-3 a). The character and depositional setting of the Eccles Formation is rather similar to that of the Monte Christo Formation but for a lesser abundance of black carbonaceous mudrock interbeds (Fig. 2-3 a). It is also constructed of a large number of stacked shallowing-upward subtidal to lagoonal fenestral stomatolitic dolomite beds overlain by intertidal small domal and columnar stromatolite beds with associated rippled dolarenite (Fig. 2-3 a). The latter often mark the top of shallowing-upward increments of sedimentation and in a few cases contain oncolites. The succession is markedly silicified with replacive chert bands especially abundant in the lower and upper parts of the succession as preserved in core KMF-5 (Fig. 2-3 a). Here silicified and unsilicified carbonates alternate on a cm to dm scale (Fig. 2-3 b).

Comparing all formations it seems in particular that there was a change in sedimentation of detrital material, as the Oaktree and the Monte Christo formations host significantly more siliciclastic mudrock interbeds than the Lyttleton and Eccles formations (Fig. 2a). This might point to a change in carbonate platform architecture and/or dynamics in the siliciclastic continental source inland from the carbonate platform. With reference to platform architecture of the carbonate platform it is interesting to note that Beukes (1987) and Sumner and Beukes (2006) indicate that the CMCP developed from a carbonate ramp setting in the lower part of the succession to a mature rimmed shelf platform in the upper part. It is quite possible that with expansion

of the carbonate platform through time, siliciclastic source areas that were available during early stages of development of the carbonate platform became flooded and covered by carbonate sediments later on.

2.1.2. BH-1 drill core and the Kuruman Kop (Campbellrand Subgroup)

The BH-1 drill core contains the Campbellrand Subgroup succession, which is composed of seven formations and can be stratigraphically correlated with the Malmani Subgroup (Fig. 2-2) (Sumner and Beukes, 2006). A detailed description of BH-1 is provided by Altermann and Siegfried (1997). The lowermost Reivilo formation shows an upward transition from intertidal to subtidal facies and corresponds to similar facies in the Oaktree formation. The upper part of Reivilo was deposited contemporaneously to the Monte Christo formation and captures sub- to intertidal facies and the development of a steep platform margin. Analogues to the Monte Christo formation, the Reivilo formation records distinct intervals of sedimentation distinguished by changing water depths (Altermann and Siegfried, 1997; Button, 1973). The uppermost Reivilo formation reflects a rapid transgression and is overlain by the Kamden Member, which is a 1 to 2 m thick Fe formation layer. The transgressive sequence in the TA is subsequently featured in the Lyttleton and the lowermost Eccles formation and marks the transition to a rimmed platform margin. This stage is characterized by lagoonal and peritidal depositional conditions during which Fairfield, Klipfonteinheuwel, Papkuil, Klippan, Kogelbeen and Gamohaan formations were deposited, each representing shifts in water depth and style of carbonate precipitation. These uppermost formations contain more silicified carbonate, just like the correlative Eccles Formation (Altermann and Siegfried, 1997). The Fairfield and Klipfonteinheuwel formations capture peritidal conditions, which subsequently transition into shallow subtidal water depth of a lagoon as reflected in the facies of the Papkuil formation. As the new accommodation state was rapidly filled, peritidal conditions dominated again, despite a transgressional event (Sumner and Beukes, 2006). Klippan Formation reflects supratidal conditions dominating almost the entire platform. The Kogelbeen formation was deposited during changing water depth and records a variety of stromatolitic structures and rapid facies changes (Altermann and Siegfried, 1997; Sumner and Beukes, 2006). A transgressional event marks the beginning of the Kogelbeen deposition under lagoonal conditions and the establishment of peritidal conditions with ongoing carbonate precipitation. The facies of the Gamohaan Formation starts with intertidal features, which rapidly change to deeper water environments, reflecting the drowning of the entire platform and the subsequent deposition of iron formations (IF; Kuruman and Penge formations)

(Fig. 2-2). The correlative carbonate formation in the TA is the Frisco formation, which is as mentioned before not preserved in the KMF-5 drill core, as it was removed during erosion.

The Kuruman Kop is an about 200 m high hill (Fig. 2-1), situated near the city of Kuruman and comprises the uppermost succession of the Campbellrand Subgroup, including Kogelbeen and Gamohaan formations, as well as a well preserved transition sequence towards the IF of the Kuruman Formation at the very top of the hill, reflecting the drowning of the carbonate platform. The Kogelbeen formation is only exposed at the very base of Kuruman Kop and is rather homogeneous with mainly lagoonal-type calcite with fenestrae, which are calcite fillings interpreted as direct seawater precipitates. In comparison, the more dolomitized Gamohaan sequence is very heterogeneous and comprises peritidal to lagoonal sedimentary features with a mixture of more clastic sediments and grainstones, indicating enhanced sediment transport as well as microbial mat layers and fenestral stromatolites with frequently occurring calcite cement. Deep subtidal features are present further up the Kuruman Kop sequence, with Fe-rich carbonate and mudrock sequences, accompanied by chert layers, which grade into the Kuruman Fe formation. The sedimentology of the Kuruman Kop is described in detail in Sumner (2002).

2.2. Concluding remarks and sampling

Studies by Eriksson et al. (1975) and Beukes (1987) indicated that by far the majority of dolomite in the CMCP is of very early diagenetic origin replacing primary sedimentary limestones. Such limestones are much better and more abundantly preserved towards the margin of the carbonate platform in the Campbellrand Subgroup of GWA, where water circulation was better and occasional flooding by open marine waters prevented complete dolomitization of the succession. However, in the interior of the carbonate platform, represented by the Malmani Subgroup, conditions were more restricted, the water circulation was poorer and exchange with open marine waters less effective. This resulted in accumulation of Mg-enriched brines and complete dolomitization of the platform carbonates (Beukes, 1987). It is also in this interior part of the carbonate platform that silicification of carbonates were most effective probably due to influx of acidic meteoric waters and partial replacement of especially intertidal carbonates by chert (Beukes, 1987; Eriksson et al., 1975). As mentioned earlier, there are examples of secondary coarsely recrystallized dolomites present in both the Malmani and Campbellrand successions. Apart from those, which are restricted to the margins of diabase sills, there are other regionally more widespread ones but confined

to veins or massive cross cutting bodies in the succession. They are more common in close proximity to small Pb-Zn deposits in the CMCP. Hydrothermal fluids that led to formation of these deposits were mainly derived during intrusion of the Bushveld Complex (Huizenga et al., 2006a; Huizenga et al., 2006b).

Sampling was done on all four formations of the Malmani Subgroup available in KMF-5. As the Oaktree and the Lyttleton formations are much more homogenous, sampling density was lower than in the Monte Christo and Eccles formations. All available lithologies, stromatolitic carbonates were sampled in their variable morphological types, in particular some subtidal to intertidal increments of sedimentation of the Monte Christo Formation, in order to gain a good chemostratigraphic characterization of the succession. Apart from core KMF-5 a small set of samples was also obtained of the BH-1 and the Kuruman Kop outcrop. Well-preserved dolomite intervals were sampled for this study, with good preservation of sedimentary textures and structures and avoided veined, crackle brecciated and coarsely recrystallized intervals.

According to the sedimentological studies by (Beukes, 1987) and (Sumner and Beukes, 2006) this study divides the CMCP into the **lower CMCP**, reflecting a steep ramp architecture and including the stratigraphical correlative formations Lower Nauga from the Campbellrand Subgroup (GKP01, GKF01; Prieska Area), Reivilo and the Kamden Member from the Campbellrand Subgroup (BH-1; GWA), and Oaktree and Monte Christo from the Malmani Subgroup (KMF-5; TA). The **upper CMCP** reflects the rimmed margin architecture and includes the formations Upper Nauga from the Campbellrand Subgroup (GKP01, GKF01; Prieska Area), Fairfield, Klipfonteinheuwel, Papkuil, Klippan, Kogelbeen, and Gamohaan from the Campbellrand Subgroup (BH-1; GWA), and Lyttleton and Eccles from the Malmani Subgroup (KMF-5; TA).

3. Analytical methods

3.1. Sample preparation

After documentation and imaging of the drill core and outcrop samples, about 1 to 2 cm thick homogeneous sections were cut, crushed and powdered for elemental and isotope geochemical analyses. Thereby, utmost care was taken to avoid any secondary mineral veins. Additionally, thin sections of representative sections were prepared for Raman and synchrotron analyses.

3.2. Major and trace element analyses

3.2.1. XRF analyses

Major and trace element concentrations of whole rock samples were determined using a wavelength dispersive X-ray fluorescence device (XRF) (Hahn-Weinheimer et al., 1984). Loss on ignition (LOI) was determined on powdered samples at 1000 °C. For fused glass beads 1.5 g of dried sample powder (after drying for 24 h at 105 °C) was mixed with 7.5 g MERCK Spectromelt A12 (mixture of 66 % Li-tetraborate and 34 % Li-metaborate) and melted at 1200 °C using an Oxiflux system from CBR analytical service. Measurements were performed on the Bruker AXS S4 Pioneer spectrometer (Rh-tube at 4kW) of the Isotope Geochemistry Group, University of Tuebingen with 32 standardized samples (Potts and Webb, 1992). Analytical error and detection limits vary and depend on element and sample composition uncertainties. Generally, uncertainties for all major elements are better than 1 % (1σ), for trace elements better than 5% (1σ). The international standards used are compiled in Govindarau (1989).

In order to determine a more accurate detrital component of nearly detritus-free carbonates, selected samples with Al_2O_3 concentrations below 1 % were analyzed by laser ablation ICP-MS on the same fused glass beads that were already used during XRF analyses for their Al concentrations. Selected mudrock samples were also measured to verify the XRF results for these elements. Measurements were carried out on a Thermo Fisher Scientific iCAP Qc® quadrupole ICP-MS, coupled with a Resonetics RESOlution M-50 excimer laser ablation system, with a frequency of 4 Hz, a spot size of 130 µm, and a wavelength of 193 nm.

Based on the comparison between XRF and laser ablation ICP-MS data of Al_2O_3 measured on the same glass beads, this study distinguishes between three groups of nearly pure carbonates, silicified carbonates and carbonates with a detectable detrital component. Below a value of 1 wt-% Al_2O_3 the obtained XRF Al_2O_3 values are always

higher compared to the laser ablation ICP-MS Al_2O_3 values, which indicate that the XRF method already reached its accuracy limit. Because it is assumed that the detrital material corresponds to the composition of Post-Archean Australian Shale (PAAS; Taylor and MacLennan (1985)), 1 wt-% Al_2O_3 is defined as threshold value to distinguish between nearly detritus-free, "pure" carbonates and carbonates with a detectable detrital component ('detritus-containing' carbonates). PAAS data are also used to define the degree of silicification. For example, a carbonate with a 1 wt-% Al_2O_3 contribution from a PAAS like detrital component (with 18.9 wt-% Al_2O_3 and 62.8 wt-% SiO_2) will carry 3.32 wt-% SiO_2 from this component. Higher SiO_2 contents in the carbonates are thus assumed to originate from silicification.

3.2.2. ICP-MS analyses

Approximately 50 mg of sample powder were dissolved in ca. 5 g 2 % HNO_3 overnight at room temperature. Dissolved samples were centrifuged for 10 minutes at 5000 rpm. Subsequently, ca. 0.5 g of the supernatant was diluted with ca. 15 g of 1 ppb In and Re solution in 2% HNO_3 (internal standard). Trace element analyses were performed using an ESI SC-2DX autosampler coupled to a Thermo Fisher Scientific iCAP Qc® quadrupole ICP-MS instrument (Isotope Geochemistry Group, University of Tuebingen). Concentration data of the samples were derived from normalization of the oxide corrected ion signals to those of W2 international rock standard (U.S. Geological Survey) and from internal standardization to correct for instrumental drift and differences in ionization efficiency. Within-session accuracy was monitored by repeated analyses of international rock standards BHVO-2 and SCo-1 (U.S. Geological Survey). Depending on the element, deviations from the reference values used (Marx and Kamber, 2010) were ≤1.8% for the well characterized BHVO-2 reference material and <5% for SCo-1.

3.3. Total organic carbon analyses

Total organic carbon (TOC) and total carbon (TC) contents were determined on mudrock samples, silicified, and unsilicified carbonates. For TOC analyses approximately 0.8 g of sample powders had to be decalcified in 15 ml centrifuge tubes by drop-wise addition of 16 % HCl to remove all inorganic carbon (TIC). Residual samples were centrifuged for 10 min at 2000 rpm, decanted and again mixed with approximately 10 mL Milli-Q water. This procedure was done for repeated 7 to 10 times until samples were neutralized. Upon complete drying of the samples, between 5 to 70 mg, depending on the estimated TOC content, of decalcified samples (for TOC analyses) and un-decalcified samples (for TC analyses) were weight into tin-capsules. TOC and TC

measurements were done with a VARIO EL Elemental Analyzer (ZAG, University of Tuebingen) and with an Elemental Analyzer NC2500 (Isotope Geochemistry Group, University of Tuebingen) by combustion at 950°C.

3.4. Molybdenum isotope analyses

Our Mo purification procedure was based on the purification protocol of Siebert et al. (2001), Voegelin et al. (2009) and Wille et al. (2007) with some modifications. Due to the low Mo content of the carbonates between 10 and 30 ng/g it was necessary to digest up to 2 g of sample powder to obtain adequate Mo isotopic signals for precise and accurate mass spectrometric analyses. The sample powder was weighed into 25 mL Erlenmeyer Duran® glass flasks and dissolved by adding 11 ml concentrated HCl dropwise to avoid sample loss due to the strong reaction of carbonate with hydrochloric acid. Siebert et al. (2003) and Voegelin et al. (2009) showed that even at low acid strength, Mo is very soluble and leached out of detrital material. Therefore, upon complete reaction at room temperature, the flasks were covered with a watch glass and placed on a hotplate for 24 h at 100°C to ensure complete leaching of detritus and organics. After cooling down, 100 µl of 30 % H_2O_2 was added to keep Mo in its oxidized, dissolved Mo^{6+} state. Subsequently, samples were centrifuged in 15 ml centrifuge tubes at 3000 rpm for 10 minutes to separate detritus and organics. Meanwhile, the Erlenmeyer glass flasks were cleaned with Milli-Q water, before transferring supernatant solution from the tubes into the flasks.

Approximately 200 mg mudrock sample material was weight into 15 ml PFA beakers and leached with 5 ml concentrated HCl to dissolve any minor carbonate fraction. Supernatant solution was transferred into 7 ml PFA beakers and residual fractions were subsequently digested with 2 ml concentrated HF and 1 ml concentrated HNO3 for 24 hours at 110°C. After drying, samples were redissolved in 1 ml 6 M HCl and placed on a hot plate for 24 hours at 130°C. Sample solutions were then added to their respective aliquots, followed by drying and dissolving in another ml of 6 M HCl. Eventually, solutions were separated from any residual material by centrifugation in 1.5 ml Eppendorf tubes® at 12000 rpm for 15 minutes. These were dried again and redissolved in 5 ml 6 M HCl.

In order to resolve any isotopic fractionation of Mo during ion exchange purification and to correct for the instrumental mass bias during isotope analyses it is necessary to add an adequate amount of a ^{100}Mo-^{97}Mo double-spike to the sample solutions. 1:1 sample to spike mixtures allow for most accurate double spike deconvolutions (Rudge et al., 2009), making it necessary to determine the sample Mo

concentrations prior to double spike addition. To do so, an aliquot of about 4 % was taken from both carbonate and mudrock sample solutions, from which Mo was chemically purified by a miniaturized ion exchange-column containing 250 µl Dowex AG-1 X8, 200-400 mesh to remove any measurement-disturbing matrix, in particular Ca, and 100 % of the Mo was collected from this fraction. The aliquot was dissolved in 250 µl 4 M HCl + 0.1 %H_2O_2 and loaded on the resin, followed by a cleaning step with 1 ml of 4 M HCl + 0.1 % H_2O_2. The Mo fraction was collected by adding 2 ml of 2 M HNO_3. Given the very low Mo to matrix ratios, this Mo purification step was necessary to allow accurate concentration determinations by solution ICP-MS on the Thermo Fisher Scientific iCAP Qc® instrument. After determination of their Mo contents the residual sample solutions were transferred to 15 ml PFA beakers, mixed with the double spike and dried on a hotplate at 130°C. Eventually, each sample was redissolved in 5 ml 4 M HCl + 0.1 % H_2O_2 and loaded stepwise onto anion exchange columns (1 ml Eichrom® 1X8 resin, 200-400 mesh). Matrix elements of the samples were eluted by adding 7 ml of 4 M HCl + 0.1% H_2O_2, and Mo was finally released from the resin with 8 ml of 2 M HNO_3. The separation protocol for mudrock samples by anion chromatography differed from that of the carbonates, as they were dissolved in 3 ml 4 M HCl + 0.1 % H_2O_2 and eluted with 7 ml 2 M HNO_3.

With a second ion exchange column (2 ml Eichrom® 50WX8 resin, 200-400 mesh) Mo purification was enhanced by removing any residual Fe (Voegelin et al., 2009). To do so, dried sample fractions were redissolved in 2 ml 0.5 M HCl + H_2O_2 and loaded stepwise on the resin, whereby the second ml was collected in PFA beakers. Mo was then completely eluted from the resin by adding 4 ml of 0.5 M HCl + 0.1 % H_2O_2 (Voegelin et al., 2009).

Additionally, the purified Mo analytes were treated with a 1:3 mixture of concentrated HCl and HNO_3 to evaporate Ru and reduce its possible isobaric interference on mass 100 (Pearce et al., 2009).

A challenging issue regarding the extremely low Mo contents of the carbonate samples was to keep procedural blanks at constantly low levels. Therefore, all laboratory material, such as Erlenmeyer flasks, centrifuge tubes, PFA beakers, pipette tips and the anion/cation resins were carefully pre-cleaned or leached with 0.5 M HCl. Hydrogen peroxide can be one of the major contributors to high Mo blanks. Therefore, Suprapur® hydrogen peroxide (30 %) was used during digestion and separation, as its Mo content is very low (< 0.1 ng/g). With all these precautions it was possible to minimize the procedural blank from 3 ng down to constantly less than 0.4 ng. This improvement of the Mo blank levels from ca. 5-30 % of the sample amounts down to

0.6-4 % was necessary to render the blank negligible on the samples' Mo isotopic compositions.

Samples were finally dissolved in 0.3M HNO_3 and measured on a Thermo-Fisher Scientific Neptune® Plus multicollector ICP-MS in low resolution mode. Sample introduction was done with a CETAC Aridus IITM desolvating nebulizer system, achieving dry plasma. Solutions had concentrations between 10 and 100 ng/g and were measured with an uptake rate of about 70 µl/min at static mode with a signal of 5 V on ^{95}Mo (using a 1011 Ω resistor) at concentrations of ~50 ppb. Mo isotopic data are reported in ‰ and calculated as $\delta^{98}Mo = \left(\frac{\frac{^{98}Mo}{^{95}Mo_{sample}}}{\frac{^{98}Mo}{^{95}Mo_{NIST3134}} \times 0.99975} - 1\right) \times 1000$, following a proposal by (Naegler et al., 2014) to set the NIST3134 standard to 0.25 ‰ (Goldberg et al., 2013; Greber et al., 2012).

Two carbonate standards, the ECRM 782-1 dolomite standard, and the BCS-CRM 393 limestone standard were measured in every session to determine the external reproducibility of carbonate measurements. Results are listed in Table 3-1. Dolomite measurements (n = 9) show an average δ^{98}Mo value of +0.20 ± 0.06 ‰ with a mean concentration of 0.117 ± 0.014 ppm, whereas the limestone measurements (n = 6) resulted in an average δ^{98}Mo value of +0.99 ± 0.11 ‰ and a concentration of 0.065 ± 0.007 ppm. These values are in agreement with data reported by (Voegelin et al., 2009), yielding values of +0.17 ± 0.11 ‰ and 0.12 ± 0.04 ppm (ECRM 782-1) and +0.96 ± 0.09 ‰ and 0.074 ± 0.004 ppm (BCS-CRM 393).

Table 3-1: Mo isotope ratio (δ^{98}Mo) and concentration results of dolomite and limestone standard measurements

ECRM 782-1 Dolomite Standard				BCS-CRM 393 Limestone Standard			
run	$\delta^{98/95}$Mo	2SE	Mo (ppm)	run	$\delta^{98/95}$Mo	2SE	Mo (ppm)
#1	0.24	0.02	0.122	#1	0.97	0.01	0.059
#2	0.22	0.03	0.132	#2	1.03	0.01	0.057
#3	0.23	0.03	0.120	#3	0.90	0.01	0.062
#4	0.20	0.03	0.113	#4	1.05	0.01	0.065
#5	0.19	0.02	0.121	#5	0.99	0.01	0.074
#6	0.16	0.01	0.113	#6	0.97	0.01	0.072
#7	0.18	0.01	0.101				
#8	0.16	0.01	0.094				
#9	0.20	0.01	0.138				
		2SD				2SD	
Avg.	0.20	0.06	0.117	Avg.	0.99	0.11	0.065

3.5. Carbon and oxygen isotope analyses

Analyses of $\delta^{13}C_{carb}$ and $\delta^{18}O_{carb}$ were performed using a Finnigan MAT 252 gas source mass spectrometer combined with a Thermo-Finnigan Gasbench II/CTC Combi-Pal autosampler (Isotope Geochemistry Lab, University of Tuebingen). Both devices are connected using the continuous flow technique with a He stream as carrier gas. This setup allows for online preparation of carbonate samples. About 0.1 mg dried sample powder is loaded into a 10 ml glass vial, sealed with a rubber septum. The vials are placed in an aluminum tray and set to 90°C. After purging with pure He gas, 20 drops of 99% phosphoric acid are added. After a minimum reaction time of 2.5 hours released CO_2 is transferred (using a GC gas column to separate other components) to the mass spectrometer using a He carrier gas. The sample CO_2 is measured relative to an internal laboratory tank gas standard which is calibrated against in house (Laaser marble) and international (NBS18, NBS19) carbonate standards. All values are given in ‰ relative to V-PDB for carbon and V-SMOW/V-PDB for oxygen. The external reproducibility is ± 0.1‰.

Analyses of $\delta^{13}C_{org}$ were conducted on an Elemental Analyzer NC2500 connected to a Thermo Quest Delta Plus XL mass spectrometer in continuous flow online-mode. Decalcified samples (see TOC analyses for further details) containing 0.05 mg carbon are weight in tin capsules and combusted at 1050°C in an oxidation tube and at 650°C in a reduction tube, before they are cooled in a watertrap and transferred through a GC gas column into the mass spectrometer. Sample C is measured relative to an internal acetanilide standard which is calibrated against in house (e.g. Laaser marble) and international (USGS24) standards.

3.6. Silicon isotope analyses

For silicon (Si) isotope analysis the sample digestion and Si purification procedure follows the method described by van den Boorn et al. (2006) and Wille et al. (2010). Basically, after ~ 1 mg of sample powder and 0.5 ml of 2 M NaOH were added into PFA beakers, this mixture was decomposed in Berghof DAB-3 Bombs at ~200 °C for three days. The sample solution and solid residue were transferred into 2 ml centrifuge tubes, centrifuged, and the supernatant was separated from the residue. Subsequently, 0.5 ml concentrated aqua regia was added to the residue, which was transferred into PFA beakers, capped and heated for 1 day at 100 °C. After complete dissolution of the residue, the solution was dried down and the residue dissolved in 0.5 ml 0.5 M HNO_3. The sample solutions of the different steps were transferred onto 5 ml Pasteur Pipettes filled with 0.5 ml Biorad AG50-X8 resin, 200-400 mesh. The Si fraction was effectively

eluted by adding 3 ml of Milli-Q water. All samples and standard solutions were adjusted to match a Si concentration of 2 ppm by adding Milli-Q water.

Samples and Si standard solutions were measured on a Thermo-Fisher Scientific Neptune® Plus multicollector ICP-MS in medium-resolution mode with standard (H) cones. Dry plasma conditions were applied using an Apex Q desolvating system by Elemental Scientific. Although sensitivity changed slightly from session to session, a 2 ppm Si solution with an uptake of 100µl/min resulted in a 20 V signal on 28Si using a 1011 Ω resistor. To correct for instrumental mass bias, a standard-sample-standard bracketing sequence was performed. Repeated analysis of internal Si Standard SP150, Demospongiae (66°19'12.0''S/144°18'36.0''E, 357m), yielded a $\delta^{30}Si_{NBS28}$ isotopic value of -3.25 ± 0.12 ‰ (n = 6), which is well within uncertainties of previously published values for this standard of -3.18 ± 0.23 ‰ (Wille et al., 2010).

3.7. Raman analyses

Raman spectroscopy is the detection of inelastically scattered photons interacting with the vibrational modes of molecular bonds or crystal lattices. This yields information on the molecular structure of the analyzed material, which includes the electronic configuration of carbonaceous material. Hence, Raman spectroscopy detects the structural order of carbonaceous material (CM), which is best parameterized by the relative intensities of the so-called D ("disordered") and G ("graphite") bands, as well as their central peak positions and peak widths. The peak intensity ratio I_D/I_G increases in the case of graphite with the size of the domains, which allows determining the structural order of CM (Fig. 3-1). Both, the D- and G-bands broaden significantly with increasing disorder. Depending on the level of disorder of the material, other defect bands (such as the D2, D3, and D4) can appear, causing an apparent shift of the G-band to higher wavenumbers (Sadezky et al., 2005). In well-characterized terrestrial kerogen, D- and G-band characteristics allow to determine the peak metamorphic temperatures experienced by the material, because the structural changes are usually irreversible (Beyssac et al., 2004; Beyssac et al., 2002; Lahfid et al., 2010). In this study, the data are reported as the ratio of the peak intensities of the D- and G-bands (I_D/I_G) and the width of the D1 band (FWHM-D). All Raman band position wavenumbers (in cm^{-1}) are given as shifts relative to the exciting laser wavelength.

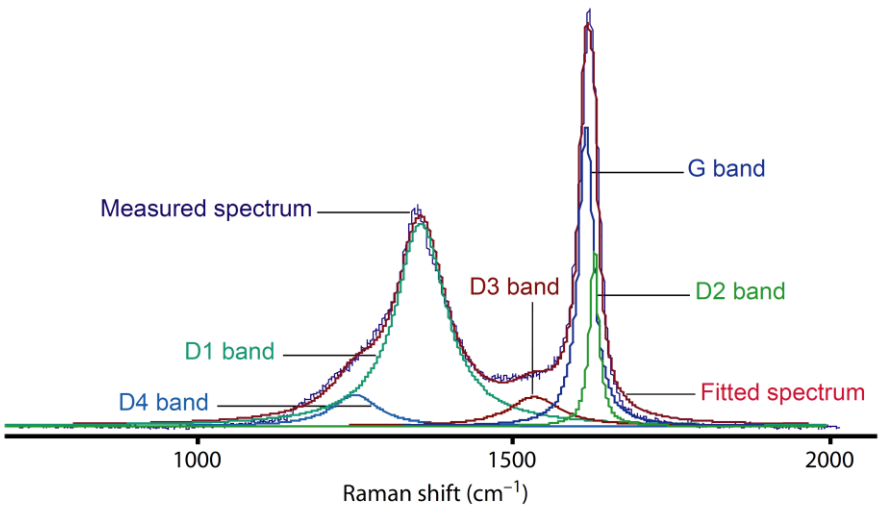

Figure 3-1: Raman spectrum of disordered carbonaceous material at low-metamorphic conditions. Measured spectrum is composed of the G- and D-bands, which include subordinate defect bands (D1, D2, D3, D4). Illustration from Lahfid et al. (2010).

Raman analyses were performed at the Institute de Physique du Globe de Paris. Selected carbonate and mudrock samples from KMF-5 and Kuruman Kop are prepared as thin sections with 30 µm thickness and polished down to 1 µm. Raman measurements were conducted on a Renishaw inVia Raman Microscope coupled to an Olympus BX61 confocal microscope, using an Ar monochromatic 514 nm laser source. Laser excitation was adjusted to an on-sample intensity of 0.4 mW at 2 x 20 s exposure time. Sample spots were focused with a 50x at 2 to 3 µm spots and acquisition was obtained in static mode within a range from 100 to 4000 cm^{-1}, with the center at 1150 cm^{-1}. Beam centering and Raman spectra calibration were performed on a Si chip with a Raman band at 520.4 cm^{-1}.

3.8. Iron isotope analyses

Between 15 and 170 mg powdered samples, corresponding to approximately 200 µg of total sample Fe, were weighted into 15 ml PFA beakers. Sample digestion for carbonates was done using 20 % acetic acid to avoid digestion of Fe oxides and clay minerals, according to the chemical protocol of von Blanckenburg et al. (2008). Mudrocks were completely digested in a 2:1 mixture of distilled HF and HNO_3. Fe purification was achieved using the method described in Schoenberg and von Blanckenburg (2005). Fe isotope measurements were performed on a ThermoFisher Scientific Neptune® Plus multicollector-inductively coupled plasma-mass spectrometer (MC-ICP-MS) at the facilities of the Isotope Geochemistry Group, University of Tuebingen, using the standard-sample-bracketing method (Schoenberg and von

Blanckenburg, 2005). Fe isotope data are reported relative to the IRMM-014 standard (Institute of Reference Material and Measurements, Geel, Belgium) as

$$\delta^{56}\mathrm{Fe} = \left(\frac{\frac{^{56}\mathrm{Fe}}{^{54}\mathrm{Fe}_{\mathrm{sample}}}}{\frac{^{98}\mathrm{Fe}}{^{95}\mathrm{Fe}_{\mathrm{IRMM014}}}} - 1 \right) \times 1000$$

and are expressed as permille (‰). Procedural blanks were between 20 and 60 ng, which is less than 0.03 % of the total amount of Fe that passed through the Fe purification procedure, and is negligible for the samples' Fe isotope composition. The external reproducibility was determined by repeated analyses of the in-house HanFe standard, which gave +0.29 ± 0.06 (2σ) ‰ for δ^{56}Fe (n = 76). Additionally, the dolomite standard ECRM 782-1 (δ^{56}Fe: -0.94 ± 0.17 ‰, n=14), the calcite standard BCS CRM 393 (δ^{56}Fe: -0.23 ± 0.13 ‰, n=18), and the IF-G reference material (Dauphas and Rouxel, 2006) (δ^{56}Fe : 0.64 ± 0.10 ‰, n=16) were also analyzed during every session.

3.9. Synchrotron-based X-ray absorption spectroscopy

3.9.1. Principles of X-Ray Absorption Near Edge Spectroscopy (XANES)

The synchrotron-based X-Ray absorption spectroscopy (XAS) is a powerful tool to explore the molecular and atomic structure and behavior of matter. Thereby, an X-ray photon is absorbed by an atom and this energy is transferred to a core-level electron, which is subsequently ejected and excited to a continuum state. This causes the emission of fluorescent X-rays that scatter around the X-ray absorbing atom and create interferences. These occur at discrete energies and can be used to identify the absorbing atom regarding its oxidation state, ligands, structure, neighboring atoms, bond length and coordination number. XAS includes two techniques, the X-Ray Absorption Near Edge Spectroscopy (XANES) and the Extended X-Ray Absorption Fine-Structure (EXAFS) (Fig. 3-2). XANES features are sensitive to changes of the oxidation state, coordination chemistry, local structure and ligand symmetry around the photoabsorber and can be used to precisely identify chemical species in mixtures and complex materials. There are three regions in the XAS, the main edge, which signals the onset of the continuum state (E_0), the pre-edge ($E < E_0$), and the post-edge ($E > E_0$) (Fig. 3-2). A higher oxidation state increases E_0, whereas the shape of the post-edge spectra can give information about the chemical environment and the ligand geometry. The weak pre-edge spectra originate from dipole forbidden bound states transitions ($s \rightarrow d$). The hybridization of electronic levels is strongly affected by details of the crystalline field caused by the ligand geometry, which means that elements can have same valence state but different local structure that becomes visible in the shape of the

spectra. Principles of synchrotron radiation are explained in detail in (Mobilio et al., 2015).

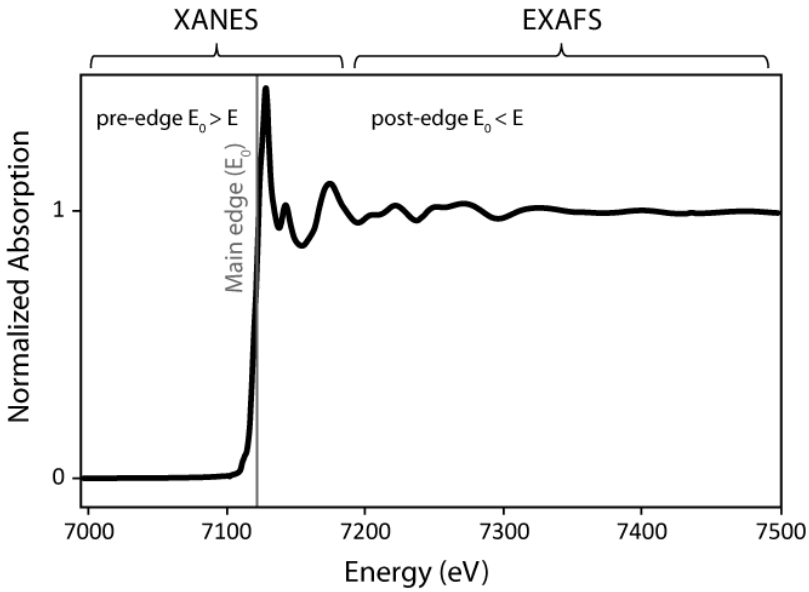

Figure 3-2: XAS Fe K-edge (7112 eV) spectrum of Fe_0 foil. The main absorption edge infers the oxidation state and increases with higher valence state.

3.9.2. Experimental setup

We conducted micro X-Ray Absorption Near Edge Structure (μ-XANES) spectroscopy mapping in fluorescence and transmission mode using the "Turbo-XAS" design at the energy-dispersive XAS beamline ID24 at the ESRF (Pascarelli et al., 1999). The advantage of this beamline is its high flux and the collection of XANES spectra on every spot. For experiments in fluorescence mode 30 μm thick polished thin sections mounted on glass slides were prepared. For experiments in transmission mode 100 μm thick unmounted thin sections were prepared (Fig. 3-3). The advantage of transmission mode is a reduced acquisition time, which allowed collecting data of a 2000 x 2000 μm map and at a spot size of 20 μm in about the same amount of time as was required to collect data of an e.g. 500 x 500 μm map in fluorescence mode. Low-Fe samples (< 0.5 wt-% Fe_2O_3) are challenging to prepare for transmission, as the signal-to-noise ratio might be too low when the section is very thin but self-absorption effects increase with thickness and amount of Fe in the sample and can distort the XANES signal. During transmission mode a Si (311) bent polychromator was used in the Bragg geometry and analyzed an energy range around the Fe K edge from 6946 to 7413 eV. For fluorescence mode a monochromatic beam was created by placing a fast-moving slit at the polychromator, to avoid interferences of fluorescent X-rays with the I_0 beam (Fig. 3-3). In this mode, measurements were conducted at an energy range from 7069 to 7311 eV.

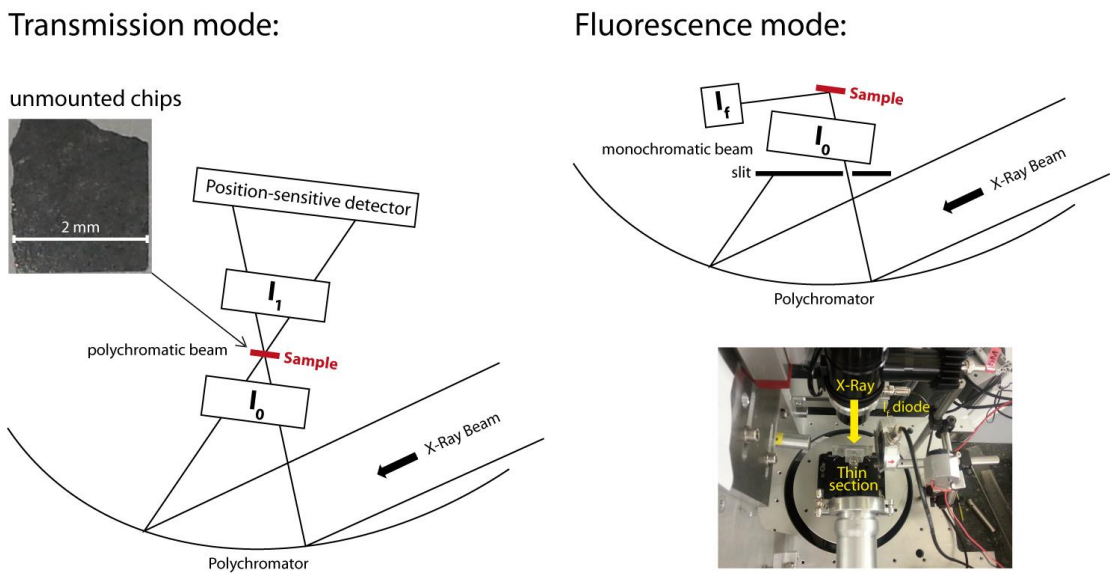

Figure 3-3: Experimental setup of ID24 for synchrotron measurements in transmission and fluorescence mode. Modified after Pascarelli et al. (1999).

3.10. X-Ray diffraction (XRD)

XRD analyses were conducted at the Materials Analysis and Research Laboratory (MARL) of the Iowa State University. For this study representative samples for 'pure' carbonates, silicified carbonates, and mudrocks were measured on a Siemens D 500 diffractometer using CuKα radiation. Powdered samples were placed in a specimen holder, covered with plexiglass, and measured under conditions of 45 kV and 30 mA. XRD patterns were acquired over a 2θ range of 4 to 75° and subsequently analyzed using JADE software.

4. Results

4.1. Major and trace elements

4.1.1. Malmani Subgroup (KMF-5, TA)

Major element data reveal that KMF-5 carbonate samples are completely dolomitized and partly silicified (Table 4-1; Fig. 4-1). However, formations containing mostly intertidal sedimentary rocks (Eccles and Monte Christo) are more heterogeneous in their chemical composition than formations with subtidal sedimentary rocks (Lyttleton and Oaktree). Pure carbonate samples contain just minor detrital material (≤ 0.62 wt-% Al_2O_3) and are unsilicified (≤ 3.26 wt-% SiO_2). Their silicified counterparts with SiO_2 contents of 3.35 to 86.76 wt-% also contain low Al_2O_3 contents, with values up to 0.52 wt-%, respectively. Carbonates with higher detrital components have Al_2O_3 contents varying from 1.01 to 17.56 wt %. Their SiO_2 contents ranges from 3.82 to 46.92 wt-%. Silicification can also be seen in mudrock samples, which otherwise contain a high detrital component, with Al_2O_3 contents of 4.89 and 27.34 wt-%.

The *Oaktree Formation* comprises shallow subtidal carbonates, which were deposited during the expansion of the carbonate platform. Sedimentary rocks from this formation range from pure carbonates, carbonates with distinct detrital contribution (Al_2O_3 up to 3.53 wt-%) to mudrock samples with TOC values up to 1.73 %. No silicification of mudrocks or of carbonates is observed in this formation.

Samples of the *Monte Christo Formation* were mainly deposited under peritidal conditions and have very heterogeneous geochemical signatures. As with samples from the Oaktree Formation, sedimentary rocks contain variable amounts of detrital material ranging from pure carbonates to mudrocks. Carbonates are mainly mixed with mudrock material, even though there are some silicified carbonates. Mudrocks occur very frequently in this formation and are silicified to various degrees. One silicate-rich carbonate sample (1265.1) occurs close to the top of the Monte Christo Formation and is exceptionally rich in iron (10.34 wt-% Fe_2O_3) compared to the other carbonate samples (0.17-2.13 wt-% Fe_2O_3). Although it contains a significant amount of detrital material (11.73 wt-% Al_2O_3), this sample strongly differs from other mudrock samples and detritus-rich carbonates, as it contains very litte organic material (0.04 wt-% TOC).

The *Lyttleton Formation* was deposited under shallow subtidal conditions like the Oaktree Formation, in that it experienced nearly no silicification. However, it differs

significantly ways from the Oaktree Formation, as almost all samples are pure carbonates and do not contain any mudrock layers (Fig. 4-1).

The *Eccles Formation* was governed by intertidal conditions and shows varying geochemical signatures. In contrast to the Monte Christo Formation, silicification is clearly dominant in the Eccles Formation and carbonate samples do not contain a significant detrital component. Moreover, this formation only hosts a few partly silicified mudrocks.

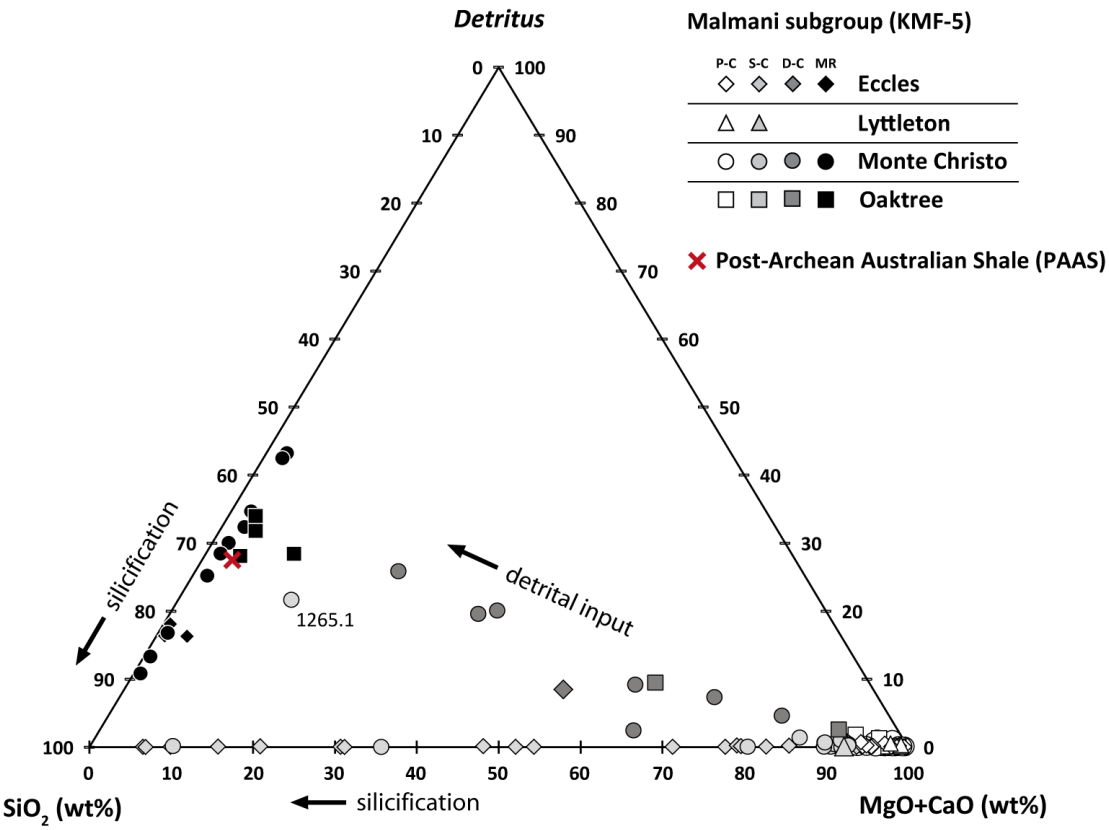

Figure 4-1: Ternary diagram illustrating the extent of detrital input and the silicification of Malmani carbonates and mudrocks (KMF-5). "Detritus" is the sum of TiO_2, Al_2O_3, Na_2O, K_2O, and P_2O_5 (all in wt-%). Sample 1265.1 is a Fe- and silicate-rich sample, probably correlative with the Kamden 'IF' Member. PAAS values from Taylor and McLennan (1985). P-C: 'pure' carbonate, S-C: silicified carbonate, D-C: detritus-containing carbonate, MR: mudrock.

4.1.2. Campbellrand Subgroup (BH-1 and Kuruman Kop outcrop; GA)

The major element chemistry of BH-1 samples have a mostly the composition of pure carbonates (Table 4-2, Fig. 4-2). In the Reivilo Formation, samples 2121 and 2131 are only partly dolomitized (Mg/Ca ratio of 0.19 and 0.45, respectively), contain more detrital material (Al_2O_3 content of up to 1.80 wt-%), and are partly silicified (SiO_2 content of up to 16.39 wt-%). Despite extensive dolomitization, there are still formations in the Campbellrand Subgroup of the GWA that contain pure limestone, in contrast to the completely dolomitized Malmani Subgroup of the TA (Beukes, 1987).

Sumner and Beukes (2006) correlated the Reivilo (GWA) with the Monte Christo Formation (TA), which was also governed by detrital input. This suggests that enhanced detrital input was not fully restricted to the tidal flat area of Transvaal area but also influenced partly the platform to the deeper regions of the Griqualand West area. Two samples from the Gamohaan Formation are also detritus-containing and silicified carbonates. Sample 1914 was deposited adjacent to the Kamden IF Member and is slightly silicified (3.73 wt-% SiO_2), but has much higher Fe concentrations (Fe_2O_3 of 3.64 wt-%).

Outcrop samples from the Kuruman Kop are mostly pure carbonates, with one exception (Table 4-3, Fig. 4-2). Sample Ku12/04 is a chert, which was sampled near a siderite band as is from the Gamohaan Formation, in the transitional zone between carbonates in the lower part and IFs in the upper part of the Kuruman Kop.

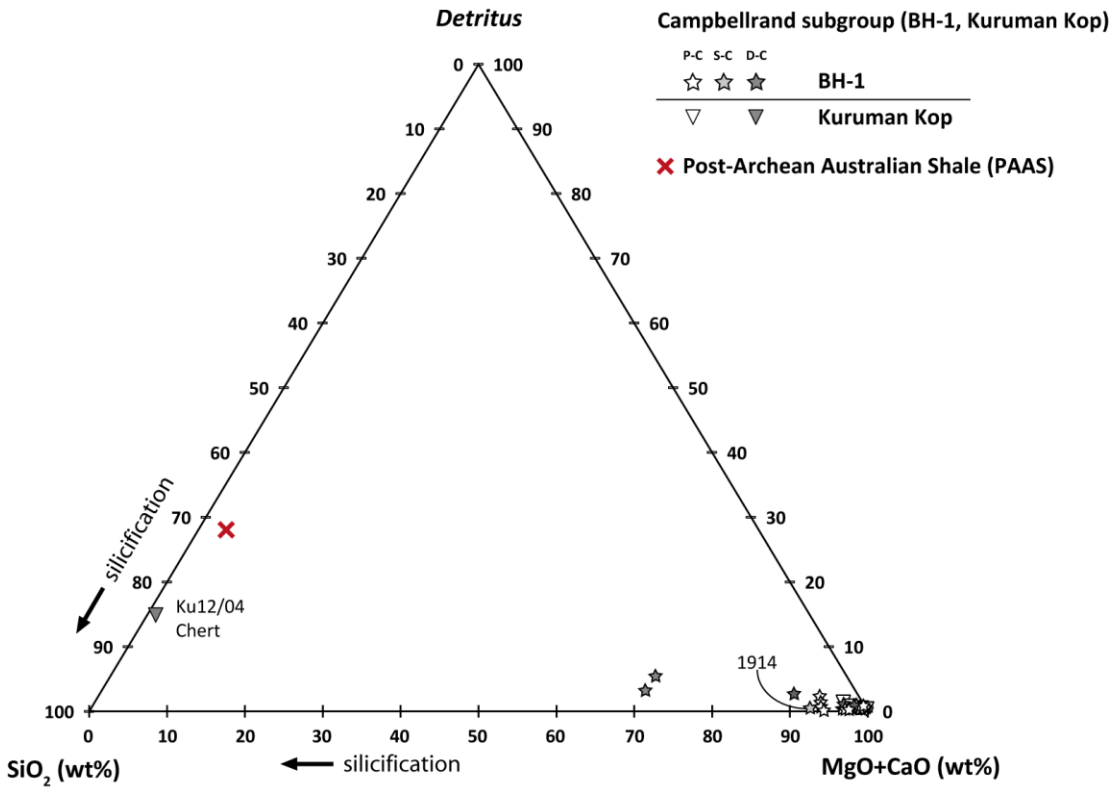

Figure 4-2: Ternary diagram illustrating the extent of detrital input and the silicification of Malmani carbonates (BH-1 and Kuruman Kop. "Detritus" is the sum of TiO_2, Al_2O_3, Na_2O, K_2O, and P_2O_5 (all in wt-%). Sample 1914 is an Fe-rich carbonate, which was deposited adjacent to the Kamden 'IF' Member in the GWA. Upper CS is the Upper part of the Campbellrand Subgroup, including formations Gamohaan, Kogelbeen, Klippan, Papkuil, Klipfonteinheuwel, and Fairfield. Lower CS is the Lower Campbellrand Subgroup, which is here represented by the Reivilo. PAAS values from Taylor and McLennan (1985). P-C: 'pure' carbonate, S-C: silicified carbonate, D-C: detritus-containing carbonate.

4.1.3. Fe numbers (Fe#)

The ratio of Fe to Mn in the samples is expressed as Fe number (Fe# is [$Fe_{tot}/(Fe_{tot}+Mn_{tot})$]). This is based on the chemostratigraphic behavior of Fe and Mn,

where Fe is precipitated in deeper waters at a lower oxygen fugacity than Mn (Beukes, 1987). The determined Fe# of Malmani and Cambellrand whole rock samples (Tables 4-1 and 4-2) show variation with water depth as well as with lithology. Subtidal pure carbonates (upper Oaktree and Lyttleton formations) yield the lowest Fe# values, which fall in a narrow range between 0.32 and 0.42. Rocks from intertidal zones (lower Oaktree, Monte Christo and Eccles formations) yielded values from 0.40 to 1.00, depending on the lithological type, with pure carbonates ranging from 0.42 to 0.68, silicified carbonates from 0.40 to 0.99, detritus-containing carbonates from 0.56 to 0.88 and mudrocks from 0.96 and 1.00.

Pure carbonates of the lower Campbellrand Subgroup succession (Reivilo Formation) have even lower Fe# than Malmani rocks (0.14 and 0.32), and two detritus-containing carbonates of the same formation have Fe# of around 0.55. Pure carbonates of the upper Campbellrand Subgroup succession (Fairfield, Klipfonteinheuwel, Papkuil, Klippan, Kogelbeen formations) show overall higher Fe# between 0.28 and 0.47 compared to the Reivilo Formation. Detritus-containing carbonates 340 and 375 from the Gamohaan Formations yielded 0.49 and 0.57 in Fe#. Fe-rich carbonate sample 1914 shows a high Fe# of 0.65. Fe# for Kuruman Kop outcrop samples yielded for pure carbonates values between 0.19 and 0.61 and for chert sample Ku12/04 a value of 0.98, due to the high detrital component.

Dolomites of the Malmani and Campbellrand Subgroup, that are near mudrock partings or which contain detrital material, show systematically higher Fe# and therefore this number also seems to be influenced by the degree of continental contamination, besides the dependence from water depth.

4.1.4. Rare Earth Element and Yttrium (REE+Y) spectra

Typical REE+Y features of reflecting seawater are depleted light REE, a positive La anomalies, as well as Y/Ho ratios higher than the PAAS value of 27 (Bau, 1999; Bau and Dulski, 1999; Kamber and Webb, 2001; Webb and Kamber, 2000). In carbonates the order of magnitude of these indicators is strongly influenced by mixing water masses from the continent and from hydrothermal vents (Kamber and Webb, 2001). Freshwater caries a continental 'PAAS' signature and would thus flatten the seawater REE+Y pattern in affected carbonates (Kamber and Webb, 2001 and references therein). A higher input of hydrothermal waters on the other hand results in an over increase in REE, more pronounced positive Eu anomalies and decreasing Y/Ho ratios (Derry and Jacobsen, 1990). In seawater with sufficient oxygen levels, Ce^{3+} is oxidized to Ce^{4+} and subsequently removed from the water column, which would be reflected in a

negative Ce anomaly in the carbonates precipitated from that seawater (Webb and Kamber, 2000). However, Ce oxidation and therefore the development of a negative Ce anomaly is inhibited when Fe and Mn concentrations in the seawater are higher than 50 nM (Seto and Akagi, 2008), as they lower the Eh. Thus, even Fe (and Mn) concentrations of several µM in the shallow-marine environment (Table 8-2), could inhibit the development of a Ce anomaly even during oxygen production.

Pure carbonates of KMF-5 and BH-1 were analyzed for their REE+Y distibutions. Additionally, four mudrock samples and the Fe- and silicate-rich sample 1265.1 from KMF-5 were measured. Absolute concentrations are listed in Tables 4-4 and 4-5. Y/Ho anomalies were calculated from absolute values. Concentrations were PAAS-normalized (index N) (Taylor and MacLennan, 1985) and La, Ce, and Eu anomalies were calculated. Positive La anomalies thereby indicated by Ce/Ce* values smaller than unity ($Ce/Ce^* = Ce_N/(0.5*La_N+0.5*Pr_N)$), negative Ce anomalies by Pr/Pr* values bigger than unity ($Pr/Pr^* = Pr_N/(0.5*Ce_N+0.5*Nd_N)$), and positive Eu anomalies by Eu/Eu* values bigger than unity ($Eu/Eu^* = Eu_N/(0.5*Sm_N+0.5*Gd_N)$) (Bau and Dulski, 1996; Webb and Kamber, 2000).

From KMF-5 almost all carbonate samples reveal positive La (0.68 to 0.99; mean 0.91 ± 0.11 (2σ)) and Eu (0.94 to 1.73; mean 1.27 ± 0.34) to anomalies as well as superchondritic Y/Ho ratios (23 to 83; mean 40 ± 26). None of them show any Ce anomaly (mean 0.99 ± 0.04). Mudrock samples lack of any La (0.95 to 1.05) and Ce (0.95 to 1.00) anomalies and have no elevated Y/Ho ratios (23 to 28). Eu/Eu* is mostly below unity (0.58 to 1.06) and only shows a clear positive anomaly in sample 1265.1 (1.26). Carbonates of BH-1 reveal more pronounced Y/Ho ratios (29 to 88; mean 72 ± 31) and La anomalies (0.75 to 0.94; mean 0.85 ± 0.11). Eu anomalies are detectable (0.97 to 1.29; mean 1.14 ± 0.16) but no Ce anomalies (0.99 ± 0.04).

REE+Y patterns are described and discussed in detail in Chapter 5.

4.2. Total organic carbon (TOC)

TOC data of KMF-5 are listed in Table 4-1. Values of pure carbonates lie between 0.01 and 0.17 wt-% (mean with 2σ: 0.03 ± 0.07 wt-%). TOC of silicified carbonates range from 0.01 to 0.15 wt-% (0.06 ± 0.09 wt-%). TOC values for detritus-rich carbonates are significantly higher, between 0.14 and 3.57 wt-% (1.80 ± 2.52 wt-%). TOC values in mudrock samples obtain a wide range between 0.83 and 8.50 wt-% (2.90 ± 4.14 wt-%). Pure carbonate samples of the BH-1 show TOC values between 0.01 and 0.29 wt-% (0.07 ± 0.13 wt-%) and two detritus-containing carbonates 340 and 375 show higher values of 0.28 and 0.20 wt-%, respectively (Table 4-2).

4.3. Carbon and oxygen isotopes

Carbon and oxygen isotope data are of KMF-5 rocks are listed in Table 4-1 and illustrated in Fig. 4-3. Pure carbonates show a range in $\delta^{18}O_{carb}$ signatures between -10.0 and -6.2 ‰ (mean with 2σ: -8.0 ± 1.5 ‰). Silicified carbonates range from -10.3 to -5.4 ‰ (-7.6 ± 2.1 ‰), detritus-containing carbonates from -12.0 to -7.5 ‰ (-8.7 ± 2.8 ‰), and mudrocks from -17.1 to -8.0 ‰ (-13.9 ± 6.0 ‰). For $\delta^{13}C_{carb}$, pure carbonates range from -0.9 and +0.3 ‰ (-0.4 ± 0.6 ‰). Silicified carbonates show values between -1.2 to +0.4 ‰ (-0.2 ± 0.8 ‰). Detritus-containing carbonates range from -1.0 to +0.1 ‰ (-0.6 ± 0.7 ‰), and mudrocks from -12.3 to -0.6 ‰ (-5.3 ± 7.9 ‰). The Fe- and silicate-rich sample 1265.1 shows relatively low $\delta^{18}O_{carb}$ and $\delta^{13}C_{carb}$ values of -16.4 and -3.2 ‰, respectively. For $\delta^{13}C_{org}$, pure carbonates range from -28.5 and -21.6 ‰ (-25.4 ± 3.5 ‰), silicified carbonates from -28.6 to -20.5 ‰ (-25.2 ± 4.7 ‰), detritus-containing carbonates from -33.2 to -22.2 ‰ (-29.5 ± 6.2 ‰), and mudrocks from -39.4 to -21.8 ‰ (-32.0 ± 8.5 ‰).

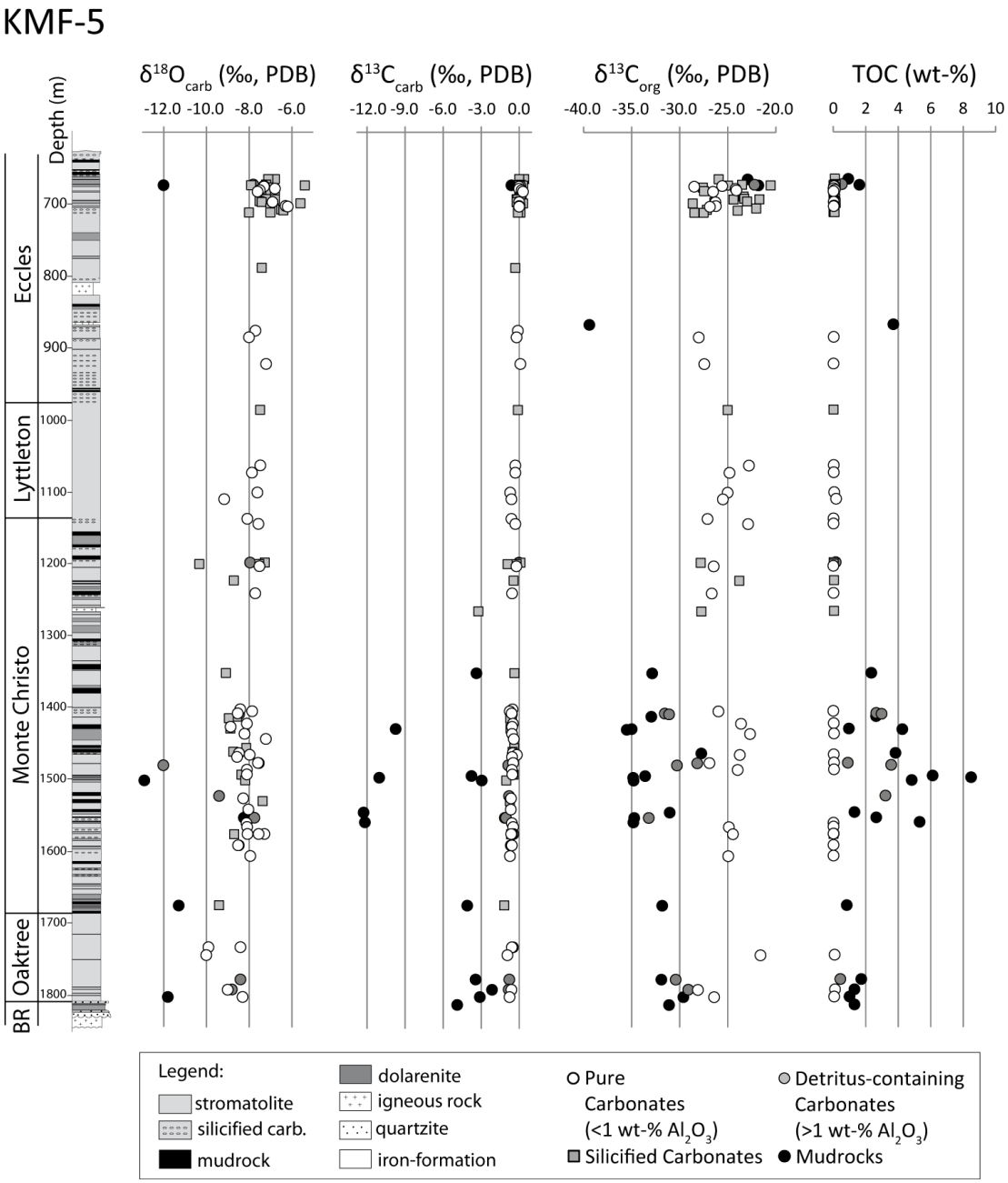

Figure 4-3: TOC content, oxygen and carbon isotope signature of carbonates and organic matter of KMF-5 samples. BR: Black Reef

Carbon and oxygen isotope data are of BH-1 rocks are listed in Table 4-2 and illustrated in Fig. 4-4. Pure carbonates yield $\delta^{18}O_{carb}$ values between -13.2 and -7.7 ‰ (mean with 2σ: -9.5 ± 2.8 ‰), $\delta^{13}C_{carb}$ signatures between -1.1 and -0.1 ‰ (-0.6 ± 0.6 ‰), and $\delta^{13}C_{org}$ signatures between -33.4 and -23.3 ‰ (-29.8 ± 4.5 ‰). Fe-rich carbonate 1914 shows values of -7.7 ‰ ($\delta^{18}O_{carb}$), -1.3 ‰ ($\delta^{13}C_{carb}$), and -28.9 ‰ ($\delta^{13}C_{org}$). Detritus-rich carbonates 340 and 375 show values of -11.5 ‰ and -9.6 ‰ ($\delta^{18}O_{carb}$), -0.1 ‰ and 0.1 ‰ ($\delta^{13}C_{carb}$), and -35.1 ‰ and -33.4 ‰ ($\delta^{13}C_{org}$), respectively.

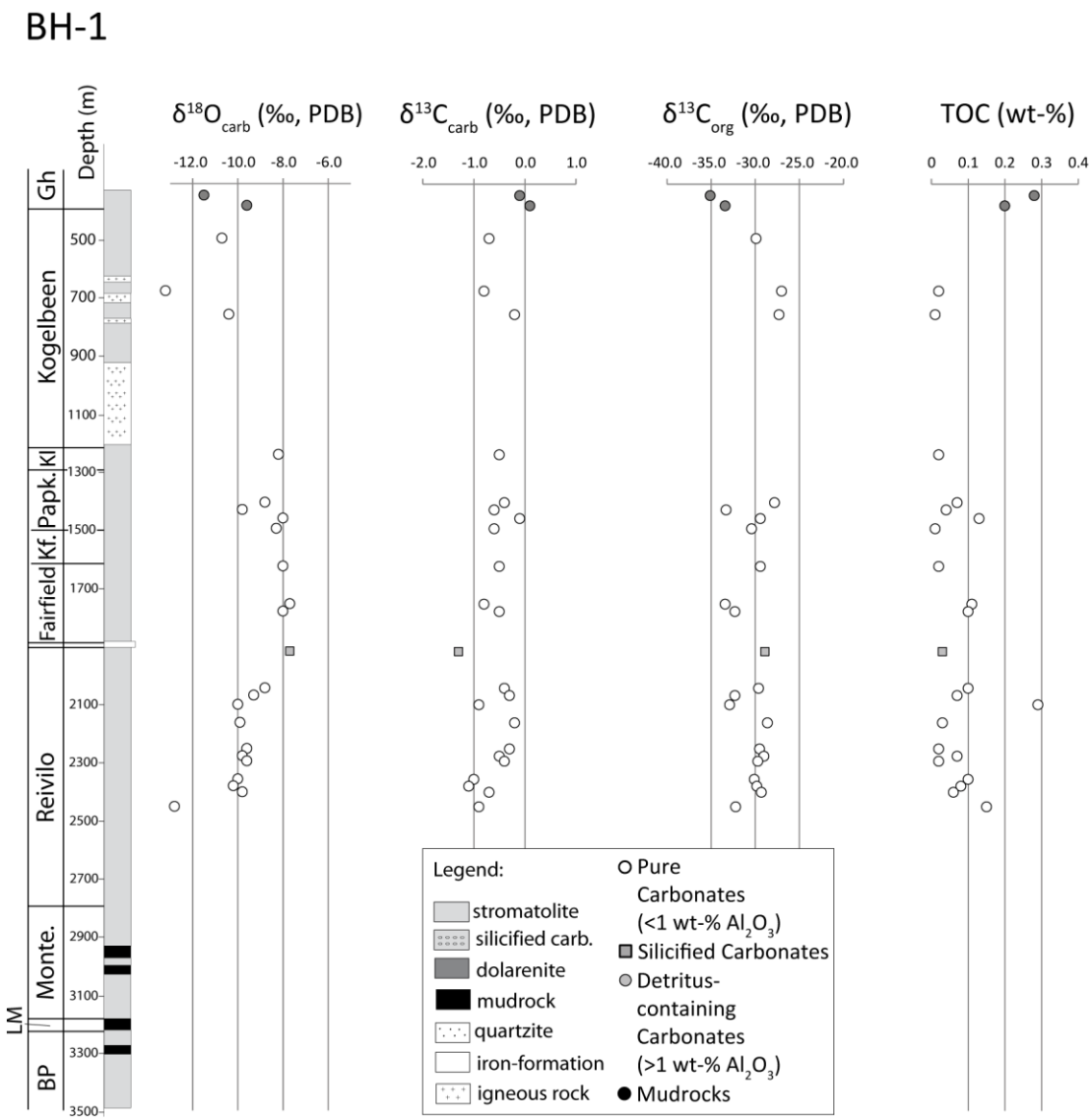

Figure 4-4: TOC content, oxygen and carbon isotope signature of carbonates and organic matter of BH-1 samples. Abbreviations of Formations: BP: Boomplaas; LM: Lokamonna; Monte.: Monteville; Kf.: Klipfonteinheuwel; Papk.: Papkuil; Kl: Klippan; Gh: Gamohaan

4.4. Silicon isotopes

Si isotope analyses on four highly silicified carbonate samples of the Eccles and Monte Christo formations yielded δ^{30}Si values of +0.53 to +2.35 ‰ (Table 4-1). This isotopic range is heavier compared to the average values of modern solid Si reservoirs including igneous rocks of the upper continental crust (-0.3 ‰), silicretes and sandstones (-0.4 ‰), clays and hydrothermal deposits (-1.3 ‰) (Basile-Doelsch et al., 2005; De la Rocha et al., 2000; Ding et al., 2004; Savage et al., 2011; van den Boorn, 2008; Ziegler et al., 2005).

Table 4-1: Major element composition, TOC content, silicon, oxygen, and carbon isotope data of carbonates and mudrocks of KMF-5 (Malmani Subgroup, TA)

Depth	Lithology	SiO_2	TiO_2	Al_2O_3	$Fe_2O_{3\text{-tot}}$	MnO	MgO	CaO	Na_2O	K_2O	P_2O_5	LOI	Sum	Fe#	TOC	$\delta^{30}Si$	$\delta^{18}O_{carb}$	$\delta^{13}C_{carb}$	$\delta^{13}C_{org}$
m		wt-%	wt-%	wt-%	wt-%	wt-%	wt-%	wt-%	wt-%	wt-%	wt-%	wt-%	wt-%		%	‰	‰	‰	‰
Eccles Formation																			
665.08	S-C	4.6	0.02	---	0.93	0.62	19.7	30.33	---	---	0.01	43.43	99.64	0.58			-6.8	0.4	
665.18	S-C	81.59	0.02	---	0.26	0.1	3.72	5.41	---	0.01	0.01	8.39	99.52	0.70	0.09	1.66	-7.1	0.0	-25.9
665.28	MR	77.27	0.65	12.56	0.27	---	0.72	0.22	0.12	3.81	0.16	2.94	98.82		0.92				-22.9
672.77	S-C	53.61	0.02	---	0.27	0.23	9.78	14.08	---	0	0.01	21.73	99.74	0.51	0.08	2.35	-7.2	0.1	-23.5
672.8	D-C	24.88	0.3	4.01	0.51	0.36	14.35	21.05	---	1.25	0.03	33.26	100.03	0.56	0.53		-7.8	0.1	-22.2
673.8	MR	78.34	0.61	11.3	0.24	0.01	0.8	0.32	0.11	3.42	0.12	3.79	99.15	0.96	1.61		-12.0	-0.6	-21.8
673.84	S-C	86.76	0.01	---	0.17	0.07	2.58	3.64	---	0.01	0.01	5.8	99.06	0.69	0.15		-7.9	0.0	-20.5
673.87	S-C	12.98	0.01	---	0.33	0.39	18.28	27.02	---	---	0.01	40.04	99.05	0.43	0.02		-5.4	0.3	-25.0
674.55	P-C	1.37	0.03	0.16	0.38	0.42	20.72	30.71	---	0.06	0.01	46.54	100.4	0.45	0.06		-7.3	0.1	-25.6
675.38	P-C	2.22	0.02	0.05	0.72	0.43	20.36	30.47	---	0.02	0.01	46	100.3	0.60	0.04		-7.3	0.0	-28.5
676.57	S-C	65.79	0.02	0.03	0.26	0.18	7.11	10.35	---	0.02	0.01	15.9	99.68	0.57	0.07		-7.1	0.0	-27.6
678.6	P-C	0.22	0.02	---	0.52	0.48	20.99	31.88	---	---	0.01	46.61	100.73	0.49	0.01		-6.8	0.0	-24.2
680.58	P-C	0.53	0.02	0.03	0.4	0.42	20.94	30.94	---	0.02	0.02	47.16	100.47	0.46	0.10		-7.5	0.2	-24.1
681.76	S-C	17.24	0.02	---	0.39	0.34	17.09	25.77	---	---	0.01	38.65	99.49	0.51	0.01		-7.0	0.0	-27.5
682.7	P-C	2.36	0.01	---	0.42	0.43	20.62	30.36	---	---	0.01	46.23	100.45	0.47	0.02		-7.6	0.3	-26.5
689.2	S-C	35.47	0.01	---	0.35	0.3	13.43	19.61	0.06	0.01	0.01	30.24	99.5	0.51	0.09		-6.8	0.1	-23.4
692.37	S-C	11.92	0.02	0.07	0.36	0.36	18.61	26.84	---	0.04	0.01	41.64	99.88	0.47	0.10		-7.4	0.2	-23.3
692.98	S-C	30.13	0.02	---	0.4	0.34	14.67	21.26	---	---	0.01	32.88	99.71	0.52	0.12		-7.2	-0.2	-21.7
693.38	S-C	3.35	0.01	---	0.37	0.39	20.16	30.18	---	---	0.01	45.45	99.98	0.46	0.02		-6.8	-0.1	-24.4
695.99	S-C	53.02	0.01	---	0.33	0.2	9.86	14.29	---	---	---	21.92	99.65	0.60	0.05		-7.5	0.1	-23.0
697.03	S-C	86.69	0.01	---	0.2	0.07	2.7	3.86	---	---	0.01	6.05	99.59	0.72	0.08	1.11	-7.4	-0.2	-26.4
697.18	P-C	2.92	0.03	---	0.79	0.5	20.21	30.13	---	0.01	0.01	45.6	100.2	0.59	0.03		-6.9	0.0	-26.3
698.89	S-C	4.79	0.02	0.1	0.74	0.45	19.64	29.5	---	0.05	0.01	44.81	100.11	0.60	0.15		-5.6	0.3	-28.6
702.6	P-C	0.71	0.02	0.05	0.5	0.42	20.63	32.3	---	0.03	0.02	45.06	99.74	0.52	0.03		-6.3	0.0	-26.2
703.3	P-C	2.65	0.02	0.07	0.48	0.44	20.36	30.7	---	0.03	0.01	44.84	99.6	0.50	0.03		-6.2	0.0	-26.9
705.7	S-C	31.97	0.01	0.01	0.53	0.36	14.18	20.69	---	0.01	0.01	31.99	99.77	0.57	0.03		-7.0	0.1	-22.0
707.6	S-C	5.69	0.02	0.03	0.5	0.46	19.68	30.28	---	0.02	0.01	42.7	99.39	0.50	0.01		-6.5	0.0	-27.2
708.7	S-C	8.19	0.02	0.06	0.45	0.43	19.19	29.48	---	0.03	0.01	41.47	99.33	0.49	0.05		-6.4	0.0	-24.0
711.7	S-C	9.64	0.02	---	0.54	0.44	18.79	27.44	---	0.01	0.01	42.59	99.49	0.53	0.01		-7.0	0.1	-28.5

Table 4-1 continued

Depth	Lithology	SiO_2	TiO_2	Al_2O_3	$Fe_2O_{3\text{-tot}}$	MnO	MgO	CaO	Na_2O	K_2O	P_2O_5	LOI	Sum	Fe#	TOC	$\delta^{30}Si$	$\delta^{18}O_{carb}$	$\delta^{13}C_{carb}$	$\delta^{13}C_{org}$
m		wt-%	wt-%	wt-%	wt-%	wt-%	wt-%	wt-%	wt-%	wt-%	wt-%	wt-%	wt-%		%	‰	‰	‰	‰
711.8	S-C	72.89	0.01	0.02	0.24	0.14	5.61	8.12	---	0.03	0.01	12.6	99.68	0.61	0.08		-8.0	-0.1	-27.5
788.5	S-C	11.57	***0.01***	***0.06***	0.66	0.43	18.45	26.92	---	0.01	0.01	41.29	99.36	0.58			-7.4	-0.3	
867.3	MR	73.25	0.39	11.18	2.54	0.06	2.88	0.75	0.08	3.27	0.03	6.93	101.44	0.97	3.70				-39.4
875.5	P-C	0.68	0.02	---	0.47	0.53	20.87	31.02	---	---	0.01	46.81	100.42	0.44			-7.7	-0.1	
884.83	P-C	2.92	***0.01***	***0.29***	0.45	0.49	20.32	30.93	---	0.09	0.01	44.36	99.85	0.45	0.02		-8.0	-0.2	-28.0
921.78	P-C	1.06	0.01	---	0.43	0.45	20.86	30.89	---	0.01	0.01	46.79	100.52	0.46	0.01		-7.2	0.1	-27.4
Lyttleton Formation																			
985.5	S-C	4.19	0.02	---	0.51	0.68	20.05	29.74	---	0.01	0.01	44.98	100.19	0.40	0.01		-7.5	-0.1	-25.0
1062.5	P-C	0.39	0.02	0.06	0.82	1.13	20.29	31.42	---	0.03	0.02	45.99	100.16	0.40	0.02		-7.5	-0.3	-22.8
1072.73	P-C	0.44	0.02	0.01	0.68	0.91	20.56	31.59	---	0.01	0.01	45.79	100.03	0.40	0.03		-7.9	-0.3	-24.8
1100.2	P-C	0.35	0.02	0.07	0.68	0.99	20.56	31.24	---	0.05	0.02	46.58	100.55	0.38	0.05		-7.6	-0.7	-25.0
1109.5	P-C														0.17		-9.2	-0.6	-25.5
1136.75	P-C	0.98	0.02	0.17	0.48	0.59	20.7	31.12	---	0.08	0.02	46.02	100.18	0.42	0.02		-8.1	-0.6	-27.1
Monte Christo Formation																			
1143.7	P-C	1.04	0.02	---	0.57	0.6	21.06	30.77	---	0.02	0.01	46.54	100.63	0.46	0.01		-7.6	-0.3	-22.9
1197.3	D-C	7.44	***0.05***	***1.89***	0.44	0.44	19.16	27.66	---	0.67	0.03	42.57	100.38	0.47	0.14		-8.0	0.0	
1197.34	S-C	4.26	***0.02***	***0.45***	0.61	0.47	20.16	29.50	---	0.15	0.02	44.86	100.47	0.54	0.03		-7.3	0.1	-27.8
1199.45	S-C	5.17	0.02	---	0.47	0.42	20.38	29.44	---	0.01	0.01	44.55	100.48	0.50			-7.5	-0.2	
1199.5	S-C	81.22	***0.01***	***0.14***	0.28	0.10	3.82	5.48	---	0.01	0.01	8.49	99.43	0.72	0.03	0.53	-10.3	-0.9	
1202.58	P-C	1.48	0.02	---	0.45	0.37	21.09	30.70	---	0.01	0.01	46.49	100.63	0.52	0.01		-7.5	-0.2	-26.5
1222.32	S-C	47.92	0.02	---	0.59	0.25	10.84	15.83	---	0.01	0.01	24.53	99.99	0.68	0.04	1.88	-8.7	-0.4	-23.8
1239.98	P-C	1.71	0.02	---	0.36	0.33	20.80	30.65	---	0.02	0.01	46.51	100.41	0.50	0.01		-7.7	-0.6	-26.6
1265.1	S-C	54.60	***1.45***	***11.73***	10.34	0.14	5.02	6.82	3.29	1.72	0.19	3.27	98.82	0.99	0.04		-16.4	-3.2	-27.7
1350.66	S-C	4.83	0.03	0.14	0.75	0.47	19.85	29.91	---	0.06	0.02	43.56	99.60	0.59			-9.1	-0.4	
1350.9	MR	48.89	2.57	27.34	0.95	0.01	2.21	0.18	0.21	8.87	0.07	7.46	98.93	0.99	2.35		-16.6	-3.4	-32.9
1401.0	P-C	0.18	0.02	---	0.53	0.44	21.38	31.00	---	0.01	0.01	47.11	100.68	0.52			-8.4	-0.5	
1403.8	P-C	1.16	0.02	---	0.50	0.35	21.24	30.69	---	0.01	0.02	46.67	100.66	0.56	0.01		-7.9	-0.7	-26.0
1406.7	D-C	27.92	0.50	10.08	1.72	0.22	12.44	15.33	0.09	3.31	0.03	28.29	100.00	0.88	2.65				-31.5
1406.8	P-C	1.28	0.02	---	0.57	0.40	21.04	30.76	---	0.02	0.01	46.52	100.62	0.56			-8.5	-0.6	
1407.9	D-C	46.92	0.90	17.56	0.94	0.17	11.08	12.66	0.18	5.89	0.15	21.87	100.00	0.83	2.98		-8.5	-0.6	-31.1

Table 4-1 continued

Depth	Lithology	SiO_2	TiO_2	Al_2O_3	$Fe_2O_{3\text{-tot}}$	MnO	MgO	CaO	Na_2O	K_2O	P_2O_5	LOI	Sum	Fe#	TOC	$\delta^{30}Si$	$\delta^{18}O_{carb}$	$\delta^{13}C_{carb}$	$\delta^{13}C_{org}$
m		wt-%	wt-%	wt-%	wt-%	wt-%	wt-%	wt-%	wt-%	wt-%	wt-%	wt-%	wt-%		%	‰	‰	‰	‰
1411.1	MR	50.33	2.71	27.23	0.70	0.01	2.21	0.05	0.18	8.72	0.02	7.66	100.00	0.98	2.63				-33.0
1411.3	S-C	6.92	0.03	0.52	1.00	0.57	19.23	28.36	---	0.20	0.03	43.42	100.29	0.61			-8.6	-0.6	
1413.34	S-C	5.42	0.03	0.22	1.31	0.63	19.33	29.89	---	0.11	0.01	42.44	99.39	0.65			-8.9	-0.7	
1420.9	P-C	1.40	0.02	0.11	0.83	0.55	20.84	30.47	---	0.05	0.02	46.31	100.60	0.58	0.03		-8.1	-0.5	-23.6
1425.4	P-C	1.01	0.02	---	0.64	0.46	21.06	30.77	---	0.01	0.02	46.69	100.67	0.56			-8.9	-0.6	
1427.85	S-C	3.97	0.02	0.27	0.47	0.29	20.17	29.96	---	0.11	0.01	45.20	100.49	0.59			-8.9	-0.7	
1428.4	MR	83.09	0.20	9.43	0.39	0.01	0.89	0.02	0.09	3.20	0.02	2.60	100.00	0.97	0.96		-16.9	-9.7	-35.0
1429.1	MR	62.24	0.77	19.91	0.47	0.01	1.91	0.04	0.16	6.71	0.04	7.61	100.00	0.98	4.25				-35.5
1435.25	P-C	1.09	0.02	0.08	0.50	0.37	21.12	30.73	---	0.05	0.01	46.61	100.60	0.55	0.04		-8.2	-0.6	-22.7
1442.17	P-C	0.93	0.02	---	0.56	0.59	20.88	30.76	---	0.01	0.01	46.69	100.46	0.46			-7.2	-0.4	
1454.61	S-C	5.53	0.02	---	0.61	0.41	19.95	28.62	---	0.01	0.01	44.58	99.74	0.57			-8.1	-0.4	
1460.05	S-C	3.81	0.02	0.13	0.58	0.44	20.39	29.64	---	0.07	0.01	45.24	100.35	0.54			-8.7	-0.5	
1461.8	P-C	2.13	0.02	0.18	0.51	0.54	20.65	30.38	---	0.07	0.02	45.97	100.48	0.46			-8.5	-0.5	
1462.1	MR														3.83				-27.7
1464.3	P-C	1.04	0.01	---	0.70	0.54	20.92	30.77	---	0.03	0.01	46.47	100.51	0.54	0.02		-8.0	-0.2	-23.8
1467.1	P-C	1.21	0.02	0.01	0.54	0.44	21.14	30.58	---	0.02	0.01	46.66	100.65	0.53			-8.6	-0.6	
1475.35	P-C	3.19	0.03	0.39	0.42	0.53	20.38	30.16	---	0.17	0.01	45.27	100.56	0.42	0.04		-7.6	-0.5	-26.9
1475.6	D-C	17.84	0.19	4.30	0.99	0.38	16.30	22.38	---	1.21	0.03	36.36	100.00	0.70	0.89		-7.5	-0.6	-28.2
1478.6	D-C	29.77	0.59	9.56	1.79	0.31	11.96	14.44	---	3.48	0.07	27.88	100.00	0.84	3.57		-12.0	-0.9	-30.3
1484.8	P-C	1.69	0.03	0.39	0.49	0.59	20.76	30.44	---	0.16	0.02	45.99	100.55	0.43	0.04		-8.1	-0.6	-24.0
1491.3	P-C	0.64	0.02	---	0.47	0.52	21.21	30.79	---	0.02	0.01	46.74	100.42	0.45			-8.1	-0.5	
1491.85	S-C	4.40	0.01	---	0.69	0.46	20.46	29.53	---	0.01	0.01	44.92	100.50	0.58			-8.4	-0.4	
1493.5	MR	65.84	0.63	16.48	0.40	0.01	1.64	0.10	0.15	5.50	0.04	9.09	100.00	0.97	6.13		-16.6	-3.8	-33.6
1495.8	MR	54.68	***1.17***	***21.84***	0.60	0.01	2.13	0.11	0.19	6.96	0.04	12.43	100.00	0.98	8.50		-16.0	-11.0	-34.8
1499.6	S-C	5.38	0.03	0.27	0.44	0.43	19.64	29.62	---	0.08	0.01	44.03	99.91	0.48			-8.2	-1.0	
1499.85	MR	57.59	1.07	20.82	0.49	0.01	2.14	0.44	0.19	6.68	0.04	9.36	98.98	0.98	4.83		-12.9	-2.9	-34.8
1521.4	D-C	11.57	0.13	3.87	0.79	0.31	18.39	23.87	---	0.27	0.02	40.77	100.00	0.70	3.21		-9.4	-0.8	
1524.7	P-C	0.80	0.01	---	0.45	0.42	21.32	30.70	---	0.02	0.01	46.88	100.63	0.49			-8.3	-0.6	
1528.48	S-C	4.18	0.03	0.38	0.46	0.51	19.86	29.75	---	0.15	0.01	44.96	100.32	0.45			-7.4	-0.7	
1539.9	P-C	1.89	0.02	0.25	0.58	0.62	20.59	27.93	---	0.11	0.02	46.02	100.49	0.46			-8.0	-0.7	

Table 4-1 continued

Depth	Lithology	SiO_2	TiO_2	Al_2O_3	$Fe_2O_{3\text{-tot}}$	MnO	MgO	CaO	Na_2O	K_2O	P_2O_5	LOI	Sum	Fe#	TOC	$\delta^{30}Si$	$\delta^{18}O_{carb}$	$\delta^{13}C_{carb}$	$\delta^{13}C_{org}$
m		wt-%	wt-%	wt-%	wt-%	wt-%	wt-%	wt-%	wt-%	wt-%	wt-%	wt-%	wt-%		%	‰	‰	‰	‰
1544.1	MR	85.15	***0.36***	***7.38***	0.40	0.01	0.91	0.03	0.11	2.60	0.03	2.91	100.00	0.97	1.30		-8.0	-12.3	-31.0
1551.6	D-C	20.00	0.05	1.16	1.08	0.30	16.63	23.89	---	0.31	0.02	35.82	99.28	0.76			-7.8	-1.0	-33.2
1551.7	MR	64.19	0.82	18.71	1.02	0.01	1.70	0.08	0.16	6.49	0.07	5.80	99.20	0.99	2.65		-8.2	-1.1	-34.7
1557.7	MR	75.66	0.51	11.04	0.36	0.01	1.15	0.07	0.13	3.80	0.06	7.12	100.00	0.97	5.32		-15.7	-12.2	-34.8
1558.88	P-C	3.26	0.02	---	0.55	0.45	20.59	29.97	---	0.02	0.02	45.63	100.53	0.52	0.02		-8.1	-0.6	
1564.3	P-C	0.81	0.01	0.01	0.40	0.45	21.27	30.75	---	0.02	0.01	46.92	100.66	0.45	0.01		-8.1	-0.5	-24.9
1574.15	P-C	0.95	***0.00***	***0.03***	0.32	0.35	21.44	30.68	---	---	0.01	46.82	100.60	0.45	0.01		-7.3	-0.5	
1574.2	P-C	0.73	***0.02***	***0.40***	0.39	0.35	21.20	30.74	---	0.14	0.01	46.66	100.59	0.50	0.03		-7.6	-0.6	-24.4
1574.25	P-C	2.67	***0.00***	***0.06***	0.31	0.36	20.97	30.32	---	0.01	0.01	45.90	100.56	0.44	0.01		-8.1	-0.6	
1574.3	S-C	11.22	***0.00***	***0.03***	0.52	0.33	19.01	27.20	---	---	0.01	41.87	100.17	0.59	0.02		-8.7	-0.6	
1589.75	P-C	0.56	0.02	0.01	0.38	0.38	21.47	30.88	---	0.03	0.01	46.92	100.65	0.47	0.02		-8.5	-0.6	
1589.9	P-C	2.08	0.01	---	0.52	0.37	21.15	30.25	---	0.01	0.01	46.10	100.50	0.56	0.01		-8.5	-0.6	
1604.6	P-C	0.32	0.02	---	0.44	0.45	21.13	31.34	---	0.00	0.02	46.57	100.29	0.47	0.02		-7.9	-0.7	-24.9
1673.1	S-C	3.82	0.02	0.06	0.94	0.57	19.80	29.79	---	0.06	0.01	44.75	99.84	0.60			-9.4	-1.2	
1673.3	MR	85.12	0.19	4.89	0.85	0.02	1.12	0.86	0.06	2.75	0.03	2.99	98.92	0.97	0.83		-11.3	-4.1	-31.8
Oaktree Formation																			
1731.1	P-C	0.58	0.02	---	0.97	1.36	20.26	30.77	---	0.02	0.01	46.18	100.17	0.39			-8.4	-0.5	
1731.3	P-C	0.61	0.02	---	1.03	1.31	20.22	30.76	---	0.01	0.01	46.20	100.17	0.42			-9.9	-0.6	
1742.3	P-C	1.20	0.03	---	1.16	2.26	19.44	30.75	---	0.01	0.01	44.91	99.76	0.32	0.08		-10.0	-0.9	-21.6
1775.8	D-C	15.94	***0.14***	***3.53***	2.03	0.65	16.22	23.19	---	2.10	0.03	35.66	99.53	0.74	0.43		-8.4	-0.8	-30.4
1776.0	MR	57.72	***1.10***	***19.44***	2.03	0.01	3.02	0.14	0.11	10.68	0.08	4.33	98.62	0.99	1.73		-15.3	-3.4	-31.9
1790.0	D-C	3.82	***0.04***	***1.01***	2.13	0.80	19.57	28.64	---	0.32	0.03	43.70	100.07	0.71			-8.8	-0.8	-29.1
1790.1	P-C	2.86	0.04	0.62	2.00	0.84	19.23	29.37	---	0.29	0.02	44.35	99.64	0.68	0.10		-9.0	-0.6	-28.1
1790.3	MR	62.03	0.76	16.74	2.68	0.01	4.05	0.10	0.09	8.26	0.04	3.84	98.72	1.00	1.31		-15.4	-2.1	
1800.1	P-C	1.53	0.03	0.46	1.56	0.98	19.68	31.53	---	0.19	0.02	43.29	99.26	0.59	0.05		-8.3	-0.8	-26.4
1800.3	MR	58.61	***0.79***	***19.61***	1.83	0.03	3.46	0.72	0.11	8.75	0.03	5.08	99.04	0.98	1.00		-11.8	-3.1	-29.6
1811.2	MR	48.99	0.83	16.78	9.20	0.15	6.65	2.14	0.07	5.23	0.07	8.77	99.06	0.98	1.30		-17.1	-4.9	-31.1

Major element data by XRF, Laser ablation ICP-MS data in bold italic; ---: below detection limit
P-C: 'pure' carbonate, S-C: silicified carbonate, D-C: detritus-containing carbonate, MR: mudrock
Extern reproducibility for $\delta^{30}Si$ is ± 0.12 ‰ (2σ); Fe-Mn ratio: Fe# = Fe/(Fe+Mn)

Table 4-2: Major element composition, TOC content, oxygen, and carbon isotope data of carbonates and mudrocks of BH-1 (Campbellrand Subgroup, GWA)

Depth	Lithology	SiO_2	TiO_2	Al_2O_3	Fe_2O_3	MnO	MgO	CaO	Na_2O	K_2O	P_2O_5	LOI	Sum	Fe#	TOC	$\delta^{18}O_{carb}$	$\delta^{13}C_{carb}$	$\delta^{13}C_{org}$
m		wt-%	wt-%	wt-%	wt-%	wt-%	wt-%	wt-%	wt-%	wt-%	wt-%	wt-%	wt-%		wt-%	‰	‰	‰
Gamohaan Formation																		
340	D-C	4.87	0.05	0.93	1.10	1.04	0.93	50.21	0.05	0.27	0.04	39.39	98.90	0.49	0.28	-11.5	-0.1	-35.1
375	D-C	1.50	0.03	0.33	1.44	0.99	18.95	30.60	0.00	0.02	0.02	45.50	99.39	0.57	0.20	-9.6	0.1	-33.4
Kogelbeen Formation																		
488	P-C	0.15	0.01	---	0.19	0.44	0.31	55.56	0.05	0.00	0.01	43.19	99.93	0.27		-10.7	-0.7	-29.9
670	P-C	1.46	0.02	---	0.24	0.41	1.61	53.40	0.05	0.00	0.01	42.05	99.26	0.34	0.02	-13.2	-0.8	-27.0
751	P-C	3.17	0.01	---	0.83	0.84	20.17	29.56	0.00	0.00	0.01	44.68	99.28	0.47	0.01	-10.4	-0.2	-27.3
Klippan Formation																		
1235	P-C	0.69	0.02	---	0.36	0.63	20.44	31.26	0.00	0.00	0.01	45.82	99.25	0.34	0.02	-8.2	-0.5	-23.3
Papkuil Formation																		
1400	P-C	0.90	0.02	0.10	0.74	0.99	20.42	30.09	0.00	0.06	0.01	46.21	99.56	0.40	0.07	-8.8	-0.4	-27.8
1425	P-C	3.32	0.02	0.06	0.53	0.60	19.78	29.97	0.00	0.05	0.01	45.21	99.58	0.44	0.04	-9.8	-0.6	-33.3
1455	P-C	3.03	0.03	0.31	0.63	0.84	19.95	29.49	0.00	0.15	0.02	44.59	99.07	0.40	0.13	-8.0	-0.1	-29.4
1490	P-C	1.59	0.01	0.01	0.47	0.82	20.51	30.00	0.00	0.02	0.01	45.65	99.11	0.34	0.01	-8.3	-0.6	-30.4
Klipfonteinheuwel Formation																		
1520	P-C	0.53	0.02	---	0.42	0.71	20.88	30.38	0.00	0.03	0.01	46.55	99.55	0.35				
Fairfield Formation																		
1620	P-C	0.88	0.02	0.01	0.35	0.51	20.92	30.38	0.00	0.03	0.01	46.24	99.36	0.38	0.02	-8.0	-0.5	-29.4
1750	P-C	2.81	0.04	0.60	0.78	1.29	19.29	29.54	0.00	0.31	0.02	44.27	98.97	0.35	0.11	-7.7	-0.8	-33.4
1776	P-C	1.83	0.01	---	0.52	0.60	20.53	30.10	0.00	0.02	0.01	45.49	99.13	0.44	0.10	-8.0	-0.5	-32.3
Kamden Formation																		
1914	S-C	3.73	0.02	---	3.64	1.73	17.30	28.75	0.00	0.00	0.01	43.80	98.99	0.65	0.03	-7.7	-1.3	-28.9
Reivilo Formation																		
2041	P-C	0.56	0.03	---	0.29	1.03	21.05	30.71	---	0.02	0.03	46.27	100.00	0.20	0.10	-8.8	-0.4	-29.6
2066	P-C	0.39	0.02	0.03	0.30	1.65	20.62	30.80	---	0.04	0.01	46.45	100.30	0.14	0.07	-9.3	-0.3	-32.3
2098	P-C	0.39	0.02	0.03	0.30	1.65	20.62	30.80	---	0.04	0.01	46.45	100.30	0.14	0.29	-10.0	-0.9	-32.9
2121	D-C	16.39	0.05	0.93	1.46	1.13	7.58	34.56	---	0.72	0.03	36.58	99.43	0.54				
2131	D-C	14.72	0.06	1.80	1.82	1.33	14.51	26.85	---	1.07	0.02	37.84	100.00	0.55				
2160	P-C	0.38	0.02	---	0.45	0.85	21.27	30.60	---	0.00	0.01	46.86	100.40	0.32	0.03	-9.9	-0.2	-28.6
2250	P-C	0.37	0.02	---	0.30	0.73	21.37	30.73	---	0.01	0.01	46.90	100.45	0.27	0.02	-9.6	-0.3	-29.5

Table 4-2 continued

Depth	Lithology	SiO_2	TiO_2	Al_2O_3	Fe_2O_3	MnO	MgO	CaO	Na_2O	K_2O	P_2O_5	LOI	Sum	Fe#	TOC	$\delta^{18}O_{carb}$	$\delta^{13}C_{carb}$	$\delta^{13}C_{org}$
m		wt-%	wt-%	wt-%	wt-%	wt-%	wt-%	wt-%	wt-%	wt-%	wt-%	wt-%	wt-%		wt-%	‰	‰	‰
2251	P-C	0.33	0.02	---	0.48	0.90	21.20	31.03	---	0.00	0.02	46.94	100.92	0.33				
2275	P-C	0.63	0.02	---	0.57	1.07	21.09	30.86	---	---	0.02	46.56	100.80	0.33	0.07	-9.8	-0.5	-29.0
2293	P-C	0.57	0.01	0.03	0.67	2.82	19.60	30.58	---	0.03	0.02	45.61	99.95	0.18	0.02	-9.6	-0.4	-29.7
2355	P-C	0.81	0.02	0.04	1.23	3.54	18.52	30.61	---	0.13	0.02	45.02	99.94	0.24	0.10	-10.0	-1.0	-30.1
2379	P-C	0.57	0.01	0.03	0.67	2.82	19.60	30.58	---	0.03	0.02	45.61	99.95	0.18	0.08	-10.2	-1.1	-29.8
2400	P-C	0.27	0.01	---	0.50	1.64	20.56	31.03	---	0.00	0.01	46.40	100.40	0.22	0.06	-9.8	-0.7	-29.3
2450	P-C														0.15	-12.8	-0.9	-32.2

Major element data by XRF, Laser ablation ICP-MS data in bold italic; ---: below detection limit
P-C: 'pure' carbonate, S-C: silicified carbonate, D-C: detritus-containing carbonate
Fe-Mn ratio: Fe# = Fe/(Fe+Mn)

Table 4-3: Major element composition of carbonate and mudrock samples of the Kuruman Kop (Campbellrand Subgroup, GWA)

Depth	Lithology	SiO_2	TiO_2	Al_2O_3	Fe_2O_3	MnO	MgO	CaO	Na_2O	K_2O	P_2O_5	LOI	Sum	Fe#
m		wt-%	wt-%	wt-%	wt-%	wt-%	wt-%	wt-%	wt-%	wt-%	wt-%	wt-%	wt-%	
Gamohaan Formation														
Ku12_04	D-C	79.72	0.30	10.18	2.42	0.04	1.11	0.18	0.31	2.84	0.08	2.70	100.90	0.98
Ku12_06	P-C	1.53	0.03	0.27	0.54	1.06	0.54	53.67	0.05	0.25	0.02	42.21	100.20	0.32
Ku12_25	P-C	1.14	0.03	0.13	1.68	0.97	19.67	30.73	0.00	0.08	0.02	45.63	100.10	
Ku12_26	P-C	0.45	0.02	0.00	0.27	0.53	1.99	53.62	0.05	0.04	0.02	43.42	100.42	
Kogelbeen Formation														
Ku12_31	P-C	0.12	0.03	0.00	0.12	0.45	0.50	55.46	0.00	0.00	0.01	42.89	99.61	0.19

Major element data by XRF, Laser ablation ICP-MS data in bold italic; ---: below detection limit
P-C: 'pure' carbonate, D-C: detritus-containing carbonate
Fe-Mn ratio: Fe# = Fe/(Fe+Mn)

Table 4-4: Rare Earth Element and Yttrium (REE+Y) concentrations (in µg/g) of KMF-5 carbonates

Depth (m)	La	Ce	Pr	Nd	Sm	Eu	Gd	Tb	Dy	Y	Ho	Tm	Er	Yb	Lu	Y/Ho	Ce/Ce*	Eu/Eu*
KMF-5 carbonates																		
674.55	1.017	2.038	0.267	1.036	0.221	0.047	0.199	0.030	0.175	0.966	0.035	0.013	0.093	0.077	0.011	28	0.90	1.04
675.38	1.112	2.142	0.244	0.919	0.179	0.041	0.177	0.027	0.162	1.085	0.034	0.013	0.091	0.075	0.011	32	0.94	1.06
678.6	1.228	2.343	0.267	1.064	0.229	0.056	0.245	0.038	0.235	1.795	0.051	0.021	0.142	0.121	0.017	35	0.94	1.09
680.58	0.739	1.273	0.137	0.526	0.097	0.019	0.093	0.013	0.073	0.575	0.015	0.005	0.041	0.029	0.004	38	0.91	0.94
697.18	0.169	0.399	0.051	0.210	0.046	0.013	0.049	0.008	0.049	0.307	0.010	0.004	0.026	0.022	0.003	31	0.98	1.27
702.6	1.308	2.503	0.285	1.035	0.192	0.058	0.177	0.027	0.153	0.958	0.031	0.012	0.083	0.072	0.010	31	0.94	1.46
703.3	1.753	3.298	0.372	1.332	0.236	0.051	0.210	0.031	0.180	1.087	0.037	0.015	0.101	0.093	0.013	29	0.94	1.07
884.83	0.644	1.579	0.204	0.817	0.164	0.051	0.147	0.021	0.117	0.701	0.023	0.008	0.058	0.047	0.006	31	0.99	1.53
921.78	0.199	0.394	0.047	0.186	0.038	0.012	0.038	0.006	0.032	0.209	0.006	0.002	0.017	0.014	0.002	33	0.94	1.50
1072.73	0.347	0.605	0.065	0.249	0.051	0.016	0.053	0.008	0.046	0.343	0.009	0.003	0.025	0.021	0.003	37	0.92	1.44
1100.2	0.727	1.150	0.141	0.561	0.121	0.042	0.154	0.023	0.149	2.138	0.036	0.015	0.107	0.093	0.015	60	0.82	1.40
1109.5	0.396	0.769	0.098	0.398	0.102	0.031	0.115	0.017	0.095	0.610	0.018	0.006	0.047	0.037	0.006	33	0.90	1.31
1136.75	1.399	2.781	0.310	1.172	0.252	0.061	0.264	0.043	0.256	1.430	0.052	0.021	0.140	0.132	0.019	28	0.97	1.10
1143.7	0.244	0.445	0.051	0.191	0.036	0.009	0.037	0.005	0.032	0.257	0.007	0.002	0.018	0.014	0.002	39	0.92	1.17
1202.58	0.322	0.542	0.059	0.217	0.040	0.011	0.041	0.006	0.034	0.272	0.007	0.003	0.020	0.015	0.002	37	0.90	1.23
1239.98	0.365	0.594	0.062	0.228	0.038	0.010	0.036	0.005	0.025	0.174	0.005	0.002	0.012	0.009	0.001	36	0.90	1.23
1401.0	0.344	0.478	0.053	0.203	0.032	0.010	0.036	0.004	0.025	0.219	0.005	0.002	0.014	0.008	0.001	44	0.80	1.37
1403.8	0.585	0.991	0.108	0.392	0.070	0.020	0.069	0.010	0.062	0.488	0.013	0.005	0.036	0.030	0.004	38	0.90	1.30
1420.9	0.521	0.954	0.110	0.416	0.077	0.021	0.076	0.011	0.067	0.877	0.015	0.006	0.046	0.041	0.007	57	0.91	1.30
1425.4	0.863	1.616	0.182	0.664	0.127	0.032	0.123	0.019	0.115	0.753	0.023	0.010	0.064	0.058	0.008	32	0.94	1.19
1435.25	0.608	1.008	0.115	0.426	0.074	0.020	0.074	0.011	0.063	0.804	0.014	0.006	0.041	0.033	0.005	57	0.87	1.24
1464.3	0.630	1.256	0.141	0.506	0.085	0.031	0.080	0.012	0.067	0.664	0.014	0.006	0.039	0.034	0.005	47	0.97	1.73
1467.1	0.514	0.914	0.105	0.387	0.068	0.018	0.069	0.010	0.060	0.789	0.014	0.006	0.041	0.036	0.006	58	0.90	1.22
1475.35	1.333	2.422	0.258	0.907	0.154	0.036	0.132	0.019	0.105	0.564	0.019	0.007	0.051	0.041	0.006	29	0.95	1.19
1484.8	0.796	1.402	0.170	0.634	0.122	0.028	0.114	0.017	0.099	1.186	0.021	0.009	0.063	0.055	0.008	56	0.87	1.12
1524.7	0.580	1.013	0.114	0.423	0.078	0.020	0.074	0.011	0.060	0.375	0.012	0.004	0.031	0.023	0.003	33	0.90	1.23
1539.9	0.830	1.414	0.164	0.621	0.119	0.033	0.123	0.018	0.111	1.766	0.026	0.011	0.079	0.065	0.011	67	0.88	1.28
1564.3	0.282	0.503	0.055	0.196	0.033	0.011	0.032	0.005	0.026	0.160	0.005	0.002	0.013	0.010	0.001	32	0.92	1.53
1574.25	0.385	0.630	0.066	0.232	0.039	0.011	0.037	0.005	0.031	0.205	0.006	0.002	0.016	0.013	0.002	34	0.90	1.28
1589.75	0.394	0.699	0.076	0.279	0.051	0.015	0.048	0.007	0.040	0.241	0.008	0.003	0.020	0.017	0.002	31	0.92	1.38
1589.9	0.289	0.540	0.060	0.218	0.041	0.013	0.040	0.006	0.034	0.217	0.007	0.002	0.017	0.014	0.002	33	0.94	1.53
1604.6	0.489	0.773	0.081	0.294	0.051	0.015	0.050	0.007	0.042	0.298	0.008	0.003	0.021	0.016	0.002	36	0.88	1.35
1731.1	0.517	0.852	0.094	0.357	0.070	0.019	0.092	0.014	0.088	1.137	0.021	0.009	0.063	0.058	0.010	54	0.88	1.09
1742.3	0.400	0.431	0.046	0.177	0.035	0.011	0.049	0.007	0.051	1.208	0.014	0.007	0.047	0.042	0.007	83	0.69	1.25
1790.1	2.350	7.210	1.091	5.184	1.707	0.436	1.847	0.323	1.946	8.774	0.382	0.154	1.028	0.939	0.137	23	0.98	1.14
1800.1	1.913	4.616	0.622	2.741	0.813	0.183	0.877	0.147	0.886	5.130	0.176	0.067	0.470	0.391	0.055	29	0.96	1.00

Table 4-5: Rare Earth Element and Yttrium (REE+Y) concentrations (in µg/g) of KMF-5 mudrocks and Fe- and silica-rich sample 1265.1 (bold italic: analyzed by LA-ICP-MS) and BH-1 pure carbonates

Depth (m)	La	Ce	Pr	Nd	Sm	Eu	Gd	Tb	Dy	Y	Ho	Tm	Er	Yb	Lu	Y/Ho	Ce/Ce*	Eu/Eu*
KMF-5																		
1265.1 S-C	***37.525***	***78.496***	***9.520***	***37.470***	***7.743***	***1.979***	***7.178***	***1.167***	***6.744***	***32.928***	***1.348***	***3.731***	***0.574***	***3.343***	***0.494***	24	0.95	1.24
1495.8 MR	***44.733***	***82.044***	***8.670***	***29.659***	***4.056***	***0.432***	***2.945***	***0.981***	***2.764***	***13.569***	***0.569***	***1.871***	***0.332***	***2.300***	***0.398***	24	0.95	0.58
1544.1 MR	***0.854***	***1.399***	***0.152***	***0.593***	***0.141***	***0.034***	***0.154***	***0.033***	***0.215***	***1.676***	***0.059***	***0.247***	***0.045***	***0.396***	***0.065***	28	0.88	1.06
1776.0 MR	***39.129***	***73.645***	***7.888***	***28.348***	***4.356***	***0.719***	***3.756***	***1.596***	***3.584***	***17.527***	***0.771***	***2.399***	***0.429***	***2.704***	***0.485***	23	0.96	0.83
1800.3 MR	***2.884***	***7.454***	***0.900***	***3.978***	***1.024***	***0.192***	***1.141***	***0.525***	***1.799***	***10.405***	***0.430***	***1.449***	***0.275***	***1.876***	***0.316***	24	1.05	0.82
BH-1 carbonates																		
2041	0.403	0.622	0.073	0.267	0.051	0.013	0.055	0.008	0.056	1.183	0.014	0.007	0.048	0.044	0.008	82	0.83	1.12
2066	0.390	0.605	0.069	0.260	0.048	0.013	0.052	0.008	0.051	1.076	0.013	0.007	0.043	0.040	0.007	82	0.84	1.20
2098	3.412	6.362	0.695	2.468	0.440	0.086	0.393	0.059	0.342	2.007	0.068	0.028	0.188	0.173	0.025	29	0.95	0.97
2160	0.218	0.359	0.043	0.162	0.030	0.007	0.033	0.005	0.032	0.695	0.008	0.004	0.027	0.026	0.005	82	0.85	1.09
2250	0.145	0.213	0.024	0.090	0.017	0.005	0.020	0.003	0.020	0.399	0.005	0.003	0.018	0.018	0.003	74	0.81	1.19
2255	0.165	0.246	0.028	0.106	0.020	0.006	0.024	0.004	0.022	0.426	0.006	0.003	0.020	0.018	0.003	70	0.82	1.17
2275	0.289	0.447	0.052	0.194	0.036	0.009	0.039	0.006	0.039	0.890	0.010	0.005	0.034	0.033	0.006	87	0.83	1.18
2293	0.143	0.171	0.017	0.061	0.010	0.003	0.012	0.002	0.009	0.157	0.002	0.001	0.006	0.005	0.001	74	0.76	1.29
2355	0.539	0.964	0.104	0.376	0.067	0.016	0.064	0.010	0.058	0.754	0.013	0.005	0.037	0.034	0.006	58	0.93	1.17
2379	0.296	0.509	0.060	0.226	0.043	0.011	0.048	0.008	0.050	0.952	0.013	0.006	0.041	0.036	0.006	75	0.87	1.13
2400	0.233	0.335	0.040	0.153	0.029	0.008	0.038	0.006	0.040	1.030	0.012	0.006	0.040	0.039	0.007	88	0.79	1.17
2450	0.860	1.735	0.214	0.848	0.181	0.043	0.207	0.031	0.185	2.475	0.040	0.017	0.114	0.101	0.016	62	0.93	1.03

S-C: silicified carbonate, MR: mudrock

4.5. Raman spectra of organic matter

Organic material of KMF-5 carbonates and mudrocks yield an I_D/I_G ratios between 1.2 and 2.1 and FWHM-D values between 39 and 71 (Table 4-6). Mudrock samples 665.1 and 665.3 show the lowest FWHM-D values and have been apparently exposed to higher metamorphic conditions then the rest of the analyzed samples (Fig. 4-5). Those two samples excluded, the remaining KMF-5 samples obtain FWHM-D values between 44 and 71.

Carbonate samples from Kuruman Kop reveal more 'disordered' signatures for organic material than those of KMF-5, with I_D/I_G ratios between 0.7 and 0.9 and FWHM-D values between 78 and 103 (Table 4-6).

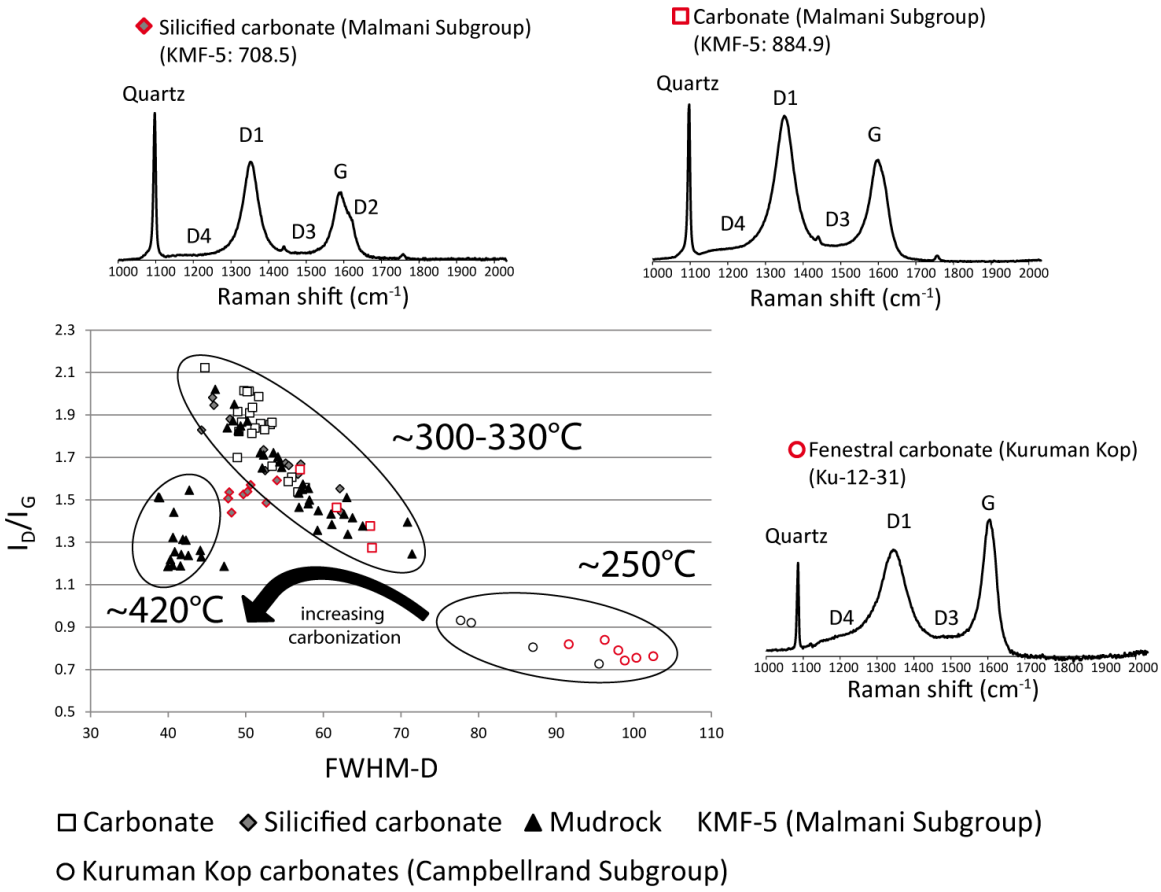

Figure 4-5: Raman data (I_D/I_G vs. FWHM-D) of marine sediments from the Malmani Subgroup (TA) and the Campbellrand Subgroup (GWA), as well as Raman spectra of characteristic lithologies. Changes in G- and D-bands implicate a change in the disorder of carbonaceous matter and reveal higher peak metamorphic conditions for some samples (in particular mudrocks 665.3 and 673.0). Temperature ranges are estimated following Kouketsu et al. (2014).

Table 4-6: Raman analyses of rock samples from KMF-5 and Kuruman Kop

KMF-5 (Session 2014)

Sample	Lithology	Analysis	I_D/I_G	FWHM-D
665.18	S-C	spec-2a	1.83	44
		spec-3a	1.94	46
665.1	P-C	spec-1a	1.85	53
		spec-2a	1.86	52
		spec-3a	1.86	50
		spec-4a	1.91	51
		spec-5a	1.84	51
676.6	S-C	spec-1a	1.66	56
		spec-2a	1.55	58
		spec-3a	1.44	62
1199.5	S-C	spec-1a	1.64	53
		spec-2a	1.55	62
		spec-3a	1.67	57
1428.4	MR	spec-1a	1.38	61
		spec-2a	1.48	58
		spec-3a	1.34	63
		spec-4a	1.46	57
1495.8	MR	spec-1a	1.72	54
		spec-2a	1.45	59
		spec-3a	1.53	57
1521.4	MR	spec-1a	1.65	52
		spec-2a	1.24	71
		spec-3a	1.36	59
1557.7	MR	spec-1a	1.41	64
		spec-2a	1.65	55
		spec-3a	1.38	65
		spec-4a	1.83	49
1776.0	MR	spec-1a	1.87	48
		spec-2a	1.55	57
		spec-3a	1.43	61
		spec-4a	1.71	52
		spec-5a	1.85	49
1790.2	MR	spec-1a	1.87	50
		spec-2a	1.83	49
		spec-3a	1.68	54
		spec-4a	1.72	52
1800.3	MR	spec-1a	1.7	54
		spec-2a	1.95	49
		spec-3a	1.55	58
		spec-4a	1.84	48

Kuruman Kop (Session 2015)

Sample	Lithology	Analysis	I_D/I_G	FWHM-D
Ku12-07 Gamohaan	fenestral carbonate	spec1	0.8	87
		spec2	0.73	96
		spec3	0.93	78
		spec4	0.92	79
Ku12-31 Kogelbeen	fenestral pure carbonate	spec1	0.76	103
		spec1b	0.79	98
		spec2	0.75	100
		spec3	0.84	96
		spec4	0.74	99
		spec5	0.82	92

KMF-5 (Session 2015)

Sample	Lithology	Analysis	I_D/I_G	FWHM-D
665.18	S-C	spec1	1.67	55
		spec2	1.74	52
665.1	P-C	spec1	2.01	50
		spec2	1.81	51
		spec3	1.91	49
665.3	MR	spec1	1.31	42
		spec2	1.23	44
		spec3	1.54	43
		spec4	1.24	43
		spec1b	1.44	41
		spec2b	1.51	39
673.0	MR	spec1	1.19	42
		spec2	1.19	41
		spec3	1.26	44
		spec4	1.24	42
		spec5	1.32	41
		spec6	1.22	40
		spec7	1.25	41
		spec1b	1.19	47
		spec2b	1.19	40
		spec3b	1.31	42
676.6	S-C	spec1	1.62	57
697.0	S-C	spec1	1.98	46
		spec2	1.88	48
708.5	S-C	spec1	1.49	53
		spec2	1.54	48
		spec3	1.57	51
		spec4	1.53	50
		spec1b	1.51	48
		spec2b	1.44	48
		spec3b	1.54	50
		spec4b	1.59	54
867.3	MR	spec1	1.39	71
		spec2	1.51	63
		spec3	1.51	39
		spec4	1.57	57
		spec5	1.43	63
		spec6	1.5	58
884.9	P-C	spec1	1.27	66
		spec2	1.38	66
		spec3	1.46	62
		spec4	1.64	57
		spec5	1.56	58
921.8	P-C	spec2	1.99	52
		spec3	1.93	51
		spec4	1.86	53
		spec5	2.12	45
1109.5	P-C	spec1	1.7	49
		spec2	1.82	49
		spec3	2.01	50
		spec4	2.01	50
		spec5	1.83	52
1136	P-C	spec1	1.61	56
		spec2	1.58	56
		spec3	1.54	57
		spec4	1.66	53
1776.0	MR	spec1	2.02	46

Notes: I_D/I_G is the ratio of peak-intensities of the D1- and G-bands, FWHM-D is the width of the D1 band

4.6. Molybdenum isotopes

The Mo concentrations and isotope signatures of KMF-5 and BH-1 are illustrated in Fig. 4-6.

Mo data of KMF-5 samples are listed in Table 4-7. Unsilicified, pure carbonates range between 5 and 56 ng/g Mo (mean with 2σ: 18 ± 19 ng/g), with corresponding δ^{98}Mo values between -0.82 and +1.08 ‰ (+0.43 ± 0.56 ‰). Silicified carbonates have total Mo amounts of 5 to 158 ng/g (56 ± 90 ng/g) and δ^{98}Mo values between -0.09 and +1.37 ‰ (+0.56 ± 0.58 ‰), similar to the pure carbonates. Detritus-containing carbonates have even higher Mo concentrations than pure and silicified carbonates, ranging between 0.04 and 1.31 µg/g (0.43 ± 0.86 µg/g), yet have Mo isotopic compositions that lie in the same range as the other carbonate samples, between -0.27 and +1.40 ‰ (+0.65 ± 0.71 ‰). The Fe- and silicate-rich sample 1265.1 contains 110 ng/g Mo and has a δ^{98}Mo signature of +0.84 ‰. Mudrock samples show the highest Mo concentrations, varying between 0.44 and 5.27 µg/g (1.64 ± 2.29 µg/g), the δ^{98}Mo signatures range from +0.13 and +1.24 ‰ (+0.49 ± 0.64 ‰) and are thus in the same range as the carbonates. Compared to average continental crust, which has a Mo concentration of ~1.1 µg/g (Rudnick and Gao, 2004), mudrocks of Malmani Subgroup have an overall higher Mo content.

Most rocks with δ^{98}Mo signature heavier than continental crust (-0.2 to +0.6 ‰, Voegelin et al. (2014)) are hosted in the Oaktree and the Monte Christo formations that were deposited when the carbonate platform received relatively high input of suspended siliciclastic muds (Figs. 2-3 and 4-1). Rocks of the Eccles and Lyttleton formations show rather continental δ^{98}Mo signatures (+0.11 to +0.60 ‰), with three exceptions of +0.63 ‰ (sample 705.7), +0.66 ‰ (985.5), and +1.24 ‰ (788.5), and were governed by other conditions with reduced input of detrital material but instead higher silicification. Presumably, these different depositional conditions had an effect on the Mo isotopic composition.

Carbonate samples of BH-1 (Table 4-8) show Mo concentrations between 19 and 130 ng/g (mean with 2σ: 46 ± 75 ng/g) and δ^{98}Mo values from -0.32 to +0.68 ‰ (+0.40 ± 0.61 ‰).

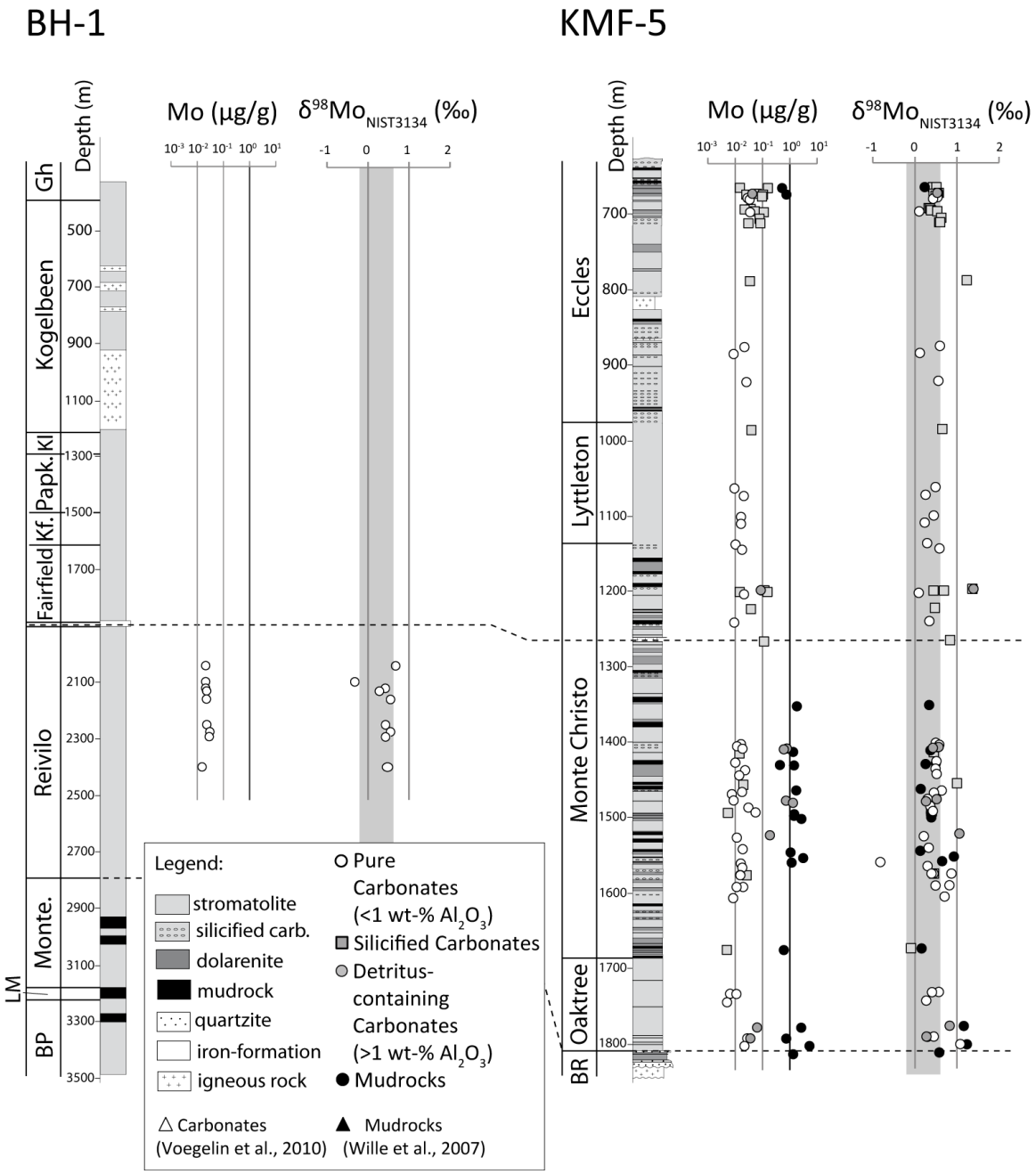

Figure 4-6: Mo concentrations and isotopic compositions of carbonates and mudrocks from KMF-5 and BH-1. Shaded area at δ^{98}Mo columns indicates the range of continental signatures from -0.2 to +0.6 ‰ (Voegelin et al., 2014), Mo concentration of continental crust is 1 µg/g (Taylor and MacLennan, 1985). Dashed black line shows stratigraphical relation of formations which belong to the Campbellrand-Malmani slope-platform succession. Abbreviations of Formations: BP: Boomplaas; LM: Lokamonna; Monte.: Monteville; Kf.: Klipfonteinheuwel; Papk.: Papkuil; Kl: Klippan; Gh: Gamohaan.

4.7. Iron isotopes

The Fe concentration and δ^{56}Fe data of carbonates and mudrocks from KMF-5 and BH-1 are displayed in Fig. 4-7. Data are complemented with previously published data of carbonates and mudrocks from the slope drill cores GKP01 and GKF01 (Czaja et al., 2012). Analogous to this study, the $\delta^{56}Fe_{carb}$ data (carbonate fraction) of the carbonate samples and the $\delta^{56}Fe_{WR}$ data (whole rock) of the mudrock samples were used (Czaja et al. (2012).

Carbonate and mudrock samples of KMF-5 are listed in Table 4-7. Pure carbonates contain between 1422 and 12941 µg/g Fe and shows δ^{56}Fe signatures between -0.88 and +0.08 ‰ (mean with 2σ: -0.48 ± 0.42 ‰). Silicified carbonates show concentrations from 580 to 6270 µg/g and δ^{56}Fe signatures from -0.88 to -0.24 ‰ (-0.53 ± 0.41 ‰). Carbonates of the Oaktree Formation shows a very good correlation (R^2 = 0.93) of Fe concentrations and isotope composition. In the Monte Christo, Lyttleton, and Eccles Formations no such correlation can be observed. Mudrocks show, relative to the carbonate samples, mostly similar Fe contents between 366 and 1368 µg/g, whereby one mudrock shows a very high Fe concentration of 65032 µg/g. However, δ^{56}Fe signatures of most mudrocks show heavier values between -0.37 and +0.79 ‰ (+0.25 ± 0.75 ‰). The carbonate fraction of Fe- and silicate-rich sample 1265.1 also shows a higher Fe concentration of 17148 µg/g and a δ^{56}Fe signature of -0.04 ‰.

Carbonate samples of BH-1 are listed in Table 4-8. Pure carbonates show Fe contents between 388 and 9546 µg/g and δ^{56}Fe signatures between -1.24 and -0.23 ‰ (mean with 2σ: -0.83 ± 0.5 ‰). Detritus-containing carbonates 340 and 375 contain 4415 and 8526 µg/g Fe and have a δ^{56}Fe composition of -1.82 and -0.85 ‰, respectively. Fe-rich carbonate 1914 has a very high Fe concentration of 27655 µg/g and shows a δ^{56}Fe signature of -0.95 ‰. ‰). Three BH-1 samples (340, 488 and 670) are calcitic (>50 wt-% CaO) whereas samples 488 and 670 have isotope values of -0.88 and -0.56 ‰, respectively, and are isotopically in the same range as the dolomitized samples. Sample 340 yields a light isotope signature of -1.82 ‰ and is from the Gamohaan Formation, which was deposited during drowning of the platform.

Kuruman Kop outcrop samples (Table 4-9) encompass a range of δ^{56}Fe values from -1.74 to +0.45 ‰ and Fe concentrations between 463 and 12058 µg/g. Two samples from the Kogelbeen (Ku12/31) and the lowermost Gamohaan (Ku12/25) formations are detritus-free (fenestrate) limestones, which were deposited under lagoonal conditions and yield isotope values of -0.95 and -0.70 ‰ and Fe concentrations of 463 and 1076 µg/g, respectively. The other three samples are further up in the sequence of the Gamohaan and show variable values. Sample Ku12/26 is a detritus-poor Fe-rich dolostone (12058 µg/g, -0.29 ‰), whereas Ku12/06 yields δ^{56}Fe values of -1.74 ‰ and moderate Fe values of 3225 µg/g. Ku12/04 is a clay-rich chert, which was deposited within a siderite-rich mudrock interval and shows heavy signatures of 0.45 ‰ and an Fe concentration of 4031 µg/g.

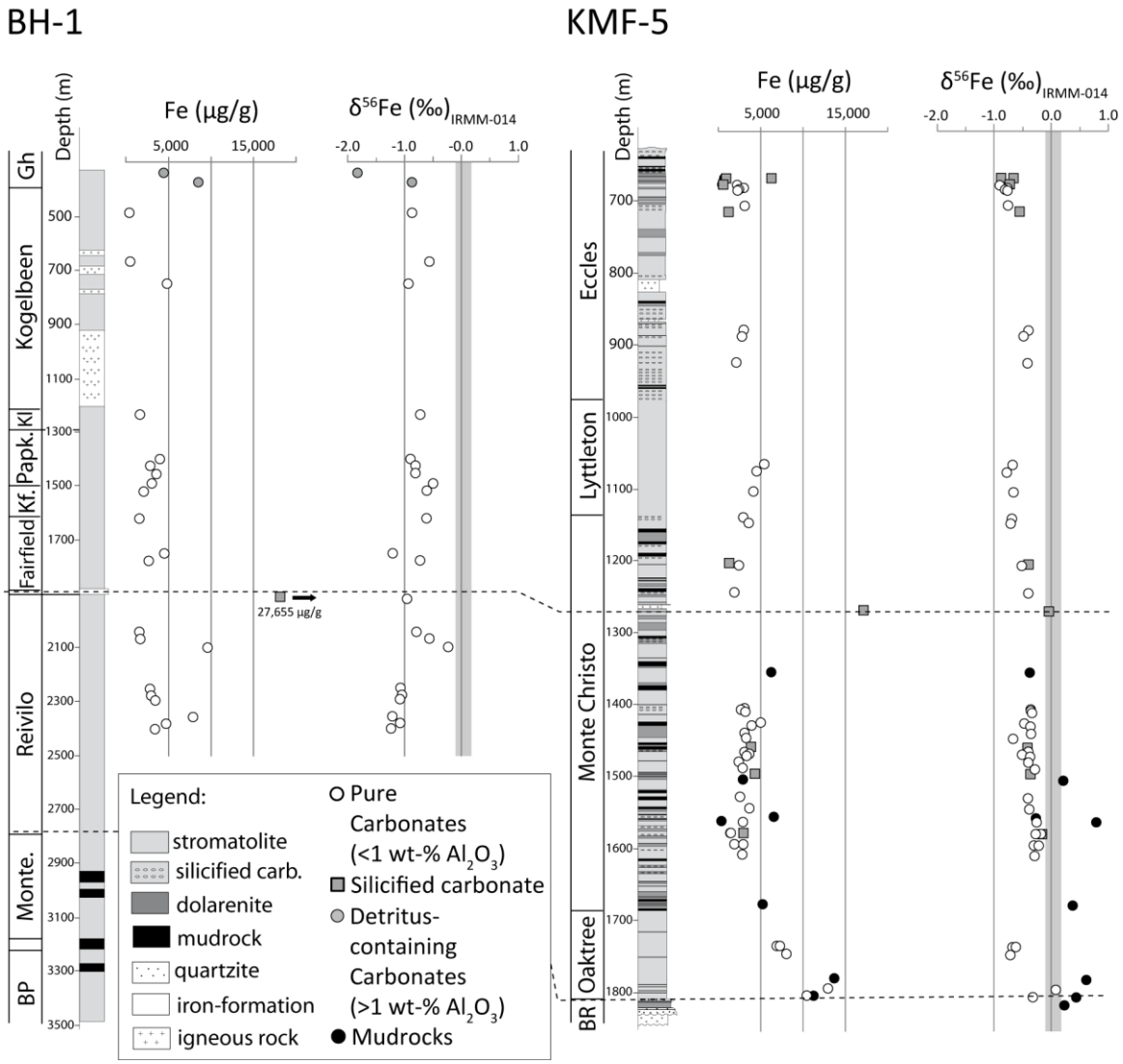

Figure 4-7: Fe concentrations and isotopic compositions of carbonates and mudrocks from KMF-5 and BH-1. Shaded area at δ^{56}Fe columns indicates the range of continental signatures from -0.1 to +0.2 ‰ (e.g. Craddock et al., 2013; Schoenberg and von Blanckenburg, 2006; Wang et al., 2014; Weyer et al., 2005). Dashed black line shows stratigraphical relation of formations which belong to the Campbellrand-Malmani slope-platform succession. Abbreviations of Formations: BP: Boomplaas; LM: Lokamonna; Monte.: Monteville; Kf.: Klipfonteinheuwel; Papk.: Papkuil; Kl: Klippan; Gh: Gamohaan.

Table 4-7: Mo and Fe concentration and isotope composition of KMF-5 rock samples

Depth m	Lithology	Mo µg/g	δ^{98}Mo ‰	2σ	Fe µg/g	δ^{56}Fe ‰	2σ	δ^{57}Fe ‰	2σ
Eccles Formation									
665.08	S-C	0.015	0.44	0.03	6270	-0.88	0.04	-1.13	0.10
665.18	S-C	0.158	0.52	0.01	922	-0.66	0.04	-1.02	0.09
665.28	MR	0.523	0.23	0.01					
672.77	S-C	0.061	0.57	0.02					
672.8	D-C	0.042	0.53	0.01					
673.8	MR	0.761	0.57	0.04					
673.84	S-C	0.104	0.53	0.01	580	-0.75	0.04	-1.12	0.08
673.87	S-C	0.026	0.45	0.02					
674.55	P-C				2211	-0.88	0.05	-1.30	0.08
675.38	P-C								
676.57	S-C	0.097	0.49	0.01					
678.6	P-C	0.028	0.54	0.01	2997	-0.80	0.05	-1.16	0.08
680.58	P-C	0.034	0.44	0.02	2436	-0.82	0.04	-1.25	0.08
681.76	S-C								
682.7	P-C				2275	-0.77	0.04	-1.14	0.07
689.2	S-C								
692.37	S-C								
692.98	S-C	0.037	0.33	0.02					
693.38	S-C	0.022	0.36	0.01					
695.99	S-C	0.053	0.38	0.01					
697.03	S-C	0.112	0.53	0.01					
697.18	P-C	0.035	0.11	0.05					
698.89	S-C								
702.6	P-C								
703.3	P-C				3106	-0.75	0.04	-1.11	0.07
705.7	S-C	0.078	0.63	0.01					
707.6	S-C								
708.7	S-C								
711.7	S-C	0.030	0.58	0.02					
711.8	S-C	0.083	0.60	0.01	1203	-0.6	0.045	-0.85	0.08
788.5	S-C	0.034	1.24	0.01					
867.3	MR								
875.5	P-C	0.022	0.60	0.01	2990	-0.4	0.051	-0.64	0.08
884.83	P-C	0.009	0.12	0.03	2789	-0.5	0.04	-0.71	0.09
921.78	P-C	0.026	0.56	0.01	2123	-0.4	0.032	-0.6	0.07
Lyttleton Formation									
985.5	S-C	0.039	0.66	0.01					
1062.5	P-C	0.009	0.49	0.02	5413	-0.7	0.034	-0.98	0.06
1072.73	P-C	0.021	0.26	0.02	4534	-0.8	0.043	-1.14	0.07
1100.2	P-C	0.016	0.45	0.03	4138	-0.7	0.036	-0.97	0.07
1109.5	P-C	0.016	0.24	0.03					
1136.75	P-C	0.010	0.29	0.02	2945	-0.7	0.033	-0.99	0.07
Monte Christo Formation									
1143.7	P-C	0.018	0.59	0.03	3595	-0.7	0.046	-1.04	0.08
1197.3	D-C	0.087	1.40	0.02					
1197.34	S-C	0.119	1.37	0.02					
1199.45	S-C	0.015	0.45	0.02					
1199.5	S-C	0.152	0.70	0.03	1279	-0.40	0.04	-0.63	0.08
1202.58	P-C	0.021	0.10	0.02	2422	-0.51	0.05	-0.75	0.09
1222.32	S-C	0.038	0.48	0.01					
1239.98	P-C	0.009	0.35	0.02	1885	-0.40	0.05	-0.60	0.08
1265.1	S-C	0.114	0.84	0.05	17148	-0.04	0.03	-0.03	0.07
1350.66	S-C								
1350.9	MR	1.821	0.34	0.02	6250	-0.37	0.04	-0.52	0.08
1401.0	P-C	0.016	0.50	0.03	3084	-0.35	0.04	-0.57	0.08
1403.8	P-C	0.012	0.59	0.03	2677	-0.35	0.03	-0.52	0.06
1406.7	D-C	0.782	0.57	0.03					
1406.8	P-C	0.019	0.55	0.01	3188	-0.33	0.04	-0.50	0.07
1407.9	D-C	0.604	0.43	0.03					
1411.1	MR	1.344	0.37	0.02					
1411.3	S-C								
1413.34	S-C	0.014	0.45	0.01					
1420.9	P-C				5009	-0.46	0.05	-0.74	0.08
1425.4	P-C	0.010	0.51	0.03	3935	-0.36	0.04	-0.51	0.07

Table 4-7 continued

Depth m	Lithology	Mo µg/g	δ^{98}Mo ‰	2σ	Fe µg/g	δ^{56}Fe ‰	2σ	δ^{57}Fe ‰	2σ
1427.85	S-C								
1428.4	MR	0.438	0.50	0.05					
1429.1	MR	1.427	0.26	0.02					
1435.25	P-C	0.023	0.49	0.02	3099	-0.35	0.05	-0.58	0.09
1442.17	P-C	0.014	0.52	0.01	3289	-0.66	0.04	-1.03	0.08
1454.61	S-C	0.020	1.00	0.01	3848	-0.41	0.05	-0.68	0.08
1460.05	S-C								
1461.8	P-C				3078	-0.41	0.04	-0.65	0.07
1462.1	MR	1.719	0.14	0.02					
1464.3	P-C	0.018	0.64	0.02	3675	-0.50	0.04	-0.75	0.07
1467.1	P-C	0.008	0.46	0.03	3340	-0.37	0.04	-0.59	0.08
1475.35	P-C	0.009	0.31	0.02	2398	-0.40	0.04	-0.63	0.08
1475.6	D-C	0.734	0.52	0.02					
1478.6	D-C	1.314	0.27	0.02					
1484.8	P-C	0.030	0.37	0.01	2873	-0.28	0.04	-0.41	0.07
1491.3	P-C	0.056	0.43	0.01					
1491.85	S-C	0.005	0.39	0.04	4315	-0.35	0.04	-0.56	0.08
1493.5	MR	1.474	0.38	0.02					
1495.8	MR	1.441	0.41	0.02					
1499.6	S-C								
1499.85	MR	2.674	0.40	0.01	2904	0.20	0.05	0.32	0.08
1521.4	D-C	0.189	1.06	0.01					
1524.7	P-C	0.011	0.21	0.03	2568	-0.41	0.04	-0.57	0.06
1528.48	S-C								
1539.9	P-C	0.019	0.33	0.02	3658	-0.38	0.04	-0.54	0.08
1544.1	MR	1.066	0.13	0.03					
1551.6	D-C								
1551.7	MR	3.102	0.93	0.01	6544	-0.27	0.05	-0.40	0.08
1557.7	MR	1.178	0.65	0.02	366	0.79	0.05	1.14	0.08
1558.88	P-C	0.016	-0.82	0.02	2907	-0.25	0.04	-0.34	0.08
1564.3	P-C	0.018	0.30	0.03					
1574.15	P-C	0.015	0.45	0.02	1422	-0.23	0.04	-0.33	0.09
1574.2	P-C	0.016	0.87	0.02					
1574.25	P-C	0.015	0.40	0.03	1470	-0.20	0.05	-0.29	0.09
1574.3	S-C	0.026	0.46	0.02	2969	-0.24	0.05	-0.34	0.08
1589.75	P-C	0.019	0.83	0.03	1884	-0.27	0.04	-0.40	0.08
1589.9	P-C	0.011	0.49	0.02	2941	-0.22	0.04	-0.34	0.08
1604.6	P-C	0.008	0.71	0.02	2821	-0.28	0.03	-0.45	0.07
1673.1	S-C	0.005	-0.09	0.03					
1673.3	MR	0.609	0.16	0.01	5223	0.38	0.05	0.54	0.08
Oaktree Formation									
1731.1	P-C	0.007	0.57	0.04	6884	-0.67	0.03	-0.98	0.07
1731.3	P-C	0.011	0.41	0.03	7268	-0.62	0.04	-0.88	0.07
1742.3	P-C	0.005	0.27	0.04	8028	-0.72	0.04	-1.03	0.06
1775.8	D-C	0.063	0.83	0.01					
1776.0	MR	2.653	1.17	0.02	13687	0.62	0.04	0.94	0.08
1790.0	D-C	0.036	0.28	0.01					
1790.1	P-C	0.028	0.45	0.01	12941	0.08	0.04	0.05	0.08
1790.3	MR	0.742	0.30	0.01					
1800.1	P-C	0.022	1.08	0.02	10433	-0.32	0.04	-0.51	0.07
1800.3	MR	5.267	1.24	0.01	11244	0.44	0.05	0.64	0.08
1811.2	MR	1.323	0.58	0.02	65032	0.24	0.04	0.36	0.07

P-C: 'pure' carbonate, S-C: silicified carbonate, D-C: detritus-containing carbonate, MR: mudrock
Extern reproducibility for δ^{98}Mo is ± 0.11 ‰ (2σ), and for δ^{56}Fe ± 0.06 ‰ (2σ)

Table 4-8: Mo and Fe concentration and isotope composition of BH-1 rock samples

Depth m	Lithology	Mo µg/g	δ^{98}Mo ‰	2σ	Fe µg/g	δ^{56}Fe ‰	2σ	δ^{56}Fe ‰	2σ
Gamohaan Formation									
340	D-C				4415.19	-1.82	0.04	-2.65	0.07
375	D-C				8525.88	-0.85	0.04	-1.26	0.07
Kogelbeen Formation									
488	P-C				388.23	-0.88	0.05	-0.62	0.09
670	P-C				513.84	-0.56	0.04	-0.81	0.07
751	P-C				4833.87	-0.93	0.04	-1.36	0.08
Klippan Formation									
1235	P-C				1629.05	-0.72	0.04	-1.07	0.08
Papkuil Formation									
1400	P-C				4034.57	-0.90	0.05	-1.25	0.08
1425	P-C				2831.81	-0.80	0.04	-1.20	0.06
1455	P-C				3574.02	-0.80	0.04	-1.19	0.07
1490	P-C				3075.41	-0.50	0.04	-0.78	0.09
Klipfonteinheuwel Formation									
1520	P-C				2104.83	-0.60	0.04	-0.88	0.08
Fairfield Formation									
1620	P-C				1667.11	-0.60	0.04	-0.91	0.08
1750	P-C				4491.31	-1.21	0.04	-1.82	0.08
1776	P-C				2645.31	-0.72	0.05	-1.10	0.07
Kamden Formation									
1914	S-C				27654.87	-0.95	0.04	-1.33	0.08
Reivilo Formation									
2041	P-C	0.13	0.68	0.02	1582.02	-0.79	0.03	-1.19	0.07
2066	P-C				1686.15	-0.57	0.04	-0.85	0.07
2098	P-C	0.07	-0.32	0.02	9546.17	-0.23	0.03	-0.36	0.08
2121	D-C	0.04	0.43	0.02					
2131	D-C	0.02	0.28	0.02					
2160	P-C	0.03	0.55	0.02					
2250	P-C	0.02	0.43	0.02	2817.56	-1.07	0.04	-1.57	0.06
2251	P-C								
2275	P-C	0.02	0.55	0.03	2930.77	-1.04	0.04	-1.55	0.07
2293	P-C	0.02	0.43	0.03	3474.60	-1.08	0.04	-1.63	0.08
2355	P-C				7840.77	-1.20	0.04	-1.85	0.07
2379	P-C				4719.68	-1.07	0.03	-1.61	0.07
2400	P-C	0.03	0.48	0.02	3397.90	-1.24	0.04	-1.81	0.08
2450	P-C								

P-C: 'pure' carbonate, S-C: silicified carbonate, D-C: detritus-containing carbonate
Extern reproducibility for δ^{98}Mo is ± 0.11 ‰ (2σ), and for δ^{56}Fe ± 0.06 ‰ (2σ)

Table 4-9: Mo and Fe concentration and isotope composition of Kuruman Kop rock samples

Depth m	Lithology	Mo µg/g	δ^{98}Mo ‰	2σ	Fe µg/g	δ^{56}Fe ‰	2σ	δ^{56}Fe ‰	2σ
Gamohaan Formation									
Ku12_04	D-C				4031.00	0.45	0.04	0.65	0.09
Ku12_06	P-C				3225.00	-1.74	0.06	-2.59	0.09
Ku12_25	P-C				12058.00	-0.29	0.04	-0.42	0.08
Ku12_26	P-C				1076.00	-0.70	0.05	-1.01	0.08
Kogelbeen Formation									
Ku12_31	P-C				463.00	-0.95	0.04	-1.37	0.08

P-C: 'pure' carbonate, D-C: detritus-containing carbonate
Extern reproducibility for δ^{98}Mo is ± 0.11 ‰ (2σ), and for δ^{56}Fe ± 0.06 ‰ (2σ)

4.8. XRD

In this study representative carbonate samples were analyzed by XRD to complement results of XANES analyses. Pure carbonate samples clearly show a mixture of dolomite and quartz, depending on the silicification grade (Fig. 4-8). Some minor amounts of calcite can also be included. However, no Fe-mineral phase could be detected by XRD, probably because the detection limit of this method for crystalline material is between ~ 0.1 and 0.5 wt-%. Most of the here investigated samples have Fe concentrations within this range. Thus, XANES analyses are necessary to carefully detect the Fe phase and speciation within the carbonates.

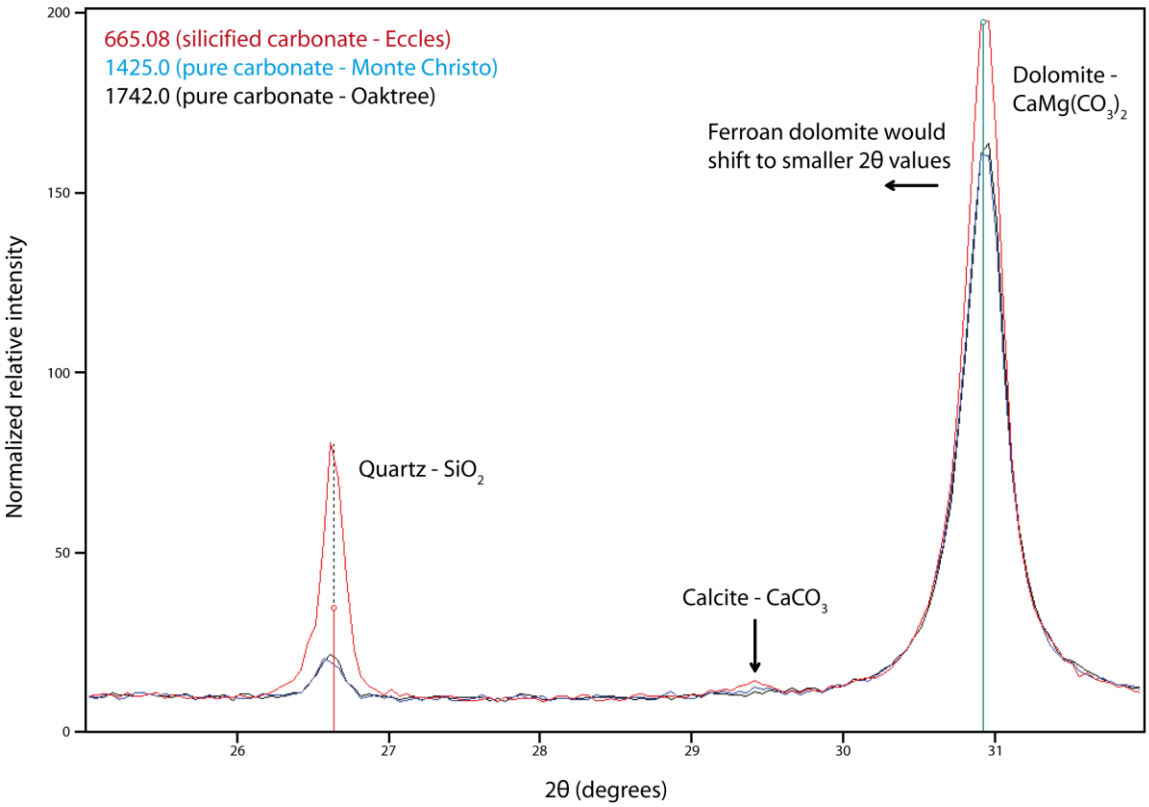

Figure 4-8: XRD pattern of three representative carbonate samples from KMF-5 show a dolomite-quartz mixture with minor amounts of calcite. No Fe-minerals could be clearly detected with this method.

4.9. XANES spectra

Fluorescence and transmission data were pre-processed using the PyMCA software package, which allows evaluation of large data sets (Sole et al., 2007). The transmission spectra were calculated as follows: $I_1 = I_0 e^{-\mu(E)} \rightarrow \mu(E) = -\ln\frac{I_1}{I_0}$, where μ is the absorption in dependence of the energy E, I_0 is the incident X-ray beam intensity, and I is the remaining beam intensity after transmission through the sample. For fluorescence spectra the absorption is defined as $\mu(E) \propto \frac{I_f}{I_0}$, where I_f is the fluorescence intensity. First, all spectra of

a selected sample were energy calibrated by analyzing metallic Fe at the same experimental setup as used for sample analyses (i.e., fluorescence or transmission mode) and setting the first inflection of Fe K-edge to 7112 eV. Subsequently, all spectra were normalized and those spectra, which were over- or undersaturated were automatically excluded by the software and not used for the statistical evaluation of the spectra. By selecting specific regions of the XANES spectra (energy range from 7100 to 7175 eV), maps of Fe concentration and oxidation state were generated (Fig. 4-9-A and -B). The edge-jump maps show the intensity of absorption or fluorescence at the Fe edge-jump, which is the qualitative representation of the Fe concentration (Munoz et al., 2006). The oxidation state of Fe is indicated by the main edge position, i.e. the maximum of the first derivative of the spectra, which is specific to each Fe redox species (O'Day et al., 2004).

For the statistical evaluation of the XANES, the number of unique mineralogical components represented by the collection of XANES spectra was determined using the 'principle component analysis' (PCA) tool from PyMCA. In Table 4-10 the variance of the first five principle components (PC01 – PC05) is shown, the percentage indicates the significance of the respective PC. According to that, all samples are represented by two to three distinct mineralogical components. A 'linear combination fitting' of the composite was performed, which are average spectra from each sample with the Athena software package (Ravel and Newville, 2005), using the number of components determined by PCA to guide the number of mineral standard spectra used. The standard database consisted of spectra from ankerite, siderite, goethite, magnetite, pyrite, marcasite, chlorite and ferrosmectite (Table 4-11). The exact proportions are listed in Table 4-10 and the corresponding linear fits are illustrated in Fig. 4-9-A/-B and Fig. 4-10. Eleven representative samples were analyzed, eight carbonates, one silicified carbonate (665.18), one mudrock (1776.0) and one Fe- and silicate-rich carbonate (1265.2) (Fig. 4-10). The results show that carbonates from the lower CMCP (Oaktree, Monte Christo, Reivilo formations; steep ramp architecture) predominantly show the coordination environment of Fe(II) mineral species, mainly ankerite, with minor amounts of siderite, Fe sulfide (pyrite, marcasite), and mixed-valence Fe oxides (magnetite). The mudrock sample 1776.0 from the Oaktree Formation contains mainly pyrite with minor magnetite and the Fe- and silicate-rich sample 1265.2 (Kamden Member equivalent) consists mainly of chlorite with minor siderite and ferrosmectite. Towards the upper CMCP (Lyttleton, Eccles, Kogelbeen formations; rimmed margin architecture) this mineral composition significantly changes in favor of Fe(III) mineral species, in particular Fe(III)-(oxyhydr)oxides (goethite) (Fig. 4-10). The Lyttleton Formation carbonates consist mainly of ankerite, but already show some admixture of goethite in the XANES spectra (1100.3). The carbonates of the Eccles Formation (665.08, 665.18 and 884.9)

show significantly different spectra from the rest of the analyzed carbonates, and best fit by the goethite standard. Other components of Eccles samples are siderite and ferrosmectite (detailed amounts in Table 4-10), whereas there is no sign of Fe-sulfide. Interestingly, also the few organic carbon rich mudrocks of the Eccles Formation lack of framboidal pyrite, in contrast to the Fe-sulfide and organic carbon rich mudrocks of the Oaktree and the Monte Christo formation, which do contain framboidal pyrite (Fig. 2-4). This indicates that the lower CMCP had more reducing conditions and the upper CMCP more oxidizing conditions, which didn't allow the formation of pyrites. Sample 340 (Gamohaan Formation, BH-1, GWA) shows mainly Fe(II)-carbonate signatures with minor amounts of pyrite that are visible as hotspots in the XANES maps (Fig. 4-9-A and -B). The Gamohaan Formation was deposited during a transgression, thus, an influx of more reducing species from the open ocean water is likeable and would explain this change in mineralogy.

As the pre-edge can also give valuable information about the oxidation state and speciation of Fe, a plot was constructed, based on the normalized absorption values θ, κ, and μ at defined energies (7110, 7113 and 7117.5 eV) (Marcus et al., 2009). As the Fe K-edge during the experiment was at 7112 eV, in contrast to the Fe K-edge of 7110.75 used by Marcus et al. (2009), θ, κ, and μ values for the samples were defined at 7111.25, 7114.25 and 7118.75 eV, respectively, and compared to the θ, κ, and μ values defined for Fe(II), FeS, mixed valence, and Fe(III) mineral standards of Marcus et al. (2009). The results are displayed in Figure 4-11 and confirm that Fe is present as FeS, Fe(II), and Fe(III) species, and that the samples indeed show an increase in the oxidation state towards the upper CMCP.

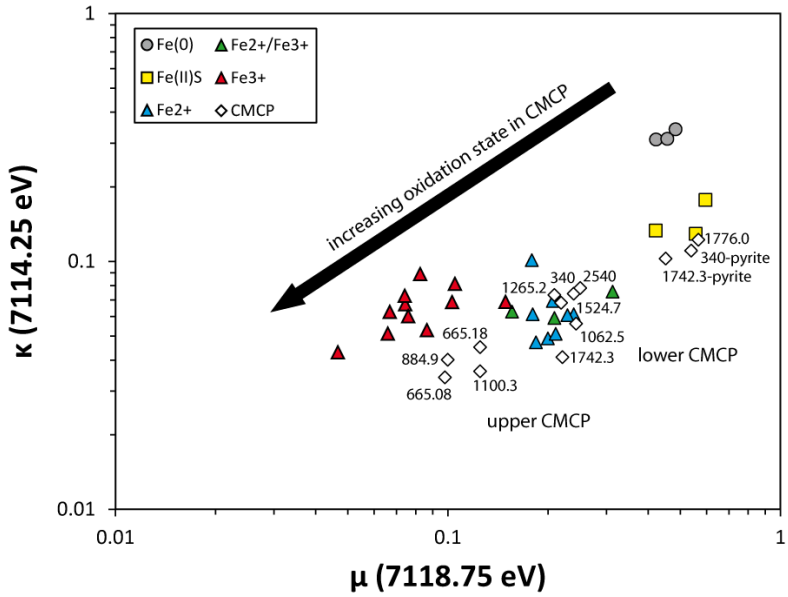

Figure 4-11: Classification of distinct Fe (redox-)species analyzed by Marcus et al. (2009), displaying the absorption at 7111.25 (θ), 7114.25(κ) and 7118.75(μ). Plotted with composite spectra from samples of the CMCP, showing that with continuing growth of the platform, the Fe oxidation state increases. See Table 4-10 for details.

Table 4-10: XAS analyses, statistical evaluation and characterization of Fe species from KMF-5 and BH-1 carbonate and mudrock samples

Formation	Sample (Depth)	XAS Method	Remarks	map size (µm*µm)	spot size (µm)	Fe-species (Adsorption intensity; Marcus et al., 2009)			Principle component analyses (variance, %)					Linear combination fitting - best fit				
						θ (eV)	κ (eV)	µ (eV)	PC01	PC02	PC03	PC04	PC05	proportion amount of iron species				
						7111.25	7114.25	7118.75										
KMF-5															total	R-factor	chi^2	chi^2 reduced
Eccles	665.08	Fluo	P-C	700x340	20	0.008	0.034	0.098	96.45	2.53	0.40	0.23	0.20	*goethite (0.846)* *siderite (0.139)*	0.99	0.0078	0.2568	0.0017
	665.18	Fluo	S-C	500x500	20	0.018	0.045	0.125	84.00	9.05	3.67	1.13	0.60	*goethite (0.649)* *siderite (0.124)* *ferrosmectite (0.233)*	1.01	0.0077	0.2543	0.0017
	884.9	Fluo	P-C	1000x1000	50	0.011	0.040	0.100	90.19	6.79	1.03	0.73	0.35	*goethite (0.603)* *ferrosmectite (0.438)*	1.04	0.0098	0.3681	0.0024
Lyttleton	1062.5	Trans	P-C	2000x2000	20	0.045	0.056	0.243	93.46	3.67	2.28	0.19	0.08	*ankerite (0.869)* *siderite (0.090)*	0.97	0.0015	0.1000	0.0003
	1100.3	Fluo	P-C	400x400	10	0.004	0.036	0.125	94.11	3.72	0.46	0.31	0.22	*ankerite (0.735)* *goethite (0.233)*	0.97	0.0128	0.4234	0.0027
Monte Christo	1265.2	Fluo	S-C (Fe-rich)	300x300	15	0.040	0.073	0.209	88.72	6.75	2.34	1.12	0.51	*chlorite (0.861)* *siderite (0.107)* *ferrosmectite (0.060)*	1.03	0.0017	0.0580	0.0004
	1524.7	Trans	P-C	2000x2000	20	0.056	0.068	0.219	92.81	4.44	1.08	0.47	0.29	*ankerite (0.939)* *siderite (0.059)*	1.00	0.0091	0.6506	0.0020
Oaktree	1742.3	Trans	P-C	2000x2000	20	0.024	0.041	0.221	94.76	3.36	1.31	0.12	0.07	*ankerite (0.909)* *siderite (0.071)*	0.98	0.0033	0.2323	0.0007
	1742.3	Trans	pyrite hotspots		20	0.046	0.103	0.457						*pyrite (0.658)* *siderite (0.296)* *ankerite(0.056)*	1.01	0.0072	0.3721	0.0011
	1776.0	Fluo	MR	700x700	23	0.041	0.122	0.567	84.64	9.60	3.73	0.93	0.21	*pyrite (0.945)* *magnetite (0.076)*	1.02	0.0012	0.0304	0.0002
BH-1																		
Gamohaan	340	Trans	D-C	2000x1700	20	0.069	0.074	0.239	94.64	4.54	0.23	0.12	0.07	*ankerite (0.670)* *siderite (0.212)* *minor pyrite(0.037)*	0.92	0.0053	0.2883	0.0009
	340	Trans	pyrite hotspots		20	0.048	0.107	0.545						*pyrite(0.829)* *siderite (0.117)* *ankerite (0.066)*	1.01	0.0018	0.0930	0.0003
Reivilo	2540	Fluo	P-C	400x400	10	0.038	0.078	0.250	84.00	6.68	3.24	1.54	1.41	*ankerite (0.936)* *marcasite (0.079)* *magnetite (0.100)*	1.12	0.0051	0.2037	0.0013

R-factor: discrepancy index, the agreement between calculated and observed intensities; chi^2: 'Goodness of fit'-test, squared difference between calculated and observed data;
chi^2 reduced: chi^2 divided by the number of degrees of freedom; Fluo: fluorescence method, Trans: transmission method;
P-C: 'pure' carbonate, S-C: silicified carbonate, D-C: detritus-containing carbonate, MR: mudrock

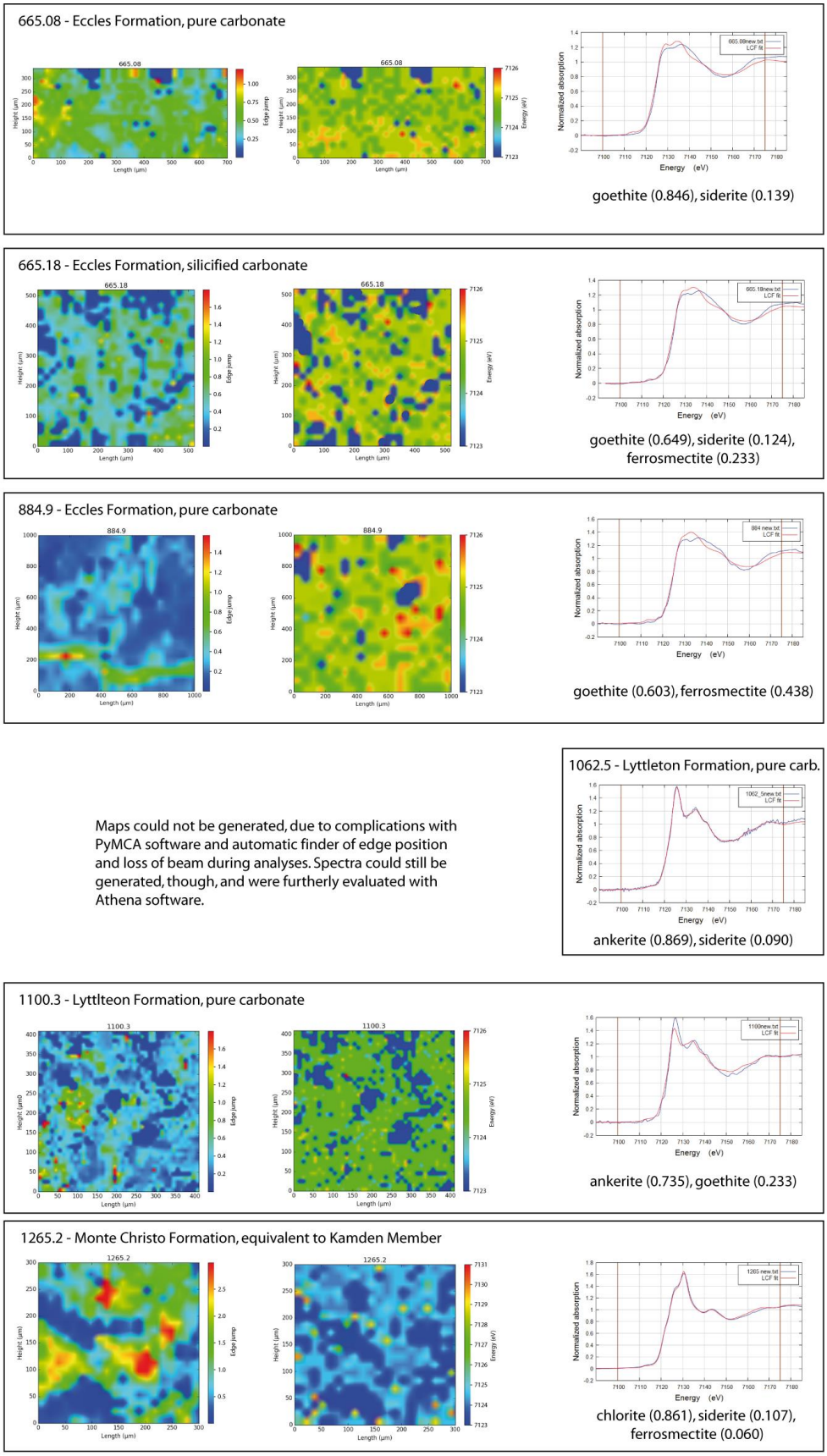

Figure 4-9-A: XAS map of edge-jump and edge-position of analyzed carbonate and mudrock samples. Dark blue fields represent excluded spectra, which were over- or under-saturated or had a poor signal-to-noise ratio. Linear combination fitting (LCA fit) was performed on representative spectra and mineral proportions are indicated below those fits.

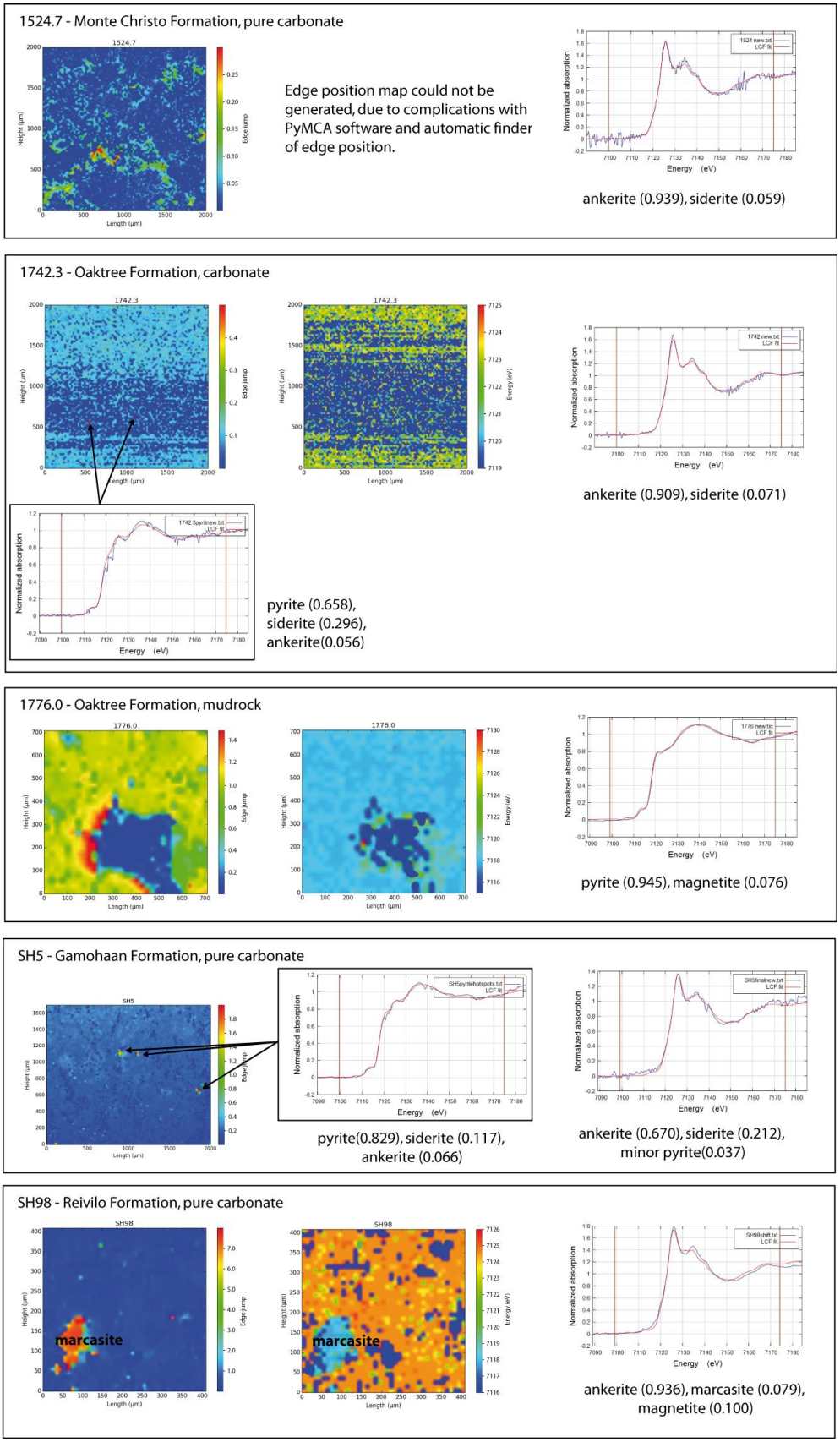

Figure 4-9-B: XAS map of edge-jump and edge-position of analyzed carbonate and mudrock samples. Dark blue fields represent excluded spectra, which were over- or under-saturated or had a poor signal-to-noise ratio. Linear combination fitting (LCA fit) was performed on representative spectra and mineral proportions are indicated below those fits.

Table 4-11: Fe mineral standards used for linear component analyses

Mineral	Structural formula	Source	Reference
Ankerite	$Ca(Fe(II),Mg, Mn)(CO_3)_2$	natural	E. Swanner
Siderite	$Fe(II)(CO_3)$	synthetic	T. Borch, C. Hansel, S. Fendorf
Goethite	α-Fe(III)O(OH)	natural	Sirine Fakra, Matthew A. Marcus
Magnetite	Fe_3O_4	natural	J. Frommer and A. Voegelin
Pyrite	FeS_2	natural	J. Frommer and A. Voegelin
Marcasite	FeS_2		E. Swanner
Chlorite (Ripidolite - CCa2)	$Ca_{0.5}(Mg_{4.44},Fe(III)_{3.47},Fe(II)_{3.02},Al_{0.60},Mn_{0.01},Ti_{0.06})(Si_{4.51},Al_{3.49})O_{20}(OH)_{16}$	Clay Mineral Society	Source Clay Repository (2001) Source clay physical/chemical data: http://web.missouri.edu/~geoscjy/SourceClay/chem.html. The Clay Minerals Society
Ferrosmectite (Fe-bearing montmorillonite)	$(Na_{0.48}Ca_{0.03}K_{0.01})(Al_{1.54}Mg_{0.33}Fe(III)_{0.09}Fe(II)_{0.02})(Si_{3.87}Al_{0.13})\ O_{10}(OH)_2 \cdot nH_2O$	natural	T. Borch, C. Hansel, S. Fendorf, J.W. Stucki

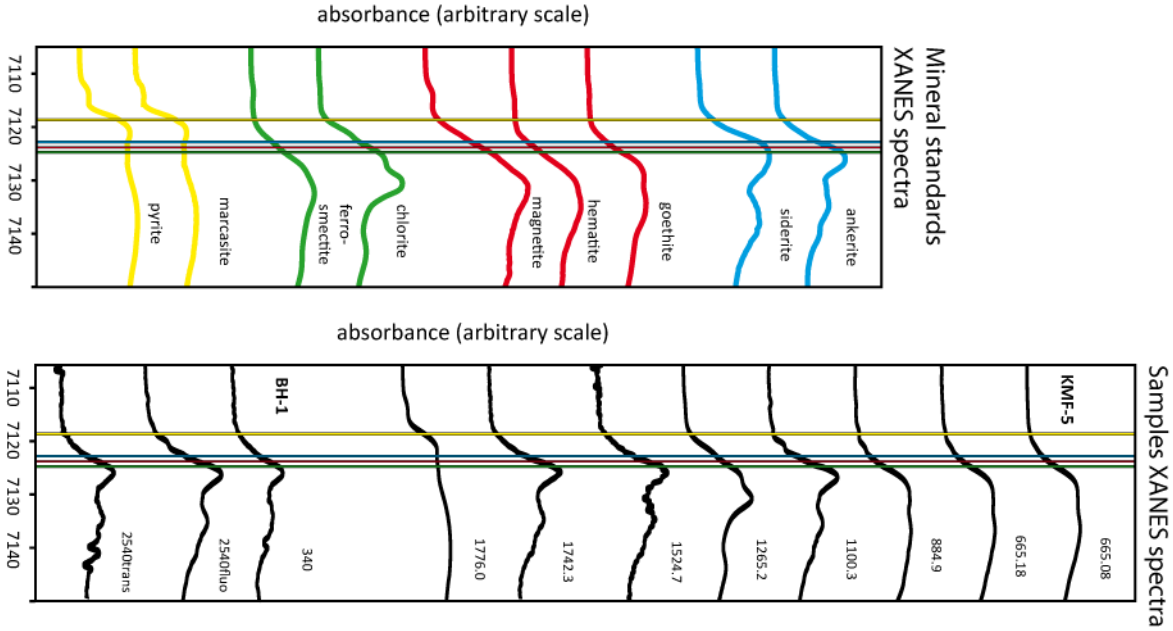

Figure 4-10: XANES spectra of analyzed samples and mineral standards used to fit the sample spectra (see Tables 4-8 and 4-9 for details and compositional reconstruction). Different Fe mineral species and characteristic edge-peak inflection point are color-coded (O'Day et al., 2004): Fe-sulfides (yellow), Fe-carbonates (blue), Fe-(hydr)oxides (red), and phyllosilicates (green). Note the change in the spectra from lower to upper part of CMCP carbonate rocks.

5. Depositional reconstruction and diagenesis of the CMCP

The geochemical and isotopic composition of marine carbonates can reflect the primary conditions during their precipitation. However, in reality these primary signatures are often altered by secondary processes, in particular post-depositional alteration by hydrothermal fluids and/or freshwater. This also applies to the Transvaal Area, because it was intruded by the 2.054 Ga old Bushveld igneous complex (Buick et al., 2001) (Fig. 2-1), raising the possibility of contact-metamorphic overprint of adjacent carbonates (Frauenstein et al., 2009). Moreover, early diagenetic dolomitization and silicification also affected large parts of the platform and clearly signal interaction of seawater with freshwater (Beukes, 1987). Thus, different geochemical proxies have to be examined carefully to unravel primary and potential secondary signals and to avoid misinterpretation. Potential effects of secondary fluid alteration during diagenesis and contact metamorphism were tested here by $\delta^{18}O_{carb}$, $\delta^{30}Si$ signatures and elemental composition. Careful determination of peak metamorphic conditions and post-depositional overprint of the samples is crucial in order to evaluate the potential of preservation of the original geochemical signatures. In this study this was investigated by Raman spectroscopy.

In the following the preservation of geochemical signatures will be carefully evaluated and subsequently the paleoenvironmental conditions of the CMCP will be reconstructed based on those findings.

5.1. Evaluation of influence of Bushveld intrusion on the Malmani Subgroup

The sediments of the Transvaal Area, including the Malmani Subgroup (KMF-5) were intruded by the Bushveld igneous complex 2.054 Ga ago (Buick et al., 2001) (Fig. 2-1). Newly grown minerals such as garnet, pyroxene, siderite, and ankerite are abundant in the carbonates near the contact aureole (Frauenstein et al., 2009) and point to strong recrystallization and alteration due to high-T fluid circulation. Although the rocks of KMF-5 are in c. 80 km distance and thus not in direct contact with the main Bushveld intrusion, they are intersected by a few mafic dykes (Fig. 2-3). The latter are probably related to the emplacement of the Bushveld complex and caused alteration of the adjacent carbonate sections resulting in the formation of secondary siderite and ankerite. Apart from these spatially limited alteration zones, which were avoided during sampling, the carbonate rocks in the drill core show no macroscopic signs of secondary mineral growth induced by the Bushveld complex. Carbonates of the far more distant Griqualand and Prieska area (Campbellrand Subgroup; BH-1, GKP01, GKF01; Figs. 2-1, 2-2), are unaffected by the Bushveld complex (Beukes, 1987).

Based on $\delta^{18}O_{carb}$ analyses, Frauenstein et al. (2009) observed that the degree of fluid alteration in the sedimentary country rocks of the Transvaal area decreases with increasing distance from the Bushveld complex. Three kilometers from the contact zone, $\delta^{18}O_{carb}$ values are as low as -22 ‰ and interpreted to be the result of intense fluid-rock interaction. With increasing distance, $\delta^{18}O_{carb}$ values increase continuously to ~ -10 ‰ at 18 km distance from the contact. Such high isotope values probably reflect rather pristine, marine signatures (Crne et al., 2014) and are close to the best estimate for Neoarchean seawater ($\delta^{18}O_{carb}$ ~ -8 ‰) (Fig. 5-1) (Shields and Veizer, 2002; Veizer et al., 1999). Pure and silicified carbonate rocks of KMF-5 (Table 4-1; Fig. 4-3) yield $\delta^{18}O_{carb}$ values between -10.3 to -5.4 ‰ (mean with 2σ: -7.8 ± 1.8 ‰), similar to stratigraphically correlative carbonate sequences of the GKP01 (-8.2 ± 3.9), GKF01 (-7.6 ± 1.8 ‰) (Fischer et al., 2009), and BH-1 (-9.5 ± 2.8 ‰), which are unaffected by the Bushveld complex fluids (Table 4-2; Fig. 5-1). The $\delta^{18}O_{carb}$ values of GKP01 and GKF01 were obtained from micritic microbialites (Fig. 5-2). In contrast, some other samples from all four drill cores are coarse-grained, show secondary carbonate veins, and yield significantly lighter $\delta^{18}O_{carb}$ values (down to -17 ‰), possibly due to alteration by fluids produced during devolatization reactions or intense recrystallization (Figs. 5-1, 5-2) (Fischer et al., 2009; Horstmann and Beukes, 2002; Valley, 1986).

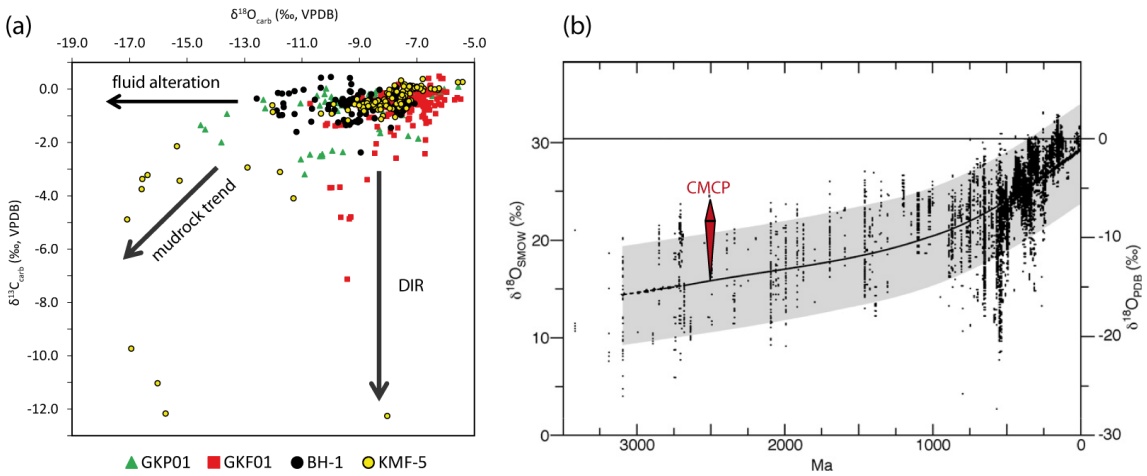

Figure 5-1: (a) Plot ($\delta^{18}O_{carb}$ vs. $\delta^{13}C_{carb}$) of all analyzed samples from KMF-5 and BH-1, analyzed for this study. $\delta^{18}O_{carb}$ vs. $\delta^{13}C_{carb}$ data of GKP01 and GKP01 are from (Fischer et al., 2009; Horstmann and Beukes, 2002). Data of all four drill cores greatly overlap and are interpreted and discussed in the text. However, some distinctive trends show the influence of fluids on the $\delta^{18}O_{carb}$ signatures, the influence of microbial induces organic carbon oxidation during dissimilatory iron reduction (DIR) on the $\delta^{13}C_{carb}$ trend and a probably a mixture of those two diagenetic processes reflected in the mudrock composition. (b) Illustration from Kasting et al. (2006) shows $\delta^{18}O$ signatures of marine calcites and calcitic fossils over the last 4 billion years, thick line is cubic smoothing spline evolution and authors suggest that values heavier than that represent pristine $\delta^{18}O$ signatures. The red diamond shows range of carbonates from CMCP with an average of about -8 ‰ relative to VPDB standard.

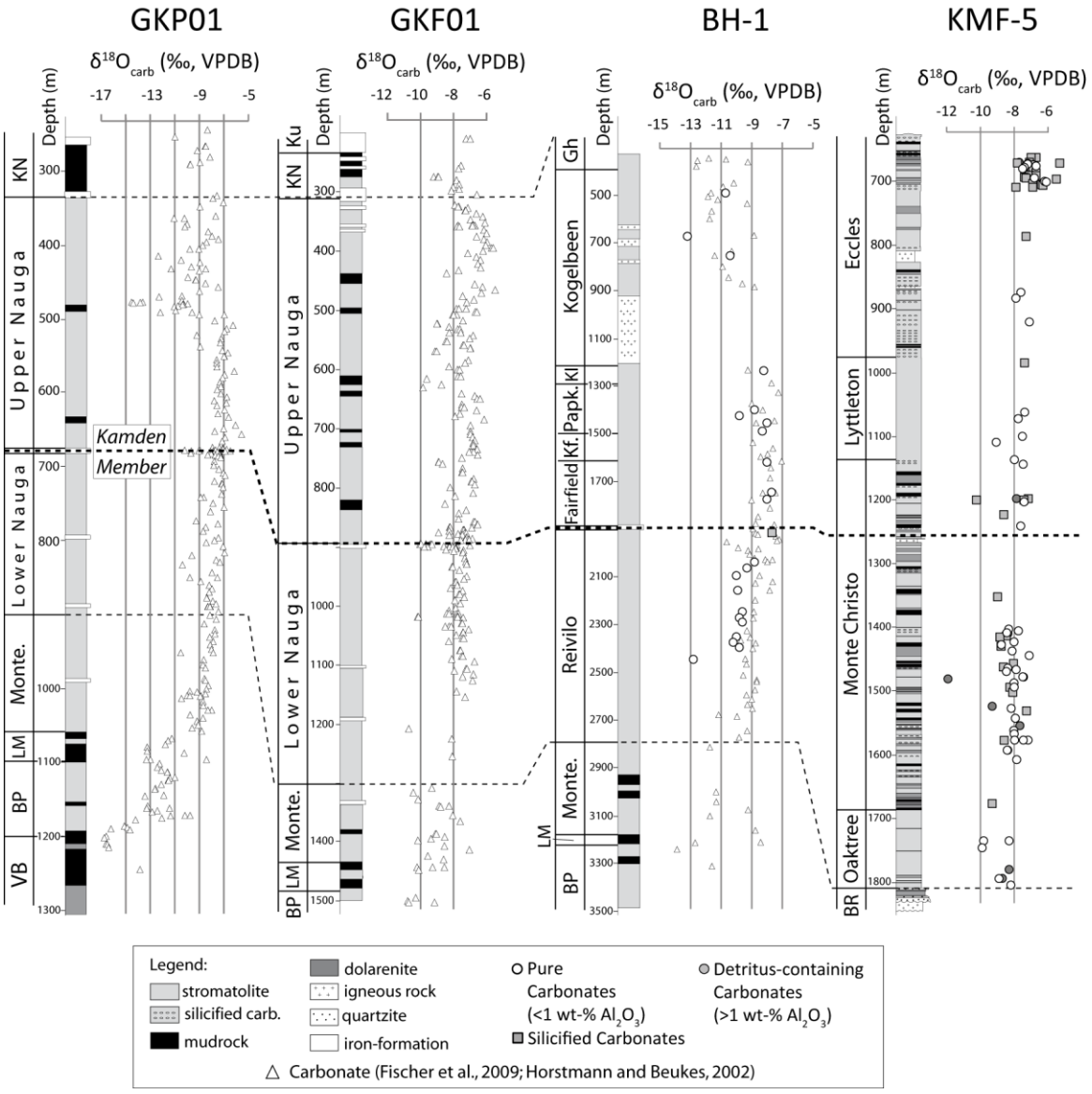

Figure 5-2: Stratigraphic correlation and $\delta^{18}O_{carb}$ data of GKP01, GKF01, BH-1 (SACHA) and KMF-5. Black triangles represent isotope data on carbonates of GKP01, GKF01 and BH-1 (SACHA) from Horstmann and Beukes (2002) and Fischer et al. (2009). Other isotope data of BH-1 and KMF-5 carbonates are from this study. Dashed black lines show stratigraphical relation of formations, which belong to the Campbellrand-Malmani slope-platform succession. Thicker dashed line indicates Kamden Member. VB: Vryburg; BP: Boomplaas; LM: Lokamonna; Monte.: Monteville; KN: Klein Naute; Ku: Kuruman; Kf.: Klipfonteinheuwel; Papk.: Papkuil; Kl: Klippan; Gh: Gamohaan; BR: Black Reef

The pristine nature of some other geochemical signatures of these carbonates have been confirmed, like the depth-variant Fe and Mn concentrations, which are supplied by hydrothermal input from the open ocean and controlled by the depositional depth below sea level as well as different solubility behavior (Beukes, 1987; Beukes and Gutzmer, 2008 and this study). As the exposure to magmatic fluids from the Bushveld complex would have led to an obliteration of the water depth related signal, a impact of such fluids on the majority of the rocks can be ruled out. Furthermore, the interaction of the carbonates with magmatic fluids is expected to produce very positive Eu anomalies, no Y anomaly as well as

an overall slight increase in abundance from light REE to heavy REE (relative to PAAS) (Maier and Barnes, 1998). However, the REE+Y spectra obtained in our study rather resemble those of seawater with variable admixtures of open ocean and riverine waters. The elemental distributions and significance for the paleoenvironment are discussed in detail in chapters 5.4 and 5.5.

Altogether, visual inspection, geochemical features, and oxygen isotope signatures of the studied samples do not reveal any indication of secondary fluid alteration resulting from the emplacement of the Bushveld igneous complex.

5.2. Preservation of organic material and metamorphic conditions

The CMCP has been described as one of the best preserved Archean platforms, which was metamorphosed very early under lower greenschist facies conditions (Button, 1973; Miyano and Beukes, 1984). However, amphibolite facies metamorphism has been observed near the contact to the Bushveld complex (Frauenstein et al., 2009). Thus, Raman analyses were conducted to examine the degree of alteration of organic matter in KMF-5 samples from the TA and Kuruman Kop samples from the GWA and to evaluate the quality of $\delta^{13}C_{org}$ signatures. The intensity ratio of the D- and G-bands (I_D/I_G) and width of the D1-peak (FWHM-D) can be used to describe the degree of carbonization of organic material (Beyssac et al., 2002; Lahfid et al., 2010; Sforna et al., 2014) (Fig. 4-5). With increasing degree of carbonization caused by progressive diagenesis and low-grade metamorphism, the FWHM-D will become smaller (from > 200 cm^{-1} to ca. 60 cm^{-1}) and the I_D/I_G-ratio will increase (from ca. 0.8 to more than 2). Further alteration at higher temperatures will cause the growth and parallel stacking of layers until graphitic structural units are formed. This process of graphitization causes the FWHM-D to further decrease (from ca 60 cm^{-1} to 30 cm^{-1}), while the I_D/I_G ratio decreases steadily to 0 (at granulite facies metamorphism). Organic material throughout KMF-5 has an I_D/I_G ratio between 1.3 and 2.1 and FWHM-D values between 45 and 70, which confirms regional lower greenschist-facies metamorphism in the TA (Table 4-6; Fig. 4-5). These samples show a large spread in $\delta^{13}C_{org}$ from -39.4 to -24.0 ‰. It should be note, however, that the $\delta^{13}C$ signature of organic material can be shifted toward heavier values already under greenschist facies conditions (Valley and O'Neil, 1981). Two mudrock samples, 665.3, 673.0 (KMF-5), are more altered and show signs of early graphitization (I_D/I_G = 1.2-1.5, FWHM-D = 39-47). Clearly, they experienced a higher peak metamorphic temperature, which is also indicated by heavy $\delta^{13}C_{org}$ signatures of -22.9 and -21.8 ‰, respectively. The strongly silicified character of these samples suggests that they were pervasively altered by fluids and are likely to have lost their primary $\delta^{13}C_{org}$ signature. However, some other strongly silicified carbonate

samples obtain similar FWHM-D values and $\delta^{13}C_{org}$ values as un-silicified samples (Table 4-1). Therefore, silicification is not the only explanation for the stronger alteration of some samples and another factor had to be involved in this process. Outcrop samples from fenestral carbonate of Kuruman Kop contain organic material that has experienced a lesser degree of carbonization than that found in KMF-5 (Fig. 4-5). Carbonates from the same formation in the BH-1 yield $\delta^{13}C_{org}$ values from -29.9 to -27.0 ‰ (Table 4-2). Furthermore, only a slight discrepancy in $\delta^{13}C_{org}$ values between mudrocks and carbonates in the slope region has been described (Fischer et al., 2009) in contrast to a larger offset between different lithologies in the peritidal region of the TA, as it is implicated by mudrock sample 867.3 ($\delta^{13}C_{org}$ = -39.4 ‰) and the stratigraphically close carbonate sample 884.9 ($\delta^{13}C_{org}$ = 28.0 ‰) (KMF-5; Table 4-1; Fig. 5-3). Although we acknowledge the possibility that some rock samples of KMF-5 were affected by higher temperatures, which might have caused an isotope shift in organic carbon toward slightly heavier values, there are more reliable indicators that primary signatures were indeed preserved. First, the majority of $\delta^{13}C_{org}$ data of Transvaal and Griqualand West samples overlap (Figs. 4-3, 4-4), revealing that higher peak metamorphic temperatures for the Transvaal area play a minor role for a shift in isotope values. Second, the abovementioned samples 867.3 and 884.9 are two of the least affected samples of KMF-5 regarding their Raman spectral characteristics (I_D/I_G down to 1.39 and 1.27, FWHM-D up to 71 and 66, respectively), and therefore argue for the actual preservation of their primary signatures, which are dependent upon the depositional environment (Fig. 5-3). Third, $\delta^{13}C_{org}$ signatures depend on the fractionation of carbon by different microbial species (Fig. 5-3). As microbial mats contain communities of several microbial species, the $\delta^{13}C_{org}$ signatures therefore rather reflect mixed signals of these species, and that a trend to lighter or heavier signatures can give us information about the dominant microbial species, depending on available nutrients, electron donors, light and other environmental factors. Thus, we propose that in KMF-5 samples with high FWHM-D the large isotope difference of $\delta^{13}C_{org}$ between carbonates and mudrocks is rather related to different microbial activity in these different environmental settings, particularly a stronger influence of cyanobacteria in the very shallow marine microbial mats, alternating with more anaerobic microbial activity during deposition of the mudrocks. This topic is further discussed in chapter 6.2.

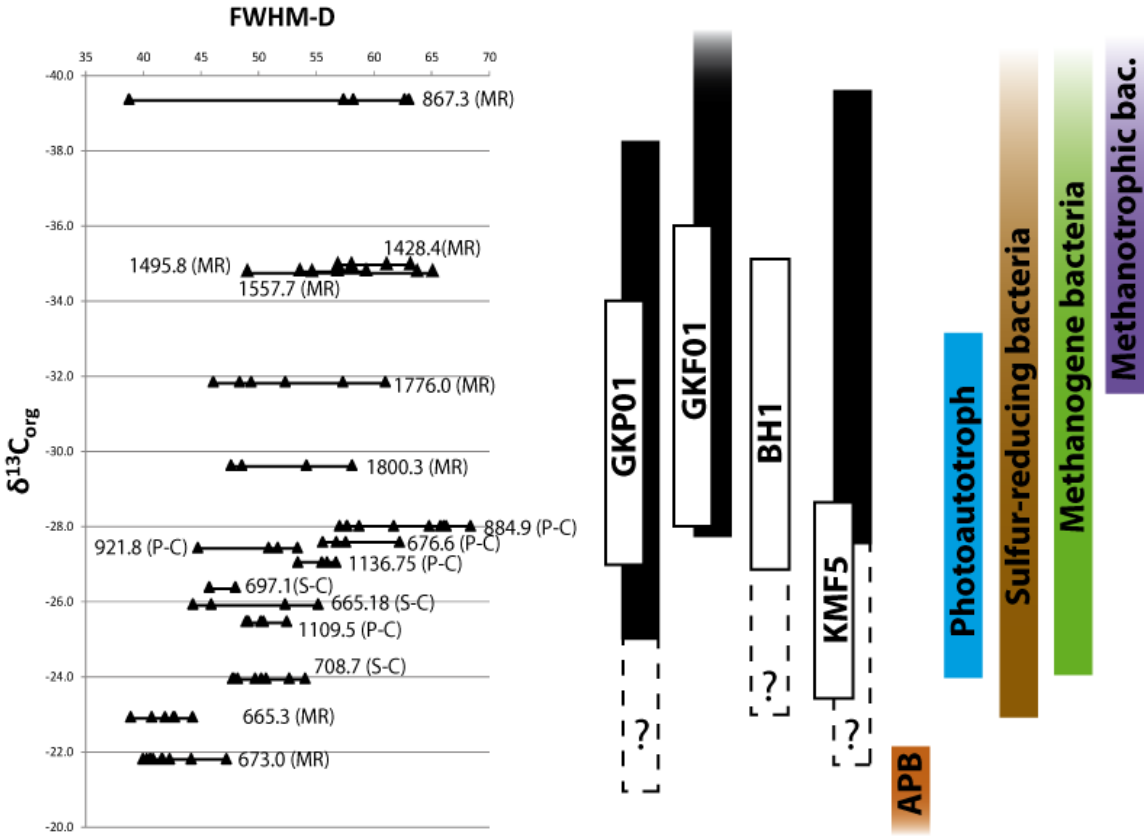

Figure 5-3: Combined Raman (FWHM-D) and $\delta^{13}C_{org}$ data of carbonate (P-C: Pure carbonate, S-C: Silicified carbonate) and mudrock (MR) samples from KMF-5 (Malmani Subgroup, TA). Mudrocks provide overall lighter isotope values than carbonates, except of two samples which also provide the lowest FWHM-D values. Solid boxes reflect $\delta^{13}C_{org}$ isotope range of GKP01, GKF01, BH-1 and KMF-5 (black boxes: mudrocks, white boxes: carbonates). Isotope data of GKP01 and GKF01 are from Fischer et al. (2009). '?' completes the full range of measured $\delta^{13}C_{org}$ isotope values, however these heavier values might be rather a sign of ^{12}C-loss due to metamorphic overprint. Isotope ranges of most common microbial communities (ABP: Anoxygenic photoautotroph bacteria) indicate a mixed $\delta^{13}C_{org}$ signal and probably change in dominance of microbial organisms, with dependence on water depth and lithology (Freeman et al., 1990; Hayes, 2001; Robinson et al., 2003; Scott et al., 2004; Sirevag, 1995; Tabita, 1999; Valentine et al., 2004).

5.3. Early diagenetic dolomitization and silicification

Geochemical data presented in Figures 4-1 and 4-2 and Tables 4-1, 4-2, and 4-3 reveal that carbonate rocks of the Malmani Subgroup (TA) are fully dolomitized and partly silicified, whereas carbonates of the Campbellrand Subgroup (GWA) are partly still calcitic (Beukes, 1987).

Dolomitization is the replacement of calcite by dolomite, according to the equation proposed by Lippmann (1973) and Morrow (1982),

$$(2-x)CaCO_3 + Mg^{2+} + xCO_3^{2-} \rightarrow CaMg(CO_3)_2 + (1-x)Ca^{2+} \text{ (x: mole)}$$

and is usually initiated by large-scale fluid flow through soft sediments and interaction between calcium-carbonate and Mg-rich saline pore fluids from seawater, which is the main source of Mg^{2+} (Purser et al., 1994). Kinetic hindrance of dolomitization can be overcome by an increase of the Mg^{2+}/Ca^{2+} ratio in the solution via evaporation (Land, 1985), a decrease of the ionic strength by dilution of seawater with freshwater (Folk and Land, 1975), and an

increase of alkalinity (CO_3^{2-} anions) by dissolution of limestone (Murray, 1960). The evaporation of seawater and the formation of highly Mg-rich brines and the pumping of this slightly hypersaline marine waters through a carbonate succession is one the most common models (Simms, 1984). Pumping of vast volumes of dolomite-oversaturated seawater through a carbonate succession has been suggested as dolomitization process for the platform in the Bahamas (Kohout, 1967; Simms, 1984). In combination, these scenarios could explain why some parts of the Campbellrand Subgroup in the GWA still contains some limestone, whereas the Malmani Subgroup is fully dolomitized. Carbonates deposited near the slope would still have had better exchange with open ocean water, in contrast to the interior platform, where poor water circulation and restricted influx of fresh open marine water allowed the formation of Mg-enriched brines and thus enhanced the complete dolomitization of the Malmani Subgroup (Beukes, 1987).

The silicification observed in the upper succession of the Malmani Subgroup is fairly typical for Precambrian carbonate platforms, partly because Si concentrations in the seawater were significantly higher than today (Knauth, 1979). The replacement of carbonate by silicic phases is an early diagenetic process, caused by the interaction between marine and meteoric pore fluids in the mixing zone of near-shore sediments, and is dependent on porosity, salinity, pH, and f_{CO2} (Knauth, 1979; van den Boorn, 2008). Increasing partial pressures of CO_2 and lower fluid pH can lead to undersaturation of carbonate and oversaturation of silica, resulting in calcite dissolution and silica precipitation, respectively. An early diagenetic origin for the silicification in the Malmani Subgroup, as opposed to a possible later hydrothermal overprint, is supported by heavy $\delta^{30}Si$ values from +0.53 to +2.35 ‰ of silicified carbonate samples from the Eccles and the Monte Christo formations (Table 4-1). Such heavy Si isotopic compositions are in the range of modern surface waters like rivers (average $\delta^{30}Si$ of +0.8 ‰) and shallow seawater (average $\delta^{30}Si$ of +1.1 ‰) (De la Rocha et al., 2000; Georg et al., 2007; Ziegler et al., 2005) and not for hydrothermal fluids with typical $\delta^{30}Si$ values between -0.3 and +0.3 ‰ (Chakrabarti et al., 2012 and references therein; van den Boorn, 2008).

It has been proposed that silicification occurred locally with dolomitization as both processes are promoted by mixing of fresh- and seawater (Knauth, 1979; Magaritz et al., 1980; Runnels, 1969; Smart et al., 1988). However, silicification in the CMCP is restricted to the supratidal environment, whereas dolomitization affected almost the complete platform, with some exceptions in the GWB (Beukes, 1987; Sumner and Beukes, 2006). The strong increase of silicification in the Eccles Formation (Figs. 2-3, 4-1) can be explained by the development of the rimmed margin in the second half of platform evolution (Sumner and Beukes, 2006), which restricted the exchange with open ocean water and thus increased the

influence of freshwater in the shallow seawater. In modern coastal carbonates the mixing with freshwater can cause a significant shift to lighter $\delta^{18}O_{carb}$ signatures, together with a shift to lighter $\delta_{13}C_{carb}$ values. The latter is caused by the oxidation of organic material, supplied by land plants in particular, which contain more ^{12}C (Holmden et al., 1998; Oehlert and Swart, 2014). Such an effect would become visible during rise and fall of seawater level. Even though the platform clearly experienced several of these trans- and regression event, such a trend to negative values related to a sea-level change is not observed for the investigated microbial carbonates, neither for $\delta^{13}C_{carb}$ nor for $\delta^{18}O_{carb}$ signatures (Figs. 4-3, 4-4, 5-2). Regarding the $\delta^{13}C_{carb}$, this can be explained with the lack of land plants during the Neoarchean, which would have affected the $\delta^{13}C_{carb}$ signature in very shallow marine settings. Instead, a change in the carbon budget on the platform is a plausible explanation for such a shift in $\delta^{13}C_{carb}$ and will be discussed in detail in Chapter 6.1. Concerning dolomitization and silicification, a shift to lighter $\delta^{13}C_{carb}$ and $\delta^{18}O_{carb}$ would be strong indicators for syndepositional interaction of seawater and (isotopically light) freshwater. However, there is no shift to more negative $\delta^{18}O_{carb}$ values in KMF-5 (Fig. 4-3) that would be associated with such a mixing (Allan and Matthews, 1982; Immenhauser et al., 2003). One likely explanation for that would be that there was no or only a little difference in the $\delta^{18}O$ signatures of the seawater and the freshwater because of warmer climate conditions and thus no shift in the isotope signature was produced during water mixing (Schmidt et al., 1999).

5.4. Preservation of geochemical signatures

Sedimentological and geochemical observations reveal that the distinctions between individual sediments of the CMCP were mainly governed by water depth, water circulation, detrital supply from the adjacent land area and diagenesis. In particular, large-scale dolomitization and silicification in the peritidal environment clearly indicate mixing of fresh- and seawater in the shallow ocean and subsequent changes in some mineralogical (dolomite) and geochemical (Mg and Si) signatures during diagenesis. Some studies note that other characteristic trace element patterns in carbonates indicate severe diagenesis and alteration that could overprint primary signals, e.g. the decrease of Sr and Na and increase of Mn and Fe concentrations (Banner, 1995; Brand and Veizer, 1980; Veizer, 1983). Mn and Fe would have been added from leaching and dissolution of siliciclastics, sulphides and oxyhydroxides to altered carbonates (Veizer, 1983). However, pure carbonates with little to no detrital component could be suitable targets reflecting primary seawater signatures (Webb and Kamber, 2000).

The input of trace elements into the carbonate structure is dependent on the concentration of trace elements in the porewater, the water-rock ratio and the effective distribution coefficient. The ionic radii of Mg^{2+}, Fe^{2+} and Mn^{2+} are very similar and their distribution coefficients are higher than unity, such that they are preferentially incorporated into the carbonate structure (Reeder, 1983). In chapter 4.1.3., it is described how the Fe/Mn ratio (expressed as Fe#) in carbonates correlate with water depth and detrital input. The dependence of Fe and Mn concentrations from water depth is a result of the lower redox potential of Fe compared to Mn. This promotes Fe precipitation from more reducing, deeper water beyond the shelf area and Mn precipitation at shallower, more oxidized waters of the platform (Beukes, 1987). As a result, the Fe/Mn ratios of pure carbonates from the slope to basinal Prieska facies (Fig. 2-2) reported in Voegelin et al. (2010) (Fe# mean with 2σ: 0.52 ± 0.15) are slightly higher in the than those of the Campbellrand shelf facies (Fe# 0.31 ± 0.11) and the subtidal carbonates of the Malmani inner shelf facies (Fe# 0.39 ± 0.06) determined in this study (Tables 4-1, 4-2 and 4-3). Pure carbonates of the subtidal lower Oaktree Formation and the intertidal Monte Christo and Eccles formations show higher Fe/Mn ratios (Fe# 0.56 ± 0.16), contradicting the concept of preferential Fe precipitation over that of Mn at lower oxygen fugacity. The lower Oaktree Formation reveals the highest Fe/Mn ratio for pure carbonates in KMF-5 (samples 1790.1 and 1800.1 with Fe# values of 0.68 and 0.59, respectively) and might indicate a higher influx of open ocean water. Intertidal carbonates on the other hand are frequently intercalated by Fe-rich mudrocks, in particular the Monte Christo Formation (Fig. 2-3). It is possible that early-diagenetic processes released iron from these mudrocks to the carbonates (Veizer, 1983). Freshwater might also have had an influence, as silicified carbonates reveal higher Fe/Mn ratios (Fe# 0.56 ± 0.16) (Table 4-1). Since freshwater can carry a continental trace element signature (Kamber and Webb, 2001 and references therein), it is likely that an aqueous Fe source from the continent might have influenced the peritidal carbonates. Nevertheless, the dependence of the Fe/Mn ratio in subtidal carbonates from the TA and GWA on the water depth indicates that those signatures are pristine and were not affected by dolomitization. It also argues for a very early dolomitization (Beukes, 1987), maybe within the first 1-2 Ma after deposition, as described for the Bahamian carbonate platform (Mcneill and Kirschvink, 1993; Swart et al., 1987). However, detrital input and mixing with freshwater seem to have perturbed peritidal settings.

Original marine signatures are also shown by PAAS-normalized REE+Y distributions of pure carbonates (Tables 4-4, 4-5), which reflect mixture of shallow seawater (Y/Ho anomaly > 27, positive La anomaly, depleted light REE over heavy REE) with deeper open ocean water carrying a hydrothermal signature (positive Eu anomaly, depleted light

REE over heavy REE) and freshwater carrying a continental 'PAAS'-signature (Y/Ho around 27, flattened patterns) (Kamber and Webb, 2001 and references therein). Carbonates of the lowermost Oaktree Formation (1790.1 and 1800.1) show elevated heavy REE patterns due to an enhanced hydrothermal influence at the beginning of carbonate growth during the first massive flooding along the Kaapvaal Craton (Figs. 5-4, 5-5) (Sumner and Beukes, 2006). Lagoonal carbonates from the upper Oaktree Formation (KMF-5) and Reivilo Formation (BH-1) carry shallow seawater REE+Y signatures with barely any hydrothermal influence (Fig. 5-5). A stronger influence from freshwater with ongoing platform growth becomes obvious from flattened REE+Y signatures in the peritidal Monte Christo and Eccles carbonates and partly in the lagoonal Lyttleton carbonates (Fig. 5-5). Overall a more pronounced average Eu anomaly of 1.53 and a lower average Y/Ho ratio of 48 for slope carbonates compared to coeval lagoonal carbonates with values of 1.19 and 75, respectively, reveal a diminishing hydrothermal influence from the slope towards the shallow-water platform and confirm Fe and Mn distributions (Fig. 5-5). The draw-down of hydrothermal influx onto the shallow-water platform might have induced an evolutionary advantage for oxygenic photosynthesis, which is independent from reduced species, and therefore set the stage for the development of a thriving aerobe ecosystem (e.g. Des Marais, 2001). This is discussed in Chapter 6.

5.5. Paleoenvironmental reconstruction of the CMCP

Even though most of the CMCP is dolomitized, sedimentological features and structures as well as some primary geochemical signals are still preserved and allow reconstructing the environmental conditions and the evolution of this carbonate platform. The Oaktree and Monte Christo formations (lower CMCP, steep ramp architecture) are detritus-dominated and chert-poor while the Lyttleton and Eccles formations are detritus-poor and in the case of Eccles chert-dominated (upper CMCP, rimmed margin architecture), which is indicated by the two trends between the carbonate-silica and carbonate-PAAS end-members and a well-defined gap in between (Fig. 4-1). These trends, particularly portrayed by the inter-tidal Monte Christo and Eccles formations, are independent of water depth but rather related to the development of the rimmed margin (Fig. 5-5). The decline in siliciclastic detrital run-off to the platform from the deposition of the Lyttleton Formation upwards in the succession could be speculated to be due to expansion of the platform and subsequent covering of the sediment source, or a change of the river flow directions in the hinterland of the basin as a consequence of a landscape change, or due to decreased weathering as a consequence of climate change. REE+Y patterns as well as Fe and Mn concentrations can be correlated with the stratigraphy, the water

depth, and the input of hydrothermal or continental fluids (Figs. 5-4, 5-5) (Voegelin et al., 2010 and this study). It is possible based on the geochemistry to distinguish between sedimentary facies that interacted with the open ocean, i.e. the slope environment and the early stages of steep platform architecture, and facies that indicate more restricted conditions on the platform, in particular at peritidal settings and the transformation to the rimmed margin architecture. Four major platform evolution stages can be distinguished (Fig. 5-4). During the initial flooding of the Kaapvaal Craton and incipient carbonate deposition, the samples of the lower Oaktree Formation show elevated Fe, Mn and REE concentrations as well as REE+Y signatures that are characteristic for hydrothermal fluids from mid-ocean ridges (Pearce, 1983), defined by depleted light REE relative to the heavy REE. This changes with the build-up of the platform and a decreasing influx of open ocean (hydrothermal) water, so that the carbonates of the upper Oaktree Formation show REE+Y signatures characteristic for Archean shallow seawater, enriched in heavy REE relative to light REE and with a positive La and Y anomaly (Fig. 5-5) (Kamber et al., 2004). After the build-up of the steep ramp platform and during a regression the peritidal Monte Christo Formation and the lagoonal Reivilo Formation were deposited. During this stage more continental material was deposited and was preserved as organic-rich mudrocks, which show REE+Y signatures of continental material (PAAS). The carbonates of the Monte Christo Formation are more depleted in REE+Y compared to the mudrocks, but show a distinct and flattened 'continental' pattern, defined by slighter La and Y anomalies and without a depletion of light REE over heavy REE, compared to the 'seawater' pattern of Oaktree and Reivilo carbonates (Fig. 5-5). We interpret that the Monte Christo carbonates were stronger influenced by continental fluids. The Kamden 'Iron Formation' Member was deposited during a temporary major transgression and is geochemically visible in Fe-rich rocks throughout the platform (Sumner and Beukes, 2006). The detritus-rich sample 1265.2 in KMF-5 shows a REE+Y pattern that resembles a mudrock composition and is close to PAAS. However, in contrast to the mudrocks, 1265.2 also reveals a positive Eu anomaly, which indicates increased influence of hydrothermal fluids from the open ocean water, probably during the transgression and deposition of the Kamden Member, which is also supported by the high Fe_2O_3 content (> 10 wt-%) (Table 4-1). Eventually, the architecture of the CMCP changed from a steep ramp to a rimmed margin, which served as a shelter against the influx of open ocean water. Thus, the influence of continental water masses prevailed over the influence of open ocean water, visible in the 'continental' REE+Y patterns of the Lyttleton and Eccles carbonates (Fig. 5-5). However, some samples retained a 'seawater' pattern and even show a slight Eu anomaly, which indicates an occasional influx of open ocean water into the lagoon. REE+Y patterns of slope carbonates (Voegelin et al., 2010) show compared

to the platform carbonates by an order of magnitude higher REE+Y values and pronounced Eu anomalies, confirming that the slope was mainly influenced by open ocean water. The influence of different trace element sources (open ocean vs. continental) are supported by the Fe/Mn ratio of carbonates (displayed in Fig. 5-5 as Fe#) and also reveal the dependence of water depth as Fe has a lower redox potential than Mn. This results in Fe# >0.4 in slope carbonates of Lower and Upper Nauga compared to platform subtidal carbonates (Reivilo, upper Oaktree, Lyttleton formations and most of the upper CMCP of BH-1) with Fe# <0.4 or close to 0.4, which reflects a simultaneous decrease of Fe and relative to that increase of Mn from slope to platform (Fig. 5-5). There is a clear difference between platform carbonates (BH-1 and KMF-5) deposited in the lower or upper CMCP. The Reivilo and Monte Christo formations (lower CMCP) were deposited coevally and whereas carbonates from the Monte Christo Formation show Fe# between 0.4 and 0.6, the Reivilo carbonates obtain Fe# values between 0.1 and 0.4 (Fig. 5-5). In the upper CMCP the platform carbonates show values between about 0.3 to 0.6, some silicified carbonates with occasional excursion up to 0.8, and are thus much more homogeneous than in the lower CMCP. This is in particular visible in BH-1 and confirms that the shift from a steep ramp to a rimmed margin architecture had an impact on source influxes from an open ocean dominated to a continental dominated influx.

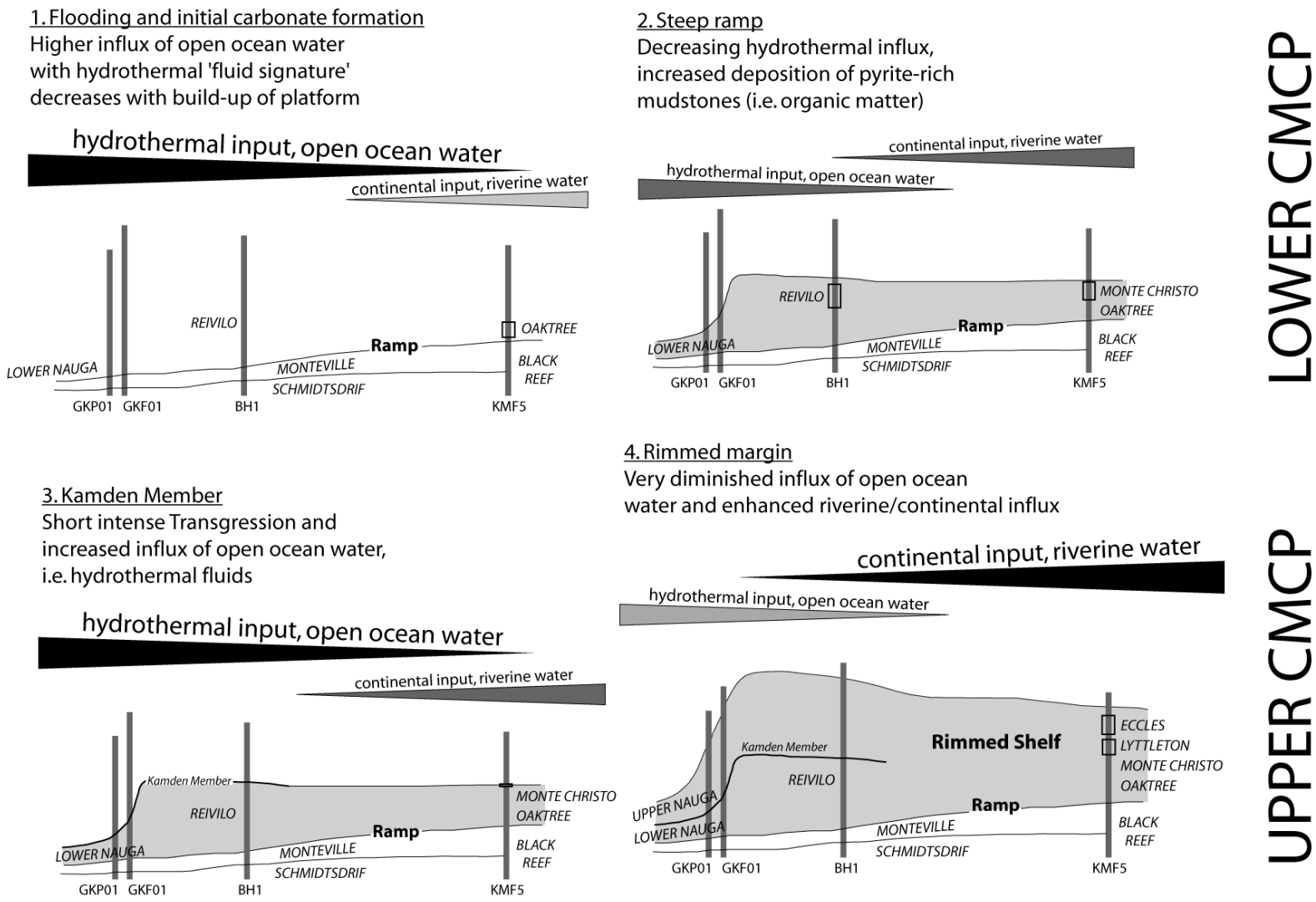

Figure 5-4: Simplified paleoenvironmental reconstruction of the CMCP over time with relative influxes of open ocean and freshwater.

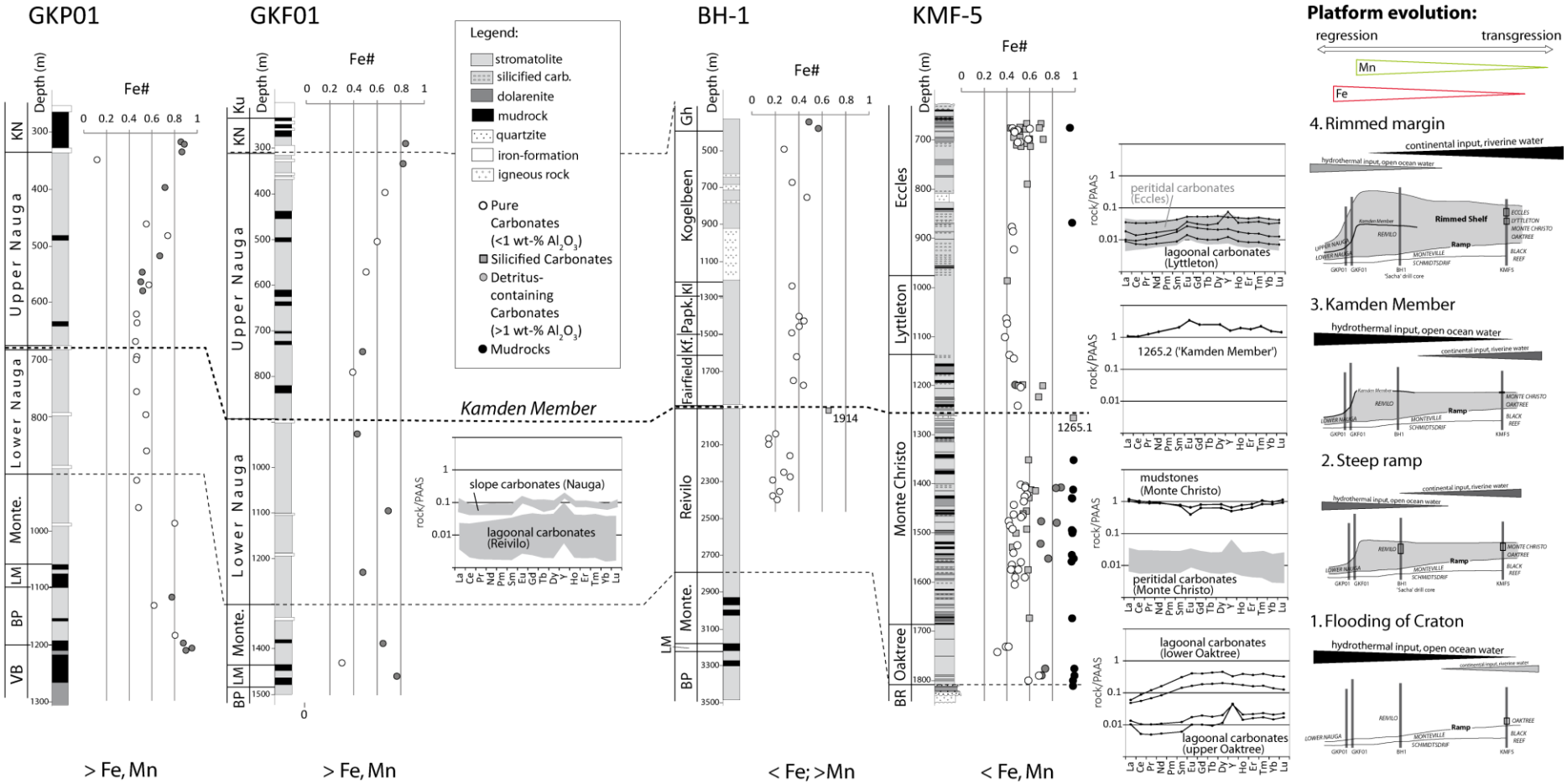

Figure 5-5: Fe# ([Fe_{tot}/(Fe_{tot}+Mn_{tot})]) and trace element data of slope and platform sediments and reveal a dependence on water depth and source water influx. Data of GKP01 and GKF01 are from Voegelin et al. (2010).

6. Reconstruction of the inorganic carbon pool and ecosystem of the CMCP

6.1. Indications for heterogeneous DIC pool in the shallow marine environment

Carbonates of the CMCP obtain some distinct $\delta^{13}C_{carb}$ values, depending on the depositional environment. Carbonates of the very shallow-marine platform facies (KMF-5) reveal an average $\delta^{13}C_{carb}$ signature of -0.38 ± 0.92 (2σ) ‰, and are somewhat isotopically heavier than the carbonates from the stratigraphically correlative lagoonal platform facies of -0.58 ± 0.80 (2σ) ‰ (BH-1) and slope facies of -0.70 ± 1.74 (2σ) ‰ (GKF01) and -0.54 ± 1.22 (2σ) ‰ (GKP01) (Fischer et al., 2009; Horstmann and Beukes, 2002 and this study). Thereby, the carbonates of KMF-5 follow an overall trend from bottom to top from ca. -1.2 ‰ towards heavier isotope signatures of ca. +0.2 ‰ (Fig. 6-1), and also the carbonates of BH-1 indicate such a trend from about -1.6 to +0.1 ‰, even though it is not very apparent. The deeper slope carbonates from the stratigraphically correlative successions of GKP01 and GKF01 lack this increasing trend but instead vary erratically between about -1.4 to +0.5 ‰, with various excursions to negative values (down to -3.7 ‰). Those excursions represent siderite-rich layers within the slope succession and are related to the deposition of siliciclastic mudrocks and discrete IF (Fig. 6-1). All four drill cores exhibit negative excursions related to the deposition of the hematite- and siderite-rich Kamden Member, where GKP01 shows values down to -1.0 ‰, GKF01 down to -7.1 ‰, BH-1 down to -2.4 ‰, and KMF-5 down to -3.2 ‰. Those negative excursions are induced during diagenetic microbial processes such as dissimilatory iron reduction (DIR), during which isotopically light organic material is likely oxidized to HCO_3^- and Fe(III)-(oxyhydr)oxides reduced to $Fe(II)_{aq}$ in the porewater, where it reacts to isotopically light Fe(II)-carbonate (Fischer et al., 2009; Heimann et al., 2010; Johnson et al., 2008a; Johnson et al., 2008b; Johnson et al., 2008c):

$$4Fe(OH)_3 + CH_2O + 3HCO_3^- \rightarrow 4FeCO_3 + 3OH^- + 7H_2O$$

The mild shift of Ca-Mg-carbonates towards isotopically heavier $\delta^{13}C_{carb}$ signatures in the platform interior from the lower CMCP to the upper part of the CMCP indicates an isotopic change of the dissolved inorganic carbon (DIC) pool in the shallow-marine environment, which was independent of the open ocean DIC pool. In order to test if this assumption is correct, a detailed analysis of the $\delta^{13}C_{carb}$ trends throughout the slope and the platform was conducted by generating histograms of the distribution of $\delta^{13}C_{carb}$ data in the single drill cores with emphasis on the lower CMCP (steep ramp architecture) and upper

CMCP (rimmed margin architecture). Results are displayed in Figure 6-1 and reveal some distinct patterns for slope and platform successions that support a heterogeneous DIC pool in the shallow-marine environment. During the deposition of the lower CMCP (Lower Nauga Formation), including the Kamden Member, the slope succession reveals mean values (with 2σ) of -0.5 ± 0.6 ‰ (GKP01) and -0.9 ± 2.5 ‰ (GKF01) and a wide distribution of $\delta^{13}C_{carb}$, where some excursions, in particular from the Kamden Member, tend to very light $\delta^{13}C_{carb}$ values and cause a high 2σ value (Figs. 6-1, 6-2). In the upper CMCP (Upper Nauga Formation), $\delta^{13}C_{carb}$ data (-0.6 ± 1.56 ‰ for GKP01 and -0.6 ± 1.08 ‰ for GKF01) are still widely distributed and negative excursions are more frequent. This coincides with the more frequent occurrence of mudrock layers in the upper Nauga Formation (Fig. 6-1), which contained organic carbon that likely fueled DIR-related diagenesis of Fe-(oxyhydr)oxides in the sediment and production of siderite with light $\delta^{13}C_{carb}$ signatures (Fischer et al., 2009; Heimann et al., 2010; Johnson et al., 2008b). The platform carbonate succession of the lower CMCP reveals similar observations with slightly lighter average $\delta^{13}C_{carb}$ signatures and an overall wider distribution than the upper CMCP, with BH-1 (Reivilo Formation) showing -0.7 ± 0.9 ‰ and KMF-5 (Oaktree and Monte Christo formations) showing -0.6 ± 0.8 ‰. The Oaktree and Monte Christo formations (KMF-5) contain mudrocks, which show bulk negative $\delta^{13}C_{carb}$ excursions down to -12.3 ‰ (Fig. 4-3), which might indicate oxidation of organic matter, however it is unclear whether this signal solely reflects siderite, since the bulk sample was analyzed and no distinctive siderite bands related to the mudrock layers were observed as in the slope succession (Fischer et al., 2009). This implicates that DIR processes were probably not as efficient in the platform interior as along the slope, potentially because not sufficient Fe-(oxyhydr)oxide was available. The carbonates of the upper CMCP, after the development of the rimmed margin, clearly show a different pattern than the Upper Nauga carbonates from the slope facies. In BH-1 (all formation from Fairfield to Gamohaan) $\delta^{13}C_{carb}$ data have a mean of -0.5 ± 0.62 ‰, a slight but clear tendency towards heavier values, no negative excursions and a more narrow distribution (Fig. 6-2). The carbonates of the upper CMCP in KMF-5 (Lyttleton and Eccles formations) show a shift in $\delta^{13}C_{carb}$ towards heavier signatures of 0.0 ± 0.5 ‰. Even though these shifts are slight, the different development of $\delta^{13}C_{carb}$ signatures in the slope and platform facies gives some indications for the environmental and maybe even the redox conditions.

The development of the CMCP from a steep ramp to a rimmed margin architecture influenced the relative input of water masses from the open ocean and the continent. This affected the trace element and Fe# signatures of the carbonates depending on their depositional environment (Fig. 5-5). The different development of $\delta^{13}C_{carb}$ signatures in the

slope and platform successions also seems to reflect an influence of this different platform architecture on the DIC pool of the shallow-marine environment. During earlier stages the steep ramp architecture allowed the exposure of the carbonates to open ocean water that is the largest carbon reservoir in the atmospheric-ocean system (Fig. 1-3) and would have mainly influenced the $\delta^{13}C$ signatures of the DIC. This is supported by similar mean $\delta^{13}C_{carb}$ signatures and distributions in the lower CMCP of slope and platform carbonates, whereby some negative excursion imply microbial-induced degradation of isotopically light organic matter (Fig. 6-2). During the rimmed margin stage the carbonates from the slope facies of the upper CMCP were still exposed to open ocean water and show similar $\delta^{13}C_{carb}$ values, distributions similar to the lower CMCP, and indications for organic matter degradation. The carbonates from the upper CMCP of the platform facies were less exposed to the open ocean water due to the development of the rimmed margin (Beukes, 1987; Sumner and Beukes, 2006) and the restricted conditions probably allowed a distinct development of the DIC pool within the very shallow environment, independent of the open ocean DIC pool. Since these carbonates record a shift towards heavier $\delta^{13}C_{carb}$ signatures (Fig. 6-2), it can be suggested that also the DIC pool from which they precipitated was isotopically heavier than coeval open ocean seawater. To explain this overall shift it is important to consider the timerange the upper CMCP represents. The platform was deposited over a timerange of about 80 Ma, and even though detailed age constraints of the single formations are still uncertain (Sumner and Beukes, 2006), the deposition of the upper CMCP took some tens of millions of years. Over such timescales the fluxes between the atmosphere-ocean system and the large sedimentary reservoirs of carbonate and organic carbon mainly influence the DIC pool (Fig. 1-3). Indeed, there is a change in organic carbon deposition along the CMCP. In the lower CMCP, mudrocks and some organic-rich carbonates from the slope reveal mean (with 2σ) TOC contents of 1.61 ± 1.70 wt.-% (GKP01) and 1.43 ± 2.52 wt-% (GKF01 – one excursion of 9.60 wt-%). In the platform facies TOC contents are even higher, showing values of 2.73 ± 4.02 wt-%. In the upper CMCP the TOC contents show a slight increase in the mean of GKF01 (1.84 ± 2.85 wt-%) and only a negligible decrease in GKP01 (1.52 ± 2.04 wt-%). The platform facies on the other hand shows a strong decline in TOC, coupled with a scarcity of mudrocks (Fig. 6-1).

The combination of higher TOC values along the slope and increase in deposition of mudrocks along the marginal slope environment, represented in GKF01, can be interpreted as an increasing burial of organic matter, which argues for enhanced primary production in the marine environment. In a detailed review of Des Marais (2001) about the carbon cycle during the Precambrian, it is shown that a shift from chemolithoautotrophy and anoxygenic photosynthesis to oxygenic photosynthesis would have induced a significant increase in

primary production. This is because chemolithoautotrophy and anoxygenic photosynthesis depend on electron donors like H_2, H_2S, or Fe^{2+} from reduced hydrothermal fluids, and estimates for the Precambrian range from 2 to 20 × 10^{12} mol/yr C from primary production via those pathways (des Marais, 1985; Turcotte, 1980). Oxygenic photosynthesis is independent of the availability and amount of reduced hydrothermal species and uses H_2O as electron donor, fueling primary productivity (modern rate in marine environment ~ 4000 × 10^{12} mol/yr C) (Field et al., 1998). The development of a rimmed margin and Fe# and trace element data implicate a reduced influx of hydrothermal fluids into the shallow-marine platform interior (Fig. 5-5). This probably reduced the activity of microorganisms depending on those reduced species and on the other hand allowed oxygenic photosynthesizers to dominate the ecosystem and increase the primary production (Des Marais, 2001). A shift to an aerobe ecosystem would also explain the low amount of organic carbon preserved on the platform facies of the upper CMCP, because the C budget of microbial mats containing cyanobacteria, is basically steady state in carbon fixation by primary production and carbon loss by heterotrophic respiration (Canfield and des Marais, 1993). The organic- and mudrock-rich slope facies on the other hand indicates that some organic material produced during enhanced primary production on the platform was transported via clay minerals to greater depths and deposited along the possibly more anoxic margin and slope of the CMCP (Klein and Beukes, 1989). This means that light ^{12}C was subsequently removed from the carbon pool of the shallow-water lagoon. Normally, the influx of fresh ocean water would balance this loss of ^{12}C by organic burial. However, since the rimmed margin architecture restricted this open ocean influx it is reasonable that the DIC pool in the shallow-marine environment became more and more depleted in ^{12}C and increased in its $^{13}C/^{12}C$ ratio. It is important to note that this increase is solely a local effect and does not reflect a global rise of $\delta^{13}C_{carb}$ like the Lomagundi-Jatuli Event (Karhu, 1993; Melezhik et al., 2007). There is no reported change in the global DIC pool during the Neoarchean (Krissansen-Totton et al., 2015), and the only reason why such a shift still can be observed in the carbonates of the upper CMCP is that the rimmed margin architecture allowed the development of special conditions, restricted to the very shallow-marine environment. Nevertheless, removal of organic carbon, an effective reductant, from the shallow-marine system does also mean an increase in the oxidation state (e.g. Garrels and Perry, 1974) and would therefore support the establishment of an oxygen oasis.

6.2. Signs of an aerobe ecosystem in the CMCP

Slope carbonates of the Lower and Upper Nauga formations show mean $\delta^{13}C_{org}$ signatures (with 2σ) of -31.5 ± 3.16 ‰ (GKP01) and -31.5 ± 4.0 ‰ (GKF01) (Fischer et al.,

2009; Horstmann and Beukes, 2002). Lagoonal carbonates show a mean of -30.2 ± 5.0 ‰, while peritidal carbonates (KMF-5) reveal with -25.8 ± 5.2 ‰ a shift to heavier signatures (Table 4-1, 4-2), although some carbonates might be altered and do not record pristine values (see detailed discussion in chapter 5.2.). Nevertheless, most carbonate signatures of organic material from the peritidal environment up to ~-25 ‰ still show a disordered structure and low carbonization (Figs. 4-5; 5-3), which might indicate a different ecosystem in the very shallow-marine environment.

Microorganisms kinetically fractionate C and produce organic material with very light $\delta^{13}C$ signatures that strongly vary, depending on the metabolic pathway (Figs. 5-3, 6-1) (for a review, see Hayes, 2001). Most of the carbonate and mudrock samples from the CMCP show signatures between -40 and -20 ‰. Assuming a marine DIC pool with a $\delta^{13}C$ signature of ~ 0 ‰, aerobe photoautotrophy (e.g., by cyanobacteria) would typically yield $\delta^{13}C_{org}$ signatures between -33 to -24 ‰, although those signatures can also be produced by some anaerobic bacteria such as photoferroautotrophic, sulfate-reducing, methanogenic and even methanotrophic bacteria (Thomazo et al., 2009 and references therein) (Fig. 6-1). However, evidence for dissolved oxygen in the shallow seawater of the Campbellrand-Malmani area, such as authigenic accumulation of redox-sensitive elements and the enrichment of carbonates and mudrocks in heavy stable molybdenum and nitrogen isotopes (Godfrey and Falkowski, 2009; Voegelin et al., 2010; Wille et al., 2007 and this study), and fossil biomarkers, in particular steranes (Waldbauer et al., 2009), makes a strong case for the existence of oxygen-photosynthesizers in marine microbial mats. This is further supported by slightly heavier $\delta^{13}C_{carb}$ signatures in the restricted platform facies that argues for an increasing oxidation state in the shallow-marine environment. Diminished ferrous iron delivery to shallow water, as indicated by trace element systematics and depth variant Fe concentrations of the carbonates (Fig. 5-5), would have favored enhanced activity of cyanobacteria, which are susceptible to ferrous iron toxicity (Swanner et al., 2015a) and would have restricted the activity of ferrous anoxygenic phototrophs. Mudrocks from the slope toward the shallow-water platform show a mean $\delta^{13}C_{org}$ value of ~-32 ‰ (Fig. 6-2), which indicates mainly heterotrophic respiration of photosynthetic mass. However, some negative excursions down to -40 ‰ and below (Fig. 6-1) argue for methane cycling or sulfate-reduction by an anaerobic microbial community within reducing sediments. Overall, $\delta^{13}C_{org}$ isotope signatures of carbonates along the CMCP show a dominance of photoautotrophic bacteria and heterotrophic respiration of the photosynthetic biomass, with the possibility of locally occurring anaerobic microbial activity in some mudrocks. Despite the possibility that some of these signatures might have been slightly shifted due to higher peak metamorphic temperatures, as indicated by Raman analyses (see chapter 5.2),

the range in $\delta^{13}C_{org}$ from ~ -40 ‰ in mudrocks to up to ~ -25 ‰ in peritidal carbonates cannot be explained by metamorphic overprinting but rather support a diverse ecosystem (Waldbauer et al., 2009) with a dominance of aerobic ecosystems in the platform's shallow waters. This is consistent with data from other Archean carbonate successions of Steep Rock (2.8 Ga, Canada) (Grassineau et al., 2006) and Hamersley Basin (2.6 Ga, Australia) (Eigenbrode and Freeman, 2006), which also contain sediments with similarly varying $\delta^{13}C_{org}$ values that point to a change from anaerobic to enhanced aerobic microbial activity on consolidated shallow marine platforms.

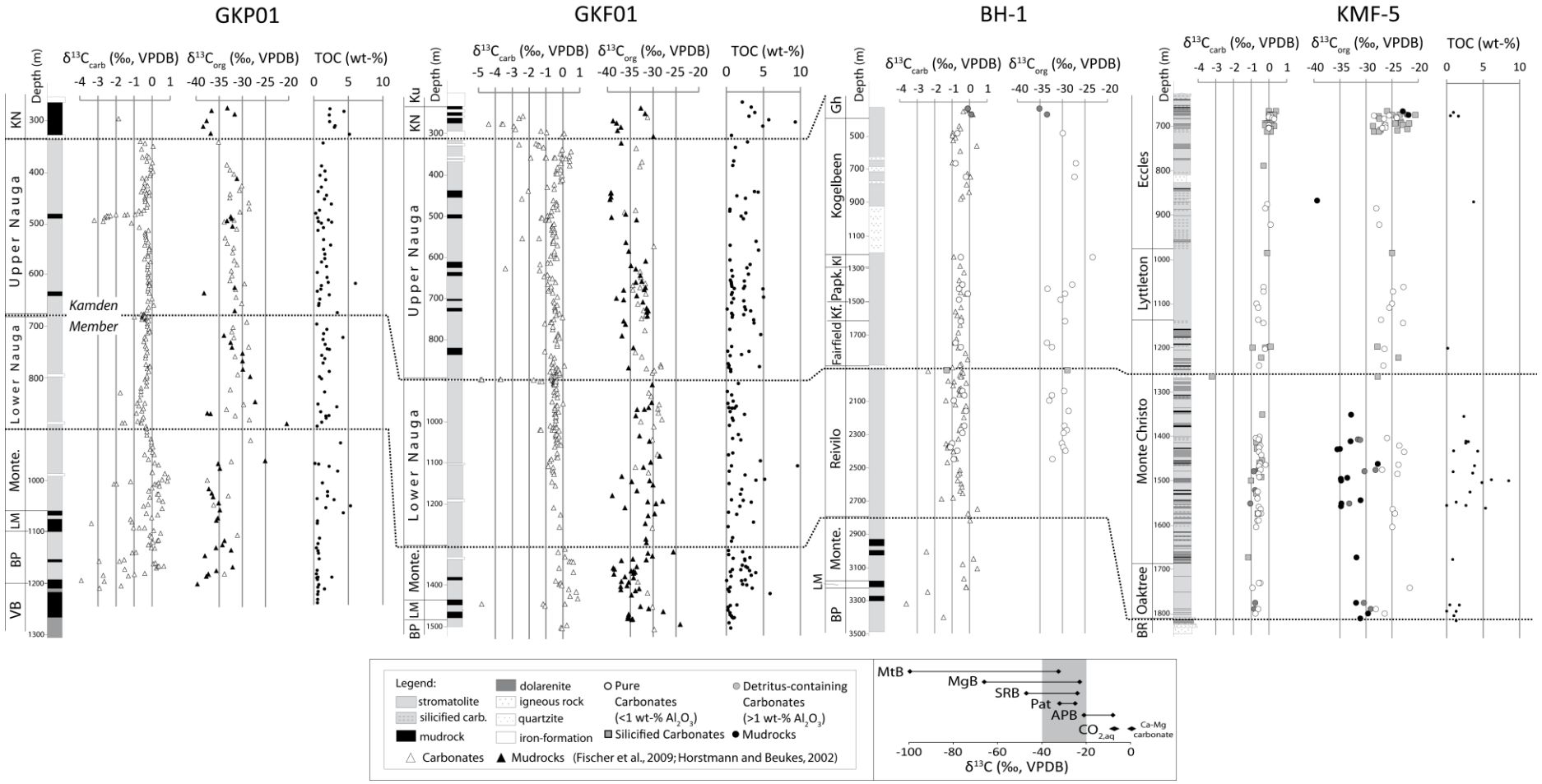

Figure 6-1: $\delta^{13}C_{carb}$, $\delta^{13}C_{org}$ and TOC data of carbonate and mudstone samples from GKP01 and GKF01 (slope) and BH-1 and KMF-5 (platform). Stratigraphy for GKP01, GKF01, and BH-1 is modified from Fischer et al. (2009). Black dashed lines mark the correlated sequences of all drill cores. Isotope data of GKP01, GKF01 and most of BH-1 are from Fischer et al. (2009) or are provided by Uwe Horstmann. The box included in the legend reflect the $\delta^{13}C$ isotope range of common marine microbial species, grey shaded area marks the range in which $\delta^{13}C_{org}$ data of CMCP samples fall (Thomazo et al. (2009) and references therein, relative to $CO_{2,aq}$. APB: anoxygenic photoautotrophic bacteria, Pat: photoautotrophic bacteria (e.g. cyanobacteria), SRB: sulfur-reducing bacteria, MgB: Methanogenic bacteria, MtB: Methanotrophic bacteria. (Formations: VB-Vryburg; BP-Boomplaas; LM-Lokamonna; Monte-Monteville; KN-Klein Naute; Ku-Kuruman; Fairfi.-Fairfield; Kf.-Klipfonteinheuwel; Papk.-Papkuil; K.-Klippan; Gh-Gamohaan; BR-Black Reef)

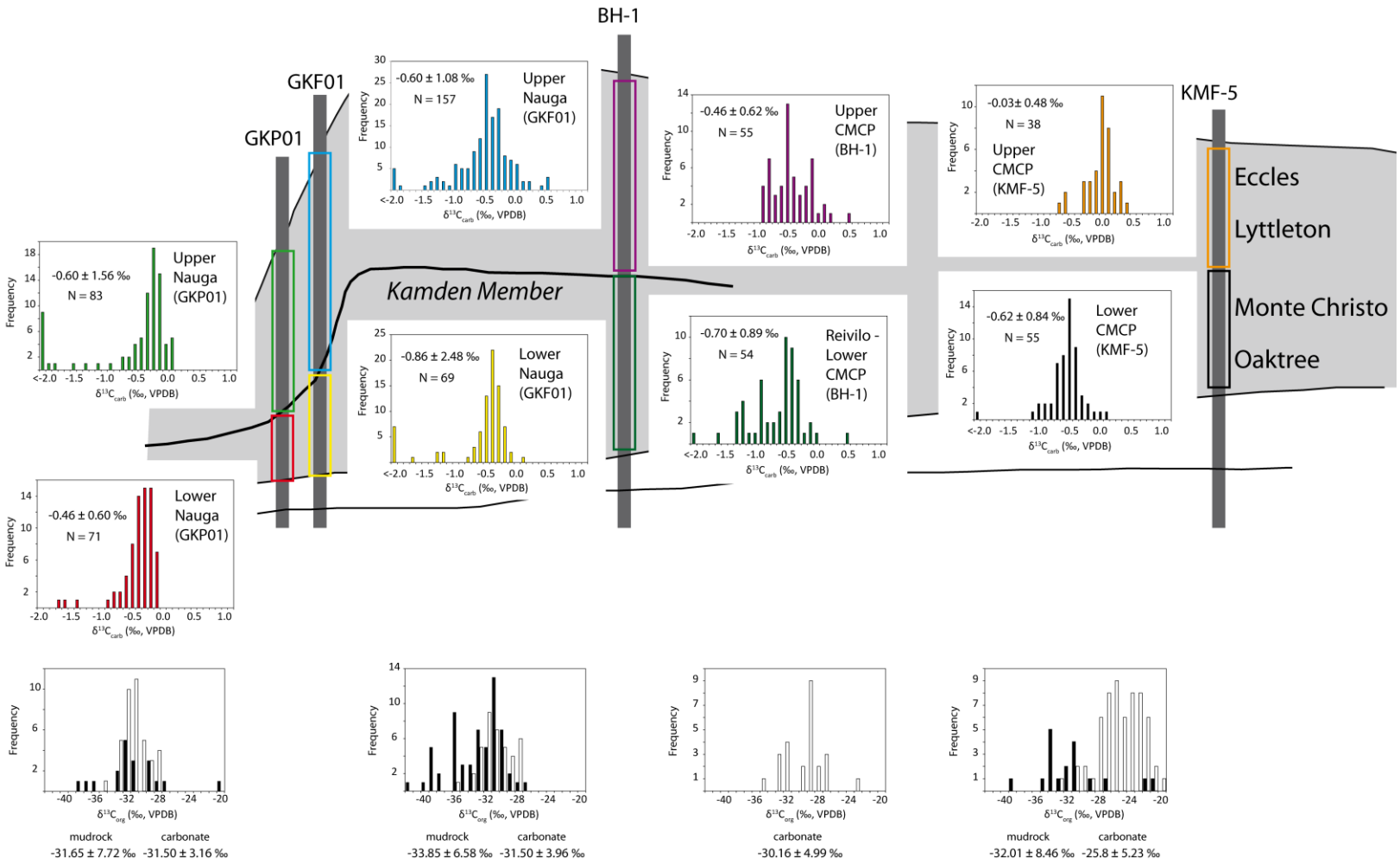

Figure 6-2: Histograms showing data distribution of $\delta^{13}C_{carb}$, $\delta^{13}C_{org}$ values from all slope and platform drill cores, with corresponding average and 2σ values. All data from GKP01 and GKF01, and most $\delta^{13}C_{carb}$ data of BH-1 are from Fischer et al. (2009) and Horstmann and Beukes (2002).

7. Molybdenum isotope systematics of the CMCP

7.1. Objectives

Redox changes of the atmosphere-hydrosphere system over geological times should perturb the marine Mo isotopic cycle by introducing heterogeneities in different sedimentary redox regimes (Fig. 1-4). This should result in an evolution of the seawater δ^{98}Mo value, which can be mirrored in black shales precipitated within an euxinic setting. Several studies suggest the build-up of small amounts of free oxygen before the GOE, based on fluctuations of Mo concentrations and isotopic compositions of Archean chemical sediments (Anbar and Rouxel, 2007; Duan et al., 2010; Planavsky et al., 2014; Voegelin et al., 2010; Wille et al., 2007).

It has been suggested that non-skeletal marine carbonates also might mirror the Mo isotopic composition of the ambient seawater and thus provide another viable rock archive to reconstruct the redox-evolution of the hydrosphere-atmosphere system over Earth's history through variations in seawater δ^{98}Mo values (Voegelin et al., 2010; Voegelin et al., 2009). Particularly, Voegelin et al. (2010) found shifts towards heavy δ^{98}Mo values in carbonates from drill core samples of the 2.6 to 2.5 Ga old Ghaap Group of the Griqualand West Basin (South Africa), which were suggested to result from changes in redox-conditions of the ambient environment, such as fluctuations in free atmospheric oxygen at that time. Contemporaneous black shales from the same drill cores follow an overall increasing trend in δ^{98}Mo up section, corroborating the interpretation of gradually rising atmospheric oxygen during this time (Wille et al., 2007). There are several advantages to exploring the carbonate record of Mo, if these sediments are indeed high fidelity records of the seawater Mo reservoir. Carbonates are deposited over a much wider range of sedimentary environments than black shales, which are deposited under specifically reducing conditions. Carbonates are also well preserved in sedimentary successions as far back as the Archean and would allow a broader sample spectrum over time compared to black shales deposited within euxinic settings. As they were formed in oxygen-producing, shallow environments they could be used as a direct proxy for the Precambrian Mo seawater composition as well as possible indicator for local O_2 fluctuations (Voegelin et al., 2009). Yet, it requires evaluation whether redox changes of seawater or the atmosphere are the only significant parameters impacting the Mo record in the carbonates or if the changing depositional environment and early diagenetic redox processes within the sediment could also have a major effect.

Therefore, carbonate and mudrock samples from the CMCP were analyzed for their Mo isotope chemistry. In contrast to a previous study investigating the Mo isotopic

composition of deeper platform settings from the Griqualand West basin (Voegelin et al., 2010), samples from this study are from the shallow shelf part of the platform, which eliminates the influence of strong sedimentary perturbations that are typical for a slope area (Schroeder et al., 2006). The goals are 1) to verify whether there is a correlation between the Mo isotopic composition of the carbonates and their depositional depth or environment, 2) to utilize Mo isotopes to interpret the chemical setting of the shallower Neoarchean Ocean, and 3) to evaluate the extent to which diagenetic and biological factors impact the sedimentary geochemical signals of carbonates. To do so, Mo concentrations and δ^{98}Mo values from closely spaced samples were combined with geochemical characteristics, stratigraphy and sedimentological observations.

7.2. Mo geochemistry of the platform succession

Earlier studies combining Mo concentration and Mo isotope composition of the CMCP are provided by Wille et al. (2007) and Voegelin et al. (2010), on mudrock and carbonate samples from GKP01 and GKF01 (Schroeder et al., 2006), representing slope to basinal sedimentary rocks (Figs. 2-1, 2-2). In Figure 7-1 δ^{98}Mo spectra and isotope signatures are combined for the entire CMCP succession. Comparison of the data from deeper platform sediments with our results from shallower platform sediments reveals some inconsistencies. Molybdenum isotopic signatures in the carbonaceous mudrocks, for instance, show decreasing values upsection from the Oaktree to the Eccles formations, which is the opposite pattern described for the mudrock samples of the slope succession (Wille et al., 2007). Our Mo isotopic values of carbonates along the Malmani succession fluctuate in the same range as the data presented by (Voegelin et al., 2010). However, our high-resolution measurements from even single increments of sedimentation span the range of Mo isotopic compositions observed throughout the entire KMF-5 and the Agouron cores (Voegelin et al., 2010; Wille et al., 2007). An example of these small-scale spatial stratigraphic variations is supplied by a ~15 cm long carbonate section of the Monte Christo Formation in KMF-5 (Fig. 7-1). It displays significant lithological differences from oolitic dolomite structures (1574.3) as well as domal (1574.25) and fine-grained areas (1574.2 and 1574.15), indicating a change of depositional conditions influencing abiogenic carbonate formation. These short-term changing depositional conditions result in varying TOC of 0.01 - 0.03 %, Mo concentrations of 15-26 ppb, and δ^{98}Mo from +0.40 to +0.87 ‰, respectively, with heavier Mo isotopic compositions occurring in one organic rich layer (1574.2). This single sample from the KMF-5 core reveals that the carbonates most likely not only reflect the Mo isotopic composition of the ambient seawater, but rather, that local environmental redox fluctuations within the sediment affected the primary Mo isotope signals.

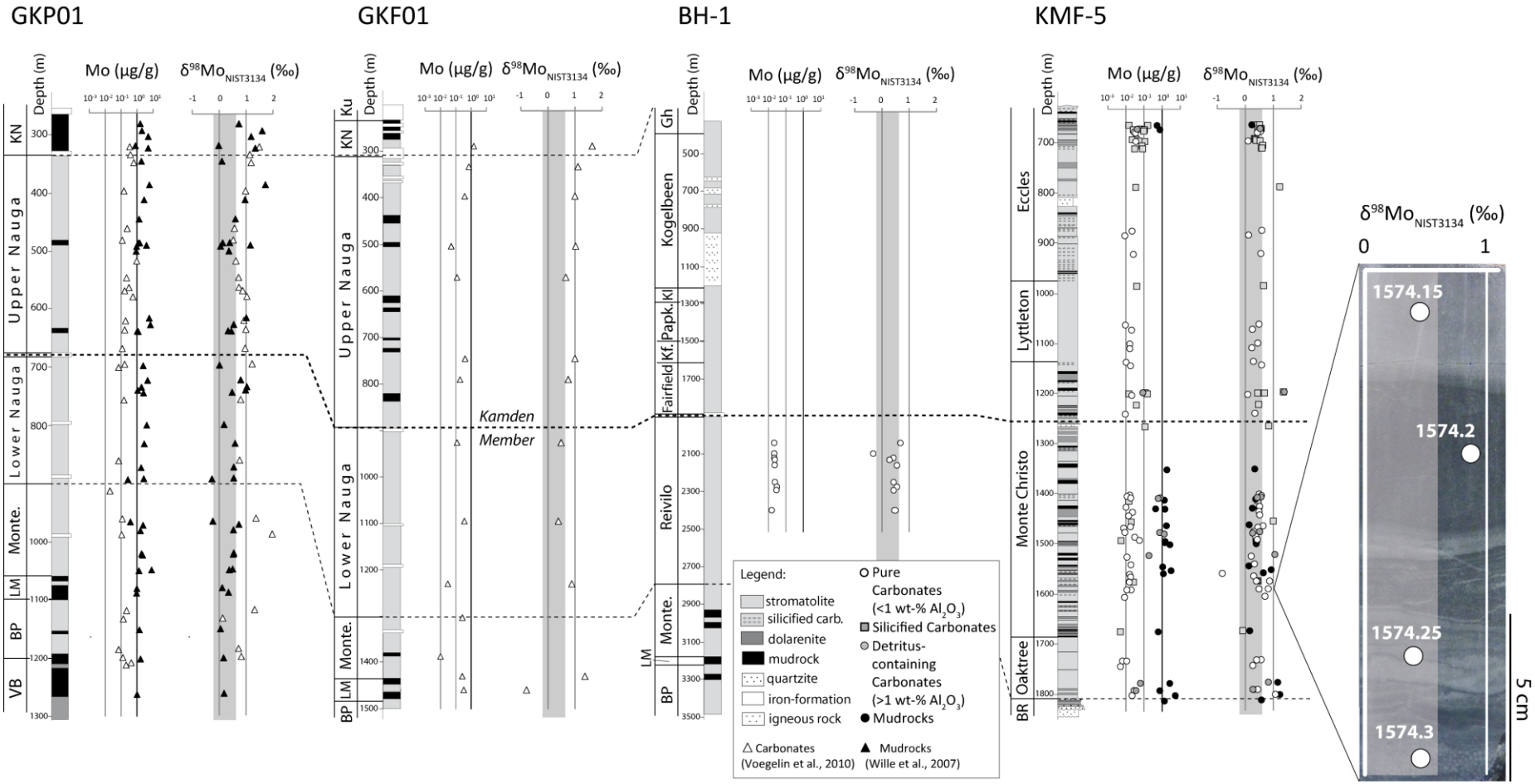

Figure 7-1: Mo concentrations and isotopic compositions of carbonates and mudrocks from KMF-5, BH-1 (platform succession), GKP01, and GKF01 (slope succession (Voegelin et al., 2010; Wille et al., 2007)). Picture of a 15 cm long hand-specimen from the Monte-Christo Formation is shown on the right, together with measured δ^{98}Mo values. Shaded area at δ^{98}Mo columns indicates the range of continental signatures from -0.2 to +0.6 ‰ (Voegelin et al., 2014), Mo concentration of PAAS as detrital component is 1 µg/g (Taylor and MacLennan, 1985). Dashed black line shows stratigraphical relation of formations which belong to the Campbellrand-Malmani slope-platform succession (Sumner and Beukes, 2006). Thicker dashed line indicates Kamden Member. Abbreviations of Formations: VB: Vryburg; BP: Boomplaas; LM: Lokamonna; Monte.: Monteville; KN: Klein Naute; Kf.: Klipfonteinheuwel; Papk.: Papkuil; Kl: Klippan; Gh: Gamohaan; BR: Black Reef

Therefore, a possible correlation between the Mo concentrations and isotopic compositions with the Al_2O_3 and TOC content of carbonates and mudrocks was examined (Fig. 7-2). Mo concentrations clearly correlate with Al_2O_3, the latter used as proxy for the detrital input (Fig. 7-2 a). Detritus-containing samples yield Mo concentrations of up to 1 µg/g, corresponding to PAAS (Taylor and MacLennan, 1985). However, detrital input does not seem to be the only contributor of Mo to carbonates and mudrocks. In pure and silicified carbonate samples with Al_2O_3 values below 0.10 wt-%, authigenic enrichment seems to dominate the detrital contribution, as these samples plot above the "PAAS-line" (Fig. 7-2 a). Authigenic enrichment, scavenging Mo, can also be assumed for seven mudrock samples (1499.85, 1544.1, 1551.7, 1557.7, 1673.3, 1776.0, and 1800.3), which have higher Mo/Al_2O_3 ratios (0.107 to 0.269) than the rest of the mudrock samples with Mo/Al_2O_3 ratios (0.042 to 0.089) similar to PAAS (0.053). Furthermore, in agreement with the data of Wille et al. (2007), a weak correlation between TOC and Mo contents (Fig. 7-2 b) and no correlation between TOC and $\delta^{98}Mo$ signatures can be observed. This can be likely explained by scavenging of Mo on organic matter (McManus et al., 2006), yet the Mo isotopic signature is obviously not solely affected by this parameter (Wille et al., 2007). Overall the same Mo isotopic spread in three of the four formations exposed in KMF-5 can be observed, which is independent of the lithology of the samples (Fig. 7-2 c) or of any mixed isotope signals caused by two different reservoirs (Fig. 7-2 d). This supports our proposition that while redox changes of the water column can be responsible for the observed $\delta^{98}Mo$ variability, the Mo isotopic signatures are likely also influenced by local sedimentary processes.

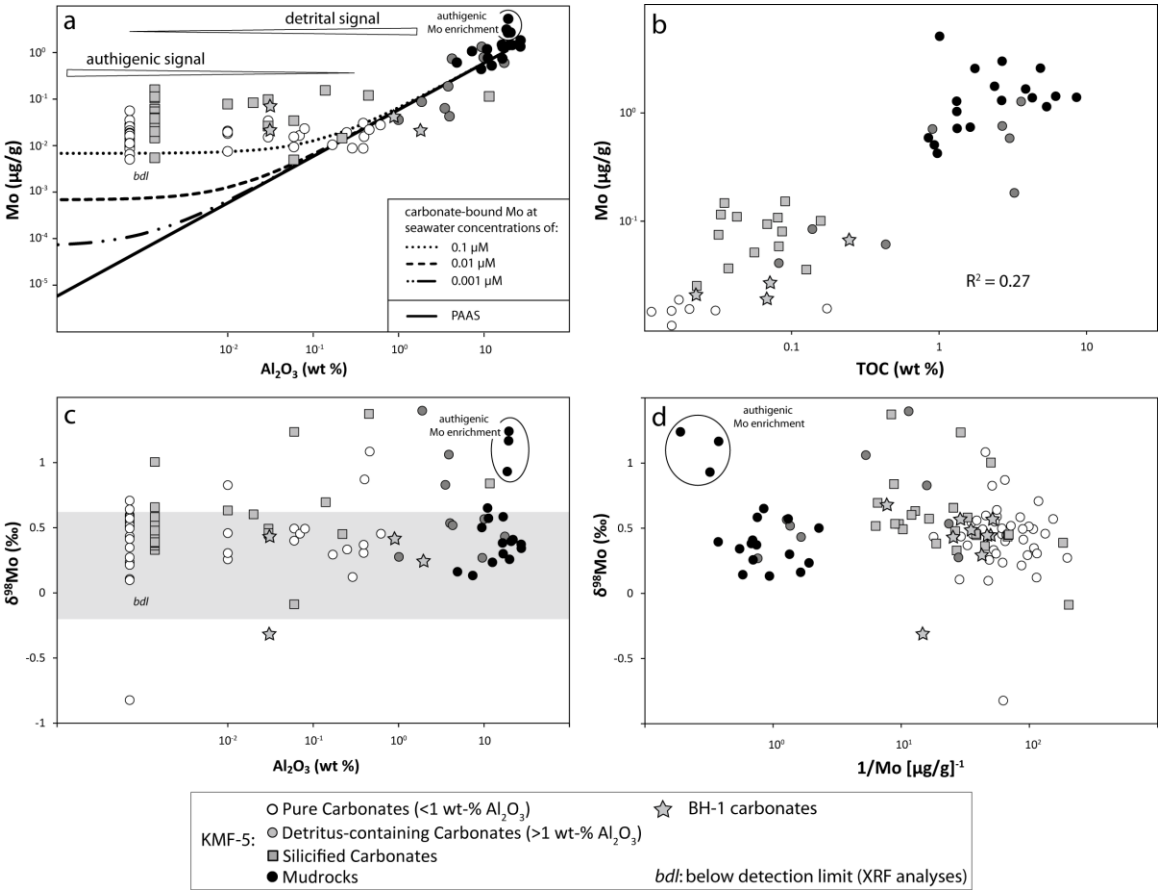

Figure 7-2: (a) – (d) Mo concentration and isotopic composition vs. Al_2O_3 and total organic carbon (TOC) content. (a) Predictions of Mo added by incorporated into marine abiogenic carbonates via sorption from seawater for a range of seawater Mo concentrations. Dotted curves are modeling carbonate-bound Mo directly adsorbed from seawater, based on experiments performed by S. Goldberg (personal communication; Appendix), and for different Mo concentrations of seawater (average modern seawater: 0.1 µM (Collier, 1985); estimated average Neoarchean seawater: 0.001 µM (Czaja et al., 2012; Duan et al., 2010) to 0.01 µM (Dahl et al., 2011; Scott et al., 2008)); Mo/Al_2O_3 ratio of PAAS is 0.053 (Taylor and MacLennan, 1985). (b) Weak correlation between Mo and TOC contents (R^2 =0.27). (c) All lithologies show δ^{98}Mo signatures heavier than continental crust. Three mudrock samples (1551.7,1776.0, and 1800.3) showing authigenic Mo enrichment combined with heavy δ^{98}Mo signatures. Shaded area indicates the range of continental δ^{98}Mo signatures from -0.2 to +0.6 ‰ (Voegelin et al., 2014). (d) No clear correlation between 1/Mo and Mo isotopic composition indicates that there was no mixture between different Mo reservoirs, which could explain the isotope signatures.

7.3. Mo systematics in carbonates, tidal flat systems, and microbial mats

7.3.1. Marine carbonates as archive of seawater Mo

Based on the Mo isotopic composition of modern oolitic samples, it has been suggested that non-skeletal abiogenic carbonates can mirror the Mo isotopic composition of contemporary seawater (Voegelin et al., 2009). However, under marine pH conditions of 8.2 the very low adsorption coefficients of Mo onto carbonates (Goldberg et al., 1996) results in a low Mo concentration within these modern oolitic samples compared to other marine sedimentary reservoirs. This raises the question of whether Mo isotope variations in platform carbonates are a good archive for seawater Mo and suitable for environmental paleo-reconstruction.

Adsorption experiments of Mo from a stock solution on synthetically manufactured carbonate (Goldberg, pers. comm.; Appendix) show enhanced Mo adsorption with decreasing pH. These results cannot be directly applied to Mo adsorption on natural carbonates in a marine environment, as natural carbonates have a much smaller surface area and batch experiments were set up with an enriched and finite soluble Mo reservoir compared to modern seawater (Goldberg, pers. comm.). However, linear extrapolation of Mo adsorption of these batch experiments to modern Mo seawater concentration of 0.1 µM will result in about 10 ng/g adsorbed Mo on carbonate, which is in agreement with measured 18 and 38 ng of adsorbed Mo per gram $CaCO_3$ of modern ooids formation from the Bahamas (Voegelin et al., 2009). This indicates that the Mo concentration on primary precipitated, unaltered, biogenic carbonates is mainly dependent on the Mo concentration of the surrounding aqueous solution from which the carbonate will form, providing that the pH is constant (Fig. 7-2 a; Appendix). Seawater Mo concentration during the Neoarchean is assumed to range from ~0.001 µM (Czaja et al., 2012; Duan et al., 2010) to ~0.01 µM (Dahl et al., 2011; Scott et al., 2008) with an Archean shallow water pH value similar to that of the modern oceans (Beukes and Gutzmer, 2008). Integration of these two Mo concentration estimates of Neoarchean seawater into our adsorption calculations yield values between about 0.1 and 1 ng/g of adsorbed Mo on carbonates. These values are much lower than measured concentrations in Malmani pure carbonate samples (18 ± 19 ng/g for pure carbonates; Fig. 7-2 a). It should be noted that a difference between the pH of the Neoarchean ocean (± 7.8) and the modern ocean (± 8.2) would not shift these results significantly. Hence, a significant amount of Mo within the analyzed carbonates must have been added by secondary processes, which overprint the original primary Mo seawater signal of the carbonates. As these processes affected the Mo content they might also have affected the Mo isotopic composition. In the following section, several possibilities for likely processes are discussed.

7.3.2. Direct adsorption of Mo on organic matter

Organic matter can scavenge molybdate (Head and Burton, 1970; Helz et al., 2011) and can act as an important sink for Mo (Dellwig et al., 2007). Temporary Mo fixation on organic aggregates in oxygen-depleted zones within tidal flat sediments and a subsequent release of Mo due to decomposition of these organics causes a non-conservative behavior of Mo in shallow waters (Dellwig et al., 2007). A weak correlation between Mo concentration and TOC content of the Malmani samples (Fig. 7-2 b), points to a coupled enrichment process of both Mo and organics within the carbonates. The preferential adsorption of isotopically light Mo isotopes on organics can lead to a significantly lighter isotope signal of

organically bound Mo compared to seawater Mo ($\Delta^{98}Mo_{seawater\text{-}organics}$ of up to +1.0 ‰; (Kowalski et al., 2013). This mechanism could have resulted in a depleted Mo isotopic composition of our sediment samples compared to the contemporary ambient seawater and could therefore explain their variable Mo isotopic composition (Fig. 7-3). A flux of organic compounds to carbonates is often associated with deposition of suspended particulate matter (SPM) and other detrital material, like clays (Kowalski et al., 2013; Potter et al., 2005). This detrital pathway can imitate authigenic Mo enrichment from seawater, which results in the Mo-TOC relationship seen in modern euxinic sediments (Algeo and Lyons, 2006; Naegler et al., 2011). For the data set of this study, it rather reflects varying contribution of Mo from lithogenic particles than Mo scavenging from sea-/ pore water. When only pure and silicified carbonates are considered, no correlation between TOC and Mo is observed. Also, the Mo isotopic compositions do not show any dependence on the presence or abundance of detrital (Fig. 7-2 c) or organic compounds or even with a certain rock type, as all of them show the same isotopic spread in $\delta^{98}Mo$. Most Mo isotope signatures show upper continental crust signatures (Fig. 4-6, 7-2 c). However, carbonates that are associated with mudrocks with a heavy $\delta^{98}Mo$ signature are also heavier and vice versa. Interestingly, three of the mudrock samples (1551.7,1776.0, and 1800.3) with the highest Mo contents also have the heaviest $\delta^{98}Mo$ values, all of them deposited in the lower section of the Malmani Subgroup (Fig. 7-2 c). This points to a rather indirect relationship between TOC and authigenic Mo accumulation possibly derived by early diagenetic processes.

7.3.3. Early diagenetic redox cycling within the sediment

The settling of organic matter will drive early diagenesis within the sediment with in-vivo organisms using different oxidants. These organisms re-mineralize organic matter with oxidants available according to the free energy yield of these reactions (Martin and Sayles, 2003). Therefore, in modern sediments, aerobic respiration first consumes free oxygen until pore water O_2 concentrations are virtually zero. Once all free oxygen is consumed, oxidants, such as nitrate or Mn(III/IV)-oxides, are used, followed by Fe(III)-oxides and sulfate. This successive consumption of different oxidants results in a vertical redox zonation within the sediment, with corresponding stratification in the pore water chemistry (Froelich et al., 1979). The occurrence and vertical extent of this different redox zonation is dependent on the depositional environment, which can have different bottom water oxygen concentrations, sediment accumulation rates, sediment composition and physical properties such as grain size, porosity and permeability. Utilizing the concepts of modern, early diagenetic sedimentary redox zonation within the framework of the Neoarchean Malmani carbonate formation, Mo concentrations and isotopic compositions in

shallow water chemical sediments are mainly governed by oxic and anoxic mechanisms of precipitates and pore fluids (Brucker et al., 2009; McManus et al., 2002; Scott and Lyons, 2012). Mo isotopic fractionation due to adsorption of soluble Mo on Mn-oxides, as it is common today, can be ruled out, as the redox conditions were insufficiently oxygen-rich to oxidize Mn, as is indicated by the lack of Mn-O layers deposited during that time. Therefore, it is likely that mainly redox processes involving Fe and sulfur cycling led to the fractionation of Mo and that the extent of suboxic to anoxic conditions within the sediment affected its Mo isotopic composition. Early diagenetic effects on Mo in modern, carbonate-rich sediments lead to Mo concentrations between 99 – 170 ppb with corresponding δ^{98}Mo isotope ratios of 1.07 to 1.24 ‰ at pore water H_2S concentrations of 3-30 µM (Romaniello et al., 2016). These higher Mo concentrations and lighter δ^{98}Mo isotopic values compared to modern ooids samples from the Bahamas (Voegelin et al., 2009) indicate that scavenging of Mo and the offset of Mo isotope composition from seawater signal is strongly dependent on depositional environment in terms of pore water sulfide and organic content (Algeo and Lyons, 2006; Erickson and Helz, 2000; Helz et al., 1996; Romaniello et al., 2016). These observations indicate a strong dependence of the Mo behavior on dissolved sulfide concentrations, and thus a dependence on early diagenetically mobilized pore fluids, which can easily overprint the isotopic information of the primary absorbed Mo in abiogenic carbonates (Fig. 7-3). Varying depositional environmental settings accompanied by Malmani carbonate formation changed the extent of vertical sedimentary redox zonation and dissolved sulfide concentrations of pore water, leading to changing Mo mobility within the sediment. Here, mudrocks are of particular interest because they contain much more Mo than carbonates, and may be a source of Mo for these carbonates during early diagenesis. Chemical exchange between carbonates and mudrocks is indicated by the Fe enriched carbonates of the shallower Eccles and the Monte Christo formations.

7.3.4. Biological effect on Mo in microbial mats

Apart from early diagenetic redox cycling fueled by organic matter sinking down to mudrocks in the water column, degradation of organics in microbiological mats could have a similar influence on early sediment redox cycling and therefore authigenic Mo accumulation. Stromatolites are laminated deposits of lithifying microbial mats and consist of Ca(Mg)-carbonate containing varying amounts of trapped and bound sediment (Burne and Moore, 1987; Dupraz and Visscher, 2005; Riding, 1991). Carbonate precipitation of microbial mats is biologically induced (organo-mineralization), which has a strong environmental dependence (e.g. pH, temperature, pressure, alkalinity, salinity), making

microbialites a useful proxy for paleo-reconstructions (e.g. Kamber et al., 2004; Kamber and Webb, 2001; Riding, 2011).

Marine microbial mats are a few cm thick and contain a variety of carbonate-precipitating and -dissolving species driven by microbial metabolic processes that cause a geochemical gradient within the mat (Dupraz and Visscher, 2005). The mats are bound by extracellular polymeric substances (EPS), which consist of sugar and protein that are involved in precipitation of calcium carbonate by serving as a physical template of Ca^{2+} cations and carboxyl groups (Dupraz and Visscher, 2005). Oxygen-producing cyanobacteria generally only inhabit the top mm of the mat, while the lower layers are dominated by anaerobic microorganisms, such as anoxygenic phototrophs and sulfate reducing bacteria (SRB). The different biogeochemical reactions cause fluctuations of oxygen, sulfide and pH within the mat that generally occur on diel cycles (Dupraz and Visscher, 2005).

Although Mo might be directly adsorbed onto $CaCO_3$ precipitated within microbial mats, redox changes during lithification might affect Mo behavior to a greater extent than adsorption. The majority of the mat contains anoxic microorganisms, such as SRB, which are capable of H_2S production. H_2S consumes OH-, which drives the pH down and enhances Mo sorption, which makes it very probable that biological sulfur cycling had a strong impact on Mo signatures in stromatolitic carbonates (Fig. 7-3).

Modern microbial mats from a hypersaline environment show an extreme enrichment of Mo compared to the crustal background (Valdivieso-Ojeda et al., 2014). Molybdenum adsorption on Mn oxides in the uppermost oxic zone has been proposed as a first authigenic Mo enrichment process from seawater. Dissolution of these oxides under anoxic conditions within the mat liberates Mo, which is subsequently scavenged by SRB-produced H_2S. Although the Mo cycling in microbial mats of an open marine Neoarchean environment would have been different to a hypersaline environment, it is very likely that a similar process of Mo scavenging and liberation during degradation occurred in the Neoarchean microbial mats.

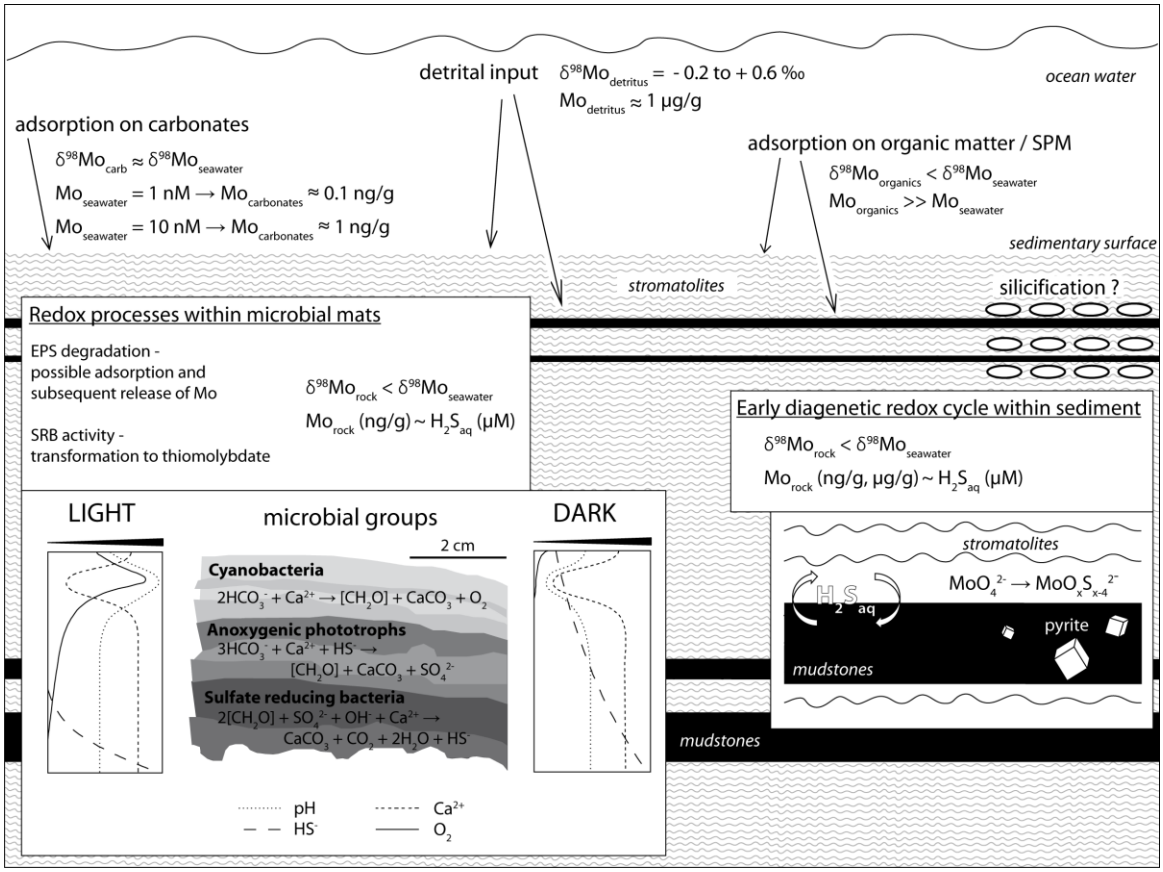

Figure 7-3: Summary of possible processes during adsorption and early diagenesis on Mo content and isotopic signature in Malmani carbonates and mudrocks (Algeo and Lyons, 2006; Collier, 1985; Czaja et al., 2012; Dahl et al., 2011; Dellwig et al., 2007; Dupraz and Visscher, 2005; Erickson and Helz, 2000; Goldberg, pers. comm.; Helz et al., 1996; Kowalski et al., 2013; Romaniello et al., 2016; Scott et al., 2008; Voegelin et al., 2014). Figure of metabolic pathways and geochemical gradients is modified after Dupraz and Visscher (2005).

7.4. Implications for Mo isotope signatures of Neoarchean shallow seawater

The Kaapvaal and Pilbara Cratons are interpreted as parts of the same epicontinental sea in the Neoarchean (Cheney, 1996; de Kock et al., 2009), and the δ^{98}Mo values preserved in their carbonates might be well suited to reconstruct the Mo isotopic composition of the contemporaneous seawater. A direct temporal δ^{98}Mo correlation of the shallow water TA samples (this study) with the deep water samples of the GWA (Voegelin et al., 2010; Wille et al., 2007) and samples from the Pilbara Craton is difficult due to missing stratigraphic markers throughout these basins and poor age constraints. Nevertheless, the heaviest δ^{98}Mo values presented in this study are up to +1.40 ‰ and in a similar range as values from samples of GKP and GKF from the GWA (Fig. 7-1). In the latter area the mudrock samples yielded δ^{98}Mo values of up to +1.72 ‰ (Wille et al., 2007) and are in good agreement with corresponding carbonate samples from the same drill cores with values up to +1.64 ‰ (Voegelin et al., 2010). Furthermore, the Neoarchean Mount McRea Shale from the Pilbara Craton in Australia yielded δ^{98}Mo values of up to +1.86 ‰, and is correlative with the upper Nauga Formation of the Kaapvaal Craton (Duan et al., 2010). Therefore, heavy Mo

isotopic signatures from carbonates of the TA are interpreted as a minimum value for Neoarchean seawater, as was already suggested in the previous studies of mudrocks and carbonates from the Pilbara Craton and the Griqualand West Basin of the Kaapvaal Craton (Duan et al., 2010; Voegelin et al., 2010; Wille et al., 2007). This study also reinforce the assumption that free atmospheric oxygen caused oxidative weathering on the continents, resulting in the built-up of a heavy oceanic Mo reservoir at that time (Anbar et al., 2007).

8. Iron speciation and isotope systematics of the CMCP

8.1. Objectives

The concentration of Fe in seawater over Earth's history largely depends on the ocean's redox state and is linked to the emergence of oxygenic photosynthesis and the GOE about 2.33 Ga ago (Luo et al., 2016). The deposition of mixed-valence Fe minerals in iron formations (IF) (Fig. 8-1 a) during the Precambrian strongly indicates that seawater had significantly higher concentrations of well-soluble $Fe(II)_{aq}$ compared to the modern ocean and that $Fe(II)_{aq}$ was removed from seawater by oxidation to form poorly soluble Fe(III) particles via photosynthetically produced oxygen (Cloud, 1968; Isley and Abbott, 1999). Alternatively, anaerobic oxidation of $Fe(II)_{aq}$ by photoautotrophic bacteria has been postulated as a way of generating Fe(III)-minerals for IF (Crowe et al., 2008; Garrels and Perry, 1974; Kappler et al., 2005; Konhauser et al., 2002). In the modern oxygenated ocean, $Fe(II)_{aq}$ concentrations are normally between 0.05 and 2 nM (e.g. de Baar and de Jong, 2001; Landing and Bruland, 1987; Martin et al., 1990) and are much lower than estimates for the Neoarchean anoxic ocean, ranging from 40 to 120 µM (Canfield, 2005). These calculations are based on the solubility product of siderite and calcite under the assumption of oversaturation and direct precipitation of those two minerals from seawater (Holland, 2004). Herzog et al. (1989) showed that at $Fe(II)_{aq}$ concentrations higher than 10 µM, aragonite and siderite would co-precipitate and calcite precipitation inhibited. Riding et al. (2014) thus proposed that $Fe(II)_{aq}$ concentrations in the shallow-marine environment reached levels below 10 µM to allow calcite precipitation. However, recent studies strongly suggest that siderite was rather formed secondarily within the sediment during diagenesis (Fischer et al., 2009; Heimann et al., 2010; Johnson et al., 2003; Johnson et al., 2008b; Johnson et al., 2013), questioning siderite saturation in seawater as a valid assumption of Fe concentration estimates.

The peak of IF deposition between 2.9 and 2.3 Ga coincides with a period of highly variable $\delta^{56}Fe$ signatures in Fe-(oxyhydr)oxides, -sulfides, and -carbonates, bulk IF, bulk mudrocks, and Ca-Mg carbonates, with excursion down to -3.68 ‰ (Fig. 8-1 b) (e.g. Czaja et al., 2012; Heimann et al., 2010; Johnson et al., 2003; Johnson et al., 2008c; Planavsky et al., 2012; Rouxel et al., 2005; Steinhoefel et al., 2010; Yamaguchi et al., 2005). Although peak IF deposition nearly coincides with the GOE, the occurrence of IF and deposition in shallower water must have occurred ~500 Ma earlier and overlaps within the suggested time-range for the onset of oxygen production by oxygenic photosynthesis, represented by the chemical equation

$$H_2O + CO_2 + h\nu \rightarrow CH_2O + O_2$$

in the shallow-marine environment (Fig. 1-1) (e.g. Anbar et al., 2007; Crowe et al., 2013; Frei et al., 2009; Kurzweil et al., 2015; Voegelin et al., 2010; Wille et al., 2007 and this study). Abiological partial oxidation of anoxic and iron-rich (ferruginous) deep seawater along a vertical chemical gradient (chemocline) by oxygen in surface waters according to $4Fe^{2+}_{aq} + O_2 + 8OH^- + 2H_2O \rightarrow 4Fe(OH)_3$

would lead to the precipitation of isotopically heavy $Fe(III)_{ppt}$ precipitates, and leave the remaining dissolved $Fe(II)_{aq}$ pool isotopically lighter (Rouxel et al., 2005). The isotopically light $Fe(II)_{aq}$ could then be recorded in marine sediments via precipitation of Fe(II)-sulfides and -carbonate minerals. Anaerobe biological Fe(II) oxidation by photoferrotrophs, $4Fe^{2+}_{aq} + HCO_3^- + 10H_2O + hv \rightarrow 4Fe(OH)_3 + CH_2O + 7H^+$

(Hegler et al., 2008) shows a similar fractionation factor $\varepsilon Fe(III)_{ppt}$-$Fe(II)_{aq}$ of 1-3 ‰ and is thus indistinguishable from aerobe oxidation (Balci et al., 2006; Beard et al., 2003a; Bullen et al., 2001; Croal et al., 2004; Kappler et al., 2010; Swanner et al., 2015b). However, the conservation of such an isotopically light Fe seawater reservoir within sediments is superimposed by benthic microbial dissimilatory Fe reduction (DIR). It has been suggested as an important pathway to produce those very negative signatures by partial reduction of Fe-oxides and oxidation of organic carbon, reacting to Fe-carbonate typically siderite, $4Fe(OH)_3 + CH_2O + HCO_3^- \rightarrow 4FeCO_3 + 3OH^- + 7H_2O$

(Heimann et al., 2010; Johnson et al., 2008a; Johnson et al., 2008b; Johnson et al., 2008c).

The ability of these minerals to record primary seawater Fe isotope signatures has been questioned based on the prevalence of secondary diagenetic Fe redox cycling in organic-rich sediments, e.g. DIR and the precipitation and dissolution processes of Fe(II)-sulfide (Johnson et al., 2013; Matthews et al., 2004; Rouxel et al., 2006; Yamaguchi et al., 2005; Yamaguchi and Ohmoto, 2006). For this reason it has been suggested that microbial Ca-Mg carbonates, like stromatolites, could be potential proxies for the Fe isotope composition of coeval seawater (Johnson et al., 2013; von Blanckenburg et al., 2008). Microbial carbonate precipitation from seawater is biologically induced (organo-mineralization) (Burne and Moore, 1987; Dupraz and Visscher, 2005) with little elemental fractionation of a wide range of trace elements and, therefore, have the potential to record seawater geochemical evolution (e.g. Webb and Kamber, 2000). However, diagenetic (fluid) alteration and dissolution of detrital components challenges the interpretation of seawater Fe geochemistry from carbonates (Banner, 1995; Brand and Veizer, 1980; Matthews et al., 2004; Veizer, 1983).

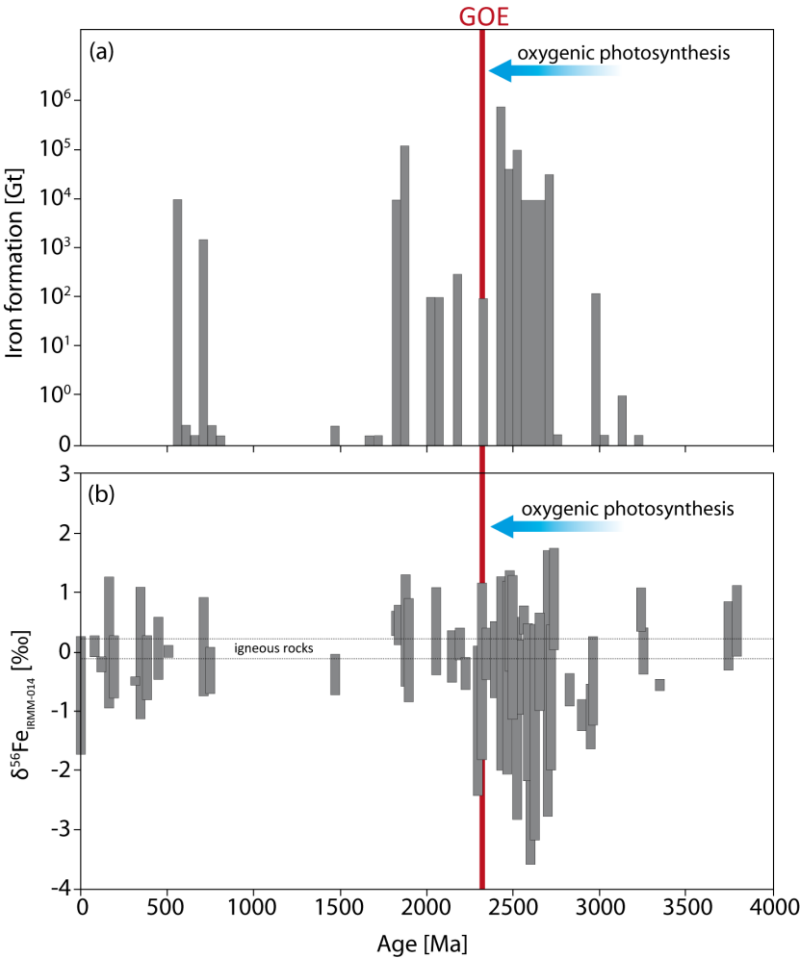

Figure 8-1: (a) Appearance of Banded Iron Formations over Earth's history (modified from Bekker et al. (2010)) (b) Compilation of analyzed δ^{56}Fe isotope signatures over Earth's history, analyzed on bulk IF, hydrothermal deposits, bulk mudrocks, Fe-(oxyhydr)oxides, -carbonates, -sufides, and Ca-Mg carbonate (modified from Busigny et al. (2014)).

In order to test the potential of Ca-Mg carbonates as proxies for the seawater Fe isotope composition, carbonate and mudrock samples of KMF-5 and BH-1 were analyzed for their Fe isotope composition and concentration. These results were combined with X-ray absorption spectroscopy (XAS) data of representative rock sections to examine the Fe-redox speciation and mineralogy. The data of the platform shelf collected in this study are further combined with published data of the platform slope (Czaja et al., 2012) and with elemental data of this study. The goal is to reconstruct the Fe cycling in a shallow-marine, possibly oxygen-producing, carbonate platform system and to decipher the factors controlling the Fe inventory.

8.2. Mineralogy and Fe speciation of platform succession

Even though the isotope signatures of carbonates and mudrocks of the CMCP differ, their Fe contents are in the same range and follow very similar paths (Fig. 4-7). Mudrocks contain significantly lower amounts of Fe (<1.50 wt-% Fe) than the average continental

crust (3.92 wt-%, Rudnick and Gao (2004)) and PAAS (5.05 wt-% Fe, Taylor and MacLennan (1985)). The low Fe content and the presence of sulfides (Table 4-10) indicate anoxic, sulfidic conditions and Fe-cycling within the sediment, even though some putatively primary Fe(III)-(oxyhydr)oxides were preserved, which implicate oxidation of Fe(II) species or detrital input of Fe(III)-(oxyhydr)oxides, and insufficient content of reductants like sulfide and/or organic carbon (Quinbyhunt and Wilde, 1994).

Data of XAS analyses reveal major differences in the oxidation state of Fe incorporated in the lower (steep ramp architecture) and upper (rimmed margin architecture) CMCP carbonates (Figure 4-10, Table 4-10). XRD data show that carbonate samples consist of dolomite ($CaMg(CO_3)_2$), with minor calcite and silica (Fig. 4-8), as it is also shown by the major element composition (Figs. 4-1, 4-2). However, the dominant Fe component of the lower part of the platform carbonates (Oaktree, Monte Christo, and Reivilo formations) is Fe-containing carbonate, in particular ankerite ($CaFe^{2+}(CO_3)_2$). This means that Fe substituted with Mg in the dolomite structure, forming $Ca^{2+}\cdot(Mg^{2+},Fe^{2+}))(CO_3)_2$, which was not traced by XRD, probably because it is below the detection limit of the method (0.1 to 0.5 wt-%), but is still detectable spectroscopically. Ankerite is heterogeneously distributed in the samples (Figure 4-9-B), minor amounts of Fe(II)-sulfides are visible as discrete particles in the XANES maps (Figure 4-9-B, samples SH98, 1742.3). Similar to secondary pyrite formation in some mudrocks of the Malmani succession (Fig. 2-4), these particles likely formed secondarily as aggregates during diagenesis by the reaction of mobilized Fe(II) and dissolved sulfide species (Wilkin and Barnes, 1997). Overall the carbonates in the Oaktree, Monte Christo and Reivilo formations solely contain Fe(II) species. This changes towards the upper part of the CMCP (Figure 4-10), where the carbonates of the Lyttleton and Eccles formations contain Fe(III)-(oxyhydr)oxide in form of goethite (FeOOH), which is a minor Fe species in the Lyttleton Formation and eventually becomes the dominant Fe species in the Eccles Formation (Table 4-10). Ankerite is still the major Fe species in the Lyttleton Formation, but is no longer a component in the Eccles Formation, where instead minor amounts of siderite and ferrosmectite are present. Neither in the Lyttleton nor in the Eccles formations Fe(II)-sulfide is present, which implies an insufficiency of organic material or sulfide species in the sediment. The scarcity of organic-rich mudrocks in the Eccles Formation supports this possibility (Figs. 4-1, 4-3).

Major and trace element data of CMCP showed that the here investigated carbonates were not subject of fluid alteration by the Bushveld complex and there is no reason why dolomitization and silicification processes would form goethite in the upper part of the CMCP but not in the lower part. A detrital input of goethite is possible, however the analyzed

samples (665.08, 665.18, and 884.9) are pure carbonates with negligible detrital component (some minor amounts in 884.9) and XAS-maps of the edge-positions show that goethite is finely distributed into the carbonate structure (Fig. 4-9-A), which rather argues for a formation within the sediment. Furthermore, detrital material most likely consist of phyllosilicates like chlorite and ferrosmectite, based on XAS spectra of detritus-rich sample 1265.1 (Table 4-10). Thus, another process must have formed goethite in the carbonates. An experimental study of Mettler (2002) investigated the adsorption of Fe(II) cations on calcite surfaces. In an oxygen-free environment adsorbed Fe(II) equilibrates with calcite and is subsequently incorporated in the calcite structure forming a mixed Fe(II)/$CaCO_3$ phase with a relative molar ratio of ~0.4 % (Dromgoole and Walter, 1990; Mettler, 2002), making Fe(II) inaccessible for later oxidation. However, in an oxygenated circumneutral environment adsorbed Fe(II) is oxidized at the carbonate surface to Fe(III)-(oxyhydr)oxides in form of goethite, which is a kinetically faster process (minutes) than Fe(II) incorporation into carbonate (hours-weeks) (Mettler et al., 2009). This kinetically fast oxygenation is necessary, as Fe(II) oxidation competes with other redox processes, in particular aerobic respiration that rapidly consumes oxygen. Another study by van der Zee et al. (2003) describes the formation of nanogoethite (~12 nm) in lake and marine sediments and proposes that diagenetic formation of goethite is the main reactive Fe phase that precipitates in aquatic sediments and is an important component for the Fe cycle along oxic-anoxic boundaries within the sediment. A possible scenario for the microbialites of the CMCP could therefore be the adsorption of $Fe(II)_{aq}$ from solution on calcite and the subsequent oxidation to goethite within the surface layer of the sediment either by photosynthetically produced oxygen or metabolically by anoxygenic photoautotrophy.

Conditions probably changed again in the uppermost CMCP, as the analyzed carbonate sample from the Gamohaan Formation (340, BH-1) was deposited during the final drowning of the platform and contains mainly ankerite and minor siderite and pyrite, indicating reducing conditions (Table 4-1).

The stratigraphical equivalent of the Lyttleton and the Eccles formations in the TA is the Upper Nauga Formation in the GWA, which represents the slope succession and, in contrast to the Lyttleton and Eccles formations, does contain Fe(II)-sulfides (Czaja et al., 2012). That means that, based on the Fe-speciation data, the lower CMCP and the slope succession were governed by an anoxic sedimentary geochemical redox regime, while the lagoonal interior during the rimmed margin architecture stage (the upper CMCP) allowed the preservation of Fe(III)-(oxyhydr)oxides (Fig. 4-11). The reason for this was probably that the organic carbon content in the upper CMCP was too low to exploit the Fe(III)-(oxyhydr)oxides (Berner, 1981; Froelich et al., 1979), in contrast to the organic-rich

lower CMCP, where Fe(III)-(oxyhydr)oxides were reductively dissolved and $Fe(II)_{aq}$ released, which could get subsequently incorporated into carbonates and sulfides. Another reason could have been the more intense interaction of the slope carbonates and platform carbonates of the lower CMCP (steep ramp architecture) with open ocean water that contained more reducing species (e.g. CH_4, Fe^{2+}, Mn^{2+}) from hydrothermal vents, while the lagoonal interior was protected from those species by the rimmed margin. Either way, the presence of Fe(III)-(oxyhydr)oxides in the upper part of the CMCP argue for increasing oxidizing conditions in the shallow marine environment and emphasize the dependence on the platform architecture, as well as hydrothermal and continental input.

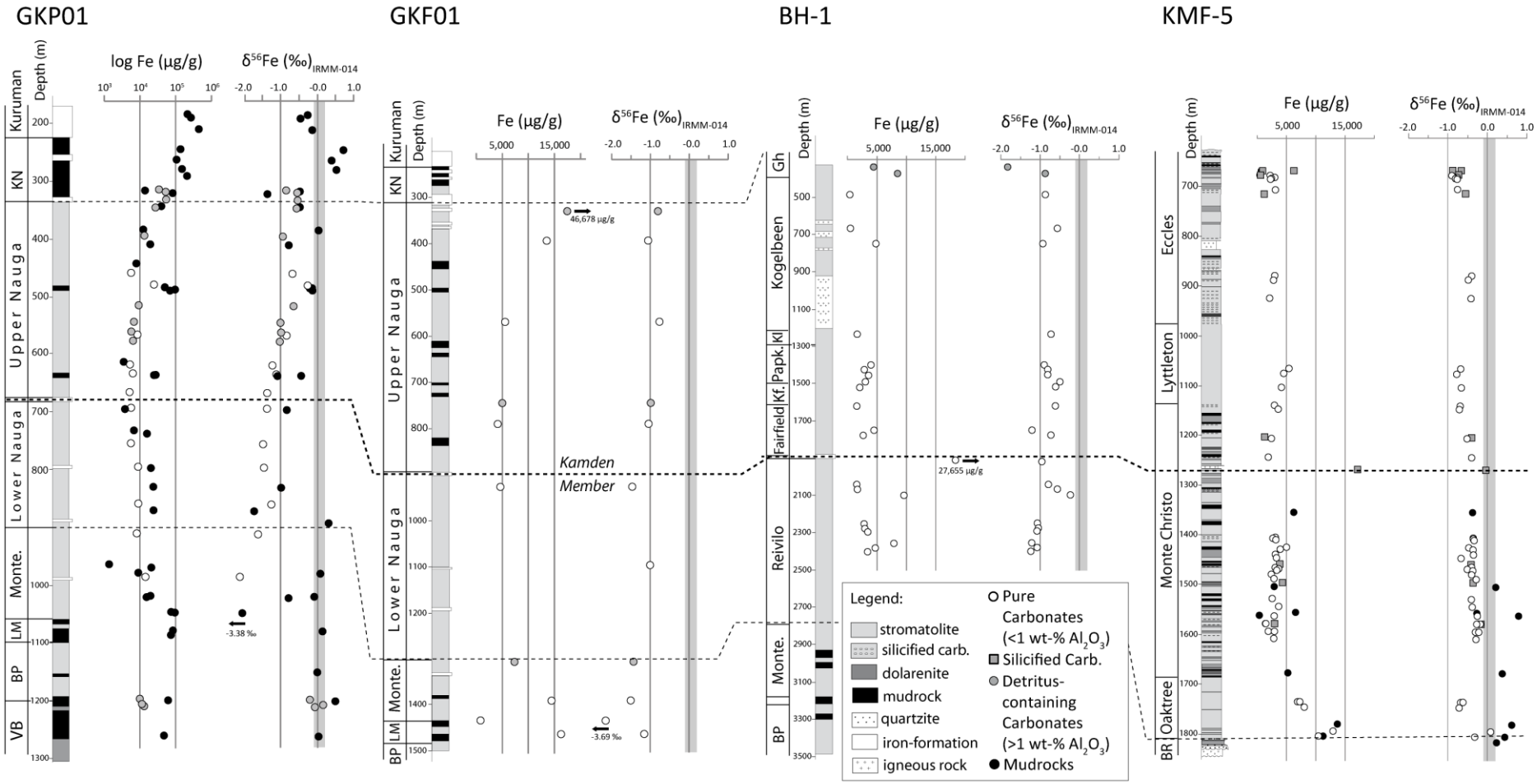

Figure 8-2: Fe concentrations and isotopic compositions of carbonates and mudrocks from KMF-5, BH-1 (platform succession), GKP01, and GKF01 (slope succession (Czaja et al., 2012)). Shaded area at δ^{56}Fe columns indicates the range of continental signatures from -0.1 to +0.2 ‰ (e.g. Craddock et al., 2013; Schoenberg and von Blanckenburg, 2006; Wang et al., 2014; Weyer et al., 2005). Dashed black line shows stratigraphical relation of formations which belong to the Campbellrand-Malmani slope-platform succession. Thicker dashed line indicates Kamden Member. Abbreviations of Formations: VB: Vryburg; BP: Boomplaas; LM: Lokamonna; Monte.: Monteville; KN: Klein Naute; Kf.: Klipfonteinheuwel; Papk.: Papkuil; Kl: Klippan; Gh: Gamohaan; BR: Black Reef

8.3. Fe isotope geochemistry of the platform succession

It is difficult to depict a clear systematic trend in the Fe isotope and concentration data throughout the stratigraphy of slope (GKP01, GKF01) and platform (BH-1, KMF-5) carbonates and mudrocks displayed in Fig. 8-2. It is obvious, however, that mudrocks from the platform (KMF-5) show overall positive δ^{56}Fe signatures (mean with 2σ: +0.25±0.75 ‰; n = 8) and are heavier than the typical Fe isotopic composition of igneous rocks with values from -0.1 to +0.2 ‰ (e.g. Craddock et al., 2013; Schoenberg and von Blanckenburg, 2006; Wang et al., 2014; Weyer et al., 2005), while the mudrocks from the slope succession of the CMCP (Boomplaas, Lokammona, Monteville, lower and upper Nauga - GKP01) mostly show overall negative δ^{56}Fe signatures (-0.67 ± 1.81 ‰; n = 21) (Czaja et al., 2012) and are lighter than the δ^{56}Fe range of igneous rocks. The dominant Fe mineral in the platform and slope mudrocks are Fe(II)-sulfides as shown by XANES (this data) and XRD (Czaja et al., 2012) analyses and thus control the Fe isotope composition. This indicates that the slope and platform environments were dominated by different Fe cycling processes.

Ca-Mg carbonates of slope and platform successions consistently show δ^{56}Fe signatures lighter than the igneous rock range, with one exception in the lower Oaktree Formation (1790.1, δ^{56}Fe of 0.08 ‰). Silicified carbonates plot in the same range as pure carbonates, indicating that silicification did not alter the δ^{56}Fe signature. When plotting δ^{56}Fe signatures vs. Fe concentrations of pure carbonates including data of Kuruman Kop carbonates (Fig. 8-3), some dependence on the depositional environment and water depth becomes apparent. Two positively correlating trends in the dataset ('Platform' and 'Slope') are revealed as well as a cluster of data in a more restricted range of lower Fe concentrations (marked by a circle). The 'Platform' trendline involves Oaktree (KMF-5) and Reivilo samples (BH-1), which were deposited during the earlier steep platform stage and therefore were partly exposed to open ocean water. Samples Ku12/06 and Ku12/25 from the Gamohaan Formation (Kuruman Kop) also line up in this trend, were deposited during the drowning of the CMCP, and thus also in contact with open ocean water. The 'Slope' trendline consists of samples from the slope facies (GKP01, GKF01) and signifies stronger exposure to Fe-rich deep ocean water. This is reflected in the higher Fe concentrations of the slope pure carbonates (up to 27700 µg/g) (Czaja et al., 2012).

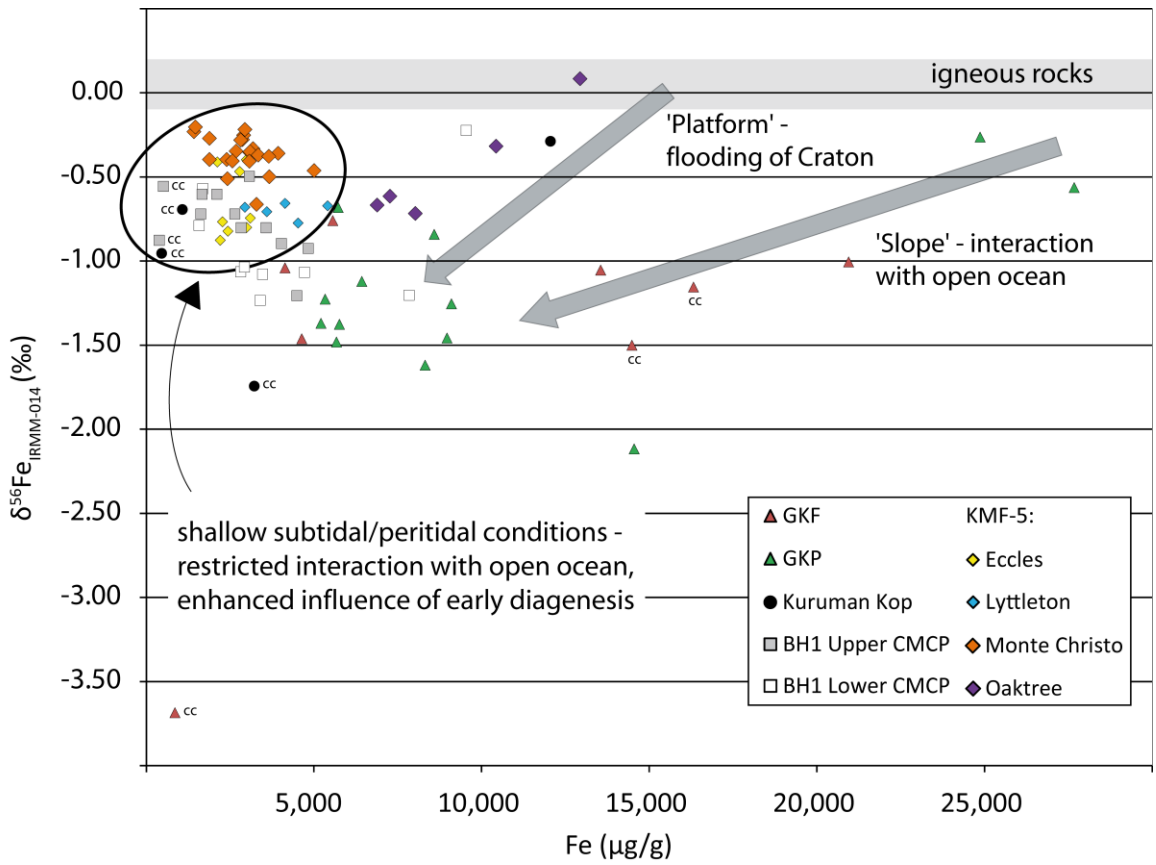

Figure 8-3: Fe concentration vs. δ^{56}Fe isotope data of pure carbonate (cc = calcitic) samples from CMCP. Data of GKP01 and GKF01 are from (Czaja et al., 2012), data from BH 1 and KMF-5 are from this study. Trendline 'Platform' represent carbonates from the Oaktree, Reivilo and Gamohaan formations and trendline 'Slope' carbonates from the slope succession. Both were exposed to ferruginous open ocean water. Both trendlines show a positive correlation between Fe isotopes Fe content, which probably reflects Rayleigh fractionation processes during oxidation of $Fe(II)_{aq}$ and deposition of isotopically heavy $Fe(III)_{ppt}$. Carbonates deposited in shallow settings, and after development of a rimmed platform margin/lagoonal setting, likely reflect a predominantly continental Fe source and the presence of free oxygen. Heavy δ^{56}Fe signatures in carbonates of the Monte Christo Formation probably reflect the composition to adjacent pyrite-containing and isotopically heavy mudrocks (Fig. 8-2).

Platform carbonates, which fall into the circled cluster have Fe concentrations below 5000 µg/g. Those samples are from peritidal settings and/or were deposited in the context of the rimmed platform architecture, so they represent restricted shallow-marine conditions, with poor exchange with open ocean water, but exposed to riverine water and detrital material from the continent. Carbonates of the Monte Christo Formation show overall heavier δ^{56}Fe signatures (mean with 2σ: -0.38 ± 0.25 ‰; n = 23) than platform carbonates from the Upper CMCP, including the Lyttleton and Eccles formations (-0.73 ± 0.36 ‰; n = 12) (Fig. 8-3). Since the Monte Christo Formation contains isotopically heavy mudrocks, it seems obvious that those affected the adjacent carbonates. All these observations are confirmed by other geochemical and sedimentological data, which show flattened REE+Y patterns and fluctuations in the Fe# that are connected to the input of siliciclastic mudrocks and interpreted as localized remobilization of Fe from the mudrocks into the adjacent carbonates (Fig. 5-5).

8.3.1. Sources of $Fe(II)_{aq}$ in the Neoarchean marine environment

Fe isotope analyses reveal that there is no isotope difference between calcitic and dolomitic samples (Fig. 8-3; Tables 4-7, 4-8), which supports a study of von Blanckenburg et al. (2008), showing that dolomitization has no effect on the $\delta^{56}Fe$ isotope composition of carbonate. There is no experimentally determined fractionation factor for $Fe(II)_{aq}$ into Ca-Mg carbonates yet. However, dolomitization itself does not invoke a redox change, i.e. a shift in the reduction potential (Eh), which means that a Fe isotope fractionation due to redox-reactions is not expected and that any such fractionation must have been independent from dolomitization.

Even though $\delta^{56}Fe$ signatures seem to be unaffected by dolomitization, dolomite samples from the platform facies have one to two order of magnitude higher Fe concentrations than their calcitic counterparts. This might indicate that even though dolomitization did not invoke a shift in the Fe isotope signature, it caused a rise in the Fe concentration. However, not all calcitic samples do show lower Fe contents. Some limestones from the slope facies show Fe contents similar to dolomite and even follow the same 'Slope' trend. This can also be observed for sample Ku12/06, which contains 3225 µg/g Fe, but has a light $\delta^{56}Fe$ signature of -1.74 ‰. This can rather be explained by titration of Fe from seawater that results in a low Fe concentration and isotope signature. Calcitic samples with an equally low Fe content but heavier $\delta^{56}Fe$ signature were deposited in the Upper CMCP and all fall into the cluster of carbonates reflecting peritidal and restricted conditions. Thus, the calcitic carbonates can, like the dolomitic carbonates, be distinguished by their depositional environment. Following from the observed dependence of the Fe concentration on water depth (Fig. 5-5), $Fe(II)_{aq}$ was mainly delivered from seawater and interacted with the sediment surface, where it could have been directly incorporated into the calcite structure (Dromgoole and Walter, 1990; Mettler, 2002). Thus, for the Ca-Mg carbonates, which were exposed to the open ocean, it can be suggested that the Fe incorporated into the dolomite structure rather stemmed from the recrystallized calcite itself and not from an external (i.e. continental) source. In contrast to that, a detrital and riverine input of Fe into the peritidal environment clearly affected the local carbonates (Fig. 5-5) and can explain the significantly higher Fe concentrations of the dolomite in those restricted settings (circled sample group in Fig. 8-3). All these observations agree with the trace element results and show that the Fe budget was controlled by the depositional environment and the relative input from the open ocean and the continent. This affirms the quality of dolomitized carbonate as a proxy for Fe in ancient marine environments and allows drawing implications on the redox processes in coeval seawater and sediment.

8.3.2. Fe systematics along an aqueous redox-boundary

Fe isotope behavior in aqueous environments is complex as Fe is redox active and shows a change in chemical behavior along chemoclines. In modern aqueous environments redox-boundaries exist in a variety of lakes and restricted marine basins, which are considered as analogues to a potential Archean seawater situation with deep anoxic and shallow oxic layers allowing implications for the Fe isotope evolution of ancient seawater (Busigny et al., 2014; Severmann et al., 2008; Staubwasser et al., 2013; Staubwasser et al., 2006). Aerobe oxidation of $Fe(II)_{aq}$ to $Fe(III)_{ppt}$ causes an enrichment of heavy Fe isotopes in the precipitate by 1-2 ‰ (Beard et al., 2003a; Bullen et al., 2001) and is similar to anaerobe microbial Fe(II) oxidation that shows an enrichment of about 1.5 ‰ (Croal et al., 2004). The oxidation of $Fe(II)_{aq}$ in the water column along a chemocline separating anoxic ferruginous deeper water from oxic shallow water and the subsequent precipitation of Fe(III)-(oxyhydr)oxides along this chemocline is a commonly cited scenario for the formation of some Precambrian IFs (e.g. Cloud, 1968; Isley and Abbott, 1999). Incomplete oxidation causes the remaining dissolved Fe(II) pool to become isotopically lighter, due to the separation of the precipitated Fe(III)-(oxyhydr)oxides and the reservoir of dissolved Fe(II) remaining in seawater (Rouxel et al., 2005). A study of Busigny et al. (2014) examined in the ferruginous, anoxic Lac Pavin if the Fe cycle is rather influenced by water column redox chemistry or by benthic microbial Fe reduction. The Fe isotope composition of pyrite along the chemocline is variable, overall negative and mirrors the Fe isotope composition of aqueous Fe. They conclude that Fe sulfide formation induces only a limited Fe isotope fractionation and that the observed isotope fractionation in the Lac Pavin setting is not connected to pyrite formation but to the Fe(II) oxidation within the water column. The implication is that the strong Fe isotope variability in the Neoarchean (Fig. 8-1 b) can rather be linked to partial ferrous Fe oxidation in upwelling water masses (Kurzweil et al., 2016).

Oxidation of Fe(II) along a chemocline probably played an important role in the CMCP, as several studies indicate the presence of oxygen in the shallow water (Brucker et al., 2009; Czaja et al., 2012; Godfrey and Falkowski, 2009; Kendall et al., 2010; Sumner and Grotzinger, 1996; Voegelin et al., 2010; Wille et al., 2007). The appearance of minor Fe formations, like the Kamden Member that formed in course of a short transgressive event, shows the presence of coeval ferruginous deeper water (Fig. 5-5) (Beukes and Gutzmer, 2008; Sumner and Beukes, 2006). Rayleigh distillation through partial Fe(II) oxidation, resulting in lower Fe concentrations and isotopically lighter $Fe(II)_{aq}$ would be consistent with the 'Platform' and 'Slope' trendlines (Fig. 8-3) and Ca-Mg carbonates would therefore reflect such a process in the environment of the CMCP.

8.3.3. Rayleigh distillation along the CMCP

It was tested in this study if Rayleigh distillation could explain the 'Platform' and 'Slope' carbonate trends. The hypothesis hereby is that $Fe(II)_{aq}$ from seawater is directly incorporated into carbonates and that any isotopic difference between the carbonates is from Rayleigh fractionation between $Fe(II)_{aq}$ and $Fe(III)_{ppt}$ along a redox boundary between ferruginous deeper water, which was supplied via upwelling into oxygenated shallow seawater. The goal was to determine the initial $Fe(II)_{aq}$ concentration of the seawater and the fractionation factor α (converted to permille units via $\varepsilon = (\alpha - 1) \times 1000$) between $Fe(II)_{aq}$ and $Fe(III)_{ppt}$. As initial $\delta^{56}Fe$ signature of seawater $Fe(II)_{aq\text{-initial}}$ of 0 ‰ was chosen to reflect hydrothermal derived Fe(II), which was probably the dominant contributor of $Fe(II)_{aq}$ into the anoxic ocean and assuming that higher hydrothermal activity in the Archean decreased fractionation effects along those systems (Fig. 1-5) (Bau and Moller, 1993; Beard et al., 2003b; Derry and Jacobsen, 1990; Jacobsen and Pimentelklose, 1988).

The 'Platform' and 'Slope' trendlines were calculated separately with the Solver tool of Microsoft Office Excel by minimizing the sum of chi^2 values (Σchi^2) for the fractionation factor α (expressed as $\varepsilon Fe(III)_{ppt}\text{-}Fe(II)_{aq}$) and $Fe(II)_{aq\text{-initial}}$, which was determined by comparing the fit to the $\delta^{56}Fe$ carbonate dataset. The fit was based on the Rayleigh equation for $\delta^{56}Fe(II)_{aq}$ and the corresponding $\delta^{56}Fe(III)_{ppt}$ under the assumption that the $\delta^{56}Fe$ signature of the carbonates represents the $\delta^{56}Fe_{aq}$ signature of the remaining $Fe(II)_{aq}$ after the precipitation of $Fe(III)_{ppt}$:

$$\delta^{56}\mathrm{Fe(II)_{aq}} = \left(\delta^{56}\mathrm{Fe(II)_{aq-initial}} + 1000\right)\mathrm{f}^{\alpha-1} - 1000$$

$$\delta^{56}\mathrm{Fe(III)_{ppt}} = \left(\delta^{56}\mathrm{Fe(II)_{aq-initial}} + 1000\right) \times \left(\frac{1-\mathrm{f}^{\alpha}}{1-\mathrm{f}}\right) - 1000$$

with $\mathrm{f} = \frac{\mathrm{Fe(II)aq}}{\mathrm{Fe(II)aq,initial}}$.

The $Fe(II)_{aq}$ concentration was calculated on the Fe concentration of the carbonates, based on precipitation experiments and Fe incorporation into calcite from Dromgoole and Walter (1990), which is controlled by the distribution factor D_{Fe2+}. The distribution factor is mainly dependent on the temperature and precipitation rate and is defined as:

$$\mathrm{D}_{Fe^{2+}} = \frac{\frac{Fe^{2+}}{Ca^{2+}}_{\mathrm{calcite}}}{\frac{\mathrm{a}_{Fe^{2+}}}{\mathrm{a}_{Ca^{2+}}}_{\mathrm{solution}}}$$

where $\frac{Fe^{2+}}{Ca^{2+}}_{\mathrm{calcite}}$ is the molar ratio of Fe^{2+} and Ca^{2+} in the precipitated calcite and $\frac{\mathrm{a}_{Fe^{2+}}}{\mathrm{a}_{Ca^{2+}}}_{\mathrm{solution}}$ is the activity ratio of Fe^{2+} and Ca^{2+} (Dromgoole and Walter, 1990). The activity *a* of a chemical species *i* is the product of its concentration [*i*] and the activity coefficient γ_i ($a_i = \gamma_i \times [i]$). The activity coefficient γ_i depends on the ionic strength, but was during the experiments of Dromgoole and Walter (1990) always close to unity. This means that a_i

basically corresponds to the concentration of the chemical species in solution. Several distribution factors D_{Fe2+} were determined by Dromgoole and Walter (1990), depending on temperature and activity ratio. For the carbonates of this study, we used the equation for precipitation experiments at 25°C and an activity ratio $\frac{a_{Fe^{2+}}}{a_{Ca^{2+}}}$ of 0.001:

$$\log D_{Fe^{2+}} = 0.98 - 0.158 \times \log(rate)$$

where *rate* is the precipitation rate of the calcite. The precipitation rate was calculated from the assumed sedimentation rate along the slope (~10 m/Ma) and the platform (~100 m/Ma) of the CMCP (Altermann and Nelson, 1998). Furthermore, as an approximation, it was assumed that all Fe(II) in the dolomite was originally incorporated into calcite before dolomitization. Furthermore, not the real molar Ca concentration of the dolomite was used, but an artificial molar Ca concentration to simulate a calcite composition (Table 8-1). For Ca^{2+}_{aq} concentrations, 20 mM were assumed (Horita et al., 2002). The results are summarized in Table 8-1 and illustrated in Figure 8-4 and give for the Rayleigh fit of the 'Platform' trend a $Fe(II)_{aq\text{-}initial}$ of 180 µM and an $\varepsilon Fe(III)_{ppt}$-$Fe(II)_{aq}$ of 0.75 ‰, with a Σchi^2 of 0.922. The Rayleigh fit of the 'Slope' trend yields a $Fe(II)_{aq\text{-}initial}$ of 555 µM and an $\varepsilon Fe(III)_{ppt}$-$Fe(II)_{aq}$ of 0.58 ‰, however the Σchi^2 of 5.437 is very poor. A Rayleigh fit of the 'Slope-Limestone' (only calcitic slope carbonates) (GKF01: 1386.26, 1458.42, and 1429.08 (Czaja et al., 2012)) yields a similar $Fe(II)_{aq\text{-}initial}$ of 573 µM and a higher $\varepsilon Fe(III)_{ppt}$-$Fe(II)_{aq}$ of 0.82 ‰, with a Σchi^2 of 0.011. However, those samples were deposited at the lowermost CMCP and there is the possibility that they not represent the complete slope succession. The high Σchi^2 value of the 'Slope' trendline indicates that secondary processes, like DIR, might have had disturbed the primary Fe isotope composition of some samples (Czaja et al., 2012; Heimann et al., 2010; Johnson et al., 2008b; Johnson et al., 2013). The activity ratios $\frac{a_{Fe^{2+}}}{a_{Ca^{2+}}}$ for all calculated samples are >0.001, which would affect the precipitation equation and probably yield slightly higher $Fe(II)_{aq}$ concentrations. However, this increase will not be significant, as the activity ratios are still in the same order of magnitude (Dromgoole and Walter, 1990).

In this simulation, $Fe(II)_{aq\text{-}initial}$ decreases at higher temperatures, lower Ca^{2+}_{aq} concentrations, and a lower sedimentation rate and increases at lower temperatures, higher Ca^{2+}_{aq} concentrations, higher sedimentation rate (Table 8-2). Based on the calculations, it can be suggested, that $Fe(II)_{aq\text{-}initial}$ concentrations along the slope were between 61 µM (50 °C, 10 mM Ca^{2+}_{aq}, 2 m/Ma sedimentation rate) and 1368 µM (10 °C, 30 mM Ca^{2+}_{aq}, 20 m/Ma sedimentation rate), whereas $Fe(II)_{aq\text{-}initial}$ concentrations in the shallow marine environment of the platform were between 28 µM (50 °C, 10 mM Ca^{2+}_{aq}, 50 m/Ma sedimentation rate) and 394 µM (10 °C, 30 mM Ca^{2+}_{aq}, 150 m/Ma sedimentation rate). This

is a huge span and emphasizes the strong dependency of dissolved $Fe(II)_{aq}$ in seawater on external factors. Early estimates of seawater temperatures for the Archean of ~70 to 80 °C, based on oxygen isotope data of cherts, have been revisited as too high and recent estimates argue for a maximum of 40 (Hren et al., 2009) or 60 °C (Brock and Madigan, 1991). Blake et al. (2010) proposed a range between 26 and 35 °C, based on oxygen isotopes in phosphates. Assuming that seawater temperatures were between 25° and 50°C, this limits the range of $Fe(II)_{aq}$ concentrations in this simulation between 61 and 928 µM for the slope and 28 to 288 µM for the platform succession for varying Ca^{2+}_{aq} (Canfield, 2005; Horita et al., 2002) and sedimentation rates (Altermann and Nelson, 1998). This is still a large range but whatever the exact conditions were that prevailed in the seawater, two important implications are gained. First, that $Fe(II)_{aq}$ concentrations in seawater were probably significantly higher than previously assumed and second, that a concentration gradient existed, with higher $Fe(II)_{aq}$ concentrations along the deeper slope facies and lower $Fe(II)_{aq}$ concentrations in the shallow platform environment. This implicates the removal of $Fe(II)_{aq}$ supplied during upwelling along the carbonate platform margin, probably due to a chemocline between ferruginous deeper water and oxygenated shallow water. This is also implicated by the fractionation factors of the Rayleigh fits ($\varepsilon Fe(III)_{ppt}$-$Fe(II)_{aq}$ of +0.58 ‰ or +0.82 ‰ for the 'Slope' trend and +0.75 ‰ for the 'Platform' trend), even though those are slightly lower than the reported fractionation factors of 1-3 ‰, during oxidation by dissolved oxygen or by microbially-induced oxidation (Balci et al., 2006; Beard et al., 2003a; Bullen et al., 2001; Croal et al., 2004; Kappler et al., 2010; Swanner et al., 2015b). The decreasing $Fe(II)_{aq}$ concentrations on the platform would also lower the risk of Fe toxicity for cyanobacteria and increase their thriving (Swanner et al., 2015a). This reinforces the assumption of a change from an anaerobe to an aerobe ecosystem in the CMCP, as already indicated by heavier $\delta^{13}C_{org}$ signatures in KMF-5.

Table 8-1: Rayleigh fit of 'Platform' and 'Slope' trendlines (Fig. 8-4) based on $Fe(II)_{aq}$ incorporation into calcite

PLATFORM TRENDLINE

Precipitation rate: 309 µmol/h/m^2 (100 m/Ma, Altermann and Nelson, 1998); Ca^{2+}_{aq} = 20 mM; 25 °C

Σchi^2 = 0.922; $\varepsilon Fe(III)_{ppt}$-$Fe(II)_{aq}$ = 0.75 ‰; $Fe(II)_{aq\text{-}initial}$: 180 µM

Location	Formation	Sample	Fe (wt-%)	Ca (wt-%)	$\frac{Fe^{2+}}{Ca^{2+}}_{calcite}$	$\frac{a_{Fe^{2+}}}{a_{Ca^{2+}}}_{solution}$	$Fe(II)_{aq}$ (mM)	$\delta^{56}Fe$ (‰)
Kuruman Kop (GWA)	Gamohaan	Ku12_06	0.32	**38.36**	0.006	0.002	0.031	-1.74
		Ku12_25	1.21	35.74	0.024	0.006	0.125	-0.29
BH-1 (GWA)	Reivilo	2098	0.95	35.74	0.019	0.005	0.099	-0.23
		2250	0.28	35.74	0.006	0.001	0.029	-1.07
		2275	0.29	35.74	0.006	0.002	0.030	-1.04
		2293	0.35	35.74	0.007	0.002	0.036	-1.08
		2355	0.78	35.74	0.016	0.004	0.082	-1.20
		2379	0.47	35.74	0.009	0.002	0.049	-1.07
		2400	0.34	35.74	0.007	0.002	0.035	-1.24
KMF-5 (TA)	Oaktree	1731.1	0.69	35.74	0.014	0.004	0.072	-0.67
		1731.3	0.73	35.74	0.015	0.004	0.076	-0.62
		1742.3	0.80	35.74	0.016	0.004	0.084	-0.72
		1790.1	1.29	35.74	0.026	0.007	0.135	0.08
		1800.1	1.04	35.74	0.021	0.005	0.109	-0.32

SLOPE TRENDLINE

Precipitation rate: 31 µmol/h/m^2 (10 m/Ma, Altermann and Nelson, 1998); Ca^{2+}_{aq} = 20 mM; 25 °C

Σchi^2 = 5.44; $\varepsilon Fe(III)_{ppt}$-$Fe(II)_{aq}$ = 0.57 ‰; $Fe(II)_{aq\text{-}initial}$: 555 µM

Location	Formation	Sample	Fe (wt-%)	Ca (wt-%)	$\frac{Fe^{2+}}{Ca^{2+}}_{calcite}$	$\frac{a_{Fe^{2+}}}{a_{Ca^{2+}}}_{solution}$	$Fe(II)_{aq}$ (mM)	$\delta^{56}Fe$ (‰)
GKP01 (GWA)	upper Nauga	346.9	2.77	35.74	0.056	0.010	0.200	-0.56
		460.3	0.57	35.74	0.012	0.002	0.041	-0.68
		480.64	2.49	35.74	0.050	0.009	0.180	-0.26
		567.4	0.86	35.74	0.017	0.003	0.062	-0.84
		619	0.53	35.74	0.011	0.002	0.039	-1.23
		634.45	0.64	35.74	0.013	0.002	0.047	-1.12
		667	0.52	35.74	0.010	0.002	0.038	-1.37
	lower Nauga	693.84	0.58	35.74	0.012	0.002	0.042	-1.38
		755.51	0.57	35.74	0.011	0.002	0.041	-1.48
		796.22	0.90	35.74	0.018	0.003	0.065	-1.46
		859.9	0.91	35.74	0.018	0.003	0.066	-1.25
		911.8	0.83	35.74	0.017	0.003	0.060	-1.62
	Monteville	987.24	1.46	35.74	0.029	0.005	0.105	-2.12
GKF01 (GWA)	upper Nauga	395.4	1.36	35.74	0.027	0.005	0.098	-1.06
		570.16	0.56	35.74	0.011	0.002	0.040	-0.76
		790.18	0.41	35.74	0.008	0.001	0.030	-1.04
	lower Nauga	925.9	0.46	35.74	0.009	0.002	0.034	-1.46
		1094.84	2.09	35.74	0.042	0.008	0.152	-1.01
	Monteville	1386.26	1.45	**36.40**	0.029	0.005	0.103	-1.50
		1429.08	0.09	**34.43**	0.002	0.000	0.006	-3.69
	Lokammona	1458.42	1.63	**32.23**	0.036	0.007	0.131	-1.16

SLOPE TRENDLINE - LIMESTONES

Precipitation rate: 31 µmol/h/m^2 (10 m/Ma, Altermann and Nelson, 1998); Ca^{2+}_{aq} = 20 mM; 25 °C

Σchi^2 = 0.011; $\varepsilon Fe(III)_{ppt}$-$Fe(II)_{aq}$ = 0.82 ‰; $Fe(II)_{aq\text{-}initial}$: 573 µM

Location	Formation	Sample	Fe (wt-%)	Ca (wt-%)	$\frac{Fe^{2+}}{Ca^{2+}}_{calcite}$	$\frac{a_{Fe^{2+}}}{a_{Ca^{2+}}}_{solution}$	$Fe(II)_{aq}$ (mM)	$\delta^{56}Fe$ (‰)
GKF01 (GWA)	Monteville	1386.26	1.45	**36.40**	0.029	0.005	0.103	-1.50
		1429.08	0.09	**34.43**	0.002	0.000	0.006	-3.69
	Lokammona	1458.42	1.63	**32.23**	0.036	0.007	0.131	-1.16

Ca concentration in bold are from XRF analyses and represent limestones. All other Ca concentrations represent an artificial calcite composition of the analyzed dolomite. All Fe concentrations and isotope signatures are from ICP-MS analyses.

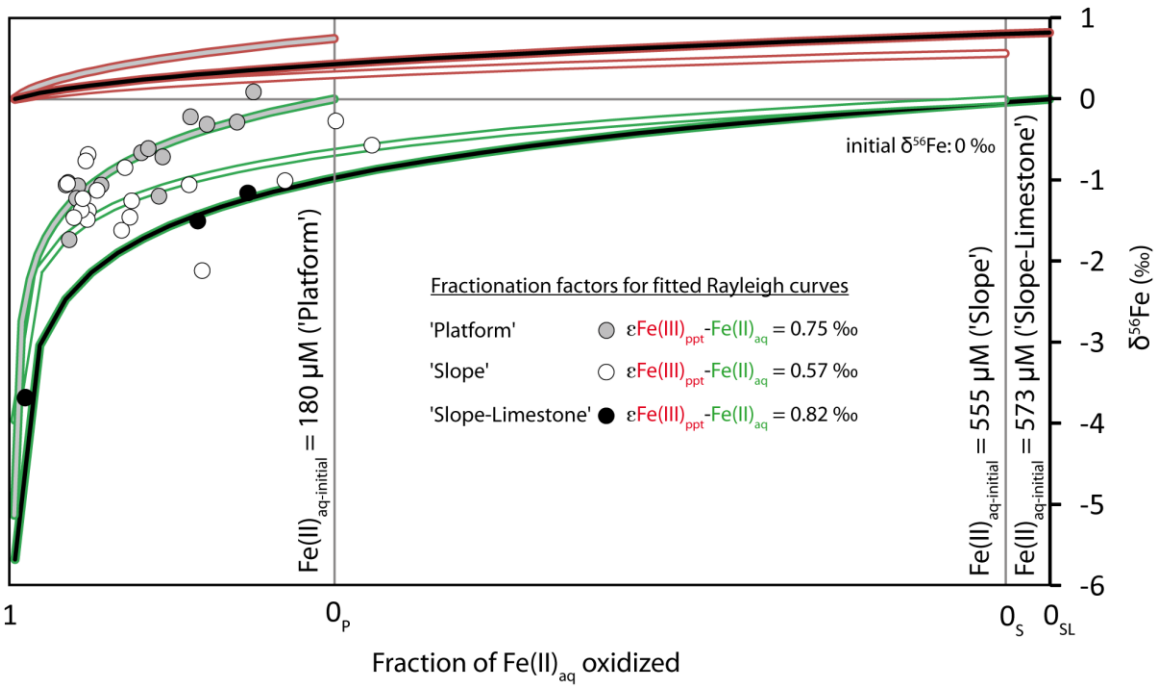

Figure 8-4: Rayleigh fitted curves for 'Platform' and 'Slope' trendlines (Fig. 8-3), based on the calculations in Table 8-1. 'Slope-Limestone' curve is fitted for calcitic carbonate samples from the slope succession (GKF01). Curves have different initial $Fe(II)_{aq}$ concentration. 0_P, 0_S, and 0_{SL} are the initials of 'Platform', 'Slope', and 'Slope-Limestone' trendline, respectively.

Table 8-2: Calculated $Fe(II)_{aq\text{-}initial}$ concentrations on different temperatures, $Ca^{2+}{}_{aq}$ concentrations and sedimentation rates

$Ca^{2+}{}_{aq}$ = 10 mM	SLOPE			PLATFORM		
Sedimentation rate	2 m/Ma	10 m/Ma	20 m/Ma	50 m/Ma	100 m/Ma	150 m/Ma
Temperatur	**$Fe(II)_{aq\text{-}initial}$ (µM)**					
10°C	334	415	456	113	124	131
25°C	215	277	309	81	90	96
50°C	61	87	102	28	32	36
$Ca^{2+}{}_{aq}$ = 20 mM	SLOPE			PLATFORM		
Sedimentation rate	2 m/Ma	10 m/Ma	20 m/Ma	50 m/Ma	100 m/Ma	150 m/Ma
Temperatur	**$Fe(II)_{aq\text{-}initial}$ (µM)**					
10°C	668	831	912	226	248	262
25°C	430	555	619	161	180	192
50°C	122	174	203	56	65	71
$Ca^{2+}{}_{aq}$ = 30 mM	SLOPE			PLATFORM		
Sedimentation rate	2 m/Ma	10 m/Ma	20 m/Ma	50 m/Ma	100 m/Ma	150 m/Ma
Temperatur	**$Fe(II)_{aq\text{-}initial}$ (µM)**					
10°C	1003	1246	1368	339	373	394
25°C	645	832	928	242	270	288
50°C	182	261	305	83	97	107

Regression equations for Fe(II) incorporation into calcite, based on the distribution coefficient $D_{Fe^{2+}}$ for an activity ratio $\frac{a_{Fe^{2+}}}{a_{Ca^{2+}}} = 0.001$ at $10°C$: $\log D_{Fe(II)} = 0.79 - 0.135 \times \log(rate)$; $25°C$: $\log D_{Fe^{2+}} = 0.98 - 0.158 \times \log(rate)$; $50°C$: $\log D_{Fe^{2+}} = 1.58 - 0.223 \times \log(rate)$ (Dromgoole and Walter, 1990)
(rate = precipitation (sedimentation) rate in µmol/h/m²)

8.3.4. Fe remobilization during synsedimentary redox processes

The circulation of porefluids in marine benthic sediments is an essential aspect in early diagenetic processes, and the source of these fluids is not only from sea- and freshwater, but also from dewatering processes within the sediment. Thereby, associated

redox processes and changes in Fe speciation within the bulk sediment, microbial processes, as well as fresh- and seawater mixing in estuaries can impact the fractionation of Fe isotopes (Beard et al., 2003a; Butler et al., 2005; Préat et al., 2011; Rouxel et al., 2008; Severmann et al., 2006). Modern suboxic and anoxic sediments from continental margins typically show light Fe isotope signatures as a result of incomplete reduction of Fe(III) particles, mostly by microbial processes (DIR), leaving the residual reactive Fe(III) in the sediment isotopically heavy, while isotopically light $Fe(II)_{aq}$ diffuses back into the seawater, or is reoxidized above the Fe(III) reduction zone at the sediment surface (Rouxel et al., 2008; Severmann et al., 2006; Severmann et al., 2008; Staubwasser et al., 2006). An alternative way of Fe(III) reduction is abiotically by dissolved sulfide in the sediment, typically H_2S, which can subsequently form Fe(II)-sulfides and also favors light Fe isotopes (Butler et al., 2005; Raiswell and Canfield, 1998). Due to the process Fe(II)-sulfide precipitation, Fe is rather removed from the porewater (Raiswell and Canfield, 1998), while during DIR-driven diagenesis Fe is remobilized and recycled.

Mudrocks of the CMCP contain Fe(II)-sulfides, which is the dominant Fe mineral phase and show negative $\delta^{56}Fe$ signatures in the slope facies (Czaja et al., 2012), while the peritidal facies show positive $\delta^{56}Fe$ signatures up to +0.79 ‰ (Table 4-7; Fig. 8-2). This seems to be in contradiction to studies that show sulfides favoring light Fe isotopes (Busigny et al., 2014; Rouxel et al., 2005). There is no simple explanation for this difference, but it is probably related to the distinct environmental conditions. Severmann et al. (2006) reported of such isotopic differences in porewaters of continental margins dominated by different pathways of organic carbon oxidation. In marine settings, which are dominated by bacterial sulfate reduction processes (BSR) and only shows limited DIR, produced dissolved sulfide forms Fe(II)-sulfide with positive $\delta^{56}Fe$ signatures. DIR is probably limited by the low concentration of Fe(III)-(oxyhydr)oxides in the sediment. Severmann et al. (2008) suggested that along continental shelves high organic fluxes from primary production allow the reduction of isotopically heavy Fe(III)-(oxyhydr)oxides (Berner, 1981). Given complete reduction of the heavy Fe(III), BSR would immobilize it and form isotopically heavy Fe(II)-sulfides. In contrast to that, DIR-dominated settings contain abundant Fe(III)-(oxyhydr)oxides and the precipitated Fe-sulfides show negative $\delta^{56}Fe$ signatures. Indeed, the organic-rich, pyrite-containing mudrock layers of the Monte Christo and Oaktree formations in the TA (up to 8.5 wt-% total organic carbon) indicate that anoxic/sulfidic conditions were generated within the sediment from organic decay and subsequent sulfate reduction (Berner, 1981). In this reducing, sulfide- and organic-rich environment detrital Fe(III)-containing minerals could get reduced and react to Fe(II)-sulfide (Berner, 1981). This is supported by mudrock sample 1776.0 (KMF-5), which shows a $\delta^{56}Fe$ signatures of

+0.62 ‰ and almost solely consists of pyrite as Fe species and only traces of magnetite, which might have been the originally reduced as isotopically heavy Fe(III)-oxide phase (Table 4-10), although it could have also formed secondarily in the sediment, forming from excess Fe(III)-(oxyhydr)oxides and $Fe(II)_{aq}$, according to

$3Fe^{2+}_{aq} + 6OH^- + 6Fe(OH)_3 \rightarrow 3Fe_3O_4 + 12H_2O$ (Heimann et al., 2010).

The slope setting in the GWA, on the other hand, contains more sediment layers containing Fe(III)-(oxyhydr)oxides (Sumner and Beukes, 2006), which could have been a driver for enhanced DIR in the slope facies, as indicated by siderite microbands that occasionally occur throughout the slope succession (Fischer et al., 2009; Schroeder et al., 2006).

Some carbonates in the Monte Christo Formation also show traces of Fe(II)-sulfides as indicated by XANES spectra (Table 4-10). Considering, that those carbonates were originally deposited under (sub)oxic conditions shows that strong redox gradients prevailed, and that aqueous sulfide species from the pore water likely migrated between adjacent mudrock and carbonate layers. This is supported by strongly varying $\delta^{98}Mo$ signatures (-0.82 to +1.40 ‰) in the mudrock-rich Oaktree and Monte Christo formations (Table 4-7; Fig. 7-1), as Mo is strongly influenced by the flux of dissolved sulfide and organic matter that scavenge and remobilize Mo during early diagenesis within the sediment (Fig. 7-3). Elevated Fe# values in the peritidal setting of the Monte Christo Formation also indicate localized Fe circulation during diagenesis. All these observations can explain the heavier $\delta^{56}Fe$ signatures of carbonates in the Monte Christo Formation (Fig. 8-3), which were likely influence by diagenetically mobilized $Fe(II)_{aq}$ from isotopically heavy mudrocks. A study on a carbonate succession from the Upper Jurassic (Kimmeridge Clay Formation, UK) reported that carbonates adjacent to isotopically light, organic- and pyrite-rich mudrocks also showed a lighter Fe isotope compositions relative to mudrock-free carbonate layers in the same succession. They concluded that carbonates are locally affected by mudrocks in course of diagenetic Fe circulation in the sediment (Matthews et al., 2004). Analogous to this study we propose that the isotopically heavy mudrocks of the Monte Christo formation influenced the adjacent carbonates.

Platform carbonates of the Upper CMCP were deposited in the context of the rimmed margin architecture and are isotopically lighter than the Monte Christo carbonates, but still heavier than the potentially 'Rayleigh'-dependent carbonates exposed to the open ocean. Due to the rimmed margin the interior lagoon influx of open ocean water was restricted and freshwater from the continent had a greater impact on the carbonates. This is shown by REE+Y spectra and elevated Fe#, indicating that Fe transported via riverine water influenced the carbonates. Riverine water has variable but preferentially lighter $\delta^{56}Fe$ signatures between about -0 and -1 ‰ and could thus explain the mean of -0.73 ± 0.36 ‰

in the Upper CMCP carbonates of the platform facies. The impact on the Fe isotope signature because of Fe(II) oxidation in the Eccles and Lyttleton formation, which contain goethite, is not really clear. The fractionation factor between $Fe(II)_{aq}$ and goethite is experimentally determined and reported as -1.05 ± 0.08 ‰ (Beard et al., 2010), although the fractionation factor might be different for the oxidation of adsorbed Fe(II) on carbonate (Mettler, 2002). Moreover, Lyttleton and Eccles formations show no difference in their Fe isotope composition, even though the dominant Fe phase in Lyttleton carbonates is ankerite and only minor goethite, whereas Eccles mainly contains goethite. It still remains elusive, how and if this change in Fe speciation had an effect on the isotope composition at all and if there might be a diagenetic effect after all, influencing the carbonates, similar to the processes in the Monte Christo formation.

8.4. Implications for redox state of Neoarchean shallow seawater and for carbonates as Fe redox proxy

Carbonate platforms and their shallow-marine environment are the interface of oceanic and terrestrial processes. In a predominantly anoxic Neoarchean world with a much higher $Fe(II)_{aq}$ concentration in seawater and presumably limited oxidative weathering than today, hydrothermal vents were most likely the major Fe source, with moderate contributions from continental freshwater sources. Fe concentration, isotope composition and speciation in carbonates and mudrocks of the Neoarchean CMCP give insights into the dynamics of those two sources and unravel redox processes influencing the Fe inventory in the shallow-marine system. Pure carbonates, deposited during open marine conditions, record a Rayleigh titration of ferruginous deeper water and oxygenated shallow water, although a fractionation by anaerobe photoferrotrophs cannot be ruled out. Calculations of $Fe(II)_{aq}$ incorporation into calcite indeed implicate a concentration gradient from the slope facies to the platform facies of the CMCP and support the loss of $Fe(II)_{aq}$ via oxidation and precipitation of $Fe(III)_{ppt}$. Concentration estimates of $Fe(II)_{aq}$ are around 180 µM for shallow-marine seawater and 555 µM for the open ocean and therefore higher than earlier estimates. However, those are strongly dependent on water temperature, sedimentation rate and Ca^{2+}_{aq} concentration in the seawater. Carbonates, which were deposited in the peritidal settings and during the rimmed margin stage, reveal that Fe cycling in the platform interior was dominated by freshwater input from the continent and early diagenetic Fe remobilization in the soft sediment, in particular from adjacent mudrocks. However, there is no clear indication that dolomitization and silicification affected the Fe isotope signatures. Instead, Fe would have been rather added from leaching and dissolution of siliciclastics, sulphides and oxyhydroxides to altered carbonates (Veizer, 1983). Fe speciation of CMCP

carbonates reveals an increase to higher oxidation state throughout the platform, with a Fe(II)-dominated speciation in the lower CMCP and a Fe(III)-dominated speciation in the upper CMCP. This can be explained by a lower content of reductants in the upper CMCP, in particular organic carbon and sulfide species, and by the rimmed margin architecture, protecting the environment from reducing species from the anoxic open ocean.

This study strongly implicates that Ca-Mg carbonates are good and valuable proxies for Fe systematics in ancient shallow-marine systems and can give insights into Fe sources, redox-processes and secondary Fe circulation in the sediment. An important requirement is that the depositional environment is well reconstructed by major and trace element data and sedimentological observations. Thus, further studies are necessary to refine the use of this proxy and to maybe extend it to other aquatic systems, e.g. lakes.

9. Summary and implications for the evolution of Archean oxygen oases

The emergence of oxygenic photosynthesis in the Archean shallow marine environment initiated a marine redox evolution, reflected in shifts in the concentration and isotope composition of redox-sensitive elements deposited to sediments from seawater. A great example thereby is the Neoarchean Campbellrand-Malmani carbonate platform (South Africa) that was deposited about 200 Ma before the Great Oxidation Event and contains geochemical and biological signatures that indicate early oxygen production and possibly represents an 'oxygen oases' in an otherwise anoxic world.

In order to examine if the CMCP was an oxygen oases and to understand how this oxygen oasis developed over time, a detailed biogeochemical and sedimentological reconstruction of the paleoenvironmental conditions was conducted. Thereby, the study focused on the platform succession and complimented data of other studies from the slope succession of the CMCP. In the following the aims of this study are revisited and main findings are listed:

(1) The paleoenvironmental reconstruction of the CMCP in the interface of marine and terrestrial systems

- Based on sedimentological observations, the CMCP can be divided into a lower CMCP, characterized by a steep ramp architecture, and an upper CMCP, characterized by a rimmed margin architecture.
- Changing Fe/Mn ratios of carbonates argue for a water depth dependence as a result of the lower redox potential of Fe compared to Mn, and thus varying with sea level change during trans- and regression events.
- PAAS-normalized REE+Y distributions reveal two major water sources, from the open ocean transporting hydrothermal species, and freshwater from the continent supplying detrital material. The supply of those different sources is dependent on the seawater level and the platform architecture.
- $Fe(II)_{aq}$ concentrations in seawater were probably about three times higher along the slope than on the platform due to higher exchange with open ocean water. The estimates range from 61 to 928 µM $Fe(II)_{aq}$ for the slope and 28 to 288 µM $Fe(II)_{aq}$ for the platform, depending on temperature, Ca^{2+} concentration in seawater and sedimentation rate.
- Early diagenetic remobilization of Fe and Mo can be observed in carbonate successions that contain abundant mudrock layers, and is probably driven by degradation of organic matter during dissimilatory iron reduction (DIR) and bacterial sulfate

reduction (BSR). Localized diagenetic element cycling in is also supported by secondary Fe-sulfides present in mudrocks and some carbonates.

- Large-scale dolomitization of most of the CMCP, probably within the first 1-2 Ma after deposition, argues for interaction between seawater and freshwater in particular in the very shallow-marine platform facies.
- Silicification is also caused by interaction between seawater and freshwater, however, it is more restricted to the peritidal environment and becomes more abundant in the upper CMCP, after the development of the rimmed margin.
- Deposition of siliciclastic and organic-rich mudrocks dynamically changes over time in the CMCP. In the lower CMCP, mudrocks are abundant in the shallow-marine platform, while in the upper CMCP mudrocks are scarce on the platform, but accumulate along the slope, indicating changes in the supply from the continent and maybe higher primary production and heterotrophic respiration in the platform and higher rates of organic burial along the slope.

(2) The reconstruction of the redox conditions of the CMCP

- δ^{98}Mo values of some carbonates and mudrocks from the CMCP are heavier than the crustal range, with up to +1.4 ‰ in platform sediments (this study) and +1.7 ‰ in slope sediments (Voegelin et al., 2010; Wille et al., 2007). Those can be regarded as minimum values of ocean water Mo isotopic composition at the time of deposition and indicate sufficient oxygen in the atmosphere to mobilize Mo from the continental by oxidative weathering (Greber et al., 2015), leading to the buildup of an isotopically heavy marine Mo reservoir.
- Carbonate sections that were deposited along the slope in contact with open ocean and during the early stages of carbonate platform evolution and intensive transgression events, record an Fe pool that is diminishing in concentration and becoming isotopically lighter, consistent with being the residual Fe(II) remaining after Fe oxidation. Those findings support the existence of an oxic-anoxic boundary in the Neoarchean shallow sea, although an anaerobe oxidation pathway via microbial activity cannot be ruled out.
- δ^{98}Mo and δ^{56}Fe fluctuations in mudrocks and adjacent carbonates display changing redox conditions and redox zonation within the soft sediment during early diagenesis, which influenced the Mo and Fe mobility and isotopic composition on a small scale.
- Authigenic Mo enrichment and Fe remobilization during early and probably microbial-driven diagenesis overprinted the initially incorporated seawater molybdate and Fe(II) in the precipitated carbonates. Thereby, the flux of organic carbon and

dissolved sulfur species control early diagenetic redox cycling between mudrock and carbonate sediments and affect their Mo and Fe inventory:

- Mo is scavenged and remobilized within sediment and pore water during degradation of organic matter and circulating dissolved sulfur species. Distinction between the role of supply of water column organics or organics supplied by biological mats to Mo remobilization in biologically-induced carbonates is difficult, but regardless, both scenarios likely influenced the perturbation of Mo concentration and isotopic signals.
- Heavy $\delta^{56}Fe$ signatures in mudrocks of platform succession indicate BSR as dominant pathway of organic matter oxidation, whereas light $\delta^{56}Fe$ signatures in mudrocks of the slope indicate a dominance of DIR. Those early diagenetic processes clearly affected adjacent carbonates due to circulating pore fluids.

- Fe speciation changes over time in the carbonates of the CMCP. In the lower CMCP Fe(II) species dominate, incorporated into the dolomite structure and as distinctive Fe(II)-sulfides in the sediment. This changes towards the upper CMCP, as soon as the rimmed margin was formed, when Fe(III)-(oxyhydr)oxides, in form of goethite, dominate the shallow-marine platform facies and are incorporated in the carbonate. A possible scenario would be the adsorption of $Fe(II)_{aq}$ from solution on calcite and its subsequent oxidation to goethite, likely by photosynthetically produced oxygen.
- Heavier $\delta^{13}C_{carb}$ values on the platform facies of the upper CMCP compared to the slope facies support a continued removal of light ^{12}C from the system, as indicated by the deposition of organic-rich mudrocks along the slope facies of the upper CMCP. This also implicates the supply of nutrients, presumably from local oxidative continental weathering that must have further fueled microbial growth on the platform.
- Heavier $\delta^{13}C_{org}$ signatures in peritidal platform carbonates compared to the slope facies support indications from heavier $\delta^{13}C_{carb}$ values and argue for an enhanced activity of oxygenic phototrophs in the shallow-marine environment. This is also supported by reduced exchange of in the very shallow water facies and thus hydrothermal species (i.e. Fe(II)), which diminished the activity of anaerobe photo- and chemolithotrophic microorganisms and also diminished the risk of Fe toxicity on oxygenic phototrophs. However, light $\delta^{13}C_{org}$ signatures down to ~40 ‰ in mudrocks rather indicates anaerobe activity locally within the sediment, restricted to the mudrock partings. Such negative excursions can be explained, for example, by cycling of methane or BSR during anoxic diagenetic conditions.

(3) The evaluation of the potential of ancient Ca-Mg carbonates as proxies for trace metal systematics in the shallow seawater

- Despite early diagenetic dolomitization and silicification, pristine information of geochemical indicators like Fe, Mn, and REE+Y signatures can still be connected to changes in water depth and different water sources and thus allow a paleoenvironmental reconstruction.
- Mo isotope ratios in some Ca-Mg carbonates reveal heavy signatures and might reflect primary signatures. However, early diagenetic processes dominated the Mo cycling in the carbonates, in particular adjacent to mudrock partings. Thus, at least in the CMCP, Mo analyses can rather be used to obtain information about diagenetic cycling in the sediment than about the seawater evolution of Mo. Future studies on other ancient carbonate platforms with different depositional conditions could give more implications about this issue.
- Fe isotope systematics of Ca-Mg carbonates are more promising to reflect seawater systematics than Mo, as some carbonates that were deposited during intense exchange with open ocean water reflect coupled Fe concentration and isotope signature that can be explained by titration of Fe from seawater by oxidation and allow the calculation of $Fe(II)_{aq}$ concentrations in seawater. Compared to that Fe systematics in the shallow-marine environment with restricted access of open ocean water rather reflect secondary Fe remobilization during diagenesis. However, those signatures are, similar to Mo, valuable to draw implications about the biogeochemical processes.
- Overall, we propose that Mo and Fe isotope signatures and concentrations of Ca-Mg carbonates can serve as good proxies for paleoenvironmental reconstructions and biogeochemical processes of ancient shallow-marine settings. Thereby, it is crucial to complement the isotope data with other mineralogical, sedimentological, and geochemical information of the targeted carbonate setting to evaluate diagenetic alteration of the primary isotopic signals.

Based on the findings of the study, the lower and the upper CMCP can be subdivided into two stages of platform evolution each, which are illustrated in Figures 9-1 and 9-2. Overall, the biogeochemical systematics mainly governed by water depth, water circulation, water source, detrital supply, platform architecture and diagenesis in the soft sediment.

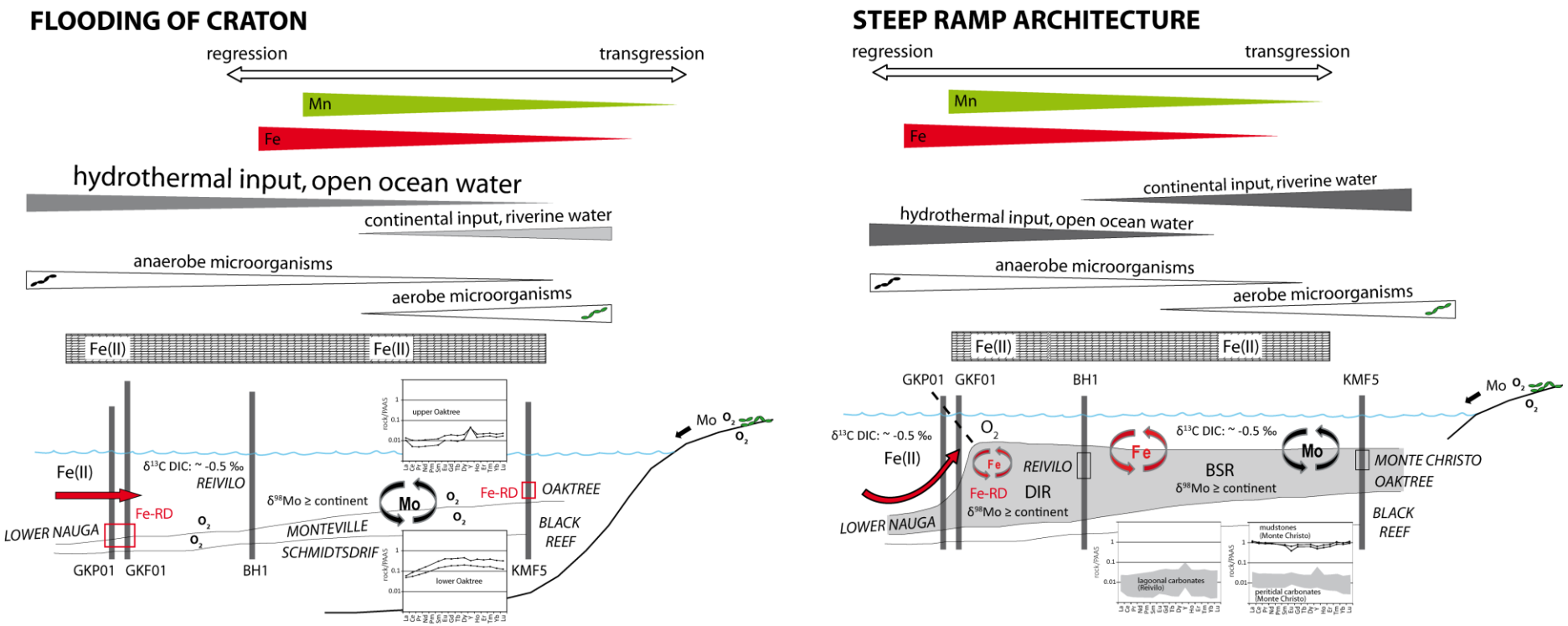

Figure 9-1: During the initial **flooding of the Kaapvaal Craton** ~2.6 Ga ago, enough accommodation space was created for sufficient carbonate sedimentation and the growth of the platform. Carbonates mainly exchanged with open ocean water, and Fe isotope signatures and concentrations indicate Rayleigh distillation of Fe (Fe-RD) by aerobe or anaerobe oxidation. Data also indicate a concentration gradient with higher $Fe(II)_{aq}$ concentrations in the slope facies than in the platform facies. This is also indicated by REE+Y data, which show a shift from hydrothermal dominated signatures to signatures typical for Archean shallow seawater. Mo isotopes signatures already indicate a heavy Mo reservoir in the ocean and supply of Mo from the continent, presumably during oxidative weathering by microbial mats in the terrestrial or supratidal environment (Lalonde and Konhauser, 2015; Reinhard et al., 2013). Even though this is highly speculative, the high influx of reducing hydrothermal species might have been an ecological benefit for anaerobe photolitho- and chemolithoautotrophic bacteria, even though aerobe microorganisms likely belonged to the microbial community. However, dominant Fe(II) species in carbonates indicate rather reducing conditions in the sediment.

With continuing growth of the platform a **steep ramp architecture** developed, which was still connected to the ocean, however during events of regression, influx of continental material and freshwater were of greater importance. This is shown by the frequent occurrence of mudrocks in the peritidal succession of the platform and the change in REE+Y signatures that record an increasing influence of the continent. Even though the influx of ocean water was probably diminished, maybe allowing a shift to a more aerobe ecosystem, the overall conditions in the sediment were still dominantly reducing, as carbonates and solely contain Fe(II) species. However, heavy Mo signatures still indicate an isotopically heavy molybdate pool in the seawater. Overall, the lower CMCP was dominated by secondary remobilization of redox-sensitive elements and microbially-driven diagenesis, whereby DIR dominated the slope facies and BSR the peritidal facies.

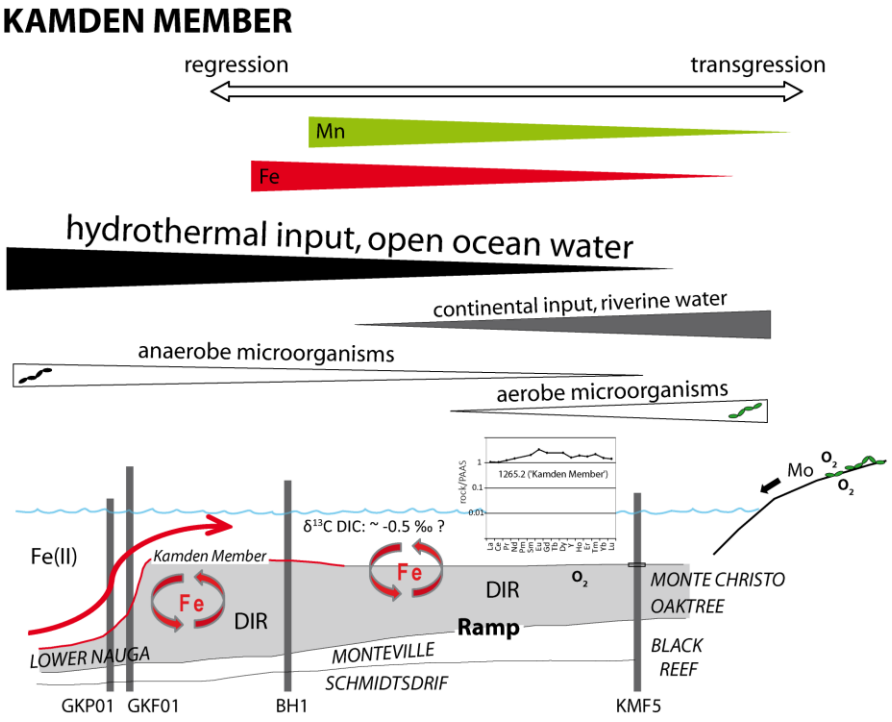

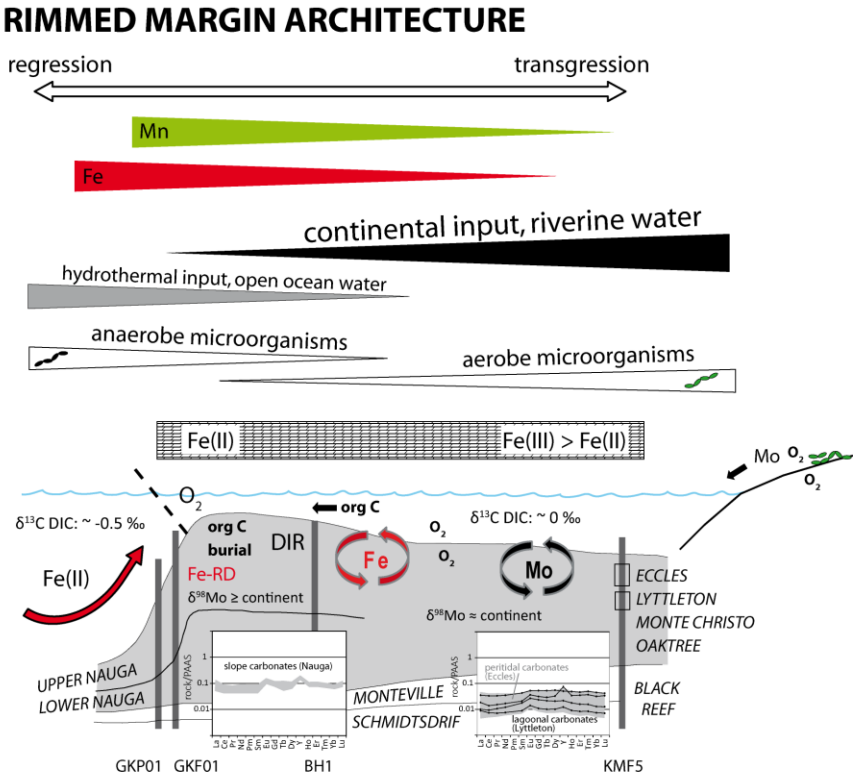

Figure 9-2: The deposition of the **Kamden Member** iron formation was a short intense transgressive event and is reflected in very Fe-rich sediments, even in the very shallow-marine platform succession. There, the intense influx of open ocean water is implicated by a clear positive Eu anomaly in a siliciclastic-rich carbonate. Low $\delta^{13}C_{carb}$ signatures implicate enhanced DIR processes, probably fueled by the enhanced availability of Fe-(oxyhydr)oxides. Furthermore, a high influx of hydrothermal species probably benefitted a rather anaerobe ecosystem.

After the deposition of the Kamden Member and in course of a major transgression, the provided accommodation space was rapidly filled and **rimmed margin architecture** developed, which drastically changed the environmental conditions in the upper CMCP. Due to the special rimmed margin the influx of open ocean water was very poor and a restricted lagoon in the platform interior could develop. Due to the reduced influx of hydrothermal species, the ecosystem probably changed and aerobe microorganisms dominated the lagoonal interior. The relatively enhanced influx of freshwater, indicated by flattened REE+Y patterns, fueled silicification in the peritidal facies. At the same time organic-rich mudrock layers are only scarce in the platform, in contrast to the slope, where more organic-rich mudrocks are deposited, leading to a slight increase in $\delta^{13}C_{carb}$ signatures. This can be explained by an increase in primary production and heterotrophic respiration, which supports a dominantly aerobe ecosystem. The slope succession shows no change in the overall $\delta^{13}C_{carb}$ signature, as it was still mainly exposed to the open ocean, which is indicated by REE+Y signatures that show higher REE+Y concentrations and a more pronounced Eu anomaly. Interestingly, carbonates of the restricted platform interior are dominated by Fe(III) species in form of goethite, that also implicate an increase in the oxidation state of the platform. Mo and Fe systematics are still mainly controlled by secondary sedimentary processes, although the lack of organic-rich mudrocks probably changed the dynamics of Mo and Fe mobilization in the sediment, which is for example indicated by fewer heavy Mo isotope excursions.

This study provided multiple indications that the CMCP indeed represents an ancient oxygen oasis or that at least the oxidation state on the platform significantly increased. However, it also shows that special environmental and depositional conditions were necessary to induce this development. The probably most important factor was the shift from a steep ramp to a rimmed margin architecture. This drastically diminished the influx of reducing hydrothermal fluids from the open ocean and therefore also impacted the respiration pathways of the local ecosystem, changing from anaerobe photo- and chemolithotrophs to dominantly aerobe phototrophs. This change in respiration with the increased supply of availability of redox-sensitive micronutrients under aerobe water column conditions might have fueled primary production and the burial rate of microbially produced organic material in siliciclastic mudrocks along the slope. Overall, increasing oxygen accumulation by oxygenic photosynthesis and decreasing the amount of reducing species in the rimmed margin stage of the CMCP is very likely and strongly supported by the preservation of Fe(III) species in the carbonates and heavier $\delta^{13}C_{carb}$ signatures that point to an increasing oxidation state.

For future studies other ancient carbonate platforms or carbonates from terrestrial freshwater systems, e.g. lakes, would be interesting targets, in order to see if there is a similar systematic like in the CMCP or if other conditions prevailed. This would further improve our knowledge about the phenomenon 'oxygen oasis' and would help to set constraints for their requirement. Furthermore, more detailed studies on the behavior of Mo and Fe in microbial mats and carbonates are necessary provide a framework for more precise interpretation of the processes impacting Mo and Fe concentrations and their isotopic composition in biologically-precipitated carbonates.

Appendices

1. Detailed log of drill core KMF-5

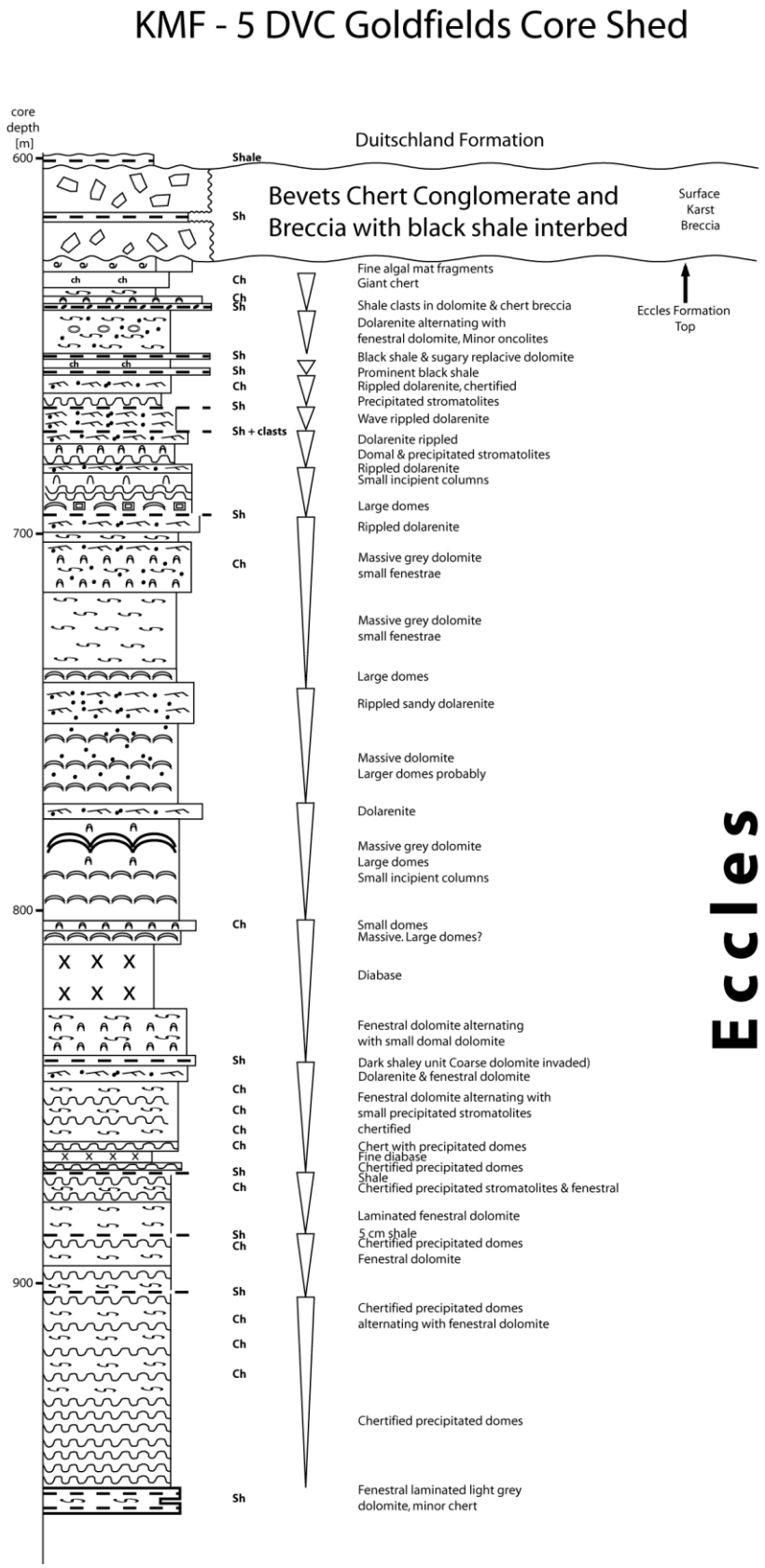

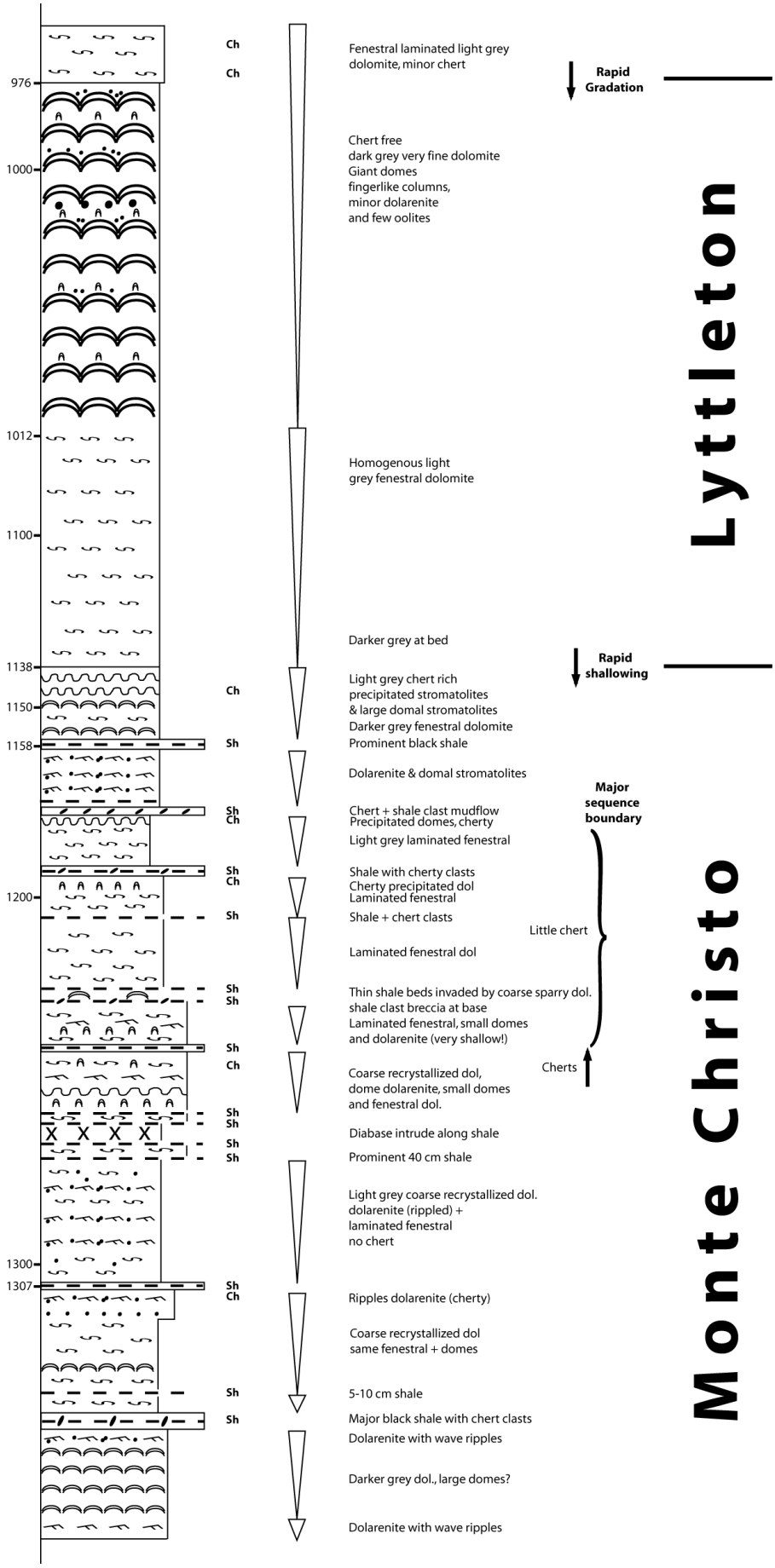
976
1000
1012
1100
1138
1150
1158
1200
1300
1307
Ch
Sh
Fenestral laminated light grey dolomite, minor chert
Rapid Gradation
Chert free
dark grey very fine dolomite
Giant domes
fingerlike columns,
minor dolarenite
and few oolites
Homogenous light
grey fenestral dolomite
Darker grey at bed
Rapid shallowing
Light grey chert rich
precipitated stromatolites
& large domal stromatolites
Darker grey fenestral dolomite
Prominent black shale
Dolarenite & domal stromatolites
Major sequence boundary
Chert + shale clast mudflow
Precipitated domes, cherty
Light grey laminated fenestral
Shale with cherty clasts
Cherty precipitated dol
Laminated fenestral
Shale + chert clasts
Little chert
Laminated fenestral dol
Thin shale beds invaded by coarse sparry dol.
shale clast breccia at base
Laminated fenestral, small domes
and dolarenite (very shallow!)
Cherts
Coarse recrystallized dol,
dome dolarenite, small domes
and fenestral dol.
Diabase intrude along shale
Prominent 40 cm shale
Light grey coarse recrystallized dol.
dolarenite (rippled) +
laminated fenestral
no chert
Ripples dolarenite (cherty)
Coarse recrystallized dol
same fenestral + domes
5-10 cm shale
Major black shale with chert clasts
Dolarenite with wave ripples
Darker grey dol., large domes?
Dolarenite with wave ripples
Lyttleton
Monte Christo

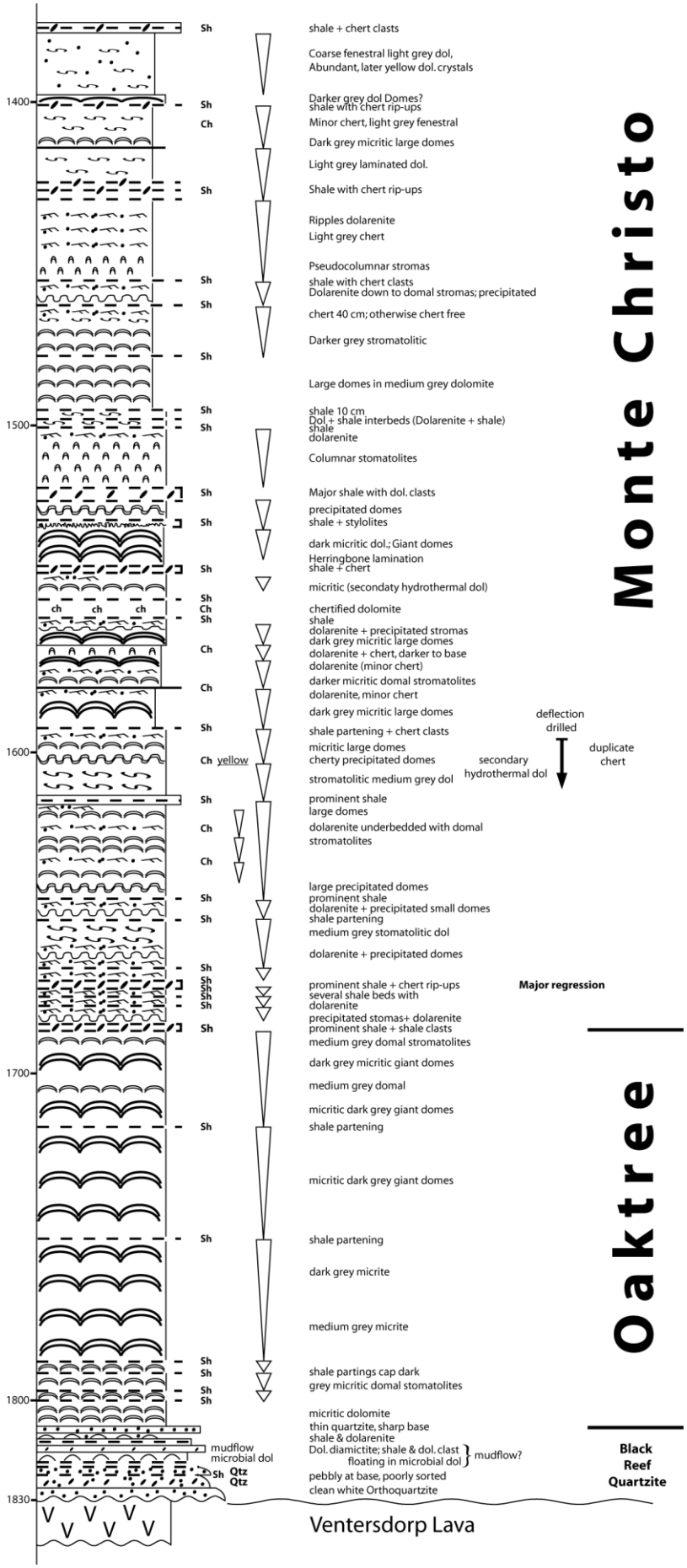
Monte Christo
Oaktree
Black Reef Quartzite
Ventersdorp Lava
1400
1500
1600
1700
1800
1830
shale + chert clasts
Coarse fenestral light grey dol, Abundant, later yellow dol. crystals
Darker grey dol Domes?
shale with chert rip-ups
Minor chert, light grey fenestral
Dark grey micritic large domes
Light grey laminated dol.
Shale with chert rip-ups
Ripples dolarenite
Light grey chert
Pseudocolumnar stromas
shale with chert clasts
Dolarenite down to domal stromas; precipitated
chert 40 cm; otherwise chert free
Darker grey stromatolitic
Large domes in medium grey dolomite
shale 10 cm
Dol + shale interbeds (Dolarenite + shale)
shale
dolarenite
Columnar stomatolites
Major shale with dol. clasts
precipitated domes
shale + stylolites
dark micritic dol.; Giant domes
Herringbone lamination
shale + chert
micritic (secondaty hydrothermal dol)
chertified dolomite
shale
dolarenite + precipitated stromas
dark grey micritic large domes
dolarenite + chert, darker to base
dolarenite (minor chert)
darker micritic domal stromatolites
dolarenite, minor chert
dark grey micritic large domes
shale partening + chert clasts
micritic large domes
cherty precipitated domes
stromatolitic medium grey dol
yellow
deflection drilled
duplicate chert
secondary hydrothermal dol
prominent shale
large domes
dolarenite underbedded with domal stromatolites
large precipitated domes
prominent shale
dolarenite + precipitated small domes
shale partening
medium grey stomatolitic dol
dolarenite + precipitated domes
prominent shale + chert rip-ups
several shale beds with dolarenite
precipitated stomas+ dolarenite
prominent shale + shale clasts
Major regression
medium grey domal stromatolites
dark grey micritic giant domes
medium grey domal
micritic dark grey giant domes
shale partening
micritic dark grey giant domes
shale partening
dark grey micrite
medium grey micrite
shale partings cap dark
grey micritic domal stomatolites
micritic dolomite
thin quartzite, sharp base
shale & dolarenite
Dol. diamictite; shale & dol. clast floating in microbial dol
mudflow?
mudflow
microbial dol
pebbly at base, poorly sorted
clean white Orthoquartzite
Sh
Ch
Qtz

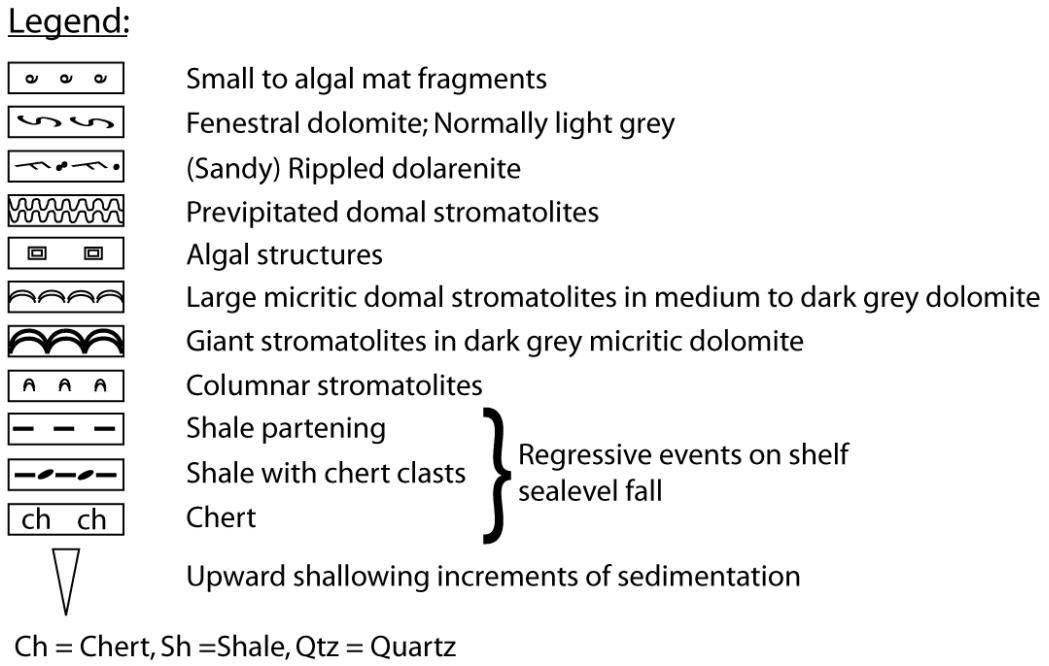

Note: Shale ≙ Mudrock (fine grained siliciclastic sedimentary rock); Core logging results were generously provided by Nic Beukes

2. Mo adsorption on Multifex calcite as a function of pH

Note: All experiments described below were performed by S. Goldberg, who generously provided information about the experimental set-up and results for this study.

Adsorption experiments were performed with Multifex calcite, which was in suspension in a Mo containing stock solution (200 g $CaCO_3$ per liter stock solution). Two stock solutions of different concentration were used during the experiment. The goal was to determine the adsorption of Mo on calcite at different pH and at different concentrations. Results are summarized in Table A-1 and A-2. Figure A-1 shows an approximation of adsorbed Mo on calcite in form of a non-linear fit, which allows making a good assumption for the amount of adsorbed Mo at a certain pH level. Obviously, the amount of adsorbed Mo is not influenced by the Mo concentration in the stock solution but rather by the prevailing pH value. Therefore, we can assume that a similar adsorption pattern also looms for seawater Mo values (Modern: 0.1 µmol/L (Collier, 1985); Neoarchean: 0.001 µmol/L (Czaja et al., 2012) to 0.01 µmol/L (Scott et al., 2008)(Scott et al., 2008)). In Figure A-2 presumable adsorption of Mo on calcite at a different solution concentrations is shown, together with concentrations of natural modern (Voegelin et al., 2009) and Neoarchean (this study) samples. Results are showing that modern samples are nearly in agreement with the adsorption line. Neoarchean samples plot clearly beside this line, indicating that other processes were involved in Mo inventory of the carbonates.

Table A-1: Stock solution = 99.82 mg Mo per liter (Goldberg, pers. comm.)

pH	Mo in solution (mg/L)	Mo adsorbed (mmol/kg $CaCO_3$)	Mo adsorbed (wt%/g $CaCO_3$)
7.2	76.68	6.03	0.116
7.31	80.61	5.01	0.096
7.43	80.32	5.08	0.098
7.45	76.63	6.04	0.1168
7.82	86.8	3.39	0.0658
8.12	83.66	4.21	0.081
8.29	89.45	2.70	0.052
8.51	91.91	2.06	0.040
8.8	92.43	1.93	0.037
8.95	85.57	3.71	0.071
9.11	93.07	1.76	0.034
9.28	93.56	1.63	0.031
9.58	92.41	1.93	0.037
9.81	95.44	1.14	0.022
9.92	92.97	1.78	0.034
9.99	93.71	1.59	0.031

Table A-2: Stock solution = 26.94 mg Mo per liter (Goldberg, pers. comm.)

pH	Mo in solution (mg/L)	Mo adsorbed (mmol/kg $CaCO_3$)	Mo adsorbed (wt%/g $CaCO_3$)
7.13	20.63	20.63	0.117
7.28	20.89	20.89	0.112
7.52	21.97	21.97	0.092
7.76	22.68	22.68	0.079
8.17	23.75	23.75	0.059
8.68	24.49	24.49	0.046
8.95	24.6	24.6	0.043
9.37	25.02	25.02	0.036
9.62	24.98	24.98	0.036
9.92	24.77	24.77	0.040
10.14	24.89	24.89	0.038
10.33	24.9	24.9	0.038
10.5	24.98	24.98	0.036
10.66	24.89	24.89	0.038
10.72	25.03	25.03	0.036
10.85	25.18	25.18	0.033

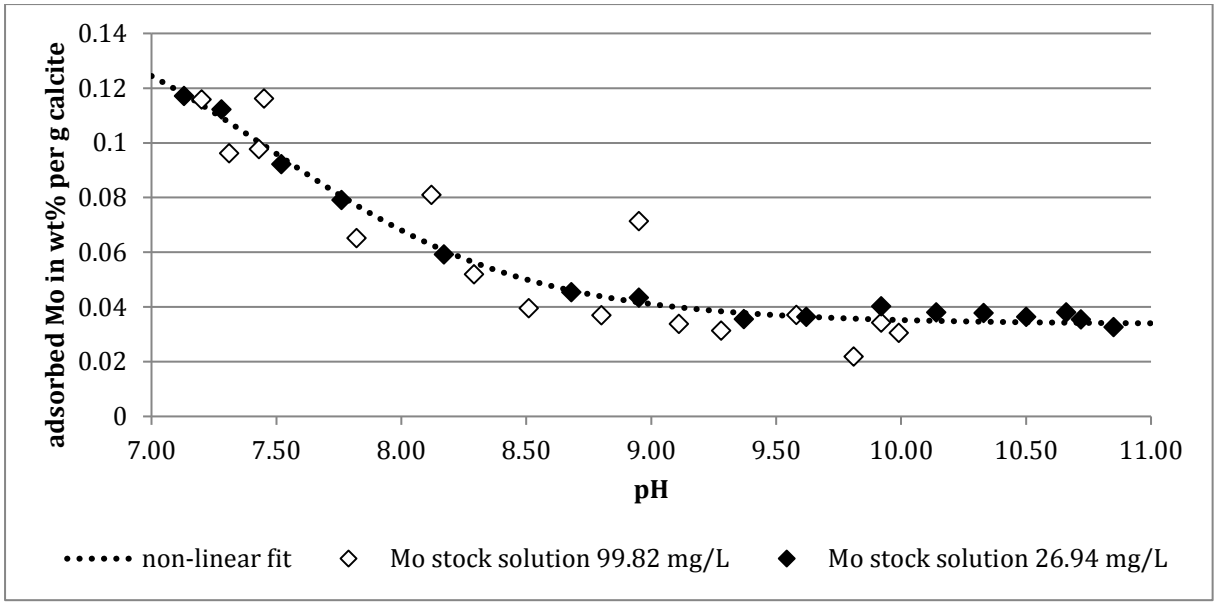

Figure A-1: Results of adsorption experiments in dependency of pH and at different solution concentrations (Goldberg, personal communication).

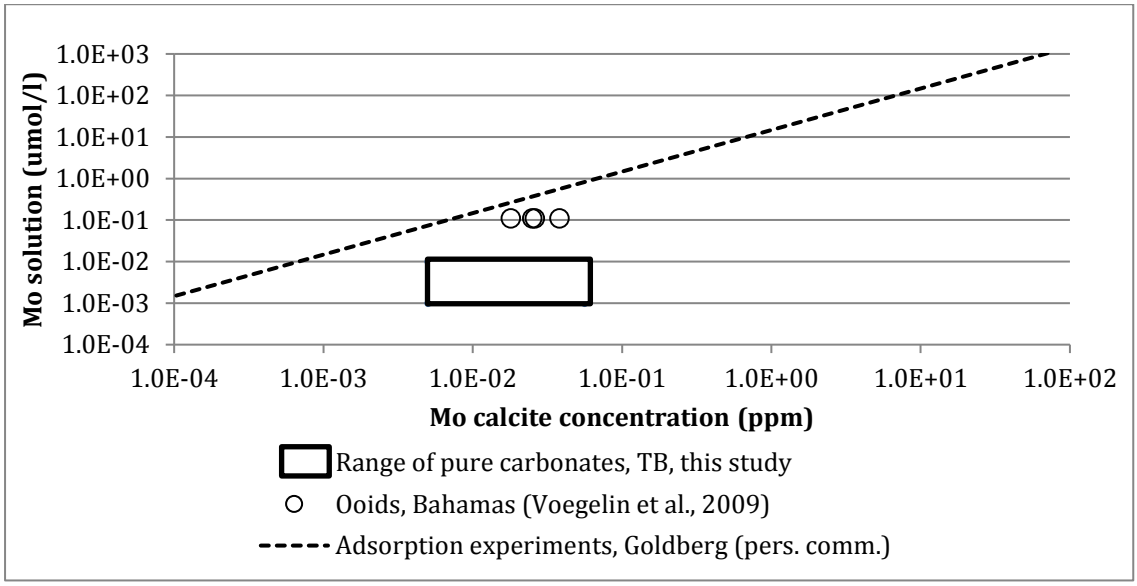

Figure A-2: Approximation for adsorbed Mo on calcite from solution and concentrations of natural modern (Voegelin et al., 2009) and Neoarchean (this study) samples. Dotted line is based on adsorption experiments performed by Goldberg (personal communication).

3. Additional tables of Fe isotope analyses

Table A-3: Sample-Standard-Bracketing Fe isotope results of single measurements of KMF-5 samples

Depth (m)	$\delta^{56}Fe_{avg}$ (‰)	$\delta^{57}Fe_{avg}$ (‰)	Analyses 1						Analyses 2						Analyses 3					
			$\delta^{56}Fe$ (‰)	2σ	$\delta^{57}Fe$ (‰)	2σ	$\delta^{58}Fe$ (‰)	2σ	$\delta^{56}Fe$ (‰)	2σ	$\delta^{57}Fe$ (‰)	2σ	$\delta^{58}Fe$ (‰)	2σ	$\delta^{56}Fe$ (‰)	2σ	$\delta^{57}Fe$ (‰)	2σ	$\delta^{58}Fe$ (‰)	2σ
665.08	-0.88	0.04	-0.85	0.04	-0.97	0.10	-1.35	0.59	-0.96	0.05	-1.46	0.09	-2.31	0.45	-0.84	0.04	-0.96	0.09	-1.38	0.66
665.18	-0.66	0.04	-0.65	0.04	-0.99	0.09	-1.58	0.48	-0.68	0.04	-1.04	0.08	-1.16	0.59						
673.84	-0.75	0.04	-0.75	0.05	-1.12	0.08	-1.96	0.56	-0.74	0.04	-1.12	0.08	-1.94	0.44						
674.55	-0.88	0.05	-0.90	0.05	-1.33	0.08	-1.94	0.49	-0.86	0.04	-1.27	0.08	-1.84	0.46						
678.60	-0.80	0.05	-0.81	0.04	-1.10	0.08	-1.01	0.49	-0.80	0.05	-1.22	0.07	-1.43	0.49						
680.58	-0.82	0.04	-0.83	0.03	-1.23	0.07	-1.34	0.44	-0.81	0.05	-1.26	0.09	-1.60	0.45						
682.70	-0.77	0.04	-0.73	0.03	-1.10	0.06	-1.22	0.37	-0.81	0.04	-1.18	0.07	-1.56	0.40						
703.30	-0.75	0.04	-0.72	0.04	-1.08	0.07	-1.59	0.48	-0.77	0.04	-1.13	0.08	-1.42	0.51						
711.80	-0.55	0.04	-0.56	0.05	-0.87	0.07	-1.04	0.49	-0.55	0.04	-0.83	0.08	-1.16	0.50						
875.50	-0.40	0.05	-0.41	0.05	-0.64	0.08	-1.46	0.52	-0.38	0.05	-0.64	0.08	-0.67	0.36						
884.83	-0.47	0.04	-0.49	0.04	-0.69	0.08	-0.51	0.46	-0.45	0.04	-0.72	0.09	-0.70	0.46						
921.78	-0.41	0.03	-0.40	0.03	-0.63	0.07	-0.71	0.44	-0.43	0.03	-0.58	0.07	-0.68	0.39						
1062.50	-0.67	0.03	-0.65	0.03	-0.92	0.07	-1.26	0.36	-0.69	0.03	-1.04	0.06	-1.18	0.35						
1072.73	-0.77	0.04	-0.77	0.04	-1.11	0.06	-1.41	0.36	-0.78	0.04	-1.16	0.07	-1.64	0.34						
1100.20	-0.66	0.04	-0.66	0.04	-0.95	0.06	-0.76	0.42	-0.65	0.03	-0.99	0.07	-1.39	0.30						
1136.75	-0.68	0.03	-0.65	0.03	-0.95	0.07	-1.29	0.42	-0.71	0.04	-1.02	0.08	-1.48	0.30						
1143.70	-0.71	0.05	-0.74	0.05	-1.06	0.08	-1.47	0.46	-0.72	0.05	-1.06	0.08	-1.37	0.48	-0.67	0.04	-0.99	0.08	-1.46	0.40
1199.50	-0.40	0.04	-0.42	0.05	-0.62	0.08	-1.11	0.50	-0.38	0.04	-0.64	0.09	-1.04	0.44						
1202.58	-0.51	0.05	-0.54	0.05	-0.77	0.07	-1.06	0.50	-0.48	0.05	-0.73	0.10	-0.78	0.49						
1239.98	-0.40	0.05	-0.43	0.05	-0.64	0.08	-0.80	0.56	-0.41	0.05	-0.56	0.09	2.12	0.44	-0.36	0.04	-0.60	0.08	-0.54	0.56
1265.10	-0.04	0.03	-0.04	0.04	-0.06	0.07	-0.19	0.36	-0.03	0.03	-0.01	0.07	0.00	0.36						
1350.90	-0.37	0.04	-0.43	0.04	-0.57	0.08	-0.67	0.45	-0.40	0.05	-0.60	0.07	-1.15	0.46	-0.27	0.04	-0.40	0.07	-1.20	0.40
1401.00	-0.35	0.04	-0.36	0.05	-0.57	0.09	-0.99	0.54	-0.35	0.04	-0.56	0.07	-0.29	0.50						
1403.80	-0.35	0.03	-0.34	0.04	-0.54	0.06	-0.80	0.33	-0.36	0.03	-0.50	0.06	-0.72	0.45						
1406.80	-0.33	0.04	-0.30	0.04	-0.43	0.06	-0.24	0.32	-0.37	0.04	-0.57	0.08	-0.70	0.38						
1420.90	-0.46	0.05	-0.47	0.05	-0.76	0.08	-1.13	0.55	-0.45	0.04	-0.72	0.07	-0.71	0.55						
1425.40	-0.36	0.04	-0.34	0.04	-0.48	0.07	-0.77	0.31	-0.39	0.04	-0.53	0.06	-0.67	0.39						
1435.25	-0.35	0.05	-0.35	0.05	-0.59	0.09	-0.72	0.49	-0.35	0.05	-0.57	0.09	-0.56	0.46						
1442.17	-0.66	0.04	-0.66	0.05	-0.95	0.09	1.71	0.49	-0.70	0.04	-1.07	0.09	-1.42	0.61	-0.64	0.04	-1.06	0.08	-1.07	0.51
1454.61	-0.41	0.05	-0.43	0.04	-0.66	0.08	-1.00	0.57	-0.39	0.05	-0.70	0.08	-0.54	0.50						
1461.80	-0.41	0.04	-0.43	0.04	-0.63	0.07	-1.36	0.49	-0.39	0.04	-0.66	0.08	-0.81	0.50						
1464.30	-0.50	0.04	-0.52	0.04	-0.73	0.08	-1.04	0.50	-0.48	0.04	-0.77	0.07	-1.34	0.47						
1467.10	-0.37	0.04	-0.41	0.04	-0.66	0.08	-1.02	0.44	-0.34	0.04	-0.53	0.08	-1.38	0.53						
1475.35	-0.40	0.04	-0.43	0.04	-0.66	0.08	-1.37	0.49	-0.36	0.04	-0.60	0.07	-1.46	0.51						
1484.80	-0.28	0.04	-0.26	0.04	-0.39	0.07	-0.57	0.38	-0.30	0.04	-0.43	0.06	-0.50	0.36						
1491.85	-0.35	0.04	-0.38	0.04	-0.59	0.08	-0.73	0.47	-0.32	0.04	-0.53	0.07	-0.99	0.50						
1499.85	0.20	0.05	0.14	0.05	0.27	0.08	0.44	0.52	0.17	0.04	0.24	0.08	-0.14	0.46	0.29	0.05	0.44	0.09	-0.28	0.44
1524.70	-0.41	0.04	-0.42	0.04	-0.61	0.06	-0.95	0.37	-0.39	0.04	-0.53	0.07	-0.89	0.34						
1539.90	-0.38	0.04	-0.40	0.04	-0.56	0.08	-0.59	0.52	-0.44	0.04	-0.60	0.07	-1.22	0.85	-0.30	0.04	-0.46	0.09	-0.94	0.44

Table A-3 continued

1551.70	-0.27	0.05	-0.30	0.05	-0.43	0.08	-0.77	0.43	-0.24	0.05	-0.37	0.07	-1.33	0.48						
1557.70	0.79	0.05	0.76	0.05	1.10	0.08	1.08	0.43	0.81	0.04	1.17	0.07	1.00	0.47						
1558.88	-0.25	0.04	-0.30	0.04	-0.40	0.09	-1.74	0.98	-0.26	0.03	-0.33	0.07	-0.84	0.54	-0.20	0.05	-0.29	0.09	-1.06	0.46
1574.15	-0.23	0.04	-0.28	0.04	-0.38	0.10	-0.52	0.43	-0.22	0.04	-0.34	0.06	-0.65	0.60	-0.19	0.04	-0.29	0.09	-0.70	0.43
1574.25	-0.20	0.05	-0.23	0.05	-0.34	0.09	-0.71	0.53	-0.18	0.05	-0.25	0.09	-0.76	0.47						
1574.30	-0.24	0.04	-0.29	0.05	-0.45	0.09	0.05	1.44	-0.23	0.05	-0.32	0.08	-3.53	0.44	-0.18	0.04	-0.26	0.08	-0.84	0.50
1589.75	-0.27	0.04	-0.31	0.05	-0.45	0.07	0.02	1.44	-0.20	0.04	-0.32	0.09	-0.75	0.43	-0.30	0.04	-0.44	0.08	-0.59	0.47
1589.90	-0.22	0.04	-0.25	0.05	-0.38	0.08	-0.54	0.45	-0.25	0.04	-0.40	0.07	0.05	0.42	-0.15	0.04	-0.23	0.09	-0.76	0.44
1604.60	-0.28	0.03	-0.24	0.03	-0.40	0.06	-0.41	0.47	-0.32	0.03	-0.50	0.07	-0.78	0.33						
1673.30	0.38	0.05	0.34	0.04	0.46	0.07	0.32	0.56	0.42	0.06	0.62	0.08	-0.28	0.47						
1731.10	-0.62	0.04	-0.63	0.04	-0.94	0.07	-1.11	0.45	-0.60	0.04	-0.85	0.06	-1.25	0.33						
1731.30	-0.67	0.03	-0.70	0.03	-1.01	0.07	-1.39	0.33	-0.63	0.03	-0.91	0.07	-1.04	0.35						
1742.30	-0.72	0.04	-0.71	0.04	-1.03	0.06	-1.68	0.42	-0.73	0.04	-1.04	0.07	-1.38	0.34						
1776.00	0.62	0.04	0.58	0.04	0.85	0.09	1.10	0.46	0.65	0.04	1.03	0.07	0.64	0.45						
1790.10	0.08	0.04	0.06	0.05	-0.01	0.08	0.13	0.48	0.10	0.04	0.11	0.09	-0.61	0.41						
1800.10	-0.32	0.04	-0.35	0.05	-0.55	0.07	-0.53	0.49	-0.28	0.04	-0.46	0.08	-1.32	0.43						
1800.30	0.44	0.05	0.40	0.05	0.59	0.07	-4.95	0.53	0.48	0.04	0.68	0.08	0.46	0.40						
1811.20	0.24	0.04	0.20	0.04	0.34	0.07	-0.32	0.52	0.28	0.04	0.39	0.08	-0.33	0.55						

2σ: 2 sigma standard deviation of 20 measurement cycles per sample analysis on ICP-MS

Table A-4: Sample-Standard-Bracketing Fe isotope results of single measurements of BH-1 samples

Depth (m)	$\delta^{56}Fe_{avg}$ (‰)	$\delta^{57}Fe_{avg}$ (‰)	Analyses 1						Analyses 2						Analyses 3					
			$\delta^{56}Fe$ (‰)	2σ	$\delta^{57}Fe$ (‰)	2σ	$\delta^{58}Fe$ (‰)	2σ	$\delta^{56}Fe$ (‰)	2σ	$\delta^{57}Fe$ (‰)	2σ	$\delta^{58}Fe$ (‰)	2σ	$\delta^{56}Fe$ (‰)	2σ	$\delta^{57}Fe$ (‰)	2σ	$\delta^{58}Fe$ (‰)	2σ
340	-1.82	-2.65	-1.82	0.04	-2.64	0.07	-3.61	0.49	-1.82	0.04	-2.67	0.06	-3.29	0.50						
375	-0.85	-1.26	-0.85	0.04	-1.23	0.07	-1.47	0.54	-0.86	0.04	-1.29	0.07	-1.63	0.46						
488	-0.91	-1.28	-0.91	0.05	-1.28	0.09	-1.85	0.42												
670	-0.56	-0.81	-0.57	0.05	-0.84	0.07	-1.41	0.42	-0.55	0.04	-0.79	0.08	-1.20	0.42						
751	-0.93	-1.36	-0.94	0.04	-1.32	0.08	-1.85	0.45	-0.91	0.04	-1.40	0.08	-1.60	0.46						
1235	-0.72	-1.07	-0.73	0.04	-1.05	0.08	-1.52	0.38	-0.71	0.05	-1.09	0.08	-1.46	0.43						
1400	-0.90	-1.25	-0.83	0.05	-1.31	0.08	-1.83	0.43	-0.95	0.04	-1.21	0.08	-1.26	0.66	-0.91	0.06	-1.23	0.08	-1.59	0.49
1425	-0.80	-1.20	-0.81	0.04	-1.19	0.06	-1.90	0.48	-0.79	0.05	-1.20	0.07	-1.34	0.46						
1455	-0.80	-1.19	-0.82	0.04	-1.20	0.07	-1.81	0.44	-0.79	0.04	-1.19	0.07	-1.36	0.45						
1490	-0.50	-0.78	-0.50	0.04	-0.76	0.09	-1.06	0.50	-0.50	0.03	-0.80	0.08	-0.31	0.48						
1520	-0.60	-0.88	-0.61	0.04	-0.96	0.07	-1.37	0.38	-0.61	0.05	-0.84	0.08	-1.20	0.51	-0.59	0.04	-0.84	0.08	-1.12	0.42
1620	-0.60	-0.91	-0.59	0.04	-0.86	0.08	-0.91	0.50	-0.61	0.04	-0.96	0.08	-1.66	0.49						
1750	-1.21	-1.82	-1.22	0.05	-1.81	0.09	-2.47	0.41	-1.20	0.04	-1.82	0.07	-2.51	0.45						
1776	-0.72	-1.10	-0.74	0.05	-1.10	0.07	-1.42	0.41	-0.70	0.04	-1.09	0.08	-1.23	0.45						
1920	-0.95	-1.33	-1.08	0.05	-1.31	0.08	-1.35	0.79	-0.90	0.04	-1.31	0.07	-1.79	0.51	-0.87	0.04	-1.35	0.09	-1.55	0.47
2041	-0.79	-1.19	-0.80	0.03	-1.22	0.06	-1.59	0.34	-0.78	0.03	-1.16	0.07	-1.36	0.39						
2066	-0.57	-0.85	-0.60	0.04	-0.84	0.07	-1.37	0.48	-0.54	0.04	-0.87	0.08	-1.04	0.49						
2098	-0.23	-0.36	-0.23	0.03	-0.39	0.08	-0.49	0.37	-0.22	0.03	-0.32	0.07	-0.45	0.40						
2250	-1.07	-1.57	-1.08	0.04	-1.60	0.06	-2.06	0.38	-1.05	0.03	-1.54	0.06	-2.35	0.35						
2275	-1.04	-1.55	-1.05	0.05	-1.55	0.07	-1.86	0.47	-1.03	0.04	-1.55	0.07	-1.99	0.42						
2293	-1.08	-1.63	-1.11	0.04	-1.67	0.07	-2.29	0.39	-1.05	0.04	-1.58	0.08	-2.07	0.34						
2355	-1.20	-1.85	-1.22	0.03	-1.89	0.07	-2.30	0.46	-1.19	0.04	-1.82	0.07	-1.81	0.47						
2379	-1.07	-1.61	-1.08	0.03	-1.59	0.06	-2.29	0.44	-1.06	0.04	-1.63	0.09	-1.98	0.41						
2400	-1.24	-1.81	-1.25	0.03	-1.81	0.07	-2.50	0.40	-1.22	0.04	-1.80	0.08	-2.22	0.37						

2σ: 2 sigma standard deviation of 20 measurement cycles per sample analysis on ICP-MS

Table A-5: Sample-Standard-Bracketing Fe isotope results of single measurements of Kuruman Kop outcrop samples

Sample Name	$\delta^{56}Fe_{avg}$ (‰)	$\delta^{57}Fe_{avg}$ (‰)	Analyses 1						Analyses 2					
			$\delta^{56}Fe$ (‰)	2σ	$\delta^{57}Fe$ (‰)	2σ	$\delta^{58}Fe$ (‰)	2σ	$\delta^{56}Fe$ (‰)	2σ	$\delta^{57}Fe$ (‰)	2σ	$\delta^{58}Fe$ (‰)	2σ
KU 12/04	0.45	0.65	0.41	0.04	0.58	0.09	0.91	0.52	0.49	0.04	0.71	0.09	0.61	0.44
KU 12/06	-1.74	-2.59	-1.77	0.05	-2.64	0.09	-4.12	0.51	-1.72	0.06	-2.53	0.10	-4.75	0.42
KU 12/26	-0.29	-0.42	-0.32	0.04	-0.47	0.08	2.46	0.57	-0.26	0.04	-0.38	0.09	-0.84	0.51
KU 12/25	-0.70	-1.01	-0.74	0.04	-1.06	0.07	-0.98	0.51	-0.65	0.05	-0.97	0.09	-1.66	0.49
KU 12/31	-0.95	-1.37	-1.01	0.04	-1.46	0.09	0.78	0.53	-0.90	0.04	-1.29	0.08	-2.50	0.45

2σ: 2 sigma standard deviation of 20 measurement cycles per sample analysis on ICP-MS

References

Achterberg, E.P., Holland, T.W., Bowie, A.R., Fauzi, R., Mantoura, C. and Worsfold, P.J. (2001) Determination of iron in seawater. Anal Chim Acta 442, 1-14.

Algeo, T.J. and Lyons, T.W. (2006) Mo-total organic carbon covariation in modern anoxic marine environments: Implications for analysis of paleoredox and paleohydrographic conditions. Paleoceanography 21.

Allan, J.R. and Matthews, R.K. (1982) Isotope Signatures Associated with Early Meteoric Diagenesis. Sedimentology 29, 797-817.

Altermann, W. and Nelson, D.R. (1998) Sedimentation rates, basin analysis and regional correlations of three Neoarchaean and Palaeoproterozoic sub-basins of the Kaapvaal craton as inferred from precise U-Pb zircon ages from volcaniclastic sediments. Sediment Geol 120, 225-256.

Altermann, W. and Schopf, J.W. (1995) Microfossils from the Neoarchean Campbell Group, Griqualand West Sequence of the Transvaal Supergroup, and Their Paleoenvironmental and Evolutionary Implications. Precambrian Res 75, 65-90.

Altermann, W. and Siegfried, H.P. (1997) Sedimentology and facies development of an Archaean shelf: carbonate platform transition in the Kaapvaal Craton, as deduced from a deep borehole at Kathu, South Africa. J Afr Earth Sci 24, 391-410.

Anbar, A.D., Duan, Y., Lyons, T.W., Arnold, G.L., Kendall, B., Creaser, R.A., Kaufman, A.J., Gordon, G.W., Scott, C., Garvin, J. and Buick, R. (2007) A whiff of oxygen before the Great Oxidation Event? Science 317, 1903-1906.

Anbar, A.D. and Rouxel, O. (2007) Metal stable isotopes in paleoceanography. Annu Rev Earth Pl Sc 35, 717-746.

Archer, C. and Vance, D. (2008) The isotopic signature of the global riverine molybdenum flux and anoxia in the ancient oceans. Nat Geosci 1, 597-600.

Arnold, G.L., Anbar, A.D., Barling, J. and Lyons, T.W. (2004) Molybdenum isotope evidence for widespread anoxia in mid-proterozoic oceans. Science 304, 87-90.

Balci, N., Bullen, T.D., Witte-Lien, K., Shanks, W.C., Motelica, M. and Mandernack, K.W. (2006) Iron isotope fractionation during microbially stimulated Fe(II) oxidation and Fe(III) precipitation. Geochim Cosmochim Ac 70, 622-639.

Banner, J.L. (1995) Application of the Trace-Element and Isotope Geochemistry of Strontium to Studies of Carbonate Diagenesis. Sedimentology 42, 805-824.

Barling, J. and Anbar, A.D. (2004) Molybdenum isotope fractionation during adsorption by manganese oxides. Earth Planet Sc Lett 217, 315-329.

Barling, J., Arnold, G.L. and Anbar, A.D. (2001) Natural mass-dependent variations in the isotopic composition of molybdenum. Earth Planet Sc Lett 193, 447-457.

Basile-Doelsch, I., Meunier, J.D. and Parron, C. (2005) Another continental pool in the terrestrial silicon cycle. Nature 433, 399-402.

Bau, M. (1999) Scavenging of dissolved yttrium and rare earths by precipitating iron oxyhydroxide: Experimental evidence for Ce oxidation, Y-Ho fractionation, and lanthanide tetrad effect. Geochim Cosmochim Ac 63, 67-77.

Bau, M. and Dulski, P. (1996) Distribution of yttrium and rare-earth elements in the Penge and Kuruman iron-formations, Transvaal Supergroup, South Africa. Precambrian Res 79, 37-55.

Bau, M. and Dulski, P. (1999) Comparing yttrium and rare earths in hydrothermal fluids from the Mid-Atlantic Ridge: implications for Y and REE behaviour during near-vent mixing and for the Y/Ho ratio of Proterozoic seawater. Chem Geol 155, 77-90.

Bau, M. and Moller, P. (1993) Rare-Earth Element Systematics of the Chemically Precipitated Component in Early Precambrian Iron Formations and the Evolution of the Terrestrial Atmosphere-Hydrosphere-Lithosphere System. Geochim Cosmochim Ac 57, 2239-2249.

Beard, B.L., Handler, R.M., Scherer, M.M., Wu, L.L., Czaja, A.D., Heimann, A. and Johnson, C.M. (2010) Iron isotope fractionation between aqueous ferrous iron and goethite. Earth Planet Sc Lett 295, 241-250.

Beard, B.L., Johnson, C.M., Cox, L., Sun, H., Nealson, K.H. and Aguilar, C. (1999) Iron isotope biosignatures. Science 285, 1889-1892.

Beard, B.L., Johnson, C.M., Skulan, J.L., Nealson, K.H., Cox, L. and Sun, H. (2003a) Application of Fe isotopes to tracing the geochemical and biological cycling of Fe. Chem Geol 195, 87-117.

Beard, B.L., Johnson, C.M., Von Damm, K.L. and Poulson, R.L. (2003b) Iron isotope constraints on Fe cycling and mass balance in oxygenated Earth oceans. Geology 31, 629-632.

Berner, R.A. (1981) A New Geochemical Classification of Sedimentary Environments. Journal of Sedimentary Petrology 51, 359-365.

Berner, R.A. (1989) Biogeochemical Cycles of Carbon and Sulfur and Their Effect on Atmospheric Oxygen over Phanerozoic Time. Global Planet Change 75, 97-122.

Beukes, N.J. (1987) Facies Relations, Depositional-Environments and Diagenesis in a Major Early Proterozoic Stromatolitic Carbonate Platform to Basinal Sequence, Campbellrand Subgroup, Transvaal Supergroup, Southern-Africa. Sediment Geol 54, 1-46.

Beukes, N.J., Dorland, H., Gutzmer, J., Nedachi, M. and Ohmoto, H. (2002) Tropical laterites, life on land, and the history of atmospheric oxygen in the Paleoproterozoic. Geology 30, 491-494.

Beukes, N.J. and Gutzmer, J. (2008) Origin and paleoenvironmental significance of major iron formations at the Archean-Paleoproterozoic Boundary. Society of Economic Geologists 15, 5-47.

Beyssac, O., Bollinger, L., Avouac, J.P. and Goffe, B. (2004) Thermal metamorphism in the lesser Himalaya of Nepal determined from Raman spectroscopy of carbonaceous material. Earth Planet Sc Lett 225, 233-241.

Beyssac, O., Goffe, B., Chopin, C. and Rouzaud, J.N. (2002) Raman spectra of carbonaceous material in metasediments: a new geothermometer. J Metamorph Geol 20, 859-871.

Blake, R.E., Chang, S.J. and Lepland, A. (2010) Phosphate oxygen isotopic evidence for a temperate and biologically active Archaean ocean. Nature 464, 1029-U1089.

Bosak, T., Greene, S.E. and Newman, D.K. (2007) A likely role for anoxygenic photosynthetic microbes in the formation of ancient stromatolites. Geobiology 5, 119-126.

Boyd, P.W. and Ellwood, M.J. (2010) The biogeochemical cycle of iron in the ocean. Nat Geosci 3, 675-682.

Boyd, P.W., Watson, A.J., Law, C.S., Abraham, E.R., Trull, T., Murdoch, R., Bakker, D.C.E., Bowie, A.R., Buesseler, K.O., Chang, H., Charette, M., Croot, P., Downing, K., Frew, R., Gall, M.,

Hadfield, M., Hall, J., Harvey, M., Jameson, G., LaRoche, J., Liddicoat, M., Ling, R., Maldonado, M.T., McKay, R.M., Nodder, S., Pickmere, S., Pridmore, R., Rintoul, S., Safi, K., Sutton, P., Strzepek, R., Tanneberger, K., Turner, S., Waite, A. and Zeldis, J. (2000) A mesoscale phytoplankton bloom in the polar Southern Ocean stimulated by iron fertilization. Nature 407, 695-702.

Brand, U. and Veizer, J. (1980) Chemical Diagenesis of a Multicomponent Carbonate System .1. Trace-Elements. Journal of Sedimentary Petrology 50, 1219-1236.

Brasier, M.D., Green, O.R., Jephcoat, A.P., Kleepe, A.K., Van Kranendonk, M.J., Lindsay, F., Steele, A. and Grassineau, N.V. (2002) Questioning the evidence for Earth's oldest fossils. Geochim Cosmochim Ac 66, A101-A101.

Brock, T.D. and Madigan, M.T. (1991) Biology of Microorganisms, 6th ed. Prentice, Englewood Cliffs, N.J.

Brocks, J.J. (2011) Millimeter-scale concentration gradients of hydrocarbons in Archean shales: Live-oil escape or fingerprint of contamination? Geochim Cosmochim Ac 75, 3196-3213.

Brocks, J.J., Logan, G.A., Buick, R. and Summons, R.E. (1999) Archean molecular fossils and the early rise of eukaryotes. Science 285, 1033-1036.

Broecker, W.S. and Peng, T.H. (1982) Tracers in the Sea. Eldigio Press, Lamont Doherty Geological Observatory.

Brucker, R.L.P., McManus, J., Severmann, S. and Berelson, W.M. (2009) Molybdenum behavior during early diagenesis: Insights from Mo isotopes. Geochem Geophy Geosy 10.

Bruland, K.W., Orians, K.J. and Cowen, J.P. (1994) Reactive Trace-Metals in the Stratified Central North Pacific. Geochim Cosmochim Ac 58, 3171-3182.

Buick, I.S., Maas, R. and Gibson, R. (2001) Precise U-Pb titanite age constraints on the emplacement of the Bushveld Complex, South Africa. J Geol Soc London 158, 3-6.

Buick, R. (1992) The Antiquity of Oxygenic Photosynthesis - Evidence from Stromatolites in Sulfate-Deficient Archean Lakes. Science 255, 74-77.

Bullen, T.D., White, A.F., Childs, C.W., Vivit, D.V. and Schulz, M.S. (2001) Demonstration of significant abiotic iron isotope fractionation in nature. Geology 29, 699-702.

Burne, R.V. and Moore, L. (1987) Microbialites; organosedimentary deposits of benthic microbial communities. Palaios 2, 241-254.

Busigny, V., Planavsky, N.J., Jezequel, D., Crowe, S., Louvat, P., Moureau, J., Viollier, E. and Lyons, T.W. (2014) Iron isotopes in an Archean ocean analogue. Geochim Cosmochim Ac 133, 443-462.

Butler, I.B., Archer, C., Vance, D., Oldroyd, A. and Rickard, D. (2005) Fe isotope fractionation on FeS formation in ambient aqueous solution. Earth Planet Sc Lett 236, 430-442.

Button, A. (1973) The stratigraphic history of the Malmani Dolomite in the eastern and north-eastern Transvaal. Transactions of the Geological Society of South Africa 76, 229-247.

Canfield, D.E. (2005) The early history of atmospheric oxygen: Homage to Robert A. Garrels. Annu Rev Earth Pl Sc 33, 1-36.

Canfield, D.E. and des Marais, D.J. (1993) Biogeochemical Cycles of Carbon, Sulfur, and Free Oxygen in a Microbial Mat. Geochim Cosmochim Ac 57, 3971-3984.

Catling, D.C., Zahnle, K.J. and McKay, C.P. (2001) Biogenic methane, hydrogen escape, and the irreversible oxidation of early Earth. Science 293, 839-843.

Chacko, T., Cole, D.R. and Horita, J. (2001) Equilibrium Oxygen, Hydrogen and Carbon Isotope Fractionation Factors Applicable to Geologic Systems, in: Valley, J.W., Cole, D.R. (Eds.), Stable Isotope Geochemistry. Mineralogical Society of America, Washinton, pp. 1-83.

Chakrabarti, R., Knoll, A.H., Jacobsen, S.B. and Fischer, W.W. (2012) Si isotope variability in Proterozoic cherts. Geochim Cosmochim Ac 91, 187-201.

Cheney, E.S. (1996) Sequence stratigraphy and plate tectonic significance of the Transvaal succession of southern Africa and its equivalent in Western Australia. Precambrian Res 79, 3-24.

Chever, F., Rouxel, O.J., Croot, P.L., Ponzevera, E., Wuttig, K. and Auro, M. (2015) Total dissolvable and dissolved iron isotopes in the water column of the Peru upwelling regime. Geochim Cosmochim Ac 162, 66-82.

Cloud, P.E. (1968) Atmospheric and Hydrospheric Evolution on Primitive Earth. Science 160, 729-&.

Coale, K.H., Johnson, K.S., Chavez, F.P., Buesseler, K.O., Barber, R.T., Brzezinski, M.A., Cochlan, W.P., Millero, F.J., Falkowski, P.G., Bauer, J.E., Wanninkhof, R.H., Kudela, R.M., Altabet, M.A., Hales, B.E., Takahashi, T., Landry, M.R., Bidigare, R.R., Wang, X.J., Chase, Z., Strutton, P.G., Friederich, G.E., Gorbunov, M.Y., Lance, V.P., Hilting, A.K., Hiscock, M.R., Demarest, M., Hiscock, W.T., Sullivan, K.F., Tanner, S.J., Gordon, R.M., Hunter, C.N., Elrod, V.A., Fitzwater, S.E., Jones, J.L., Tozzi, S., Koblizek, M., Roberts, A.E., Herndon, J., Brewster, J., Ladizinsky, N., Smith, G., Cooper, D., Timothy, D., Brown, S.L., Selph, K.E., Sheridan, C.C., Twining, B.S. and Johnson, Z.I. (2004) Southern ocean iron enrichment experiment: Carbon cycling in high- and low-Si waters. Science 304, 408-414.

Coetzee, L.L. (2001) Genetic stratigraphy of the Paleoproterozoic Pretoria Group in the western Transvaal. Rand Afrikaans University, Johannesburg, p. 184.

Collier, R.W. (1985) Molybdenum in the Northeast Pacific-Ocean. Limnol Oceanogr 30, 1351-1354.

Craddock, P.R., Warren, J.M. and Dauphas, N. (2013) Abyssal peridotites reveal the near-chondritic Fe isotopic composition of the Earth. Earth Planet Sc Lett 365, 63-76.

Craig, H. (1957) Isotopic standards for carbon and oxygen and correction factors for mass spectrometric analysis of carbon dioxide. Geochim Cosmochim Ac 12, 133-149.

Crne, A.E., Melezhik, V.A., Lepland, A., Fallick, A.E., Prave, A.R. and Brasier, A.T. (2014) Petrography and geochemistry of carbonate rocks of the Paleoproterozoic Zaonega Formation, Russia: Documentation of C-13-depleted non-primary calcite. Precambrian Res 240, 79-93.

Croal, L.R., Johnson, C.M., Beard, B.L. and Newman, D.K. (2004) Iron isotope fractionation by Fe(II)-oxidizing photoautotrophic bacteria. Geochim Cosmochim Ac 68, 1227-1242.

Crosby, H.A., Roden, E.E., Johnson, C.M. and Beard, B.L. (2007) The mechanisms of iron isotope fractionation produced during dissimilatory Fe(III) reduction by Shewanella putrefaciens and Geobacter sulfurreducens. Geobiology 5, 169-189.

Crowe, S.A., Dossing, L.N., Beukes, N.J., Bau, M., Kruger, S.J., Frei, R. and Canfield, D.E. (2013) Atmospheric oxygenation three billion years ago. Nature 501, 535-+.

Crowe, S.A., Jones, C., Katsev, S., Magen, C., O'Neill, A.H., Sturm, A., Canfield, D.E., Haffner, G.D., Mucci, A., Sundby, B. and Fowle, D.A. (2008) Photoferrotrophs thrive in an Archean Ocean analogue. P Natl Acad Sci USA 105, 15938-15943.

Czaja, A.D., Johnson, C.M., Roden, E.E., Beard, B.L., Voegelin, A.R., Nagler, T.F., Beukes, N.J. and Wille, M. (2012) Evidence for free oxygen in the Neoarchean ocean based on coupled iron-molybdenum isotope fractionation. Geochim Cosmochim Ac 86, 118-137.

Dahl, T.W., Anbar, A.D., Gordon, G.W., Rosing, M.T., Frei, R. and Canfield, D.E. (2010) The behavior of molybdenum and its isotopes across the chemocline and in the sediments of sulfidic Lake Cadagno, Switzerland. Geochim Cosmochim Ac 74, 144-163.

Dahl, T.W., Canfield, D.E., Rosing, M.T., Frei, R.E., Gordon, G.W., Knoll, A.H. and Anbar, A.D. (2011) Molybdenum evidence for expansive sulfidic water masses in similar to 750 Ma oceans. Earth Planet Sc Lett 311, 264-274.

Dauphas, N. and Rouxel, O. (2006) Mass spectrometry and natural variations of iron isotopes. Mass Spectrom Rev 25, 515-550.

de Baar, H.J.W. and de Jong, J.T.M. (2001) Distributions, sources and sinks of iron in seawater, in: Turner, D., Hunter, K.A. (Eds.), The Biogeochemistry of Iron in Seawater. Hoboken. John Wiley & Sons, New York.

de Kock, M.O., Evans, D.A.D. and Beukes, N.J. (2009) Validating the existence of Vaalbara in the Neoarchean. Precambrian Res 174, 145-154.

De la Rocha, C.L., Brzezinski, M.A. and DeNiro, M.J. (2000) A first look at the distribution of the stable isotopes of silicon in natural waters. Geochim Cosmochim Ac 64, 2467-2477.

de Laeter, J.R., Boehlke, J.K., de Bievre, P., Hidaka, H., Peisler, H.S., Rosman, K.J.R. and Taylor, P.D.P. (2003) Atomic weights of the elements: Review 2000 (IUPAC Technical Report). Pure and Applied Chemistry 75, 683-800.

Dellwig, O., Beck, M., Lemke, A., Lunau, M., Kolditz, K., Schnetger, B. and Brumsack, H.J. (2007) Non-conservative behaviour of molybdenum in coastal waters: Coupling geochemical, biological, and sedimentological processes. Geochim Cosmochim Ac 71, 2745-2761.

Derry, L.A. and Jacobsen, S.B. (1990) The Chemical Evolution of Precambrian Seawater - Evidence from Rees in Banded Iron Formations. Geochim Cosmochim Ac 54, 2965-2977.

Derry, L.A., Kaufman, A.J. and Jacobsen, S.B. (1992) Sedimentary Cycling and Environmental-Change in the Late Proterozoic - Evidence from Stable and Radiogenic Isotopes. Geochim Cosmochim Ac 56, 1317-1329.

des Marais, D.J. (1985) Carbon exchange between the mantle and crust and its effect upon the atmosphere: today compared to Archean time, in: Sundquist, E.T., Broecker, W.S. (Eds.), The Carbon Cycle and Atmospheric CO2: Natural Variations Archean to Present. American Geophysical Union, Washington, D.C., pp. 605-611.

Des Marais, D.J. (1995) The biogeochemistry of subtidal marine hypersaline microbial mats, Guerrero Negro, Baja California Sur, Mexico, in: Jones, J.G. (Ed.), Advances in Microbial Ecology. Plenum, New York, pp. 251-274.

Des Marais, D.J. (2001) Isotopic evolution of the biogeochemical carbon cycle during the Precambrian, in: Valley, J.W., Cole, D.R. (Eds.), Stable Isotope Geochemistry. Reviews in Mineralogy and Geochemistry, pp. 555-578.

Ding, T., Wan, D., Wang, C. and Zhang, F. (2004) Silicon isotope compositions of dissolved silicon and suspended matter in the Yangtze River, China. Geochim Cosmochim Ac 68, 205-216.

Dorland, H.C. (1999) Paleoproterozoic laterite, red beds and ironstone of the Pretoria Group with reference to the history of atmospheric oxygen. Rand Afrikaans University, Johannesburg, p. 147.

Dromgoole, E.L. and Walter, L.M. (1990) Iron and Manganese Incorporation into Calcite - Effects of Growth-Kinetics, Temperature and Solution Chemistry. Chem Geol 81, 311-336.

Duan, Y., Anbar, A.D., Arnold, G.L., Lyons, T.W., Gordon, G.W. and Kendall, B. (2010) Molybdenum isotope evidence for mild environmental oxygenation before the Great Oxidation Event. Geochim Cosmochim Ac 74, 6655-6668.

Duan, Y., Arnold, G.L., Gordon, G.W. and Anbar, A.D. (2008) Evidence from Mo isotopic compositions for "A whiff of oxygen" before the Great Oxidation Event. Geochim Cosmochim Ac 72, A228-A228.

Duce, R.A. and Tindale, N.W. (1991) Atmospheric Transport of Iron and Its Deposition in the Ocean. Limnol Oceanogr 36, 1715-1726.

Dupraz, C. and Visscher, P.T. (2005) Microbial lithification in marine stromatolites and hypersaline mats. Trends Microbiol 13, 429-438.

Eigenbrode, J.L. and Freeman, K.H. (2006) Late Archean rise of aerobic microbial ecosystems. P Natl Acad Sci USA 103, 15759-15764.

Eigenbrode, J.L., Freeman, K.H. and Summons, R.E. (2008) Methylhopane biomarker hydrocarbons in Hamersley Province sediments provide evidence for Neoarchean aerobiosis. Earth Planet Sc Lett 273, 323-331.

Elrod, V.A., Berelson, W.M., Coale, K.H. and Johnson, K.S. (2004) The flux of iron from continental shelf sediments: A missing source for global budgets. Geophys Res Lett 31.

Emerson, S.R. and Huested, S.S. (1991) Ocean Anoxia and the Concentrations of Molybdenum and Vanadium in Seawater. Mar Chem 34, 177-196.

Emrich, K. and Vogel, J.C. (1970) Carbon Isotope Fractionation during Precipitation of Calcium Carbonate. Earth Planet Sc Lett 8, 363-&.

Erickson, B.E. and Helz, G.R. (2000) Molybdenum(VI) speciation in sulfidic waters: Stability and lability of thiomolybdates. Geochim Cosmochim Ac 64, 1149-1158.

Eriksson, K.A. (1977) Tidal flat and subtidal sedimentation in the 2250 m.y. Malmani Dolomite, Transvaal South Africa. Sediment Geol 18, 223-244.

Eriksson, K.A., McCarthy, T.S. and Truswell, J.F. (1975) Limestone formation and dolomitization in a Lower Proterozoic succession from South Africa. Journal of Sedimentary Petrology 45, 604-614.

Eriksson, K.A. and Truswell, J.F. (1973) High inheritance elongate stromatolitic mounds from the Tranvaal dolomite. Paleontology of Africa 15, 23-28.

Eriksson, K.A. and Truswell, J.F. (1974) Stratotypes from the Malmani Subgroup northwest of Johannesburg, South Africa. Transactions of the Geological Society of South Africa 77, 211-222.

Falkowski, P.G. and Isozaki, Y. (2008) Geology - The story of O(2). Science 322, 540-542.

Farquhar, J., Bao, H.M. and Thiemens, M. (2000) Atmospheric influence of Earth's earliest sulfur cycle. Science 289, 756-758.

Farquhar, J., Zerkle, A.L. and Bekker, A. (2011) Geological constraints on the origin of oxygenic photosynthesis. Photosynth Res 107, 11-36.

Field, C.B., Behrenfeld, M.J., Randerson, J.T. and Falkowski, P. (1998) Primary production of the biosphere: Integrating terrestrial and oceanic components. Science 281, 237-240.

Fischer, A.G. (1965) Fossils Early Life and Atmospheric History. P Natl Acad Sci USA 53, 1205-&.

Fischer, W.W., Schroeder, S., Lacassie, J.P., Beukes, N.J., Goldberg, T., Strauss, H., Horstmann, U.E., Schrag, D.P. and Knoll, A.H. (2009) Isotopic constraints on the Late Archean carbon

cycle from the Transvaal Supergroup along the western margin of the Kaapvaal Craton, South Africa. Precambrian Res 169, 15-27.

Fischer, W.W., Summons, R.E. and Pearson, A. (2005) Targeted genomic detection of biosynthetic pathways: anaerobic production of hopanoid biomarkers by a common sedimentary microbe. Geobiology 3, 33-40.

Fitzsimmons, J.N., Boyle, E.A. and Jenkins, W.J. (2014) Distal transport of dissolved hydrothermal iron in the deep South Pacific Ocean. P Natl Acad Sci USA 111, 16654-16661.

Folk, R.L. and Land, L.S. (1975) Mg/Ca Ratio and Salinity - 2 Controls over Crystallization of Dolomite. Aapg Bull 59, 60-68.

Frauenstein, F., Veizer, J., Beukes, N., Van Niekerk, H.S. and Coetzee, L.L. (2009) Transvaal Supergroup carbonates: Implications for Paleoproterozoic delta O-18 and delta C-13 records. Precambrian Res 175, 149-160.

Freeman, K.H., Hayes, J.M., Trendel, J.M. and Albrecht, P. (1990) Evidence from Carbon Isotope Measurements for Diverse Origins of Sedimentary Hydrocarbons. Nature 343, 254-256.

Frei, R., Crowe, S.A., Bau, M., Polat, A., Fowle, D.A. and Dossing, L.N. (2016) Oxidative elemental cycling under the low O-2 Eoarchean atmosphere. Sci Rep-Uk 6.

Frei, R., Gaucher, C., Poulton, S.W. and Canfield, D.E. (2009) Fluctuations in Precambrian atmospheric oxygenation recorded by chromium isotopes. Nature 461, 250-U125.

Froelich, P.N., Klinkhammer, G.P., Bender, M.L., Luedtke, N.A., Heath, G.R., Cullen, D., Dauphin, P., Hammond, D., Hartman, B. and Maynard, V. (1979) Early Oxidation of Organic-Matter in Pelagic Sediments of the Eastern Equatorial Atlantic - Suboxic Diagenesis. Geochim Cosmochim Ac 43, 1075-1090.

Gaillard, F., Scaillet, B. and Arndt, N.T. (2011) Atmospheric oxygenation caused by a change in volcanic degassing pressure. Nature 478, 229-U112.

Garrels, R.M. and Perry, E.A. (1974) Cycling of carbon, sulfur, and oxygen through geologic time, in: Goldberg, E.D. (Ed.), The Sea. John Wiley & Sons, New York, pp. 303-336.

Garvin, J., Buick, R., Anbar, A.D., Arnold, G.L. and Kaufman, A.J. (2009) Isotopic Evidence for an Aerobic Nitrogen Cycle in the Latest Archean. Science 323, 1045-1048.

Georg, R.B., Reynolds, B.C., West, A.J., Burton, K.W. and Halliday, A.N. (2007) Silicon isotope variations accompanying basalt weathering in Iceland. Earth Planet Sc Lett 261, 476-490.

Godfrey, L.V. and Falkowski, P.G. (2009) The cycling and redox state of nitrogen in the Archaean ocean. Nat Geosci 2, 725-729.

Goldberg, S., Forster, H.S. and Godfrey, C.L. (1996) Molybdenum adsorption on oxides, clay minerals, and soils. Soil Sci Soc Am J 60, 425-432.

Goldberg, T., Archer, C., Vance, D. and Poulton, S.W. (2009) Mo isotope fractionation during adsorption to Fe (oxyhydr)oxides. Geochim Cosmochim Ac 73, 6502-6516.

Goldberg, T., Gordon, G., Izon, G., Archer, C., Pearce, C.R., McManus, J., Anbar, A.D. and Rehkamper, M. (2013) Resolution of inter-laboratory discrepancies in Mo isotope data: an intercalibration. J Anal Atom Spectrom 28, 724-735.

Govindarau, K. (1989) Compilation of working values and sample description for 272 geostandards. Special Issue of Geostandards Newsletter XIII.

Grassineau, N.V., Abell, P., Appel, P.W.U., Lowry, D. and Nisbet, E.G. (2006) Early life signatures in sulfur and carbon isotopes from Isua, Barberton, Wabigoon (Steep Rock), and Belingwe Greenstone Belts (3.8 to 2.7 Ga) in: Kesler, S.E., Ohmoto, H. (Eds.), Evolution of

Early Earth's Atmosphere, Hydrosphere, and Biosphere - Constraints from Ore Deposits. Geological Society of America Memoirs, pp. 33-52.

Greber, N.D., Hofmann, B.A., Voegelin, A.R., Villa, I.M. and Nagler, T.F. (2011) Mo isotope composition in Mo-rich high- and low-T hydrothermal systems from the Swiss Alps. Geochim Cosmochim Ac 75, 6600-6609.

Greber, N.D., Maeder, U. and Naegler, T.F. (2015) Experimental dissolution of molybdenum-sulphides at low oxygen concentrations: A first-order approximation of late Archean atmospheric conditions. Earth and Space Science 2, 173-180.

Greber, N.D., Siebert, C., Nagler, T.F. and Pettke, T. (2012) d98/95Mo values and Molybdenum Concentration Data for NIST SRM 610, 612 and 3134: Towards a Common Protocol for Reporting Mo Data. Geostand Geoanal Res 36, 291-300.

Grotzinger, J.P. (1989) Facies and evolution of Precambrian carbonate depositional systems: emergence of the modern platform archetype, in: Crevello, P.D., Wilson, J.L., Sarg, J.F., Read, J.F. (Eds.), Controls on Carbonate Platform and Basin Development. SEPM Special Publication, pp. 79-106.

Hahn-Weinheimer, P., Hirner, A. and Weber-Diefenbach, K. (1984) Grundlagen und praktische Anwendung der Röntgenfluoreszenzanalyse. Friedrich Vieweg & Sohn.

Hayes, J.M. (2001) Fractionation of carbon and hydrogen isotopes in biosynthetic processes, in: Valley, J.W., Cole, D.R. (Eds.), Stable Isotope Geochemistry. Mineralogical Society of America, Washington, D.C., pp. 225-278.

Hayes, J.M., Popp, B.N., Takigiku, R. and Johnson, M.W. (1989) An Isotopic Study of Biogeochemical Relationships between Carbonates and Organic-Carbon in the Greenhorn Formation. Geochim Cosmochim Ac 53, 2961-2972.

Head, P.C. and Burton, J.D. (1970) Molybdenum in Some Ocean and Estuarine Waters. J Mar Biol Assoc Uk 50, 439-&.

Hegler, F., Posth, N.R., Jiang, J. and Kappler, A. (2008) Physiology of phototrophic iron(II)-oxidizing bacteria: implications for modern and ancient environments. Fems Microbiol Ecol 66, 250-260.

Heimann, A., Johnson, C.M., Beard, B.L., Valley, J.W., Roden, E.E., Spicuzza, M.J. and Beukes, N.J. (2010) Fe, C, and O isotope compositions of banded iron formation carbonates demonstrate a major role for dissimilatory iron reduction in similar to 2.5 Ga marine environments. Earth Planet Sc Lett 294, 8-18.

Helz, G.R., Bura-Nakic, E., Mikac, N. and Ciglenecki, I. (2011) New model for molybdenum behavior in euxinic waters. Chem Geol 284, 323-332.

Helz, G.R., Miller, C.V., Charnock, J.M., Mosselmans, J.F.W., Pattrick, R.A.D., Garner, C.D. and Vaughan, D.J. (1996) Mechanism of molybdenum removal from the sea and its concentration in black shales: EXAFS evidence. Geochim Cosmochim Ac 60, 3631-3642.

Herman, E.K. and Kump, L.R. (2005) Biogeochemistry of microbial mats under Precambrian environmental conditions: a modelling study. Geobiology 3, 77-92.

Herzog, R.E., Shi, Q.H., Patil, J.N. and Katz, J.L. (1989) Magnetic Water-Treatment - the Effect of Iron on Calcium-Carbonate Nucleation and Growth. Langmuir 5, 861-867.

Hoffman, P. (1988) Pethei reef complex (1.9 Ga), Great Slave Lake, NWT, in: Geldsetzer, H.H.J., James, N.P., Tebbutt, G.E. (Eds.), Reefs, Canada and Adjacent Areas, Canadian Society of Petroleum Geologists Memoir pp. 38-48.

Hoffman, P. and Grotzinger, J. (1988) Abner/Denault Reef Complex (2.1 Ga), Labrador Trough, NE Quebec, in: Geldsetzer, H.H.J., James, N.P., Tebbutt, G.E. (Eds.), Reefs, Canada and Adjacent Areas. Canadian Society of Petroleum Geologists Memoir pp. 49-54.

Holland, H.D. (1962) Model for the evolution of the Earth's atmosphere, in: Engel, A.E.J., James, H.L., Leonard, B.F. (Eds.), Petrologic Studies: A volume in honor of A. F. Buddington. Geological Society of America, pp. 447-477.

Holland, H.D. (2004) The geological history of seawater, in: Holland, H.D., Turekia, K.K. (Eds.). Elsevier, Oxford, pp. 583-625.

Holland, H.D. (2006) The oxygenation of the atmosphere and oceans. Philos T R Soc B 361, 903-915.

Holmden, C., Creaser, R.A., Muehlenbachs, K., Leslie, S.A. and Bergstrom, S.M. (1998) Isotopic evidence for geochemical decoupling between ancient epeiric seas and bordering oceans: Implications for secular curves. Geology 26, 567-570.

Horita, J., Zimmermann, H. and Holland, H.D. (2002) Chemical evolution of seawater during the Phanerozoic: Implications from the record of marine evaporites. Geochim Cosmochim Ac 66, 3733-3756.

Horstmann, U.E. and Beukes, N.J. (2002) Stable isotope geochemistry of the Campbellrand Dolomite in the SACHA drill core. Collaborative project with SA universities, Department of Geology, Rand Afrikaans University , Report Stable Isotope Lab 2001-06.

Hren, M.T., Tice, M.M. and Chamberlain, C.P. (2009) Oxygen and hydrogen isotope evidence for a temperate climate 3.42 billion years ago. Nature 462, 205-208.

Huizenga, J.M., Gutzmer, J., Banks, D. and Greyling, L. (2006a) The Paleoproterozoic carbonate-hosted Pering Zn-Pb deposit, South Africa. II: Fluid inclusion, fluid chemistry and stable isotope constraints. Miner Deposita 40, 686-706.

Huizenga, J.M., Gutzmer, J., Greyling, L.N. and Schaefer, M. (2006b) Carbonic fluid inclusions in Paleoproterozoic carbonate-hosted Zn-Pb deposits in Griqualand West, South Africa. S Afr J Geol 109, 55-62.

Icopini, G.A., Anbar, A.D., Ruebush, S.S., Tien, M. and Brantley, S.L. (2004) Iron isotope fractionation during microbial reduction of iron: The importance of adsorption. Geology 32, 205-208.

Immenhauser, A., Della Porta, G., Kenter, J.A.M. and Bahamonde, J.R. (2003) An alternative model for positive shifts in shallow-marine carbonate delta C-13 and delta O-18. Sedimentology 50, 953-959.

Isley, A.E. and Abbott, D.H. (1999) Plume-related mafic volcanism and the deposition of banded iron formation. J Geophys Res-Sol Ea 104, 15461-15477.

Jacobsen, S.B. and Pimentelklose, M.R. (1988) A Nd Isotopic Study of the Hamersley and Michipicoten Banded Iron Formations - the Source of Ree and Fe in Archean Oceans. Earth Planet Sc Lett 87, 29-44.

Johnson, C., Beard, B. and Roden, E. (2008a) Temporal variations in Fe isotope compositions of banded iron formations record changes in the nature of redox cycling. Geochim Cosmochim Ac 72, A435-A435.

Johnson, C.M., Beard, B.L. and Albarede, F. (2004) Geochemistry of Non-Traditional Stable Isotopes. Mineralogical Society of America, Washington.

Johnson, C.M., Beard, B.L., Beukes, N.J., Klein, C. and O'Leary, J.M. (2003) Ancient geochemical cycling in the Earth as inferred from Fe isotope studies of banded iron formations from the Transvaal Craton. Contrib Mineral Petr 144, 523-547.

Johnson, C.M., Beard, B.L., Klein, C., Beukes, N.J. and Roden, E.E. (2008b) Iron isotopes constrain biologic and abiologic processes in banded iron formation genesis. Geochim Cosmochim Ac 72, 151-169.

Johnson, C.M., Beard, B.L. and Roden, E.E. (2008c) The iron isotope fingerprints of redox and biogeochemical cycling in the modern and ancient Earth. Annu Rev Earth Pl Sc 36, 457-493.

Johnson, C.M., Ludois, J.M., Beard, B.L., Beukes, N.J. and Heimann, A. (2013) Iron formation carbonates: Paleoceanographic proxy or recorder of microbial diagenesis? Geology 41, 1147-1150.

Johnson, J.E., Gerpheide, A., Lamb, M.P. and Fischer, W.W. (2014) O-2 constraints from Paleoproterozoic detrital pyrite and uraninite. Geol Soc Am Bull 126, 813-830.

Kamber, B.S., Bolhar, R. and Webb, G.E. (2004) Geochemistry of late Archaean stromatolites from Zimbabwe: evidence for microbial life in restricted epicontinental seas. Precambrian Res 132, 379-399.

Kamber, B.S. and Webb, G.E. (2001) The geochemistry of late Archaean microbial carbonate: Implications for ocean chemistry and continental erosion history. Geochim Cosmochim Ac 65, 2509-2525.

Kappler, A., Johnson, C.M., Crosby, H.A., Beard, B.L. and Newman, D.K. (2010) Evidence for equilibrium iron isotope fractionation by nitrate-reducing iron(II)-oxidizing bacteria. Geochim Cosmochim Ac 74, 2826-2842.

Kappler, A., Pasquero, C., Konhauser, K.O. and Newman, D.K. (2005) Deposition of banded iron formations by anoxygenic phototrophic Fe(II)-oxidizing bacteria. Geology 33, 865-868.

Kappler, A. and Straub, K.L. (2005) Geomicrobiological cycling of iron, in: Banfield, J.F., Cervini-Silva, J., Nealson, K.H. (Eds.), Molecular Geomicrobiology. Mineralogical Society of America, Washington, pp. 85-108.

Karhu, J.A. (1993) Paleoproterozoic evolution of sedimentary carbonates in the Fennoscandian Shield. Geological Survery of Finland Bulletin 371, 1-87.

Kasting, J.F. (1991) Box models for the evolution of atmospheric oxygen: an update. Palaeogeogr Palaeocl 97, 125-131.

Kasting, J.F. (1992) Models relating to Proterozoic atmospheric and ocean chemistry, in: Schopf, J., Klein, C. (Eds.), The Proterozoic Biosphere, A Multidisciplinary Study. Cambridge University Press, Cambridge, pp. 1185-1187.

Kasting, J.F. (2013) What caused the rise of atmospheric O-2? Chem Geol 362, 13-25.

Kasting, J.F., Howard, M.T., Wallmann, K., Veizer, J., Shields, G. and Jaffres, J. (2006) Paleoclimates, ocean depth, and the oxygen isotopic composition of seawater. Earth Planet Sc Lett 252, 82-93.

Kasting, J.F. and Siefert, J.L. (2002) Life and the evolution of Earth's atmosphere. Science 296, 1066-1068.

Kendall, B., Reinhard, C.T., Lyons, T., Kaufman, A.J., Poulton, S.W. and Anbar, A.D. (2010) Pervasive oxygenation along late Archaean ocean margins. Nat Geosci 3, 647-652.

Klein, C. and Beukes, N.J. (1989) Geochemistry and Sedimentology of a Facies Transition from Limestone to Iron-Formation Deposition in the Early Proterozoic Transvaal Supergroup, South-Africa. Econ Geol 84, 1733-1774.

Knauth, L.P. (1979) Model for the Origin of Chert in Limestone. Geology 7, 274-277.

Knoll, A.H. and Beukes, N.J. (2009) Introduction: Initial investigations of a Neoarchean shelf margin-basin transition (Transvaal Supergroup, South Africa). Precambrian Res 169, 1-14.

Kohout, F.A. (1967) Groundwater flow and the geothermal regime of the Floridan plateau. Trans. Gulf-Cst. Ass. Geol. Socs. 17, 339-354.

Konhauser, K.O., Hamade, T., Raiswell, R., Morris, R.C., Ferris, F.G., Southam, G. and Canfield, D.E. (2002) Could bacteria have formed the Precambrian banded iron formations? Geology 30, 1079-1082.

Kouketsu, Y., Mizukami, T., Mori, H., Endo, S., Aoya, M., Hara, H., Nakamura, D. and Wallis, S. (2014) A new approach to develop the Raman carbonaceous material geothermometer for low-grade metamorphism using peak width. Isl Arc 23, 33-50.

Kowalski, N. (2010) Transformation processes of redox-sensitive trace metals in the water column and sediments of temperate tidal systems. University of Greiswald, p. 272.

Kowalski, N., Dellwig, O., Beck, M., Grawe, U., Neubert, N., Nagler, T.F., Badewien, T.H., Brumsack, H.J., van Beusekom, J.E.E. and Bottcher, M.E. (2013) Pelagic molybdenum concentration anomalies and the impact of sediment resuspension on the molybdenum budget in two tidal systems of the North Sea. Geochim Cosmochim Ac 119, 198-211.

Krissansen-Totton, J., Buick, R. and Catling, D.C. (2015) A Statistical Analysis of the Carbon Isotope Record from the Archean to Phanerozoic and Implications for the Rise of Oxygen. Am J Sci 315, 275-316.

Kump, L.R. and Barley, M.E. (2007) Increased subaerial volcanism and the rise of atmospheric oxygen 2.5 billion years ago. Nature 448, 1033-1036.

Kump, L.R., Fallick, A.E., Melezhik, V.A., Strauss, H. and Lepland, A. (2013) The Great Oxidation Event, in: Melezhik, V., Prave, A.R., Hanski, E.J., Fallick, A.E., Lepland, A., Kump, L.R., Strauss, H. (Eds.), Reading the Archive of Earth's Oxygenation, Global Events and the Fennoscandian Arctic Russia - Drilling Early Earth Project. Springer Verlag, Berlin.

Kurzweil, F., Wille, M., Gantert, N., Beukes, N.J. and Schoenberg, R. (2016) Manganese oxide shuttling in pre-GOE oceans - evidence from molybdenum and iron isotopes. Earth Planet Sc Lett 452, 69-78.

Kurzweil, F., Wille, M., Schoenberg, R., Taubald, H. and Van Kranendonk, M.J. (2015) Continuously increasing delta Mo-98 values in Neoarchean black shales and iron formations from the Hamersley Basin. Geochim Cosmochim Ac 164, 523-542.

Lahfid, A., Beyssac, O., Deville, E., Negro, F., Chopin, C. and Goffe, B. (2010) Evolution of the Raman spectrum of carbonaceous material in low-grade metasediments of the Glarus Alps (Switzerland). Terra Nova 22, 354-360.

Lalonde, S.V. and Konhauser, K.O. (2015) Benthic perspective on Earth's oldest evidence for oxygenic photosynthesis. P Natl Acad Sci USA 112, 995-1000.

Land, L.S. (1985) The Origin of Massive Dolomite. J Geol Educ 33, 112-125.

Landing, W.M. and Bruland, K.W. (1987) The Contrasting Biogeochemistry of Iron and Manganese in the Pacific-Ocean. Geochim Cosmochim Ac 51, 29-43.

Lippmann, F. (1973) Sedimentary Carbonate Minerals. Springer-Verlag, berlin.

Luo, G., Ono, S., Beukes, N.J., Wang, D.T., Xie, S. and Summons, R.E. (2016) Rapid oxygenation of Earth's atmosphere 2.33 billion years ago. Science Advances 2.

Lyons, T.W., Reinhard, C.T. and Planavsky, N.J. (2014) The rise of oxygen in Earth's early ocean and atmosphere. Nature 506, 307-315.

Magaritz, M., Goldenberg, L., Kafri, U. and Arad, A. (1980) Dolomite Formation in the Seawater-Freshwater Interface. Nature 287, 622-624.

Maier, W.D. and Barnes, S.J. (1998) Concentrations of rare earth elements in silicate rocks of the Lower, Critical and Main Zones of the Bushveld Complex. Chem Geol 150, 85-103.

Marcus, M.A., Westphal, A.J. and Fakra, S.C. (2009) Classification of Fe-bearing species from K-edge XANES data using two-parameter correlation plots (vol 15, pg 463, 2008). J Synchrotron Radiat 16, 439-439.

Martin, D.M., Clendenin, C.W., Krapez, B. and McNaughton, N.J. (1998) Tectonic and geochronological constraints on late Archaean and Palaeoproterozoic stratigraphic correlation within and between the Kaapvaal and Pilbara Cratons. J Geol Soc London 155, 311-322.

Martin, J.H. and Fitzwater, S.E. (1988) Iron-Deficiency Limits Phytoplankton Growth in the Northeast Pacific Subarctic. Nature 331, 341-343.

Martin, J.H., Gordon, R.M. and Fitzwater, S.E. (1990) Iron in Antarctic Waters. Nature 345, 156-158.

Martin, W.R. and Sayles, F.L. (2003) The recycling of biogenic material at the seafloor, in: Holland, H.D., Turekian, K.K. (Eds.). Pergamon, Oxford, pp. 37-65.

Marx, S.K. and Kamber, B.S. (2010) High-precision trace-element systematics of sediments in the Murray-Darling Basin, Australia: Sediment tracing and palaeo-climate implications of fine scale chemical heterogeneity of the upper continental crust. Applied Geochemistry 25, 1221-1237.

Matthews, A., Morgans-Bell, H.S., Emmanuel, S., Jenkyns, H.C., Erel, Y. and Halicz, L. (2004) Controls on iron-isotope fractionation in organic-rich sediments (Kimmeridge Clay, Upper Jurassic, southern England). Geochim Cosmochim Ac 68, 3107-3123.

McManus, J., Berelson, W.M., Severmann, S., Poulson, R.L., Hammond, D.E., Klinkhammer, G.P. and Holm, C. (2006) Molybdenum and uranium geochemistry in continental margin sediments: Paleoproxy potential. Geochim Cosmochim Ac 70, 4643-4662.

McManus, J., Nagler, T.F., Siebert, C., Wheat, C.G. and Hammond, D.E. (2002) Oceanic molybdenum isotope fractionation: Diagenesis and hydrothermal ridge-flank alteration. Geochem Geophy Geosy 3.

Mcneill, D.F. and Kirschvink, J.L. (1993) Early Dolomitization of Platform Carbonates and the Preservation of Magnetic Polarity. J Geophys Res-Sol Ea 98, 7977-7986.

Melezhik, V.A., Huhma, H., Condon, D.J., Fallick, A.E. and Whitehouse, M.J. (2007) Temporal constraints on the Paleoproterozoic Lomagundi-Jatuli carbon isotopic event. Geology 35, 655-658.

Mettler, S. (2002) In situ removal of iron from groundwater: Fe(II) oxygenation, and precipitation products in a calcareous aquifer. Swiss Federal Insitute of Technology Zurich, p. 158.

Mettler, S., Wolthers, M., Charlet, L. and von Gunten, U. (2009) Sorption and catalytic oxidation of Fe(II) at the surface of calcite. Geochim Cosmochim Ac 73, 1826-1840.

Miller, C.A., Peucker-Ehrenbrink, B., Walker, B.D. and Marcantonio, F. (2011) Re-assessing the surface cycling of molybdenum and rhenium. Geochim Cosmochim Ac 75, 7146-7179.

Miyano, T. and Beukes, N.J. (1984) Phase relations of stilpnomelane, ferriannite, and riebeckite in very low-grade metamorphosed iron-formations. Transactions of the Geological Society of South Africa 87, 111-124.

Mobilio, S., Boscherini, F. and Meneghini, C. (2015) Synchrotron Radiation - Basics, Methods, and Applications. Springer Verlag, Berlin-Heidelberg.

Mook, W.G., Bommerso.Jc and Staverma.Wh (1974) Carbon Isotope Fractionation between Dissolved Bicarbonate and Gaseous Carbon-Dioxide. Earth Planet Sc Lett 22, 169-176.

Moore, J.K., Doney, S.C., Glover, D.M. and Fung, I.Y. (2002) Iron cycling and nutrient-limitation patterns in surface waters of the World Ocean. Deep-Sea Res Pt Ii 49, 463-507.

Morford, J.L. and Emerson, S. (1999) The geochemistry of redox sensitive trace metals in sediments. Geochim Cosmochim Ac 63, 1735-1750.

Morrow, D.W. (1982) Diagenesis 1: Dolomite - Part 1, the chemistry of dolomitization and dolomite precipitation. Geoscience Canada 9, 5-13.

Munoz, M., De Andrade, V., Vidal, O., Lewin, E., Pascarelli, S. and Susini, J. (2006) Redox and speciation micromapping using dispersive X-ray absorption spectroscopy: Application to iron chlorite mineral of a metamorphic rock thin section. Geochem Geophy Geosy 7.

Murray, R.C. (1960) The origin of porosity in carbonate rocks. Journal of Sedimentary Petrology 30, 59-84.

Naegler, T.F., Anbar, A.D., Archer, C., Goldberg, T., Gordon, G.W., Greber, N.D., Siebert, C., Sohrin, Y. and Vance, D. (2014) Proposal for an International Molybdenum Isotope Measurement Standard and Data Representation. Geostand Geoanal Res 38, 149-151.

Naegler, T.F., Neubert, N., Bottcher, M.E., Dellwig, O. and Schnetger, B. (2011) Molybdenum isotope fractionation in pelagic euxinia: Evidence from the modern Black and Baltic Seas. Chem Geol 289, 1-11.

Nisbet, E.G. and Sleep, N.H. (2001) The habitat and nature of early life. Nature 409, 1083-1091.

Noffke, N., Beukes, N., Bower, D., Hazen, R.M. and Swift, D.J.P. (2008) An actualistic perspective into Archean worlds-(cyano-)bacterially induced sedimentary structures in the siliciclastic Nhlazatse Section, 2.9 Ga Pongola Supergroup, South Africa. Geobiology 6, 5-20.

O'Day, P.A., Rivera, N., Root, R. and Carroll, S.A. (2004) X-ray absorption spectroscopic study of Fe reference compounds for the analysis of natural sediments. Am Mineral 89, 572-585.

Oehlert, A.M. and Swart, P.K. (2014) Interpreting carbonate and organic carbon isotope covariance in the sedimentary record. Nat Commun 5.

Olson, S.L., Kump, L.R. and Kasting, J.F. (2013) Quantifying the areal extent and dissolved oxygen concentrations of Archean oxygen oases. Chem Geol 362, 35-43.

Pascarelli, S., Neisius, T. and De Panfilis, S. (1999) Turbo-XAS: dispersive XAS using sequential acquisition. J Synchrotron Radiat 6, 1044-1050.

Pavlov, A.A. and Kasting, J.F. (2002) Mass-independent fractionation of sulfur isotopes in Archean sediments: Strong evidence for an anoxic Archean atmosphere. Astrobiology 2, 27-41.

Pearce, C.R., Cohen, A.S. and Parkinson, I.J. (2009) Quantitative Separation of Molybdenum and Rhenium from Geological Materials for Isotopic Determination by MC-ICP-MS. Geostand Geoanal Res 33, 219-229.

Pearce, J.A. (1983) Role of the sub-continental lithosphere in magma genesis at active continental margins, in: Hawkesworth, C.J., Norry, M.J. (Eds.), Continental Basalts and Mantle Xenoliths. Shiva Press, Nantwich, U.K., pp. 230-249.

Planavsky, N., Rouxel, O.J., Bekker, A., Hofmann, A., Little, C.T.S. and Lyons, T.W. (2012) Iron isotope composition of some Archean and Proterozoic iron formations. Geochim Cosmochim Ac 80, 158-169.

Planavsky, N.J., Asael, D., Hofmann, A., Reinhard, C.T., Lalonde, S.V., Knudsen, A., Wang, X.L., Ossa, F.O., Pecoits, E., Smith, A.J.B., Beukes, N.J., Bekker, A., Johnson, T.M., Konhauser, K.O., Lyons, T.W. and Rouxel, O.J. (2014) Evidence for oxygenic photosynthesis half a billiion years before the Great Oxidation Event. Nat Geosci 7, 283-286.

Pollard, R.T., Salter, I., Sanders, R.J., Lucas, M.I., Moore, C.M., Mills, R.A., Statham, P.J., Allen, J.T., Baker, A.R., Bakker, D.C.E., Charette, M.A., Fielding, S., Fones, G.R., French, M., Hickman, A.E., Holland, R.J., Hughes, J.A., Jickells, T.D., Lampitt, R.S., Morris, P.J., Nedelec, F.H., Nielsdottir, M., Planquette, H., Popova, E.E., Poulton, A.J., Read, J.F., Seeyave, S., Smith, T., Stinchcombe, M., Taylor, S., Thomalla, S., Venables, H.J., Williamson, R. and Zubkov, M.V. (2009) Southern Ocean deep-water carbon export enhanced by natural iron fertilization. Nature 457, 577-U581.

Posth, N.R., Konhauser, K.O. and Kappler, A. (2013) Microbiological processes in banded iron formation deposition. Sedimentology 60, 1733-1754.

Potter, P.E., Maynard, J.B. and Depetris, P.J. (2005) Mud and Mudstones. Springer-Verlag, Berlin Heidelberg.

Potts, P.J. and Webb, P.C. (1992) X-Ray-Fluorescence Spectrometry. J Geochem Explor 44, 251-296.

Préat, A.R., De Jong, J.T.M., De Ridder, C. and Gillan, D.C. (2011) Possible Fe Isotope Fractionation During Microbiological Processing in Ancient and Modern Marine Environments, in: Tewari, V., Seckbach, J. (Eds.), STROMATOLITES: Interaction of Microbes with Sediments. Springer Netherlands, Dordrecht, pp. 651-673.

Purser, B., Tucker, M.E. and Zenger, D., 21. , . (1994) Dolomites: A Volume in Honour of Dolomieu. Blackwell Science, Oxford.

Quinbyhunt, M.S. and Wilde, P. (1994) Thermodynamic Zonation in the Black Shale Facies Based on Iron-Manganese Vanadium Content. Chem Geol 113, 297-317.

Radic, A., Lacan, F. and Murray, J.W. (2011) Iron isotopes in the seawater of the equatorial Pacific Ocean: New constraints for the oceanic iron cycle. Earth Planet Sc Lett 306, 1-10.

Raiswell, R. and Canfield, D.E. (1998) Sources of iron for pyrite formation in marine sediments. Am J Sci 298, 219-245.

Rasmussen, B., Buick, R. and Holland, H.D. (1999) Redox state of the Archean atmosphere: Evidence from detrital heavy minerals in ca. 3250-2750 Ma sandstones from the Pilbara Craton, Australia: Reply. Geology 27, 1152-1152.

Rasmussen, B., Fletcher, I.R., Brocks, J.J. and Kilburn, M.R. (2008) Reassessing the first appearance of eukaryotes and cyanobacteria. Nature 455, 1101-U1109.

Ravel, B. and Newville, M. (2005) ATHENA, ARTEMIS, HEPHAESTUS: data analysis for X-ray absorption spectroscopy using IFEFFIT. J Synchrotron Radiat 12, 537-541.

Reeder, R. (1983) Crystal chemistry of the rhombohedral carbonates, in: Reeder, R. (Ed.), Carbonates: Mineralogy and Chemisty. Bookcrafters, Chelsea, pp. 1-47.

Reinhard, C.T., Lalonde, S.V. and Lyons, T.W. (2013) Oxidative sulfide dissolution on the early Earth. Chem Geol 362, 44-55.

Riding, R. (1991) Classification of Microbial Carbonates, in: Riding, R. (Ed.), Calcareous Algae and Stromatolites. Springer-Verlag, Berlin Heidelberg, pp. 21-51.

Riding, R. (2011) Microbialites, stromatolites, and thrombolites, in: Reitner, J., Thiel, V. (Eds.), Encyclopedia of Geobiology. Springer Netherlands, pp. 635-654.

Riding, R., Fralick, P. and Liang, L.Y. (2014) Identification of an Archean marine oxygen oasis. Precambrian Res 251, 232-237.

Robinson, J.J., Scott, K.M., Swanson, S.T., O'Leary, M.H., Horken, K., Tabita, F.R. and Cavanaugh, C.M. (2003) Kinetic isotope effect and characterization of form II RubisCO from the chemoautotrophic endosymbionts of the hydrothermal vent tubeworm Riftia pachyptila. Limnol Oceanogr 48, 48-54.

Romaniello, S.J., Herrmann, A.D. and Anbar, A. (2016) Syndepositional diagenetic control of molybdenum isotope variations in carbonate sediments from the Bahamas. Chem Geol 438, 84-90.

Rosing, M.T. and Frei, R. (2004) U-rich Archaean sea-floor sediments from Greenland - indications of > 3700 Ma oxygenic photosynthesis. Earth Planet Sc Lett 217, 237-244.

Rouxel, O., Sholkovitz, E., Charette, M. and Edwards, K.J. (2008) Iron isotope fractionation in subterranean estuaries. Geochim Cosmochim Ac 72, 3413-3430.

Rouxel, O.J., Bekker, A. and Edward, K.J. (2006) Response to comment on "Iron isotope constraints on the archean and paleoproterozoic ocean redox state". Science 311.

Rouxel, O.J., Bekker, A. and Edwards, K.J. (2005) Iron isotope constraints on the Archean and Paleoproterozoic ocean redox state. Science 307, 1088-1091.

Rubinson, M. and Clayton, R.N. (1969) Carbon-13 Fractionation between Aragonite and Calcite. Geochim Cosmochim Ac 33, 997-&.

Rudge, J.F., Reynolds, B.C. and Bourdon, B. (2009) The double spike toolbox. Chem Geol 265, 420-431.

Rudnick, R.L. and Gao, S. (2004) Composition of the Continental Crust, in: Holland, H.D., Turekian, K.K. (Eds.). Elsevier, Amsterdam, pp. 1-64.

Runnels, D.D. (1969) Diagenesis, chemical sediments, and the mixing of natural waters. Journal of Sedimentary Petrology 39, 1188-1201.

Sadezky, A., Muckenhuber, H., Grothe, H., Niessner, R. and Poschl, U. (2005) Raman micro spectroscopy of soot and related carbonaceous materials: Spectral analysis and structural information. Carbon 43, 1731-1742.

Savage, P.S., Georg, R.B., Williams, H.M., Burton, K.W. and Halliday, A.N. (2011) Silicon isotope fractionation during magmatic differentiation. Geochim Cosmochim Ac 75, 6124-6139.

Schauble, E.A. (2004) Applying Stable Isotope Fractionation Theory to New Systems, in: Johnson, C.M., Beard, B.L., Albarede, F. (Eds.), Geochemistry of Non-Traditional Stable Isotopes. Mineralogical Society of America, Washington, pp. 65-111.

Schmidt, G.A., Bigg, G.R. and Rohling, E.J. (1999) Global Seawater Oxygen-18 Database, Volume 2015: http://data.giss.nasa.gov/o18data/.

Schoenberg, R. and von Blanckenburg, F. (2005) An assessment of the accuracy of stable Fe isotope ratio measurements on samples with organic and inorganic matrices by high-resolution multicollector ICP-MS. Int J Mass Spectrom 242, 257-272.

Schoenberg, R. and von Blanckenburg, F. (2006) Modes of planetary-scale Fe isotope fractionation. Earth Planet Sc Lett 252, 342-359.

Schopf, J.W. (1993) Microfossils of the Early Archean Apex Chert - New Evidence of the Antiquity of Life. Science 260, 640-646.

Schroeder, S., Beukes, N.J. and Sumner, D.Y. (2009) Microbialite-sediment interactions on the slope of the Campbellrand carbonate platform (Neoarchean, South Africa). Precambrian Res 169, 68-79.

Schroeder, S., Lacassie, J.P. and Beukes, N.J. (2006) Stratigraphic and geochemical framework of the Agouron drill cores, Transvaal Supergroup (Neoarchean-Paleoproterozoic, South Africa). S Afr J Geol 109, 23-54.

Scott, C. and Lyons, T.W. (2012) Contrasting molybdenum cycling and isotopic properties in euxinic versus non-euxinic sediments and sedimentary rocks: Refining the paleoproxies. Chem Geol 324, 19-27.

Scott, C., Lyons, T.W., Bekker, A., Shen, Y., Poulton, S.W., Chu, X. and Anbar, A.D. (2008) Tracing the stepwise oxygenation of the Proterozoic ocean. Nature 452, 456-U455.

Scott, K.M., Schwedock, J., Schrag, D.P. and Cavanaugh, C.M. (2004) Influence of form IA RubisCO and environmental dissolved inorganic carbon on the delta C-13 of the clam-chemoautotroph symbiosis Solemya velum. Environ Microbiol 6, 1210-1219.

Seto, M. and Akagi, T. (2008) Chemical condition for the appearance of a negative Ce anomaly in stream waters and groundwaters. Geochem J 42, 371-380.

Severmann, S., Johnson, C.M., Beard, B.L. and McManus, J. (2006) The effect of early diagenesis on the Fe isotope compositions of porewaters and authigenic minerals in continental margin sediments. Geochim Cosmochim Ac 70, 2006-2022.

Severmann, S., Lyons, T.W., Anbar, A., McManus, J. and Gordon, G. (2008) Modern iron isotope perspective on the benthic iron shuttle and the redox evolution of ancient oceans. Geology 36, 487-490.

Sforna, M.C., van Zuilen, M.A. and Philippot, P. (2014) Structural characterization by Raman hyperspectral mapping of organic carbon in the 3.46 billion-year-old Apex chert, Western Australia. Geochim Cosmochim Ac 124, 18-33.

Shields, G. and Veizer, J. (2002) Precambrian marine carbonate isotope database: Version 1.1. Geochem Geophy Geosy 3.

Shimmield, G.B. and Price, N.B. (1986) The Behavior of Molybdenum and Manganese during Early Sediment Diagenesis - Offshore Baja-California, Mexico. Mar Chem 19, 261-280.

Siebert, C., Nagler, T.F. and Kramers, J.D. (2001) Determination of molybdenum isotope fractionation by double-spike multicollector inductively coupled plasma mass spectrometry. Geochem Geophy Geosy 2, art. no.-2000GC000124.

Siebert, C., Nagler, T.F., von Blanckenburg, F. and Kramers, J.D. (2003) Molybdenum isotope records as a potential new proxy for paleoceanography. Earth Planet Sc Lett 211, 159-171.

Simms, M. (1984) Dolomitization by Groundwater-Flow Systems in Carbonate Platforms. Aapg Bull 68, 1219-1220.

Sirevag, R. (1995) Carbon metabolism in green bacteria, in: Blankenship, R.E., Madigan, M.T., Bauer, C.E. (Eds.), Anoxygenic Photosynthetic Bacteria: Advances in Photosynthesis, Dordrecht, pp. 871-883.

Skulan, J.L., Beard, B.L. and Johnson, C.M. (2002) Kinetic and equilibrium Fe isotope fractionation between aqueous Fe(III) and hematite. Geochim Cosmochim Ac 66, 2995-3015.

Smart, P.L., Dawans, J.M. and Whitaker, F. (1988) Carbonate Dissolution in a Modern Mixing Zone. Nature 335, 811-813.

Sole, V.A., Papillon, E., Cotte, M., Walter, P. and Susini, J. (2007) A multiplatform code for the analysis of energy-dispersive X-ray fluorescence spectra. Spectrochim Acta B 62, 63-68.

Staubwasser, M., von Blanckenburg, F. and Schoenberg, R. (2006) Iron isotopes in the early marine diagenetic iron cycle. Geology 34, 629-632.

Steinhoefel, G., von Blanckenburg, F., Horn, I., Konhauser, K.O., Beukes, N.J. and Gutzmer, J. (2010) Deciphering formation processes of banded iron formations from the Transvaal and the Hamersley successions by combined Si and Fe isotope analysis using UV femtosecond laser ablation. Geochim Cosmochim Ac 74, 2677-2696.

Sumner, D. (2002) Neoarchean Carbonates - Clues to Early Life and Early Ocean Chemistry, 16th International Sedimentological Congress. International Association of Sedimentologists, Rand Afrikaans University - Johannesburg, South Africa.

Sumner, D.Y. and Beukes, N.J. (2006) Sequence stratigraphic development of the Neoarchean Transvaal carbonate platform, Kaapvaal Craton, South Africa. S Afr J Geol 109, 11-22.

Sumner, D.Y. and Grotzinger, J.P. (1996) Were kinetics of Archean calcium carbonate precipitation related to oxygen concentration? Geology 24, 119-122.

Sumner, D.Y. and Grotzinger, J.P. (2004) Implications for Neoarchaean ocean chemistry from primary carbonate mineralogy of the Campbellrand-Malmani Platform, South Africa. Sedimentology 51, 1273-1299.

Sumner, D.Y., Hawes, I., Mackey, T.J., Jungblut, A.D. and Doran, P.T. (2015) Antarctic microbial mats: A modern analog for Archean lacustrine oxygen oases. Geology 43, 887-890.

Swanner, E.D., Mloszewska, A.M., Cirpka, O.A., Schoenberg, R., Konhauser, K.O. and Kappler, A. (2015a) Modulation of oxygen production in Archaean oceans by episodes of Fe(II) toxicity. Nat Geosci 8, 126-130.

Swanner, E.D., Wu, W.F., Schoenberg, R., Byrne, J., Michel, F.M., Pan, Y.X. and Kappler, A. (2015b) Fractionation of Fe isotopes during Fe(II) oxidation by a marine photoferrotroph is controlled by the formation of organic Fe-complexes and colloidal Fe fractions. Geochim Cosmochim Ac 165, 44-61.

Swart, P.K., Ruiz, J. and Holmes, C.W. (1987) Use of Strontium Isotopes to Constrain the Timing and Mode of Dolomitization of Upper Cenozoic Sediments in a Core from San Salvador, Bahamas. Geology 15, 262-265.

Tabita, F.R. (1999) Microbial ribulose 1,5-bisphosphate carboxylase/oxygenase: A different perspective. Photosynth Res 60, 1-28.

Taylor, P.D.P., Maeck, R. and De Bievre, P. (1992) Determination of the Absolute Isotopic Composition and Atomic-Weight of a Reference Sample of Natural Iron. International Journal of Mass Spectrometry and Ion Processes 121, 111-125.

Taylor, S.R. and MacLennan, S.H. (1985) The Continental Crust: Its Composition and Evolution. Blackwell, Oxford.

Teutsch, N., von Gunten, U., Porcelli, D., Cirpka, O.A. and Halliday, A.N. (2005) Adsorption as a cause for iron isotope fractionation in reduced groundwater. Geochim Cosmochim Ac 69, 4175-4185.

Thomazo, C., Pinti, D.L., Busigny, V., Ader, M., Hashizume, K. and Philippot, P. (2009) Biological activity and the Earth's surface evolution: Insights from carbon, sulfur, nitrogen and iron stable isotopes in the rock record. Cr Palevol 8, 665-678.

Tossell, J.A. (2005) Calculating the partitioning of the isotopes of Mo between oxidic and sulfidic species in aqueous solution. Geochim Cosmochim Ac 69, A210-A210.

Tribovillard, N., Algeo, T.J., Lyons, T. and Riboulleau, A. (2006) Trace metals as paleoredox and paleoproductivity proxies: An update. Chem Geol 232, 12-32.

Truswell, J.F. and Eriksson, K.A. (1972) The morphology of stromatolites from the Malmani Dolomite north-west of Johannesburg, South Africa. Transactions of the Geological Society of South Africa 75, 99-110.

Truswell, J.F. and Eriksson, K.A. (1975) A palaeoenvironmental interpretation of the Early Proterozoic Malmani Dolomite from Zwartkops, South Africa. Precambrian Res 2, 277-303.

Turcotte, D.L. (1980) On the Thermal Evolution of the Earth. Earth Planet Sc Lett 48, 53-58.

Urey, H.C. (1947) The Thermodynamic Properties of Isotopic Substances. Journal of the Chemical Society, 562-581.

Valdivieso-Ojeda, J.A., Huerta-Diaz, M.A. and Delgadillo-Hinojosa, F. (2014) High enrichment of molybdenum in hypersaline microbial mats of Guerrero Negro, Baja California Sur, Mexico. Chem Geol 363, 341-354.

Valentine, D.L., Chidthaisong, A., Rice, A., Reeburgh, W.S. and Tyler, S.C. (2004) Carbon and hydrogen isotope fractionation by moderately thermophilic methanogens. Geochim Cosmochim Ac 68, 1571-1590.

Valley, J.W. (1986) Stable isotope geochemistry of metamorphic rocks, in: Valley, J.W., Taylor, H.P., O'Neil, J.R. (Eds.), Stable Iso-topes in High Temperature Geological Pro-cesses. Mineralogical Society of America, pp. 445-498.

Valley, J.W. and O'Neil, J.R. (1981) C-13-C-12 Exchange between Calcite and Graphite - a Possible Thermometer in Grenville Marbles. Geochim Cosmochim Ac 45, 411-419.

van den Boorn, S.H.J.M. (2008) Silicon isotopes and the origin of Archaean cherts. University of Utrecht, p. 277.

van den Boorn, S.H.J.M., Vroon, P.Z., van Belle, C.C., van der Wagt, B., Schwieters, J. and van Bergen, M.J. (2006) Determination of silicon isotope ratios in silicate materials by high-resolution MC-ICP-MS using a sodium hydroxide sample digestion method. J Anal Atom Spectrom 21, 734-742.

van der Zee, C., Roberts, D.R., Rancourt, D.G. and Slomp, C.P. (2003) Nanogoethite is the dominant reactive oxyhydroxide phase in lake and marine sediments. Geology 31, 993-996.

Van Kranendonk, M.J. (2006) Volcanic degassing, hydrothermal circulation and the flourishing of early life on Earth: A review of the evidence from c. 3490-3240 Ma rocks of the Pilbara Supergroup, Pilbara Craton, Western Australia. Earth-Sci Rev 74, 197-240.

Veizer, J. (1983) Chemical diagenesis of carbonates: theory and application of trace element techniques, in: Arthur, M.A., Anderson, T.F., Kaplan, I.R., Veizer, J., Land, L.S. (Eds.), Stable Isotopes in Sedimentary Geology. Society of Economic Paleontologists and Mineralogists Short Course Notes, pp. III-1-III-100.

Veizer, J., Ala, D., Azmy, K., Bruckschen, P., Buhl, D., Bruhn, F., Carden, G.A.F., Diener, A., Ebneth, S., Godderis, Y., Jasper, T., Korte, C., Pawellek, F., Podlaha, O.G. and Strauss, H. (1999) Sr-87/Sr-86, delta C-13 and delta O-18 evolution of Phanerozoic seawater. Chem Geol 161, 59-88.

Voegelin, A.R., Nagler, T.F., Beukes, N.J. and Lacassie, J.P. (2010) Molybdenum isotopes in late Archean carbonate rocks: Implications for early Earth oxygenation. Precambrian Res 182, 70-82.

Voegelin, A.R., Nagler, T.F., Samankassou, E. and Villa, I.M. (2009) Molybdenum isotopic composition of modern and Carboniferous carbonates. Chem Geol 265, 488-498.

Voegelin, A.R., Pettke, T., Greber, N.D., von Niederhausern, B. and Nagler, T.F. (2014) Magma differentiation fractionates Mo isotope ratios: Evidence from the Kos Plateau Tuff (Aegean Arc). Lithos 190, 440-448.

Vogel, J.C., Grootes, P.M. and Mook, W.G. (1970) Isotopic Fractionation between Gaseous and Dissolved Carbon Dioxide. Z Phys 230, 225-&.

von Blanckenburg, F., Marnberti, M., Schoenberg, R., Kamber, B.S. and Webb, G.E. (2008) The iron isotope composition of microbial carbonate. Chem Geol 249, 113-128.

Waldbauer, J.R., Sherman, L.S., Sumner, D.Y. and Summons, R.E. (2009) Late Archean molecular fossils from the Transvaal Supergroup record the antiquity of microbial diversity and aerobiosis. Precambrian Res 169, 28-47.

Wang, K., Savage, P.S. and Moynier, F. (2014) The iron isotope composition of enstatite meteorites: Implications for their origin and the metal/sulfide Fe isotopic fractionation factor. Geochim Cosmochim Ac 142, 149-165.

Webb, G.E. and Kamber, B.S. (2000) Rare earth elements in Holocene reefal microbialites: A new shallow seawater proxy. Geochim Cosmochim Ac 64, 1557-1565.

Welch, S.A., Beard, B.L., Johnson, C.M. and Braterman, P.S. (2003) Kinetic and equilibrium Fe isotope fractionation between aqueous Fe(II) and Fe(III). Geochim Cosmochim Ac 67, 4231-4250.

Weyer, S., Anbar, A.D., Brey, G.P., Munker, C., Mezger, K. and Woodland, A.B. (2005) Iron isotope fractionation during planetary differentiation. Earth Planet Sc Lett 240, 251-264.

Wickman, F.E. (1956) The cycle of carbon and the stable carbon isotopes. Geochim Cosmochim Ac 9, 136-153.

Wiesli, R.A., Beard, B.L. and Johnson, C.M. (2004) Experimental determination of Fe isotope fractionation between aqueous Fe(II), siderite and "green rust" in abiotic systems. Chem Geol 211, 343-362.

Wilkin, R.T. and Barnes, H.L. (1997) Formation processes of framboidal pyrite. Geochim Cosmochim Ac 61, 323-339.

Wille, M., Kramers, J.D., Nagler, T.F., Beukes, N.J., Schroder, S., Meisel, T., Lacassie, J.P. and Voegelin, A.R. (2007) Evidence for a gradual rise of oxygen between 2.6 and 2.5 Ga from Mo isotopes and Re-PGE signatures in shales. Geochim Cosmochim Ac 71, 2417-2435.

Wille, M., Sutton, J., Ellwood, M.J., Sambridge, M., Maher, W., Eggins, S. and Kelly, M. (2010) Silicon isotopic fractionation in marine sponges: A new model for understanding silicon isotopic variations in sponges. Earth Planet Sc Lett 292, 281-289.

Yamaguchi, K.E., Johnson, C.M., Beard, B.L. and Ohmoto, H. (2005) Biogeochemical cycling of iron in the Archean-Paleoproterozoic Earth: Constraints from iron isotope variations in sedimentary rocks from the Kaapvaal and Pilbara Cratons. Chem Geol 218, 135-169.

Yamaguchi, K.E. and Ohmoto, H. (2006) Comment on "Iron isotope constraints on the archean and paleoproterozoic ocean redox state". Science 311.

Young, G.M., Long, D.G.F., Fedo, C.M. and Nesbitt, H.W. (2001) Paleoproterozoic Huronian basin: product of a Wilson cycle punctuated by glaciations and a meteorite impact. Sediment Geol 141, 233-254.

Zeebe, R.E. and Wolf-Gladrow, D.A. (2001) CO2 in Seawater: Equilibrium, Kinetics, Isotopes, Amsterdam.

Ziegler, K., Chadwick, O.A., Brzezinski, M.A. and Kelly, E.F. (2005) Natural variations of delta Si-30 ratios during progressive basalt weathering, Hawaiian Islands. Geochim Cosmochim Ac 69, 4597-4610.